USC

UNIVERSITY OF SOUTHERN CALIFORNIA

USC OMDL 1901 ②

INTEGRATED OPTICAL INFORMATION PROCESSING

AFOSR-85-0312

FINAL RESEARCH REPORT
(RESEARCH PERIOD: 09/01/85 - 08/31/87

DTIC
ELECTE
OCT 0 6 1988
D

Submitted To:

Air Force Office of Scientific Research
Electronics and Materials Science Division
AFOSR/NE
Bolling AFB, Bldg. 410
Washington, D.C. 20332
Attn: Dr. C. Lee Giles

Submitted By:

Dr. Armand R. Tanguay, Jr.
Optical Materials and Devices Laboratory
University of Southern California
University Park, MC-0483
Los Angeles, California 90089

OMDL OPTICAL MATERIALS AND DEVICES LABORATORY

REPORT DOCUMENTATION PAGE

1a. REPORT SECURITY CLASSIFICATION	1b. RESTRICTIVE MARKINGS
UNCLASSIFIED	

2a. SECURITY CLASSIFICATION AUTHORITY	3. DISTRIBUTION/AVAILABILITY OF REPORT
	APPROVED FOR PUBLIC RELEASE:
2b. DECLASSIFICATION/DOWNGRADING SCHEDULE	DISTRIBUTION UNLIMITED

4. PERFORMING ORGANIZATION REPORT NUMBER(S)	5. MONITORING ORGANIZATION REPORT NUMBER(S)
USC OMDL-1901	AFOSR-TR- 8 8 - 0 9 9 4

6a. NAME OF PERFORMING ORGANIZATION	6b. OFFICE SYMBOL (If applicable)	7a. NAME OF MONITORING ORGANIZATION
UNIVERSITY OF SOUTHERN CALIFORNIA		AIR FORCE OFFICE OF SCIENTIFIC RESEARCH

6c. ADDRESS (City, State and ZIP Code)	7b. ADDRESS (City, State and ZIP Code)
UNIVERSITY OF SOUTHERN CALIFORNIA UNIVERSITY PARK, MC-0483 LOS ANGELES, CALIFORNIA 90089-0483	AFOSR/NE BUILDING 410 BOLLING AFB, DC 20332

8a. NAME OF FUNDING/SPONSORING ORGANIZATION	8b. OFFICE SYMBOL (If applicable)	9. PROCUREMENT INSTRUMENT IDENTIFICATION NUMBER
AFOSR	NE	AFOSR-85-0312

8c. ADDRESS (City, State and ZIP Code)	10. SOURCE OF FUNDING NOS.			
Bldg 410 Bolling AFB, DC 20332	PROGRAM ELEMENT NO.	PROJECT NO.	TASK NO.	WORK UNIT NO.
11. TITLE (Include Security Classification) INTEGRATED OPTICAL INFORMATION PROCESSING	61102F	2305	B4	

12. PERSONAL AUTHOR(S)
DR. ARMAND R. TANGUAY, JR.

13a. TYPE OF REPORT	13b. TIME COVERED	14. DATE OF REPORT (Yr., Mo., Day)	15. PAGE COUNT
FINAL REPORT	FROM 09/01/85 TO 08/31/87	1988, AUGUST	249

16. SUPPLEMENTARY NOTATION

17.	COSATI CODES		18. SUBJECT TERMS (Continue on reverse if necessary and identify by block number)
FIELD	GROUP	SUB. GR.	OPTICAL INFORMATION PROCESSING, OPTICAL COMPUTING, INTEGRATED OPTICS, GUIDED WAVE OPTICS, SYNTHETIC APERTURE RADAR,

19. ABSTRACT (Continue on reverse if necessary and identify by block number)

The principal objective of this research program was the advancement of novel integrated optical and optoelectronic device technology suitable for inherently nonplanar optical information processing applications. As a first demonstration, a compact, low cost, low power optical synthetic aperture radar (SAR) processor was investigated for real time image formation aboard airborne and spaceborne platforms. The key to implementation of the integrated optical SAR processor is the use of a time- and space-integrating architecture, which allows two-dimensional processing to be performed with inherently one-dimensional signal processing devices. This permits the monolithic or hybrid integration of all of the necessary components into a single compact structure. An additional novel feature of this concept is the utilization of partial waveguide confinement (selective outcoupling) to achieve either uniform or modulated light emission vertically out of the integrated optical substrate plane. This feature in turn permits the realization of three dimensional optical signal processing architectures.

20. DISTRIBUTION/AVAILABILITY OF ABSTRACT	21. ABSTRACT SECURITY CLASSIFICATION
UNCLASSIFIED/UNLIMITED ☒ SAME AS RPT ☐ OTIC USERS ☐	UNCLASSIFIED

22a. NAME OF RESPONSIBLE INDIVIDUAL	22b. TELEPHONE NUMBER (Include Area Code)	22c. OFFICE SYMBOL
Giles	202-767-4931	NE

DD FORM 1473, 83 APR

EDITION OF 1 JAN 73 IS OBSOLETE

88 10 5 303

19. <u>ABSTRACT</u> (continued)

The unique features of this optical processing concept include:

1. The implementation of two-dimensional information processing utilizing both integrated optics and time- and space-integration;

2. Vertical integration of an optical waveguide with extra-planar optoelectronic components such as a CCD image sensor;

3. Use of in-plane rib or channel waveguiding to retain image dissection integrity;

4. Surface acoustic wave generation in optical waveguide materials with slow acoustic velocity to achieve large effective time delays;

5. Selective partial waveguide outcoupling of channelized light from an integrated optical chip;

6. Potential monolithic integration of optical waveguides with two-dimensional optoelectronic detector technology.

The integrated optical architecture described in this report is potentially programmable to allow additional types of computational algorithms to be implemented. These include the compensation of SAR images for changes in platform variables and geometric distortions; two-dimensional correlation, convolution, and Fourier transform operations; selective frequency cross-correlations; and real time computation of ambiguity functions.

During the contract period, significant progress has been achieved in the design, development and implementation of the advanced integrated optical components necessary to achieve the required degree of integration. These components include wide aperture low F-number integrated optical lenses fabricated by titanium indiffusion within a titanium-indiffused and proton exchanged waveguide, large area rib waveguide arrays with a pitch appropriate for the focal properties of the system (660 individual rib waveguides 8 microns wide with 2 micron gaps), and submicron resolution outcoupling gratings fabricated on top of the rib waveguide arrays.

The degree of integration achieved to date incorporates all of the above elements on a single integrated optical chip. The near diffraction limited performance obtained from the integrated lenses allowed for the demonstration of focusing into a single rib within the entire array. Uniform outcoupling from the single rib waveguide was also achieved, well within the sensitivity range of typical CCD detector arrays for modest input optical power levels.

INTEGRATED OPTICAL INFORMATION PROCESSING

TABLE OF CONTENTS

INTEGRATED OPTICAL INFORMATION PROCESSING

LIST OF FIGURES

INTEGRATED OPTICAL INFORMATION PROCESSING

LIST OF APPENDICES

A-1

INTEGRATED OPTICAL INFORMATION PROCESSING

ABSTRACT

The principal objective of this research program was the advancement of novel integrated optical and optoelectronic device technology suitable for inherently nonplanar optical information processing applications. As a first demonstration, a compact, low cost, low power optical synthetic aperture radar (SAR) processor was investigated for real time image formation aboard airborne and spaceborne platforms. The key to implementation of the integrated optical SAR processor is the use of a time- and space-integrating architecture, which allows two-dimensional processing to be performed with inherently one-dimensional signal processing devices. This permits the monolithic or hybrid integration of all of the necessary components into a single compact structure. An additional novel feature of this concept is the utilization of partial waveguide confinement (selective outcoupling) to achieve either uniform or modulated light emission vertically out of the integrated optical substrate plane. This feature in turn permits the realization of three dimensional optical signal processing architectures.

The unique features of this optical processing concept include:

1. The implementation of two-dimensional information processing utilizing both integrated optics and time- and space-integration;

2. Vertical integration of an optical waveguide with extra-planar optoelectronic components such as a CCD image sensor;

3. Use of in-plane rib or channel waveguiding to retain image dissection integrity;

4. Surface acoustic wave generation in optical waveguide materials with slow acoustic velocity to achieve large effective time delays;

5. Selective partial waveguide outcoupling of channelized light from an integrated optical chip;

6. Potential monolithic integration of optical waveguides with two-dimensional optoelectronic detector technology.

The integrated optical architecture described in this report is potentially programmable to allow additional types of computational algorithms to be implemented. These include

the compensation of SAR images for changes in platform variables and geometric distortions; two-dimensional correlation, convolution, and Fourier transform operations; selective frequency cross-correlations; and real time computation of ambiguity functions.

During the contract period, significant progress has been achieved in the design, development, and implementation of the advanced integrated optical components necessary to achieve the required degree of integration. These components include wide aperture low F-number integrated optical lenses fabricated by titanium indiffusion within a titanium-indiffused and proton exchanged waveguide, large area rib waveguide arrays with a pitch appropriate for the focal properties of the system (660 individual rib waveguides 8 microns wide with 2 micron gaps), and submicron resolution outcoupling gratings fabricated on top of the rib waveguide arrays.

The degree of integration achieved to date incorporates all of the above elements on a single integrated optical chip. The near diffraction limited performance obtained from the integrated lenses allowed for the demonstration of focusing into a single rib within the entire array. Uniform outcoupling from the single rib waveguide was also achieved, well within the sensitivity range of typical CCD detector arrays for modest input optical power levels.

INTEGRATED OPTICAL INFORMATION PROCESSING

1. INTRODUCTION

The primary goal of the research program described herein was the development of novel integrated optical devices that can be used in the implementation of optical information processing systems constructed in three dimensions. The development of optical processors thus far has progressed along two basically separate paths: integrated or guided wave optics, and bulk or free space propagation systems. The principal advantage of bulk systems is the fact that they can be readily configured in three dimensions and consequently can exhibit extremely high computational power. The three dimensional nature of these systems gives optics a clear advantage over semiconductor technology, which is inherently planar.

The principal advantage of semiconductor technology is the very advanced state of development of the device technology involved. In contrast, the devices used in bulk optical processors are highly specialized, typically requiring a long development cycle to produce a few devices that are suitable for system applications. This is not only very expensive, but also impedes the progress of the whole field since system architects are forced to rely on a very small number of available devices, which in turn severely limits the range of architectures that can be optically implemented.

Integrated optics, on the other hand, shares to a large extent the generic character of the fabrication technology that is the hallmark of semiconductor devices. We believe that this feature is the most significant attribute of integrated optical processors. The obvious limitation of currently investigated integrated or guided-wave optical systems, on the other hand, is that they are planar, and therefore do not utilize the most distinctive and powerful features of optics. The research we describe herein was aimed at developing optical processors that share the positive attributes of both integrated and bulk systems, and hopefully have the limitations of neither. Specifically, we have developed a new class of integrated optical devices that exhibit the capability for communicating information from the planar structure into the third dimension, are fabricated using standard or modified microfabrication techniques, and allow the flexible hybrid integration of optical, electrooptical, and possibly purely electronic devices into a powerful computing structure. The objective is to produce a flexible, generic device technology for optical information processing systems that are configurable in three dimensions.

There are several ways that signals in a planar structure can be optically communicated into the third dimension. For instance, if the signals in the device plane are electrical, then they can be used to optically modulate an incident light beam. This

function is representative of an electrically addressed spatial light modulator. If optical signals are guided within the plane as well, then we need to provide mechanisms for vertical outcoupling. We can also imagine hybrid devices in which optical signals guided in the plane interact with electrically applied signals, following which the light is broadcast into the third dimension. If the planar structures are implemented on semiconductor substrates, or if dielectric and semiconductor substrates are combined into a single multilayer structure, then signals can be electronically processed within the plane and then optically communicated into the third dimension. All such devices create very interesting architectural possibilities. Thus the proposed development of devices that are fabricated using conventional or modified planar microfabrication techniques and that are suitable for the implementation of three dimensional processors can have a broad impact in optical signal processing and computing.

We have selected synthetic aperture radar as a specific problem to which we have applied the general ideas outlined above. SAR is a two dimensional signal processing problem that normally requires a three dimensional optical implementation. We have identified an optical architecture, that will be discussed in more detail below, for performing SAR imaging utilizing integrated optics. This processor makes use of all of the essential features of the integrated optical devices we propose to develop. Namely, it requires that optical processing be performed both within and outside the planar structure, it requires that light is coupled vertically out of the plane of the integrated optics chip, it requires the integration of optical and electro-optical devices, and it requires that a combination of optical and electronic processing be performed. We have thus chosen SAR as a specific application towards which we will focus our efforts in developing integrated optical devices suitable for the implementation of three dimensional processors. In addition to providing a focused vehicle for the development of the necessary technologies, this particular choice of SAR image formation will also demonstrate the power of the proposed approach by providing an elegant solution to a difficult problem.

Synthetic aperture radar (SAR) is a very powerful imaging technique that allows the formation of high resolution images using radar-frequency probes. In a conventional real aperture imaging radar, the resolution is inversely proportional to the aperture dimension of the imaging system. Thus, improved resolution can only be obtained at the expense of a large radar antenna, which is in general too bulky to carry aboard an airborne or spaceborne platform. In many cases, the desired resolution would require antennas of truly massive size, which are impractical for any platform. In a SAR system, on the other hand, the resolution is approximately equal to the antenna aperture in the azimuth direction, and it is entirely independent of the antenna aperture in the range dimension.

The signal detected by a SAR system, however, is not a focused image; extensive

processing is required to form the image from the received signal. Film based optical processing systems have been very effectively used in the past twenty-five years to perform the required SAR processing. More recently, digital computers have been also used extensively in SAR image formation. However, film based optical processors and high speed minicomputers are not suitable for real time image formation aboard the radar platform because of computational speed limitations, and also because of the large size, weight and power consumption of such systems.

In order to circumvent such difficulties, optical techniques have been demonstrated at both Caltech and USC that allow real time SAR image formation with relatively compact and power efficient optical systems. These systems were implemented with discrete components [1,2,3]. In one approach [1,2], an acoustooptic cell was employed to input each radar return into a time-and-space integrating optical architecture comprised of several lenses, a CCD area array detector, and a proximity-coupled mask. In this approach, the range compression derives from self-focusing of the chirped radar pulse, while azimuth compression is achieved by mask multiplication and sequential time-integration on the CCD array, operated in the shift-and-add mode. This architecture is explained in more detail in Section 2 and in Appendix A. In the second approach [3], the incoming radar return at a given azimuth coordinate is written onto one column of a two-dimensional real-time spatial light modulator such as the PROM (Pockels Readout Optical Modulator) [4]. Sequential pulses are written onto adjacent columns. This input function is performed by a serial-to-parallel converter such as the Linear Array Total Internal Reflection Spatial Light Modulator [5]. Range and azimuth compression are then both achieved in parallel by means of an anamorphic imaging system, which relies on the self-focusing properties of the radar return Fresnel zone plate in both dimensions.

A further reduction in the size, weight, power and cost requirements of a real-time SAR processor can be realized if these optical components could be integrated onto a single optical waveguide substrate. The value of such an achievement can be immediately realized by comparison of several pertinent characteristics of existing real-time SAR processors. For example, a current digital implementation comprises the equivalent of two vertical six-foot equipment racks, weighs about 1500 pounds, consumes from one to five kilowatts of power, and costs several hundred thousand dollars [6]. The optical implementations described above are of order one-half cubic meter in size, weigh about twenty pounds, consume less than five watts of power, and cost about ten thousand dollars. The integrated optical approach proposed herein will be of order four cubic inches in size, weigh about one-half pound, consume less than 200 milliwatts of power, and cost no more than a few hundred dollars in quantity.

The novel aspect of the research reported herein is the computation of two-dimensional

operations using integrated optics. The formation of a SAR image is inherently a two-dimensional operation, in that both azimuth and range information must be extracted from the microwave radar returns. Integrated optics, on the other hand, is a planar technology usually thought suited for only one-dimensional processing functions (and to which it has been recently applied [7,8,9]. In this research program, we have proposed to implement two-dimensional processing within an integrated optics structure, using the time-and-space integrating architecture [10]. With this method, two-dimensional data is encoded in time and one spatial coordinate, and the data is processed by a combination of spatial and temporal integration within the optical system to achieve the requisite range and azimuth compression functions. Although only one spatial coordinate is utilized, it is possible to accomplish extremely complicated two-dimensional signal processing functions such as SAR image formation within the confines of the planar integrated optics structure by means of a novel architecture that involves the vertical extraction of image intensity from an array of parallel waveguides. Temporal integration is provided by a proximity-coupled area array CCD detector.

2. BACKGROUND OF RESEARCH PROGRAM

Microfabrication techniques that are commonly used in the semiconductor industry have also been used extensively for the fabrication of optical devices, most notably semiconductor light sources, detectors, and of course integrated optics. Our primary interest is in using these fabrication techniques to build integrated optical devices that can be used in three dimensional architectures. Some of the recent work on spatial light modulators is largely based on these same fabrication techniques. Such spatial light modulators include the Litton magnetooptic device [11], the gallium arsenide CCD spatial light modulator under development at Lincoln Labs [12], and the Xerox Linear Array TIR Spatial Light Modulator [5]. We believe that it is not accidental that the three devices mentioned above are among the most exciting device developments in optical processing. The development of semiconductor chips with optical sources and detectors that has been undertaken recently for providing optical communications within and among semiconductor circuits is another relevant area. As such, there is a significant accumulation of knowledge and experience that allowed us to achieve rapid progress in the fabrication of integrated optical devices for three dimensional optical systems and the implementation of the SAR system in particular.

The integrated optical implementation of the SAR processor is based on principles previously developed for a bulk acoustooptic implementation. A schematic diagram of the acoustooptic SAR processor [1,2] is shown in Fig. 1. The theory of operation of this processor is described in detail in Appendix A. Briefly, the input to the processor is the radar signal return, which is applied to the acousotooptic device (AOD) in Fig. 1. The light diffracted by the AOD is expanded uniformly in the vertical direction and it self-focuses horizontally due to the linear FM pulse shape of the radar signal. The self-focusing of the diffracted light produces a focused radar image in the range dimension only. The range focused image is multiplied by a fixed two-dimensional mask, on which the azimuth phase history is recorded, and the product is detected on a two-dimensional CCD detector array. The photogenerated charge on the CCD is continuously transferred step-wise in the vertical direction during the exposure of the device to light. The relative motion between the signal on the CCD and the stationary mask results in the required correlation in the azimuth direction. Thus the output video signal from the CCD is the two-dimensional, focused radar image. In this architecture the simultaneous use of time and space integration allows the two-dimensional image-forming operation to be implemented with the one-dimensional AOD as the input transducer. This implementation utilizes two transverse spatial coordinates; the second dimension is needed to uniformly expand the light in order to address the two-dimensional mask and CCD. In the integrated optics (IO) implementation of such a processor, a method must therefore be found
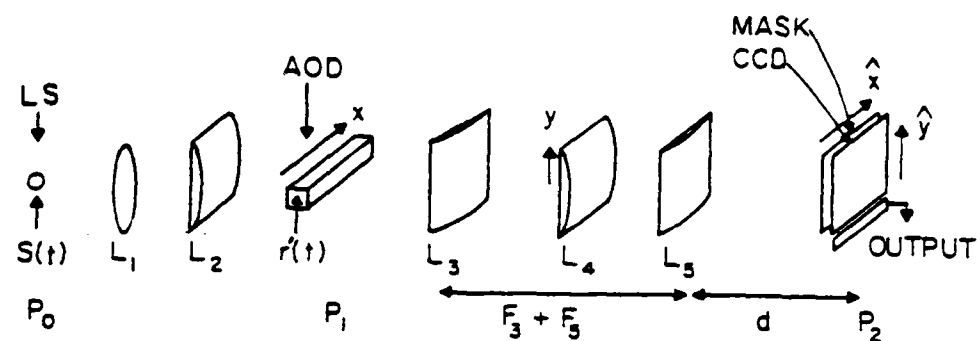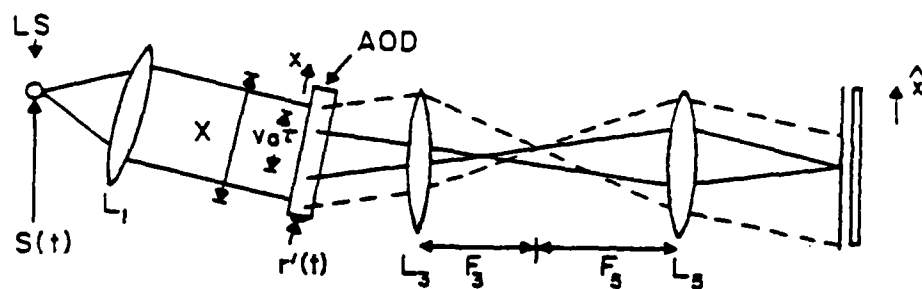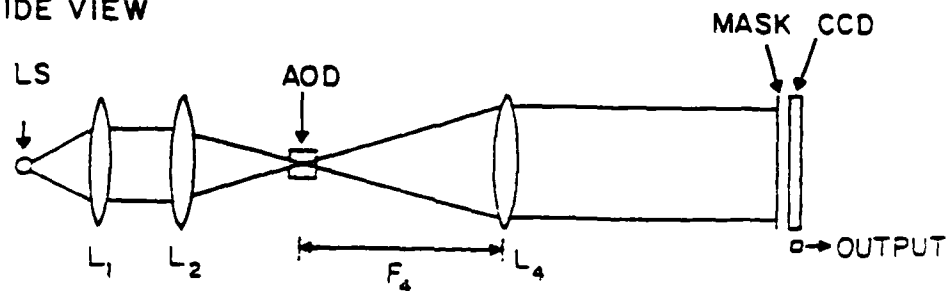
Fig. 1. Acoustooptic synthetic aperture radar processor utilizing discrete components [1]. The top view shows the range focus due to the linear FM SAR return; the side view shows the vertical expansion in a given range bin required for time integration on the CCD array detector.

for addressing the mask and CCD in a planar geometry. This method is described in Section 4.

The components of the SAR processor that we are interested in integrating on a single substrate are the light source, detector, lenses, waveguides, and modulators. Therefore, in selecting a substrate material, consideration must be given to the technology that is available for fabricating each of the individual components with this material. At present, no one material exists within which all the required components can be optimally fabricated. Consequently, fully integrated optical systems are not yet feasible. The material most commonly used thus far is $LiNbO_3$, within which optical waveguides, lenses, electrooptic and acoustooptic (SAW) modulators can be monolithically fabricated. The laser diode source and detector are typically butt-coupled at the two ends of the integrated optics chip. Materials such as GaAs and III-V multiple quantum well structures show promise for full integration in future years.

To date, integrated optical spectrum analyzers [9, 13], one-dimensional correlators [8, 14], and simple vector-matrix multipliers [15] have already been demonstrated. However, until now the implementation of two dimensional signal processing operations has not been possible with integrated optics. The time and space integrating method, combined with in-plane waveguiding and vertical outcoupling into the third dimension (as described below) provides a potentially powerful and elegant solution to this problem.

As described in the Introduction, the incorporation of a surface acoustic wave transducer, an integrated optical waveguide, a rib or channel parallel waveguide array, vertical outcoupling, two-dimensional masking, and a CCD array detector into a single hybrid integrated structure provides significant potential for compact, reliable, and low power optical processing and computing systems. Many possible versions and modifications of the basic structure can be envisioned, ranging from algorithmic changes imposed by the two-dimensional mask, through time-and space-integration variations, to multiply layered structures that implement extremely sophisticated functions. In this section, we describe one possible architecture for implementing synthetic aperture radar image formation. As discussed previously, the purpose of the initial focus on this particular implementation was to provide a specific vehicle for the development of technologies and concepts that will both allow immediate implementation of a processor that is competitive with other electronic and optical approaches, and allow generalization to a broader class of problems.

The Integrated Optical Synthetic Aperture Radar Processor (IOSARP) is shown in Fig. 2. It consists of a single crystal substrate which has been modified to change the index of refraction of a shallow layer near the surface and thus form a planar waveguide.
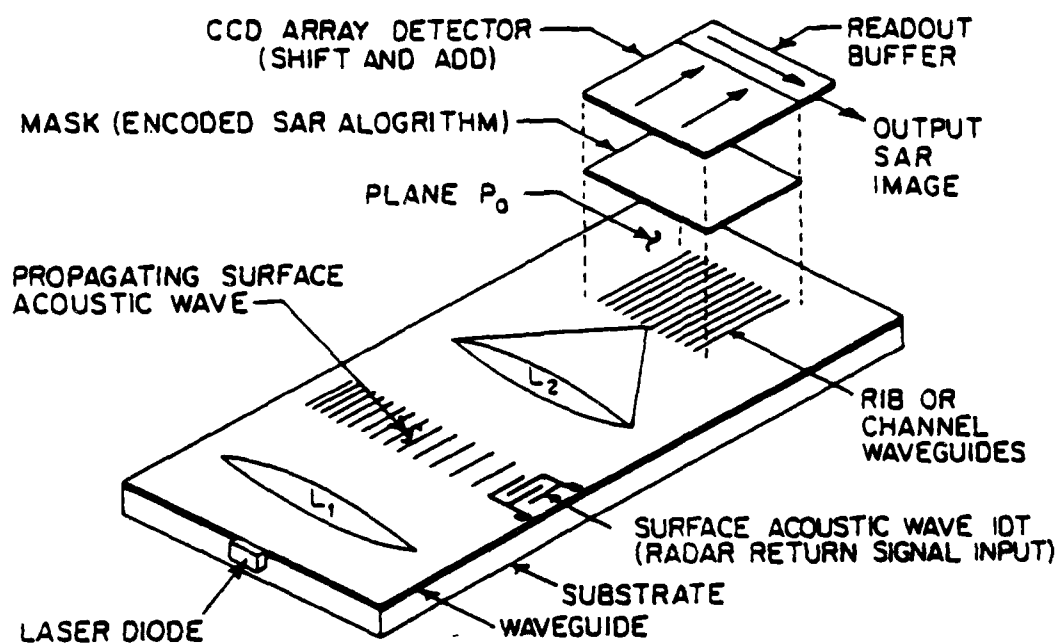
Fig. 2. Schematic diagram of the Integrated Optical Synthetic Aperture
Radar Processor, as described in Sect. 4 of the text.

Light from a semiconductor laser (attached to the integrated optics (IO) chip) is butt-coupled at the left and is guided in the vertical direction along the surface of the chip. In the horizontal direction the light is diverging and waveguide-lens L_1 is used to collimate it. A surface acoustic wave (SAW) is launched along the top surface of the chip in a direction approximately perpendicular to the direction of propagation of the light. The SAW is modulated by the radar signal and causes a portion of the incident light to be diffracted. Lens L_2 focuses the diffracted light at plane P_0. The one dimensional light distribution at plane P_0 is the radar image focused in the range dimension only. An array of rib waveguides is fabricated on the IO chip after plane P_0. The rib waveguides serve a two-fold purpose. First, they retain the integrity of the range focused image after plane P_0 (i.e., they prevent the image from going out of focus as it propagates away from plane P_0). Second, they expand the range focused-image in the plane of the chip so that the two-dimensional mask and CCD that are part of the acoustooptic SAR processor can be addressed. This is accomplished by making the top surface of the rib waveguides selectively leaky, so that a portion of the light escapes upwards as it travels in each waveguide. Several methods for achieving this are discussed later. The mask and CCD are then placed in contact with the surface of the IO chip so that the escaping light will be multiplied by the transmittance of the mask and detected by the CCD. The radar image is focused in the second (azimuth) direction by transferring and integrating the photogenerated charge on the CCD precisely as in the the acoustooptic SAR processor described in Appendix A.

3. STATEMENT OF TECHNICAL OBJECTIVES

The research program described herein involved a wide range of definable tasks, including design, fabrication, and characterization of a hybrid-integrated (commercial) laser diode, a waveguide surface acoustic wave transducer, several integrated optical collimation lenses, a rib or channel waveguide array, SAR azimuth compression masks, a charge-coupled device (CCD)-to-waveguide interface, system integration, device characterization, demonstration of real-time SAR image formation, and the exploration of applications to other significant problems amenable to solution by optical processing algorithms. Our perspective was such as to recognize clearly the importance of utilizing wherever possible established technological advances, such that the primary research effort described herein was devoted to the proof of novel conceptual principles, and the development of improved or modified fabrication technologies only in those cases that are deemed critical to the eventual implementability of the processor concept. In order to accomplish these tasks, a collaborative effort between research groups at the University of Southern California (Principal Investigator: Professor Armand R. Tanguay, Jr.) and the California Institute of Technology (Principal Investigator: Professor Demetri Psaltis) was proposed, as represented by two separate proposals. In general, the algorithmic and architectural considerations, source hybridization, surface acoustic wave device design and fabrication, specialized time delay integration CCD considerations, and SAR algorithm mask designs were the responsibility of Caltech, while the integrated optical lens design and fabrication, electrooptic multiple element transducer investigations, rib or channel waveguide design and fabrication, selective optical outcoupling techniques, and CCD detector interface were the responsibility of USC. System integration, device characterization and analysis, and real time SAR image formation tasks were shared by both institutions, as were the investigation of other optical processing applications of the novel architecture.

Our principal goal for the current research period was the demonstration of the feasibility of the approach, and the solution of the key issues that will make it practical. In what follows, the specific research task items that were pursued are listed, as given in the original statement of work.

1. A detailed study was performed of optical processing and computing applications that are amenable to solution by an integrated optical processor of the type outlined in this report.

2. A substrate material was chosen for study that allowed for simultaneous optical waveguiding, surface acoustic wave propagation, and rib or channel waveguide fabrication. Optical waveguides were formed in this substrate material, and charac-

terized in terms of optical propagation uniformity and loss.

3. Integrated optical means for one-dimensional spatial light modulation were investigated, including scrolling (e.g. surface acoustic wave) and fixed pattern (e.g. electrooptic multiple element) transducers.

4. The central issues that bear on fabrication of a parallel array rib waveguide structure were examined in detail. Rib waveguide structures were fabricated by means of photolithographic pattern definition and ion beam milling.

5. The central issues that bear on fabrication of a parallel array channel waveguide structure were examined in detail. Channel waveguide structures were initially fabricated in lithium niobate by means of the titanium in-diffusion process. Comparison of rib and channel waveguide performance criteria with respect to various optical processor architectures was undertaken.

6. Mechanisms for introducing a controllable vertical intensity loss from the rib or channel waveguides were investigated, including uniform overlayer, nonuniform overlayer, uniform grating, nonuniform grating, and area modulation techniques. Characterization of the resultant loss uniformity and overall optical efficiency was performed.

7. The fabrication of large aperture single element and multiple element integrated optical lenses in the chosen substrate system was studied to ascertain the most promising technology to pursue. Preliminary lens design calculations were performed.

8. The rib or channel waveguide structure was designed to be interfaced with a masked two-dimensional CCD detector array by means of proximity coupling or fiber optic relay plates.

9. The feasibility of monolithically integrating and interfacing optical waveguides and CCD detector arrays in a semiconductor substrate such as GaAs was investigated.

4. SUMMARY OF RESEARCH PROGRAM

The research program described herein is a follow-on to AFOSR-84-0352, "Integrated Optical Synthetic Aperture Radar Processor", for which the research period was 9/1/84 through 11/30/85. The research period for the current program was 9/1/85 through 8/31/87. Results of preliminary investigations that anticipate the contents of this report are described in the previous Final Research Report, USC-OMDL-1601, September, 1987. In the summary outlined below, the major accomplishments of the current research program are highlighted in order to detail the status of the research effort. Further details on all of the topics discussed below are provided in Appendix A.

The principal accomplishment of this research program has been the successful demonstration of proof-of-principle for advanced integrated optical signal processing components that can address multidimensional computational problems in an extremely compact format. As described below, all of the major novel features of this unique integrated optical approach have been explicitly demonstrated, and a significant level of component integration achieved. Integrated optical signal processing chips with in excess of 1000 frequency or time delay channels and in excess of 1000 time-delayed integration operations can be foreseen.

4.1 Substrate for Integration

During the research program, a number of potential substrate materials were investigated in order to provide an optimum compromise between expected system performance and availability of the critical technologies required to implement the desired spectrum of individual components. On this basis, lithium niobate ($LiNbO_3$) was chosen for the proof-of-principle phase of the research, as it has been intensively researched, many of the important physical and optical properties are now well documented, several processing technologies have been successfully developed, and it is capable of supporting all of the necessary components for a fully configured processor in a hybrid integrated format.

The current state of the art of thin film and ultrathin film structures within the compound semiconductor system is such as to suggest additional research in this area as applied to the advanced integrated optical signal processing components described herein. The primary advantage of the compound semiconductors such as gallium arsenide is the potential for full integration of the mask and CCD array functions on top of the outcoupling array, and more particularly the prospect of incorporating a fully programmable outcoupling function by employing electric field induced optical perturbations to fulfill both the outcoupling and mask functions.

4.2 TI and TIPE Waveguides in LiNbO$_3$

Both titanium indiffused (TI) and titanium indiffused, proton exchanged (TIPE) waveguides were fabricated in lithium niobate substrates in order to provide a uniform slab waveguide within which the individual components could be fabricated. Loss measurements were made on both waveguide types, resulting in 1-2 dB/cm for the TI waveguides, and 4-6 dB/cm for the TIPE waveguides. Since the change in the extraordinary index of refraction is much higher for the TIPE process, these waveguides exhibit significantly better mode confinement than that provided by the TI guides, at the expense of additional loss. Efforts in our laboratory as well as in other laboratories are currently in progress to reduce the losses characteristic of TIPE waveguides, in order that they may be incorporated in standard processing sequences even for large area integrated optical components.

4.3 Large Aperture Low F-Number Integrated Optical Lenses

For fully configured processors with upwards of 1000 individual rib waveguides in the array, large aperture (1-3 cm) integrated lenses are required that simultaneously exhibit diffraction limited performance, relatively short focal lengths (low F-numbers of order 1-5), and process compatibility with the full array of required processor components. In addition, we required from the outset that any of the lens fabrication processes contemplated be capable of straightforward incorporation in a microphotolithographic processing sequence, in order that the resultant complex chip be capable of eventual inexpensive mass production.

To this end, we experimented with three novel integrated lens structures during the course of the research. In one such approach, ion beam milling was employed on a Ti:LiNbO$_3$ slab waveguide to produce a lens-shaped recess. Titanium dioxide (TiO$_2$) was then vacuum evaporated to fill the recess with higher index material, simultaneously creating an index mismatch from the slab waveguide to the lens waveguide regions, and from the lens waveguide region to the substrate for maintenance of vertical mode confinement. In the second approach, the same recessed region was coated first with magnesium flouride (MgF) and then with silicon dioxide (SiO$_2$) to provide a lower index lens within a higher index waveguide. In both cases, preliminary attempts at depositing films of the desired bulk index were not successful, and the investigation of such thin film coated recessed lenses is continuing. The primary advantage of such structures is the extremely large index difference that can be anticipated, which yields either very low F-number lenses or modest F-number lenses with very low profiles and associated chip real estate.

A third approach involved a modification of the successful technique employed by

Tsai and coworkers [16] to fabricate TIPE lenses in TI waveguides. In our experiments, TI lenses were fabricated in TIPE waveguides, which by employing concave curvature lens surfaces resulted in positive focal behavior. This approach has numerous advantages, including the use of SiO_2 as a processing mask that does not require post-processing removal, minimization of the lens footprint on the integrated optical chip, and capability for integration with large area TIPE rib waveguide arrays characterized by a concomitantly high degree of mode confinement. Lenses fabricated by this process included several with apertures of 0.25 cm and F-numbers of 4.8 that exhibited nearly diffraction limited performance, and proved in fact to be integrable with both rib waveguide arrays and surface outcoupling gratings, as described in Sect. 4.6 below.

4.4 Large Area Rib Waveguide Arrays

Since preliminary calculations of overall system performance indicated that several processor configurations could be envisioned with in excess of 1000 individual rib waveguides, and that the focal spot sizes determined by the input linear FM chirp in combination with the integrated lens would be in the range 5-20 μm, we chose as a proof-of-principle goal to demonstrate the fabrication of a 10 μm pitch rib waveguide array with of order 1000 individual elements. During the program, this goal was achieved with the fabrication by ion beam milling of a 660 element (mask-geometry-limited) rib waveguide array in a Ti:LiNbO$_3$ waveguide, consisting of 8 μm wide ribs 1 μm in height with 2 μm gaps. Demonstration of guiding in individual ribs of the array was achieved, as well as integration with other components.

4.5 Surface Outcoupling Gratings on Large Area Rib Waveguide Arrays

Although thin film outcoupling layers were thoroughly analyzed during the course of the research (see Appendix A), surface outcoupling gratings were chosen as the primary vehicle for investigation, principally due to ease of integrability, degree of functional control, and the possibility of nonuniformity compensation by direct modulation of the grating period.

Surface outcoupling gratings were fabricated both on TI slab waveguides, and on large area rib waveguide arrays as shown schematically in Fig. 3. Both holographic exposure and direct contact mask photolithographic methods were employed, with the latter producing the most reproducible results with the lowest degree of optical scatter. Using the direct masking method, both 2 μm and 4 μm gratings periods were fabricated. Standard photolithographic methods were found to produce gratings of exceptional quality, even on the surfaces of individual 8 μm rib waveguides in a high density array. Outcoupling efficiencies were determined, and were in substantial agreement with theoretical estimates. Losses of 10-100 %/mm are within the range of straightforward processing parameters,
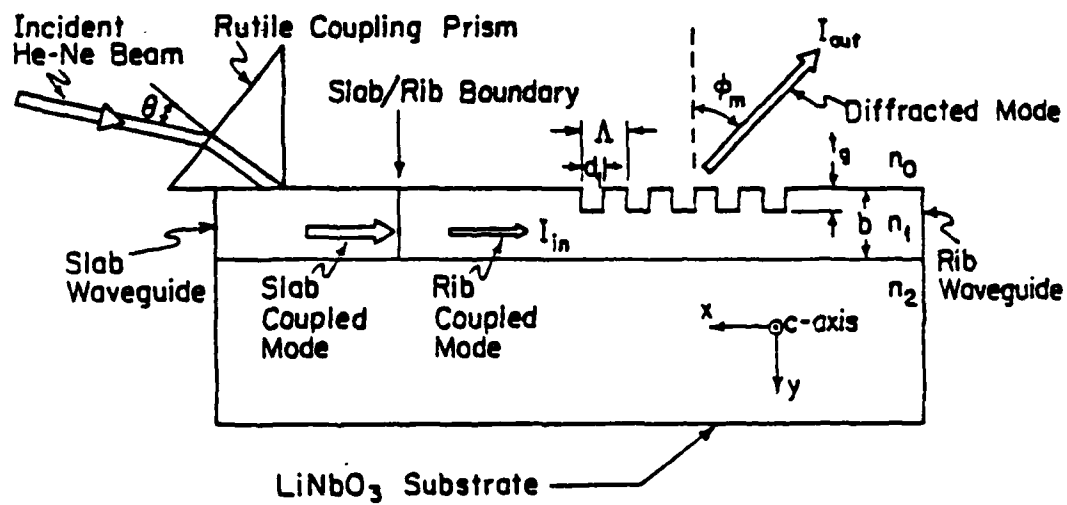
Fig. 3. Waveguide outcoupling from a rib or channel waveguide by uniform periodic modulation of the waveguide surface.

as required for the envisioned spectrum of advanced integrated optical signal processing components.

4.6 Integration of Advanced Integrated Optical Signal Processing Components

In order to test the performance of each of the components described above in an integrated architecture, large aperture lenses, large area rib waveguide arrays, and surface outcoupling gratings were successfully integrated onto a common substrate, as shown schematically in Fig. 4. Characteristics of the individual components were as described above.

Experimental tests of the integrated structures were also successful. In one such experiment, prism incoupled light was focused by the integrated lens into a single rib within a 660 element array, as observed by a CCD detector array focused on the end of the substrate shown in Fig. 4. In addition, vertical outcoupling from the surface grating fabricated on top of this single rib was clearly observed. Integrated optical chips designed to use both the first order and second order modes (producing substantially different focal lengths in the integrated lenses) were fabricated and successfully tested.

4.7 Systems Performance Evaluations

During the course of the research, our perspective has been such as to continually evaluate both the fundamental physical limitations to the computational performance that can be expected from such advanced integrated optical signal processing structures, as well as potential technological limitations that derive from the particular implementation choices made in a given system design. Such systems performance evaluations can yield relatively surprising research directions, as well as specific insight into inadvertant system compromises.

To this end, we have estimated the performance characteristics of the Integrated Optical Synthetic Aperture Radar Processor described earlier, as a specific implementation of the key features of such novel computational modules. Using lithium niobate as the substrate, and employing a surface acoustic wave (SAW) transducer to input the radar return signal, an assumed radar bandwidth of 50 MHz with a pulse duration of 1 usec is capable of generating 333 individual range bins with a resolution of 3 m for a total swath of 1 km. In this example, the required integrated lens aperture is about 2.7 cm.

The swath size is limited in the case described above by the extraordinarily high surface acoustic velocity of lithium niobate. Utilizing a material with a much slower SAW velocity such as tellurium dioxide (TeO_2), and employing a 1 cm aperture lens to compensate for the higher acoustic attentuation in TeO_2, the swath can be more than doubled at fixed range resolution to approximately 758 individual range bins.
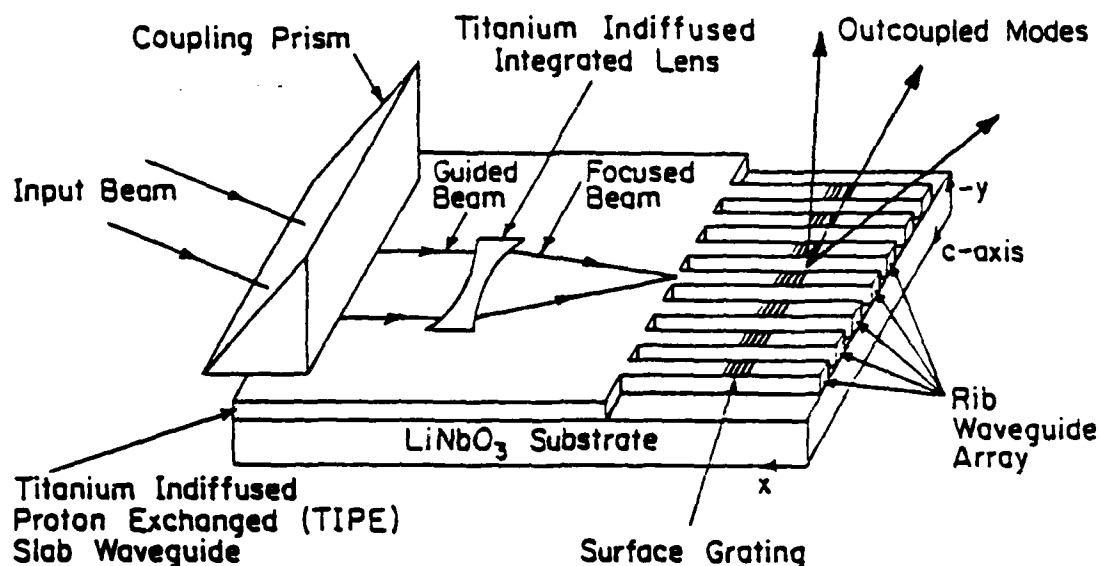
Fig. 4. Schematic diagram of the guided wave optical chip with the following integrated IOSAR processor elements: TI lens in TIPE slab waveguide, rib waveguide array, and surface outcoupling grating. The input beam is coupled into the TIPE slab waveguide via a prism, and the guided beam is focused by the TI integrated lens into individual rib waveguides which can be observed at its cleaved end. The light guided in the rib waveguides is subsequently outcoupled by the surface grating.

Another method for inserting the radar return signals into the processor involves the use of an integrated electrooptic modulator array, similar in structure to that of the Linear Array Total Internal Reflection Spatial Light Modulator [5]. In this case, the processor capability can be increased to in excess of 1175 elements for a specific processor geometry. For the radar parameters discussed above, this would yield a swath size of 3.5 km with 3 m resolution.

Another issue that was addressed during the research effort was the question of the bias buildup that accompanies any time-delay-and-integrate architecture [1]. One means of eliminating such a bias can be provided by the architecture shown in Fig. 5, in which a second rib waveguide array without a mask is utilized to detect the space-variant bias distribution, which can than be directly subtracted from the output signal.

4.8 Extensions of the Concept

The specific example of synthetic aperture radar image formation was used throughout this research program in order to provide a systems focus to the scientific and technological development effort. The integration concept described herein, however, has much broader applicability, due primarily to the flexibility inherent in the choice of input signal format, mask (correlation) function, CCD orientation, and CCD readout mode. For example, the input signal format can be chosen to be a linear FM chirp as described herein to produce a temporal delay (range) distribution in the plane of the rib waveguide (image dissection) array, or it can be chosen to be temporal frequency encoded, which produces a temporal frequency segmentation in the output plane. Choice of appropriate masking functions and CCD array orientation/readout mode can then allow additional types of computational algorithms to be implemented, including two-dimensional correlation, convolution, and Fourier transform operations; selective frequency cross-correlations; real time computation of ambiguity functions; vector-matrix operations; and matrix-matrix multiplications.
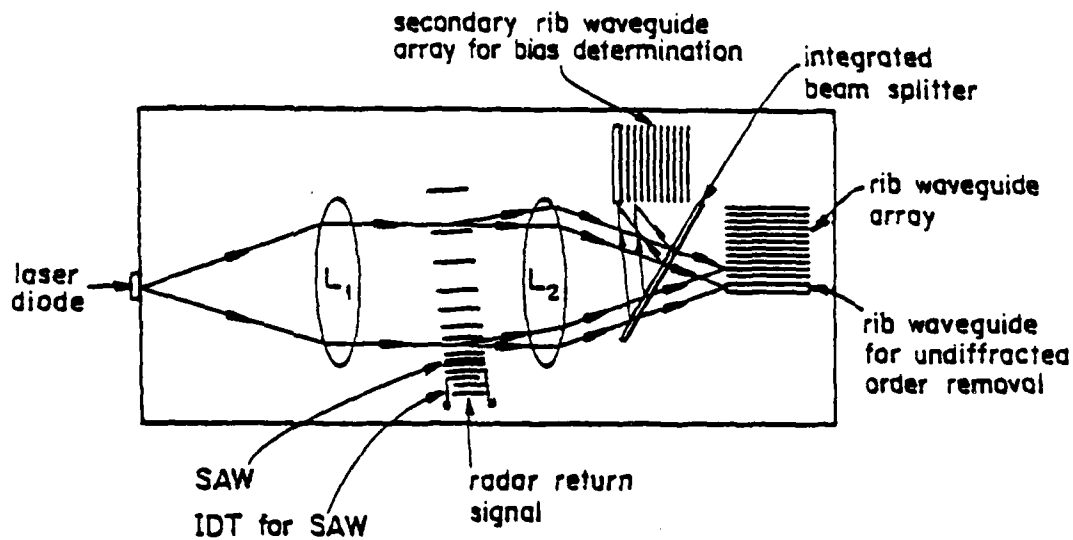
Fig. 5. Modified version of the IOSAR processor architecture which can correct for bias buildup. A secondary rib waveguide array with surface outcoupler is used to excite a secondary CCD array to determine the bias (see text). A wide rib waveguide is used to remove the undiffracted order. Other components are similar to the preliminary IOSAR architecture.

5. PUBLICATIONS

5.1 Published Manuscripts (AFOSR Sponsorship)

1. A. R. Tanguay, Jr., "Integrated Optical Processing and Computing", Optics News, Special Issue on Integrated Optics: Evolution and Prospects, 14(2), 23-26, (1988); (Invited Paper).

2. A. R. Tanguay, Jr., D. Psaltis, and T. J. Bicknell, "An Integrated Optical Synthetic Aperture Radar Processor", in preparation for Optics Communications, (1988).

3. K. Rastani and A. R. Tanguay, Jr., "Advanced Integrated Optical Signal Processing Components", in preparation for Applied Optics, (1988).

4. K. Rastani and A. R. Tanguay, Jr., "Grating Outcoupling from Large Area Rib Waveguide Arrays Fabricated on Titanium Indiffused Lithium Niobate Substrates", in preparation for Journal of Lightwave Technology, (1988).

5. K. Rastani and A. R. Tanguay, Jr., "Large Aperture Low F-Number Integrated Lens Fabrication in Titanium Indiffused Proton Exchanged Lithium Niobate Substrates", in preparation for Applied Physics Letters, (1988).

5.2 Conference Presentations (AFOSR Sponsorship)

1. A. R. Tanguay, Jr., "Functional Requirements for Optical Processing and Computing", ITT Corporation Symposium on Ultra-High Bandwidth Communications, SEL Laboratories, Stuttgart, Federal Republic of Germany, (1985); (Invited Paper).

2. A. R. Tanguay, Jr., "Optical Computing Components: Fundamental Issues", 1985 Annual Meeting of the Optical Society of America, Washington, D.C., (1985); (Invited Paper).

3. T. Bicknell, D. Psaltis, and A. R. Tanguay, Jr., "Integrated Optical Synthetic Aperture Radar Processor", 1985 Annual Meeting of the Optical Society of America, Washington, D.C. (1985); J. Opt. Soc. Am. A, 2(13), P8, (1985).

4. S. Sriram, T. Waiss, K. Rastani, S. W. McCahon, and A. R. Tanguay, Jr., "Integrated Optical Devices in Lithium Niobate", SPIE International Symposium. Los Angeles, California, (1986).

5. A. R. Tanguay, Jr., "Optical Processing and Computing Devices: The Materials Perspective", Southern California Crystal Growers Association Meeting, El Segundo, California, (1986); (Invited Paper).

6. A. R. Tanguay, Jr., "Optical Processing and Computing Devices: The Materials Perspective", Jet Propulsion Laboratory, Pasadena, California, (1986); (Invited Paper).

7. A. R. Tanguay, Jr., "Optical Processing and Computing Devices: The Materials Perspective", Microelectronics and Computer Technology Corporation, Austin, Texas, (1986); (Invited Paper).

8. A. R. Tanguay, Jr., "Research in the Center for Photonic Technology at USC", USC Board of Trustees Annual Retreat, Palm Springs, California, (1986); (Invited Presentation).

9. A. R. Tanguay, Jr., "Optical Processing and Computing Devices: The Materials Perspective", Minnesota Mining and Manufacturing Co., St. Paul, Minnesota, (1986); (Invited Colloquium).

10. A. R. Tanguay, Jr., "Research in the Center for Photonic Technology at USC", Minnesota Mining and Manufacturing Co., St. Paul. Minnesota, (1986); (Invited Presentation).

11. A. R. Tanguay, Jr., "Optical Processing and Computing Devices: The Materials Perspective", Honeywell Physical Sciences Center, Bloomington, Minnesota, (1986); (Invited Colloquium).

12. A. R. Tanguay, Jr., "Research in the Center for Photonic Technology at USC", Honeywell Physical Sciences Center, Bloomington, Minnesota, (1986); (Invited Presentation).

13. A. R. Tanguay, Jr., "Optical Processing and Computing Devices: The Materials Perspective", Lockheed Palo Alto Research Laboratories, Palo Alto, California, (1986); (Invited Colloquium).

14. S. Kim, R. V. Johnson, and A. R. Tanguay, Jr., "Observation of Electric Field Enhanced Electrode Indiffusion in Lithium Niobate", 1986 Annual Meeting of the Optical Society of America, Seattle, Washington, (1986).

15. K. Rastani, Z. Karim, R. V. Johnson, and A. R. Tanguay, Jr., "Optical Information Processing Components", Gordon Research Conference on Optical Information Processing and Holography, Santa Barbara, California, (1987); (Invited Paper).

16. A. R. Tanguay, Jr., "Optical Information Processing Components", Celanese Research Company, Summit, New Jersey, (1987); (Invited Presentation).

17. A. R. Tanguay, Jr., "Optical Information Processing Components", Hewlett-Packard Research Laboratories, Palo Alto, California, (1987); (Invited Presentation).

18. A. R. Tanguay, Jr., "Optical Information Processing Components", Georgia Institute of Technology, Atlanta, Georgia, (1987); (Invited Colloquium).

19. A. R. Tanguay, Jr., "Optical Information Processing Components", GEC Research, Marconi Research Centre, Chelmsford, England, (1987); (Invited Colloquium).

20. A. R. Tanguay, Jr., "Optical Information Processing Components", University of California, Santa Barbara, Santa Barbara, California, (1987); (Invited Colloquium).

21. A. R. Tanguay, Jr., "Optical Information Processing Components", Bell Communications Research, Morristown, New Jersey, (1987), (Invited Colloquium).

22. A. R. Tanguay, Jr., "Optical Information Processing Components", IBM Almaden Research Center, San Jose, California, (1987); (Invited Colloquium).

23. K. Rastani and A. R. Tanguay, Jr., "Grating Outcoupling from Large Area Rib Waveguide Arrays Fabricated on Titanium Indiffused Lithium Niobate Substrates", Integrated and Guided Wave Optics '88, Albuquerque, New Mexico, (1988).

24. A. R. Tanguay, Jr., "Electro-Optical Information Processing and Computing Components", Conference on Lasers and Electro-Optics, Anaheim, California, (1988); (Invited Paper).

25. K. Rastani, Z. Karim, and A. R. Tanguay, Jr., "Selective Focusing into Large Rib Waveguide Arrays via Large Aperture Integrated Lenses on $LiNbO_3$", 1988 Annual Meeting of the Optical Society of America, Santa Clara, CA, (1988).

5.3 Degrees Awarded

1. Kasra Rastani, "Advanced Integrated Optical Signal Processing Components", Ph.D. Dissertation, University of Southern California, August, (1988).

6. SCIENTIFIC PERSONNEL

The following scientific personnel contributed to the research summarized in this report, and were either supported in part by the Air Force Office of Scientific Research or were supported in part by the University of Southern California through cost-sharing.

1. Professor Armand R. Tanguay, Jr., Principal Investigator

2. Kasra Rastani, Graduate Research Assistant

3. Bruce Damer, Graduate Research Assistant

4. Zaheed Karim, Graduate Research Assistant

5. Frank Lum, Senior Research Technician

7. REFERENCES

1. D. Psaltis and K. Wagner, "Real-Time Synthetic Aperture Radar (SAR) Processor", Opt. Eng., 21, 822-828, (1982).

2. D. Psaltis, M. Haney, and K. Wagner, "Real Time Synthetic Aperture Radar Processing", Proc. NASA Conference on Optical Information Processing for Aerospace Applications. II, Langley, Virginia, (1983).

3. I. Abramov, Y. Owechko, A. R. Tanguay, Jr., and T. J. Bicknell, "Real Time Synthetic Aperture Image Formation Utilizing an Electrooptic Spatial Light Modulator", Proc. NASA Spaceborne Imaging Radar Symposium, Jet Propulsion Laboratory Publication No. 83-11, (1983).

4. B. A. Horwitz and F. J. Corbett, "The PROM–Theory and Applications for the Pockels Readout Optical Modulator", Opt. Eng., 17, 353-364, (1978).

5. R. V. Johnson, D. L. Hecht, R. A. Sprague, L. N. Flores, D. L. Steinmetz, and W. D. Turner, "Characteristics of the Linear Array Total Internal Reflection (TIR) Electrooptic Spatial Light Modulator for Optical Information Processing", Opt. Eng., 22, 665-674, (1983).

6. T. J. Bicknell, Jet Propulsion Laboratory, California Institute of Technology, private communication. See also D. A. Ausherman, "Digital versus Optical Techniques in Synthetic Aperture Radar (SAR) Data Processing", Opt. Eng., 19, 157-167, (1980).

7. C. M. Verber, "Integrated Optical Approaches to Signal and Data Processing", Proc. National Aerospace and Electronics Conference (NAECON 84), Dayton, Ohio, May, (1984).

8. C. M. Verber, R. P. Kenan, and J. R. Busch, "Correlator Based on an Integrated Optical Spatial Light Modualtor", Appl. Opt., 20, 1626-1629, (1981).

9. L. Thylen and L. Stensland, "Electrooptic Approach to an Integrated Optics Spectrum Analyzer", Appl. Opt., 20, 1825-1832, (1981).

10. D. Psaltis, "Two Dimensional Optical Processing Using One Dimensional Input Transducers", Proc. IEEE, July, (1984), in press.

11. W. E. Ross, D. Psaltis, and R. H. Anderson, "Two-Dimensional Magneto-Optic Spatial Light Modulator for Signal Processing", Opt. Eng., 22(4), 485, (1983).

12. R. H. Kingston, B. E. Burke, K. B. Nichols, and F. J. Leonberger, "Spatial Light Modulation Using Electroabsorption in a GaAs CCD", Appl. Phys. Lett., 41, 413-415, (1982).

13. D. Mergerian, et al., "Advances in Integrated Optical Spectrum Analyzers", Proc. SPIE, 269, 129-135, (1981).

14. C. S. Tsai, "Wideband Real-Time Signal Processing Using INtegrated Optics", Proc. SPIE, 209, 107-112, (1979); also C. M. Verber, R. P. Kenan, and J. R. Busch, "Design and Performance of an Integrated Optical Digital Correlator", J. Lightwave Tech., 1, 256-261, (1983).

15. C. M. Verber, "Integrated-Optical Approaches to Numerical Optical Processing", Proc. IEEE, 72(7), 942-953, (1984).

16. D. Y. Zang and C. S. Tsai, "Single-Mode Waveguide Microlenses and Microlens Arrays Fabrication in $LiNbO_3$ Using Titanium Indiffused Proton Exchange Technique", Appl. Phys. Lett., 46(8), 703-705, (1985).

APPENDIX A

ADVANCED INTEGRATED OPTICAL SIGNAL PROCESSING
COMPONENTS

by

Kasra Rastani

A Dissertation Presented to the

FACULTY OF THE GRADUATE SCHOOL

UNIVERSITY OF SOUTHERN CALIFORNIA

In Partial Fulfillment of the

Requirements for the Degree

DOCTOR OF PHILOSOPHY

(Electrical Engineering)

December 1988

Acknowledgments

First I would like to dedicate this work to my parents Mr. and Mrs. Rastani, and to my two sisters, Shiva and Gilda. Without their continuous encouragement and support, the completion of this dissertation would not have been possible.

I am indebted to many people for their invaluable help and advice while in graduate school at USC. In particular, I would like to thank Professor Armand R. Tanguay, Jr. for suggesting the topic of this dissertation, and for his superb guidance and insight involving every aspect of the research work.

My sincere thanks are also owed to the following:

Professor Richard V. Johnson, for many useful discussions concerning different aspects of this research.

Professor P. D. Dapkus, Professor M. Gershenzon, and Professor H. H. Kuehl for reviewing the dissertation. I am especially grateful for their friendly personalities, valuable criticism and constant encouragement throughout the entire period of the research.

Mr. Zaheed Karim, with his knowledge and expertise in thin film deposition and ion beam milling techniques, provided invaluable assistance during the course of this research.

Ms. Karen Tierney, Mr. Frank Lum, and the other members of the Optical Materials and Devices Laboratory at USC, for their friendly assistance during the period of this study.

Contents

List of Figures

Abstract

This research was aimed at the development of advanced integrated optical components suitable for devices capable of processing multi-dimensional inputs. In such processors, densely packed waveguide arrays with low crosstalk are needed to provide dissection of the information that has been partially processed. Waveguide arrays also expand the information in the plane of the processor while maintaining its coherence. Rib waveguide arrays with low loss, high mode confinement and highly uniform surface quality (660 elements, 8 μm wide, 1 μm high, and 1 cm long with 2 μm separations) were fabricated on LiNbO$_3$ substrates through the ion beam milling technique.

A novel feature of the multi-dimensional IO processor architecture proposed herein is the implementation of large area uniform outcoupling (with low to moderate outcoupling efficiencies) from rib waveguide arrays in order to access the third dimension of the processor structure.

As a means of outcoupling, uniform surface gratings (2 μm and 4 μm grating periods, 0.05 μm high and 1 mm long) with low outcoupling efficiencies (of approximately 2-18 %/mm) were fabricated on the nonuniform surface of the rib waveguide arrays. As a practical technique of modulating the low outcoupling efficiencies of the surface gratings, it was proposed to alter the period of the grating as a function of position along each waveguide.

Large aperture (2.5 mm) integrated lenses with short positive focal lengths (1.2-2.5 cm) were developed through a modification of the titanium-indiffused proton exchanged (TIPE) technique. Such integrated lenses were fabricated by increasing the refractive index of the slab waveguides by the TIPE process while maintaining the refractive index of the lenses at the lower level of Ti:LiNbO$_3$

waveguide. By means of curvature reversal of the integrated lenses, positive focal length lenses have been fabricated while providing high mode confinement for the slab waveguides.

The above elements performed as expected when integrated on the same substrate. Guided modes of slab waveguides were focused into individual rib waveguides, followed by selective outcoupling via surface gratings.

Finally, the example of an integrated optical synthetic aperture radar (IOSAR) processor on $LiNbO_3$ and its limitations were considered. In addition, we analyzed the geometrical performance characteristics of advanced IO systems.

Chapter 1

Introduction

The advent of optics into information processing and computing brought with it new possibilities and capabilities that were not possible before. The three dimensionality of optical information processing systems provides the capability of processing complex information in parallel. Such parallelism in computing, which is highly desired in operations such as the two-dimensional correlation or convolution of complex information, is not possible in current digital computers.

Bulk optical systems that are used in information processing are highly specialized, relatively bulky, and difficult to fabricate. Recently, lessons learned from the field of semiconductor integrated circuits regarding large scale integration of individual components provided strong motivation for the miniaturization and integration of bulk optical systems on the same substrate. Integrated optics could potentially provide fast, inexpensive, compact, and rugged alternatives to bulk optical information processors.

Despite the young age of the integrated/guided wave optics field, tremendous accomplishments have taken place in the development of integrated optical processors. This is partially due to the knowledge of photolithography and fabrication techniques learned from the field of semiconductors. Modification of some of the above techniques provided a head start in the development of integrated optical building blocks such as optical waveguides, integrated lenses, integrated in/outcouplers, surface acoustic wave (SAW) transducers, and others.

Although different materials have been investigated over the years as possible

substrates in integrated optics, LiNbO$_3$ (3m symmetry, $n_e = 2.2005$, and $n_o = 2.291$) has emerged as a popular substrate material [1]. An important reason for the popularity of this uniaxial crystal is that waveguide fabrication techniques in it are well established. Waveguides are typically fabricated by the titanium indiffusion technique, which causes increases in both the ordinary ($\Delta n_o = 0.005$) and the extraordinary ($\Delta n_e = 0.05$) refractive indices of LiNbO$_3$ (Ti:LiNbO$_3$) [2,3,4,5,6,7].

As an example of an integrated optical information processor that has been previously developed on LiNbO$_3$, let us consider the real-time RF spectrum analyzer shown schematically in Fig. 1.1 [8]. This processor consists of a SAW transducer (needed to input the RF signal), a pair of integrated lenses (for guided beam collimating and focusing), a laser diode source, and a linear array of photodetectors.

In the IO spectrum analyzer, the Bragg cell driven by the RF signal deflects the guided beam at an angle which is proportional to the frequency of the RF signal. The second lens along the path of the guided beam brings the Fourier plane closer, and as such acts as an angle-to position encoder. Fourier transformed guided modes are focused into the linear array of image sensors. The spectral power density of the signal is obtained on the photodetector in the form of the light intensity distribution.

The acoustooptic and SAW propagation properties of LiNbO$_3$ are very promising, which makes this single crystal material particularly suitable for use in IO spectrum analyzers. The reported bandwidths for such spectrum analyzers are about 1 GHz, with resolutions of about 2 MHz [9]. The response time of the IO spectrum analyzer is about 2 μs, and the dynamic range is in excess of 20 dB.

The integrated lenses shown in Fig. 1.1 are graded thickness Fresnel lenses. The refractive index of the lens region is increased by the proton exchange technique in Ti:LiNbO$_3$ waveguides [10]. This technique of fabricating lenses
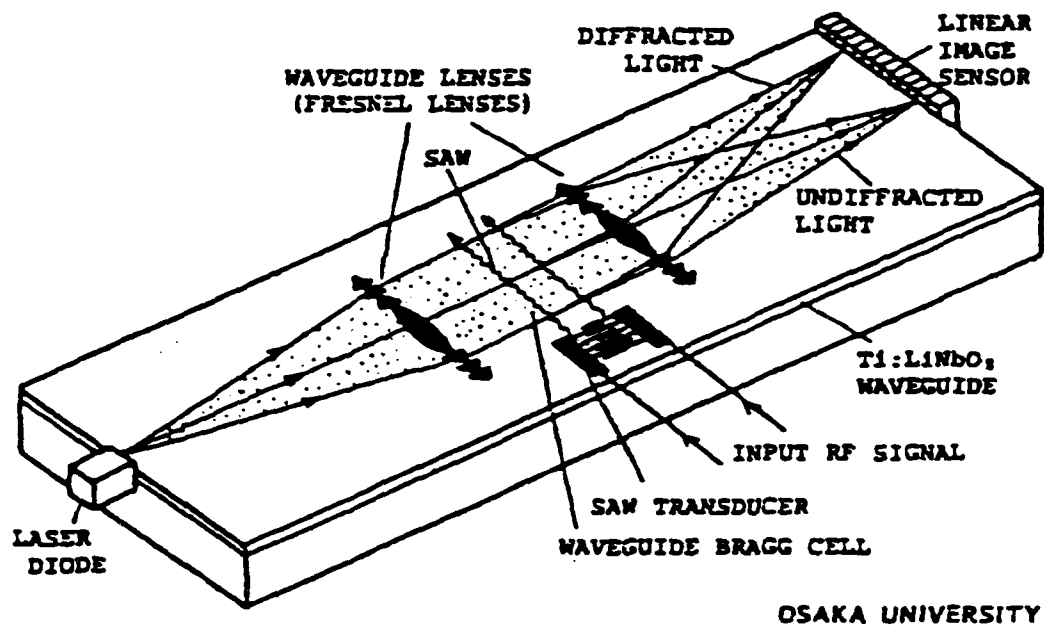
Figure 1.1: An integrated optical RF spectrum analyzer (after Ref. [8]).

is not unique, and other types of lenses such as geodesic and Luneburg lenses have been demonstrated in LiNbO$_3$ [9]. However, proton exchanged lenses have proven to be easier to fabricate in Ti:LiNbO$_3$ waveguides than the other types of integrated lenses.

From the schematic diagram of Fig. 1.1 it is obvious that all of the information within the IO spectrum analyzer is confined to the plane of the processor. In some IO applications, the light is outcoupled from the waveguide in order to provide extra flexibility for the system. An example of an integrated optical device that makes use of such outcoupling is the integrated optical disk pickup shown in Fig. 1.2, which has applications in optical disk memory systems [9]. This device is constructed in a glass/SiO$_2$/Si waveguide. The choice of a Si substrate allows for the integration of photodiodes that are used in calculating the readout signal, focusing error, and tracking error.

The guided light from the laser diode is outcoupled by a chirped surface grating that focuses the light onto the disk. The reflected light from the disk is coupled back into the waveguide via the grating. The reflected guided wavefront is first divided in half, then deflected and focused into two sets of photodiodes by a twin grating focusing beam splitter. By electronically summing the signals from the photodiodes, the complete optical disk readout signal is generated, as shown in Fig. 1.2.

Integrated optical devices with higher levels of integration have also been developed by others. A high level integration of elements on the same substrate could include components such as arrays of input and output channel waveguides, large aperture lens and microlens arrays, and electrooptic or SAW modulators. A vivid example of multiple components integrated on the same substrate is the integrated acousto-optic Bragg modulator in LiNbO$_3$ (shown in Fig. 1.3) which can be used in applications such as matrix-vector multiplication [11].

4
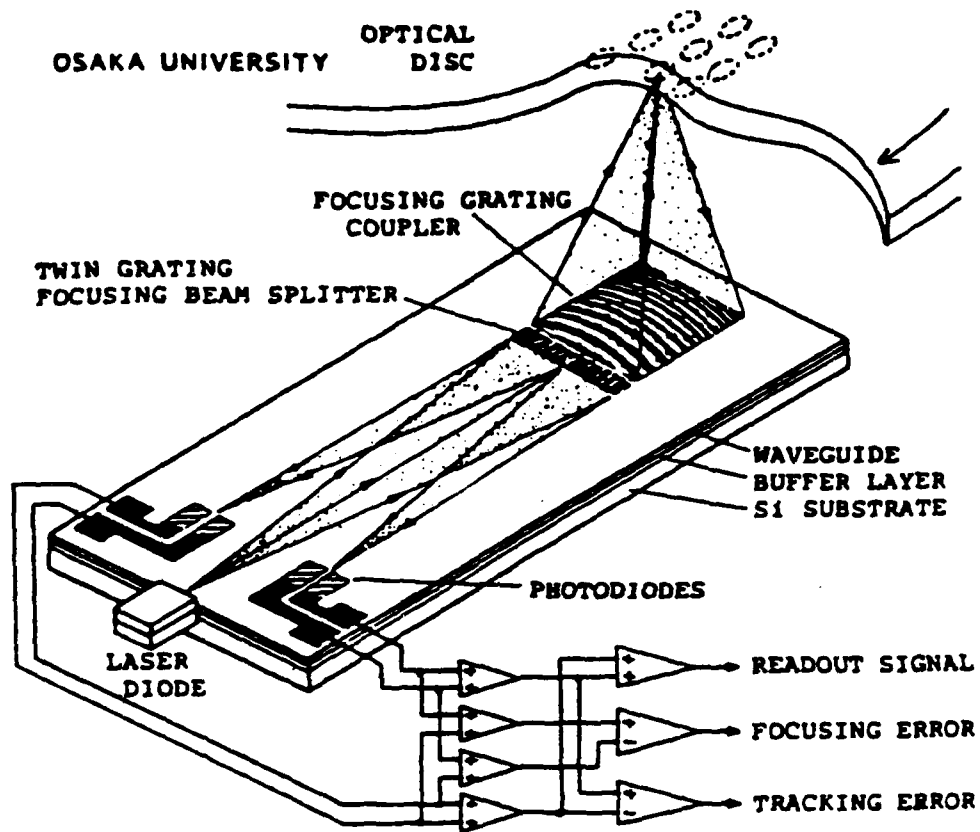
Figure 1.2: An integrated optical disk pickup device (after Ref. [9]).
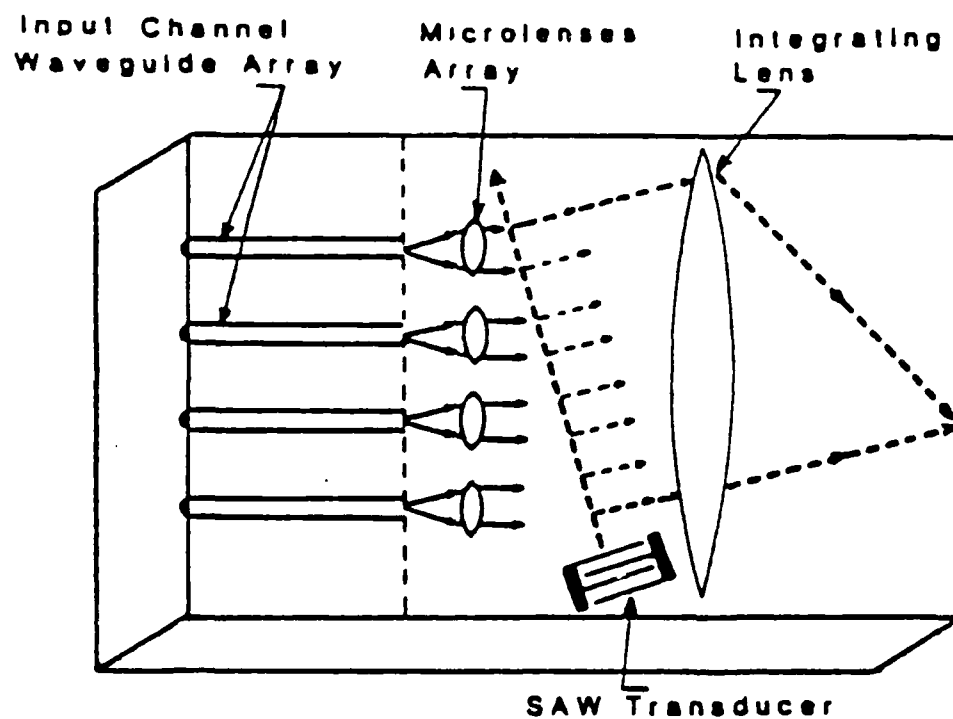
Figure 1.3: Integrated acousto-optic Bragg modulator in a LiNbO$_3$ channel planar composite waveguide (after Ref. [11]).

6

The use of integrated optics is not merely confined to the analog domain, and its uses in D-A conversion and A-D conversion have also been shown [12]. However, from the examples given so far, it is evident that integrated optics is currently limited to processing one dimensional input information only [13,14,15,16,17,18]. This is a significant road block hampering the maturity of this technology.

In some multi-dimensional processing applications, the above problem can be surmounted if the full potential of integrated optics is employed. This is conceivable if one of the input dimensions is processed in the plane of the processor (similar to the integrated optical spectrum analyzer example). Partially processed information is then selectively outcoupled from the plane of the integrated optical processor (similar to the integrated optical disk pickup example) in order to utilize its third dimension. Additional processing may then be accomplished (either electronically or optically) out of the plane of the IO processor substrate.

There are numerous applications that can readily benefit from the development of multi-dimensional IO processors. The proposed Integrated Optical Synthetic Aperture Radar (IOSAR) processor employs such processing capability to provide focused radar images from SAR radar returns [19,20].

The range information is determined when the linear FM radar return is applied to a SAW device on the IO processor (similar to the IO spectrum analyzer example). This is shown in Fig. 1.4, in which the position of the focused spot (range information) is proportional to the time delay of the radar return. The large array of waveguides situated at the back focal plane of the integrated lens performs two essential functions. First, it dissects the range focused information. Second, this information is expanded in the plane of the waveguides while maintaining its coherence; this function is equivalent to the anamorphic expansion provided by a cylindrical lens.

IOSAR PROCESSOR: RANGE COMPRESSION
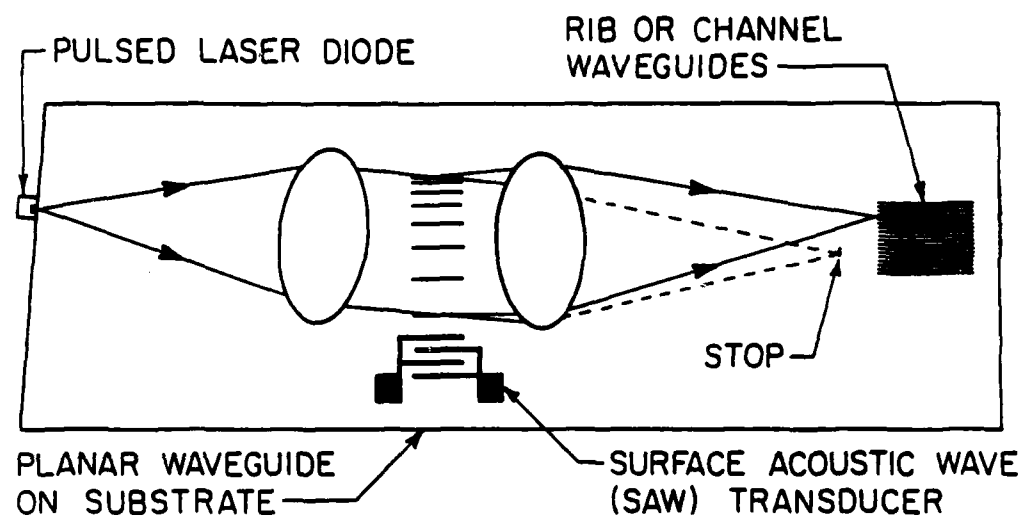
Figure 1.4: Range compression of the radar return as performed in IOSAR processors.

The information confined to the rib waveguide array is then redirected vertically out of the waveguides along its entire length by means of a surface outcoupler. The outcoupled light is multiplied by a mask containing the azimuth (doppler) phase history as shown in Fig. 1.5. This light is then incident onto a CCD array operated in the shift-and-add mode. The azimuth compression is thus accomplished by temporal integration.

The principal features of such processors are outlined below:

1. Guided wave optical devices capable of processing multi-dimensional inputs

2. Compact, relatively inexpensive processors

3. Potential for use in applications other than SAR such as optical matrix-matrix multiplication

4. Potentially faster with lower power consumption than digital systems performing comparable tasks

5. Potential for monolithic integration

6. Potential for programmability in advanced systems in which the outcoupling region or the mask function can be programmed

Transformation of such IO processors from design concepts into realizable and working devices, however, requires the development of advanced integrated optical components that have not heretofore been available. For example, although Ti:LiNbO$_3$ channel waveguides have been developed by other investigators, high density large area waveguide arrays exhibiting low crosstalk suitable for multi-dimensional IO processors have not been reported previously [2,5].

Surface relief gratings on channel and slab waveguides have been developed by others to outcouple light from such waveguides [21,9]. Normally, the primary purpose of such gratings has been the high efficiency outcoupling of light

9
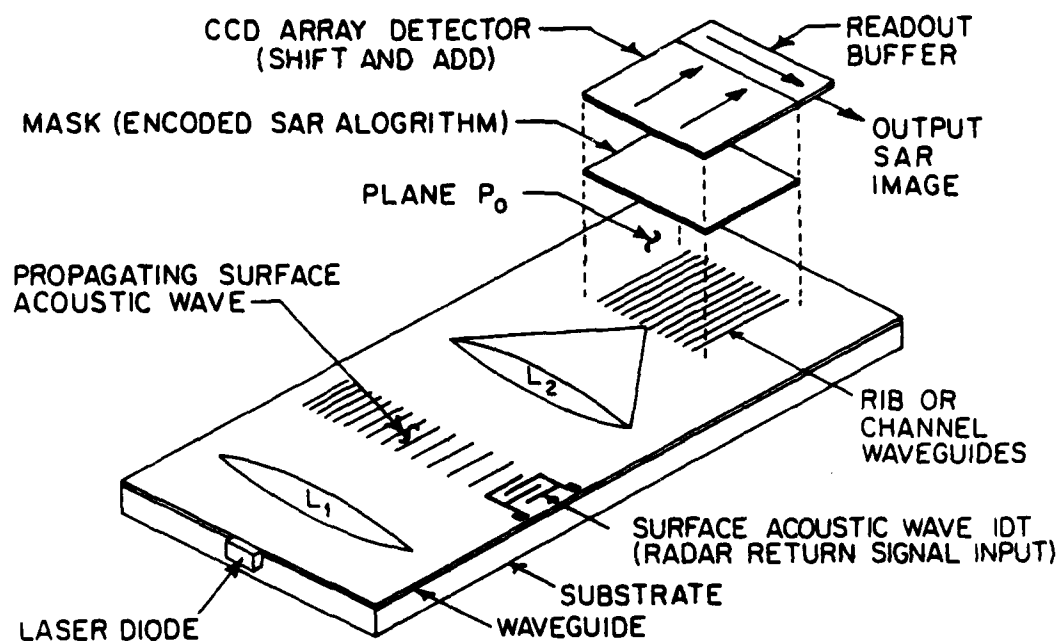
Figure 1.5: Schematic diagram of the Integrated Optical Synthetic Aperture Radar (IOSAR) Processor (after Ref. [19,20]).

from waveguides within the minimum distance possible. However, in some of the multi-dimensional IO processor applications, since the uniform outcoupling function needs to be performed over a large area, the outcoupling efficiency per unit length should be significantly lower as well as highly uniform over large distances (cms). In these applications, it might also be desirable to modulate the outcoupling efficiencies of different pixels according to their location.

Integrated lenses play important roles in IO processors and guided wave optical communication systems. As was mentioned earlier, the development of integrated lenses needed to focus or collimate the guided modes in waveguides has been the subject of numerous studies [10,9,22,23,24]. In order to explore new possibilities in integrated lenses, more effort needs to be directed towards the development of large aperture integrated lenses with short focal lengths that are relatively easy to fabricate.

Due to the state of technology available at the present time, only hybrid IO processors such as the one shown in Fig. 1.5 are considered herein. Recent advances in the development of waveguides, modulators, and integrated lenses in the III-V compound semiconductor system of materials, however, project new possibilities of monolithically integrated optical systems in the future.

In this research program, the development of advanced integrated optical components needed for multi-dimensional signal processing has been addressed. Design parameters and performance guidelines of these components have been directed initially towards the development of IOSAR processors. However, the analysis and fabrication of the elements can easily be appropriately modified for other advanced IO processing applications.

Synthetic aperture radar comprises an airborne or spaceborne radar system, moving along the azimuth direction, capable of producing high resolution images from radar returns [25]. Image generation in SAR, however, requires extensive processing of the radar return signal in order to extract the range and azimuth

11

information of the point scatterers on the ground [26]. Such processing has been traditionally performed with digital systems. Bulk optical systems have also been reported for use in processing SAR signals [27,28,29,30]. Specifically, Psaltis, *et al.* reported on an acousto-optic/CCD (A-O/CCD) based real time SAR processor [29]. This processor performs a combination of space and time integration of the SAR signals in order to obtain the range and azimuth information characteristic of the point scatterers [27].

In the course of this research, we investigated the possibility of integrating the elements of the acousto-optic/CCD SAR processor according to the architecture proposed in Fig. 1.5. The advantages of the integrated optical synthetic aperture radar (IOSAR) processor over other electronic and bulk optical processors are small size, low power consumption, and fast computational speeds. The integrated system should also prove relatively inexpensive to manufacture in quantity. The above advantages will allow for *in situ* real time processing of radar returns in airborne systems, a task which is severely limited by the present state of technology.

The same basic architecture of space and time integration used in A-O/CCD SAR processors is employed in the IOSAR processor architecture. An understanding of the radar return signals that are employed to drive such A-O/CCD (or IOSAR) processors, and the methods by which the images are formed, are crucial to the development of performance criteria for both individual elements and their interactions. Hence, a review of the basic nature of SAR signals and of the A-O/CCD technique of processing SAR signals is provided.

1.1   Synthetic Aperture Radar (SAR)

Synthetic aperture radar (SAR) comprises a radar system which employs a small air/spaceborne antenna flying at height h along the direction η (azimuth)

12

with a constant velocity v [28,29,25]. The objective of this system is to determine the range and azimuth information of the point scatterers on the ground. This operation is linear; hence determining the range and azimuth of a general point scatterer completely describes the system by giving its impulse response.

A point scatterer can be assumed to be located at coordinates $\eta = \eta_0$ and $\xi = \xi_0$ as depicted in Fig. 1.6 [28]. The instantaneous range of the point scatterer from the aircraft is R(t). The SAR signals are periodically transmitted linear FM pulses with chirp rate B, pulse repetition frequency (PRF) equal to 1/T and pulse duration τ. The radar signal is FM in order to conserve the transmitted peak power. Therefore, the size of the required transmitter is relatively small, making them practical for air/spaceborne systems. The transmitted waveform is given by

$$S(t) = \sum_s rect\left[\frac{t - sT}{\tau}\right] exp\left[jB(t - sT)^2\right] exp(j2\pi f_0 t) \qquad (1.1)$$

in which s is the number of the transmitted pulse and f_0 is the microwave frequency.

The radar signal illuminates a patch on the ground and the wave reflected from the point scatterer is received aboard the aircraft. The objective here is to form an image of the scatterers from the received signal which are of the form:

$$r(t) = S(t - 2R/c). \qquad (1.2)$$

From the geometry of Fig. 1.6, the instantaneous range R(t) can be written as

$$R(t) = \sqrt{(\eta_0 - \eta)^2 + R_0{}^2} = \sqrt{(\eta_0 - vt)^2 + R_0{}^2} \qquad (1.3)$$

in which $R_0 = \sqrt{h^2 + \xi^2}$ is the range when the antenna crosses $\eta = \eta_0$. In most cases range variations in time can be neglected within the duration of a single radar pulse; therefore $R(t) \simeq R(sT)$. In addition, the range R_0 is typically much greater than the distance $|\eta - \eta_0|$. This allows Eq. 1.3 to be written in the form:

$$R(t) \simeq R(sT) \simeq R_0 + \frac{(vsT - \eta_0)^2}{2R_0}. \qquad (1.4)$$

13
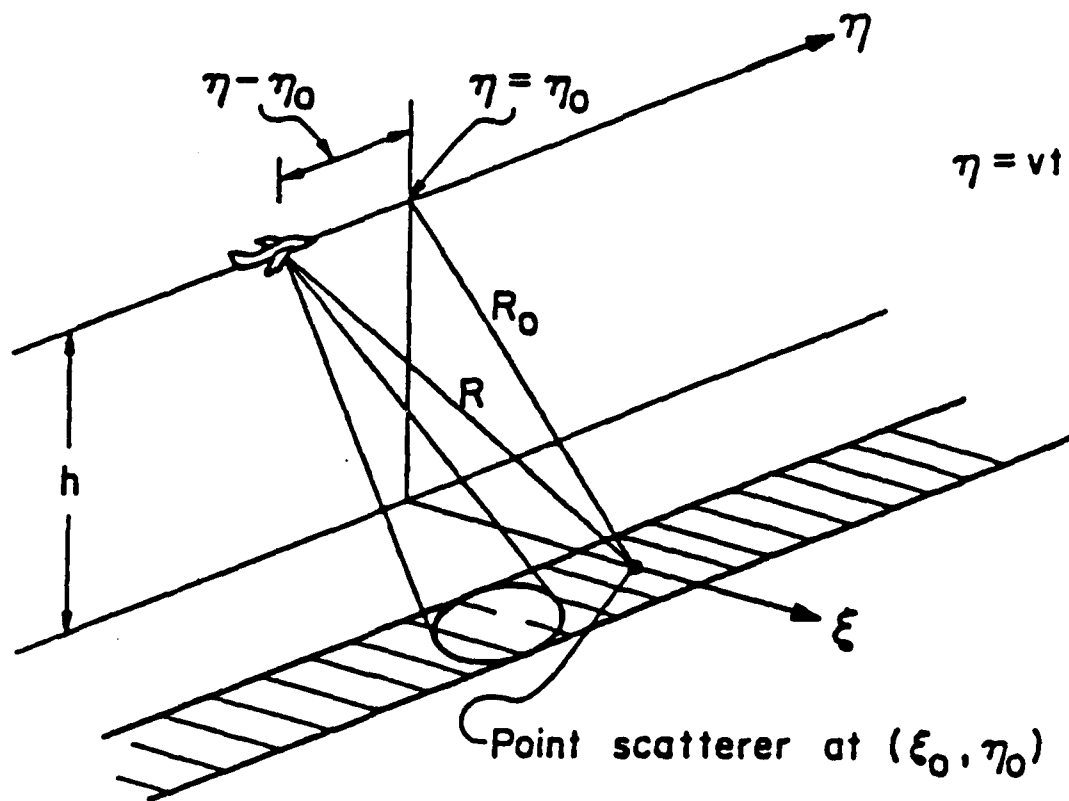
Figure 1.6: The synthetic aperture radar (SAR) geometry (after Ref. [28]).

14

Using Eqs. 1.4 and 1.1 in Eq. 1.2, we obtain the returned signal, which after simplification is of the form [28]:

$$r(t) = \sum_s rect\left[\frac{t-2R_0/c-sT}{\tau}\right] exp\left[jB(t-2R_0/c-sT)^2\right]$$
$$exp\left[-j(2\pi f_0/cR_0)(vsT-\eta_0)^2\right] exp(j2\pi f_0 t). \qquad (1.5)$$

This is the signal that needs to be processed to yield the image of the point scatterer on the ground. Next, I will summarize the acousto-optic/ CCD SAR processor and its imaging capability as reported by Psaltis, et al. [29].

1.2 Acousto-Optic/CCD SAR Processor

A schematic diagram of the A-O/CCD processor is shown in Fig. 1.7 [28,29,27]. The radar return signal is applied to the processor through the AOD device. The linear FM pulse shape of the radar signal causes the acoustic waves to form a traveling chirped grating, which produces focusing of the light incident onto the AOD. The range of the point scatterer determines the roundtrip radar pulse propagation time delay to the target. This time delay corresponds to the propagation time of the acoustic wave in the AOD device. Hence, targets with smaller range cause focusing further from the AOD transducer than targets with longer range. The light diffracted by the AOD is expanded uniformly in the vertical direction. The self-focusing of the diffracted light produces a focused radar image in the range dimension. This is also shown in the upper half of Fig. 1.8.

The range focused image is multiplied by a fixed two-dimenaional mask, on which the azimuth phase history is recorded. A typical mask function is shown in Fig. 1.9. The product is then detected on a two-dimensional CCD detector array. The CCD array operates in the shift-and-add mode; hence the received signal is time correlated against the mask function to perform the azimuth compression function. Azimuth compression by the A-O/CCD processor is shown in the lower half of Fig. 1.8.

15
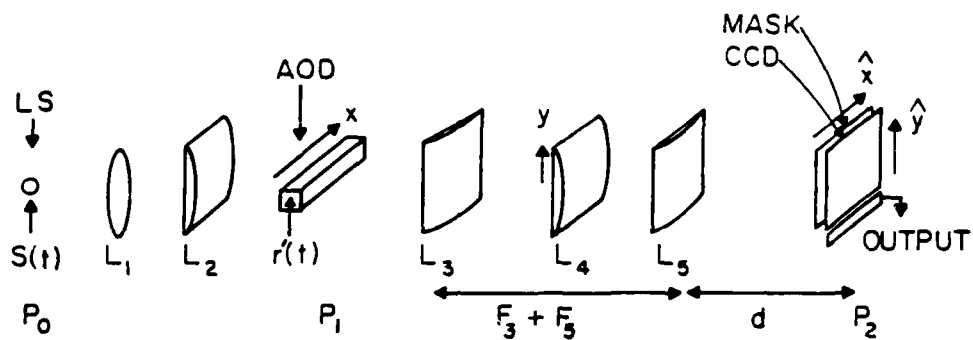
TOP VIEW
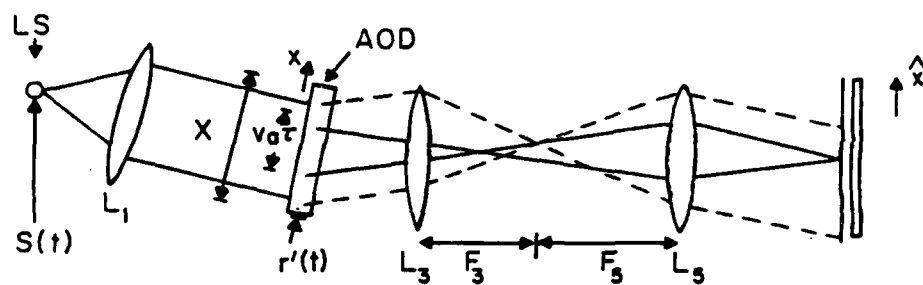
SIDE VIEW
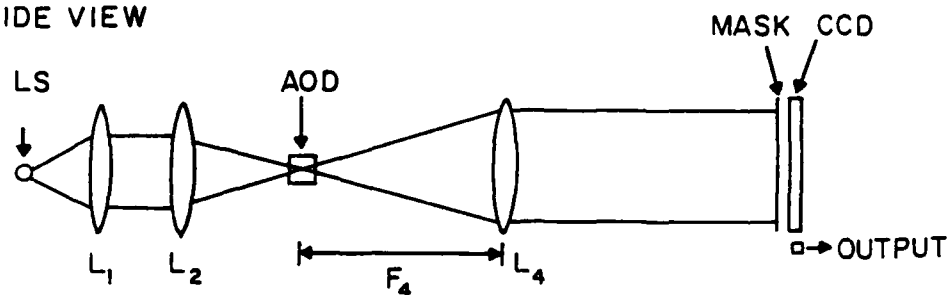
Figure 1.7: Acousto-optic/CCD SAR processor. The elements of the processor include: LS–light source, AOD–acousto-optic device; F_i is the focal length of the lens L_i, and the broken lines indicate the path of the rays of the reference wave (after Ref. [28]).

16

The acousto-optic/CCD SAR processor performs two tasks: spatial integration for range compression, and temporal integration for azimuth compression. In this architecture, the simultaneous use of these two integrations allows the two-dimensional image-forming operation to be implemented with a one-dimensional AOD as the input transducer. A more detailed explanation of the acousto-optic/CCD SAR processor is given next.

The light amplitude of the source is modulated by

$$P(t) = \sum_s rect\left[\frac{t - sT}{\tau_0}\right] \tag{1.6}$$

in which τ_0 is the duration of each light pulse. The duration of the light pulse should be short enough such that the surface acoustic modulation in the AOD can be considered frozen during this period. This requirement is to ensure that range smearing in the processor is negligible.

The repetition rate of the light pulse (1/T) is the same as the radar pulse repetition frequency (PRF). The coherence of the light source is critical in maintaining the phase information needed for subsequent azimuth compression. The spherical lens L_1 collimates the incoming beam, and the cylindrical lens L_2 focuses this beam in the vertical (y) dimension into the aperture of the AOD device.

The piezoelectric transducer of the AOD is modulated by the following signal

$$r\prime(t) = r(t)exp\left[-j2\pi(f_0 - f_1)t\right] + Aexp(j2\pi f_2 t). \tag{1.7}$$

The signal $r\prime(t)$ is the summation of the signal $r(t)$ heterodyned to the center frequency of the AOD (f_1), and a reference signal. The inclusion of the reference signal in the A-O/CCD device allows us to record on the CCD an amplitude dependent on the phase of the detected signal. This is necessary because the doppler information that is essential for the focusing in the azimuth direction is encoded as a phase modulation of the range compressed signal. When the

17

RANGE COMPRESSION BY SPATIAL INTEGRATION

CCD ARRAY
DETECTOR

PULSED
LASER
DIODE

AO
BRAGG
CELL

INPUT
RADAR (SAR)
SIGNAL

ZERO ORDER
STOP
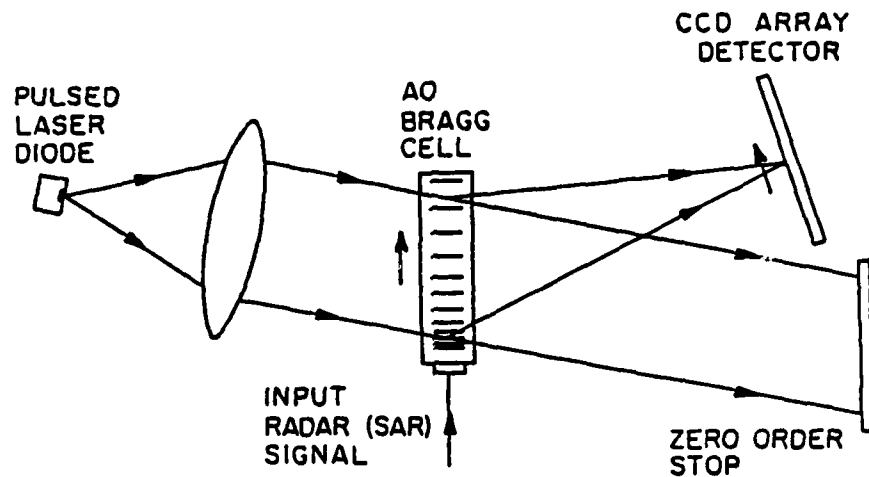
AZIMUTH COMPRESSION BY TEMPORAL INTEGRATION

TEMPORALLY
MODULATED,
SPATIALLY
UNIFORM
ILLUMINATION

SHIFT
AND
ADD

STATIONARY MASK   CCD DETECTOR ARRAY
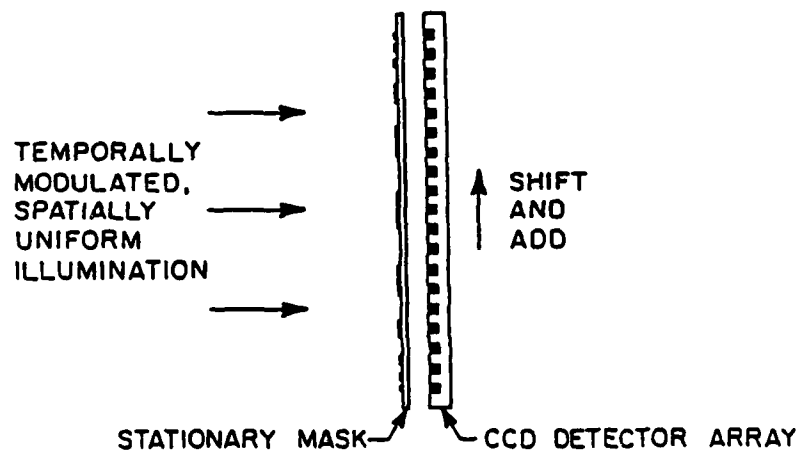
Figure 1.8: The upper diagram depicts the range compression technique described in detail in the text. The lower diagram shows the azimuth compression technique.

18
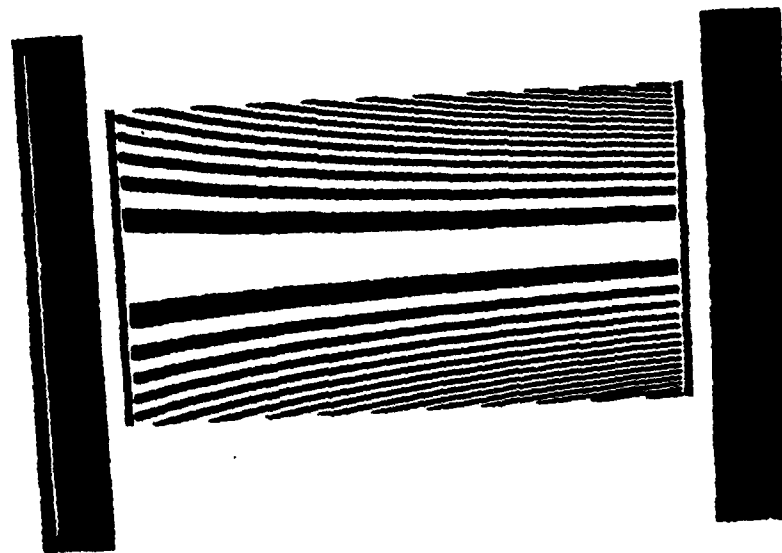
Figure 1.9: A typical mask function, bearing the azimuth doppler phase history in the vertical dimension, and the range dependence of the azimuth phase history in the horizontal dimension.

antenna approaches targets, the returned signal is upshifted in frequency compared to the transmitted signal. This effect is reversed when the antenna recedes from targets, in which case the frequency is down shifted. The level of up or down shift depends on the azimuth of the target.

The light focused into the aperture of the AOD will be modulated by the following signal

$$S_1(t) = P(t) \, r\prime \left(t + \frac{x}{v_\alpha} \right).$$ (1.8)

In Eq. 1.8, x is the direction of the acoustic wave propagating with the velocity v_α.

The lenses L_3 and L_5 in Fig. 1.7 focus and tilt the beam in the x direction on the plane P_2 (see Ref. [28]). This is needed since the beam after the AOD is tilted from the propagation axis due to Bragg diffraction. The lens L_4 recollimates the light in the vertical y direction so that the amplitude of the light entering plane P_2 does not vary along y.

The mask function bearing the azimuth doppler phase history is located at plane P_2, and the two dimensional transmissivity of this transparency is given by:

$$T(\hat{x}, \hat{y}) = \frac{1}{2} + \frac{1}{2} cos \left[2\pi u_0 \hat{x} + \frac{b_2 \hat{y}^2}{\hat{x}} \right].$$ (1.9)

The spatial frequency u_0 is given by $(f_2 - f_1)/v_\alpha$ and the parameter b_2 is given by [28]

$$b_2 = \frac{4 f_0 v^2 T^2 v_\alpha}{c^2 \Delta y^2}.$$ (1.10)

The parameters in this equation are as defined earlier.

Immediately behind the mask with the azimuth phase history, there is a two dimensional CCD detector array, which is operating in the shift-and-add mode [28]. In this mode of operation, the periodically generated charge pattern is electronically shifted by one pixel during each integration time. In the A-O/CCD processor the charge transferring is done in synchronism with the PRF

of the radar , and the integration period is set equal to the period T of the radar. The charge generated on the CCD during the sth radar pulse is $Q(\hat{x}, \hat{y}, s)$. After N exposures have occurred, the charge pattern gets shifted along the $\hat{y}$ direction of the CCD array by (N - s) pixels. The total charge that accumulates at each pixel located at coordinates $(\hat{x}, \hat{y})$ after N exposures is [28]

$$Q(\hat{x}, \hat{y}) = \sum_s^N Q\left[\hat{x}, \hat{y} + (N - s)\Delta y, s\right] = \frac{A v_\alpha \tau \eta}{2} sinc\left[\frac{B\tau}{\pi v_\alpha}\left(\hat{x} - \frac{2R_0 v_\alpha}{c}\right)\right]$$
$$\times sinc\left[\frac{2N f_0(vT)^2}{c\Delta v R_0}\left(\hat{y} - \eta_0\frac{\Delta y}{vT} + N\Delta y\right)\right]cos\left[4\pi u_0 \hat{x} + \varphi\right]$$
$$+\text{bias terms.} \qquad (1.11)$$

In the above equation Δy is the CCD pixel separation, and φ is a constant phase term. The final output of the processor $Q(\hat{x}, \hat{y})$ is the focused image of the scatterer. Due to the inclusion of the reference wave, the output is formed on a carrier; hence it is easily separated from the bias term. This image arrives at the edge of the device (at $\hat{y} = N\Delta y$) where a separate CCD stage transfers the slice of the image for each azimuth position to the output pin of the CCD. The azimuth slices are continuously produced as long as the flight continues.

In the $\hat{x}$ (range) direction the focused image of Eq. 1.11 is a *sinc* function with width $\pi v_\alpha / B\tau$ and centered at $\hat{x} = 2R_0 v_\alpha / c$. The range resolution on the ground is given by the inverse of the coefficient of the range dimension given in the first *sinc* function of Eq. 1.11. This is

$$\delta_R = \frac{\pi v_\alpha}{B\tau} \times \frac{c}{2v_\alpha} = \frac{\pi c}{2B\tau}. \qquad (1.12)$$

This is a well known result for SAR images stating that the resolution in the range dimension is inversely proportional to the temporal bandwidth of the transmitted signal $(B\tau/\pi)$.

In the $\hat{y}$ (azimuth) direction, $Q(\hat{x}, \hat{y})$ is also a *sinc* function whose position is proportional to η_0 (azimuth). The width of this function is given by the inverse of the coefficient of $\hat{y}$ in the second *sinc* function of Eq. 1.11, and is equal to

$(c\Delta y R_0)/(2Nf_0(vT)^2)$. In the same *sinc* function the inverse of the coefficient of η_0 gives the azimuth resolution:

$$\delta_\eta = \frac{c\Delta y R_0}{2Nf_0(vT)^2} \times \frac{vT}{\Delta y} = \frac{cR_0}{2Nf_0vT} = \lambda_0 R_0/2D_s \qquad (1.13)$$

in which $D_s = NvT$ is the distance that the aircraft travels during the integration period (NT), which is equal to the synthetic aperture of the system.

The driving signals of IOSAR processors are similar to the ones given for the A-O/CCD processors. A surface acoustic wave (SAW) transducer on the substrate of the IOSAR processor (see Fig. 1.5) is driven by a radar signal similar to the one driving the AOD device for the bulk processor. The surface acoustic waves are launched in a direction approximately perpendicular to the direction of light propagation. For a short duration light pulse, the acoustic-wave-induced refractive index distribution can be considered stationary in time. The refractive index distribution can be written as:

$$n_{dist.} \propto S_1(t - 2R(t)/c - x/v_\alpha) \propto \exp\left(-j\frac{Bx^2}{v_\alpha^2}\right) \exp\left(4j\frac{BxR_0}{v_\alpha c}\right). \qquad (1.14)$$

The term S_1 is the signal driving the SAW device in an IOSAR processor, and is given by Eq. 1.8. The two exponentials given in Eq. 1.14 are the result of substituting the argument $(t - 2R(t)/c - x/v_\alpha)$ for the parenthetical expression in the first exponential term in Eq. 1.5 and considering the x dependent terms. The refractive index distribution given above has both a quadratic and a linear phase dependence in x. The former causes focusing, and the latter causes tilting of the incident beam. The coordinates of this focus are given by:

$$x = \frac{2v_\alpha R_0}{c}, \quad z = \frac{\beta v_\alpha^2}{2B}. \qquad (1.15)$$

The above coordinates are measured from the SAW transducer. The parameter β in Eq. 1.15 is the longitudinal mode number of the guided mode (B and v_α have been defined earlier). Range compression is performed when the guided

22

light incident onto the surface acoustic wave is diffracted and focused by this wave (as shown in Fig. 1.4). The focal length of the SAW device driven by the radar signal can be of order meters. This length is adjusted to a manageable size by using lens L_2 (see Fig. 1.5).

In range compression, point scatterers that are situated at closer ranges cause focusing of the incoming beam into rib waveguides located farther from the SAW transducers than that caused by the farther scatterers.

The integrated lens L_2 adjusts the distance from the SAW to the output plane. This lens also allows for more effective removal of the undiffracted light. The range-focused image is confined to an array of channel/rib waveguides in order to preserve its spatial distribution as it propagates along the waveguide (along the z direction). The function of the waveguide array is similar to the function of the cylindrical lens L_4 described in the bulk processor case.

Selective outcoupling of light from the channels in the plane perpendicular to the substrate will make the third dimension accessible to the processor. This technique surmounts the inherent limitation of current IO processors that are confined to the plane of the substrate. The outcoupled light is incident on a two dimensional CCD array through a transmission mask sandwiched between the substrate and the CCD. The CCD array operates in the shift-and-add mode along the waveguide array, which provides the time integration correlation of the incident light to extract the azimuth information. The intensity transmission function and the operation of the CCD is similar to that of the A-O/CCD processor. Consequently, the processing and image generation is similar to that of the bulk optical system.

1.3 Outline of Dissertation

In this dissertation, the theoretical and technological feasibility of developing advanced integrated optical signal processing components is analyzed. These components are essential for the development of multi-input IO processors. Such components include densely packed waveguide arrays, integrated outcouplers, and large aperture integrated lenses with short focal lengths.

In Ch. 2, preliminary considerations of the requirements of multi-input IO processor components are presented. This will include requirements, limitations, and critical issues affecting the individual elements of these processors. The elements considered therein are: substrates, slab waveguides, laser diodes, surface acoustic wave (SAW) transducers, integrated optical lenses, discrete waveguide arrays, outcoupling elements, and the mask/CCD interface. In cases for which the design requirements need to be specified more exactly, the IOSAR processing application is used as an example.

In Ch. 3, a theoretical overview of the components studied in this research is presented. This will include the transverse mode distribution in rib/channel waveguides, and the characteristic equations for such modes. Examples of wave numbers and effective refractive indices of the guided modes in typical rib and channel waveguides of IOSAR processors are given. Also, we will present a comparison of the crosstalk problem associated with different types of waveguides. The theoretical analysis of both evanescent field and grating outcouplers is given next in this chapter, in order to understand the effect of each of the controlling parameters of such outcouplers (such as buffer thin film thickness and grating period) on their outcoupling efficiencies. The focal properties of integrated lenses will also be analyzed here. The theoretical analysis of Ch. 3 will provide essential guidelines for the fabrication of rib waveguide arrays, grating outcouplers, and integrated lenses. Finally in this chapter, the overall

throughput efficiency of IOSAR processors will be discussed.

In Ch. 4, the fabrication issues affecting each of the components are presented. Specifically, the fabrication of slab waveguides on lithium niobate substrates through titanium indiffusion (Ti:LiNbO$_3$) will be discussed. Fabrication steps of rib waveguide arrays on Ti:LiNbO$_3$ substrates will follow. The method by which surface gratings are generated on rib waveguide arrays is discussed next in this chapter. Two methods of fabricating integrated lenses are also discussed. The first method is through the refractive index modification by thin film deposition in ion milled recessed lens regions in the substrates. The second approach is through index modification by the proton exchange technique in Ti:LiNbO$_3$ waveguides [10].

In Ch. 5, we will examine the fabricated elements experimentally. The actual performance of the components will be compared to the theoretical calculations. The experimental results include the determination of guiding properties and propagation losses of individual and rib waveguide arrays. The performance of surface gratings with different periods on rib waveguide arrays will be presented. Deviations from the expected performance of these gratings will be partially explained. The performance of integrated optical lenses fabricated by means of different techniques will be examined. Finally in this chapter, the performance of an optical chip with a rib array, grating outcoupler on the ribs, and lenses integrated on the same substrate will be analyzed.

In Ch. 6, we will examine the example of the IOSAR processor more closely in order to determine how it can be implemented with the technology that is currently available. In this chapter we also investigate the limitations of using LiNbO$_3$ as the substrate for the IOSAR processor, and examine whether or not variation of the radar parameters can rectify some of these limitations. Alternative input modulators that can potentially alleviate some of the shortcomings associated with SAW input transducers and the high surface acoustic

wave velocity of $LiNbO_3$ are discussed.

Concluding remarks concerning advanced integrated optical signal processors are given in Ch. 7. In this final chapter several directions for future research will be presented.

Chapter 2

Advanced IO Processors: Preliminary Considerations

In this chapter, first we will consider the geometrical aspects of advanced IO signal processors; we will then present the performance requirements and limitations of components for such processors.

2.1 Geometry

It is important to develop an understanding of how guided light in an advanced IO processor interacts with the refractive index modulations caused by inputing the signal. Such understanding is needed in order to determine the optimum geometric orientation of the critical elements of IO processors and also to determine the fundamental limitations in their performance.

In the geometrical analysis of advanced IO processors we consider here a fairly common configuration, which is shown in Fig. 2.1. In this configuration, a refractive index distribution with linear FM modulation is induced by the input signal. The input index modulation has a length L_c and it is bounded by its lowest spatial frequency $\frac{1}{\Lambda_{0c}}$ and the highest spatial frequency $\frac{1}{\Lambda_{1c}}$. Therefore, the spatial bandwidth of the input index modulation is $\frac{1}{\Lambda_{1c}} - \frac{1}{\Lambda_{0c}}$ and the chirp rate of the modulation is the bandwidth divided by the length L_c.

Here we will consider a collimated guided light beam in the processor to be incident upon the index modulation at angle θ_c as shown in Fig. 2.1. In this
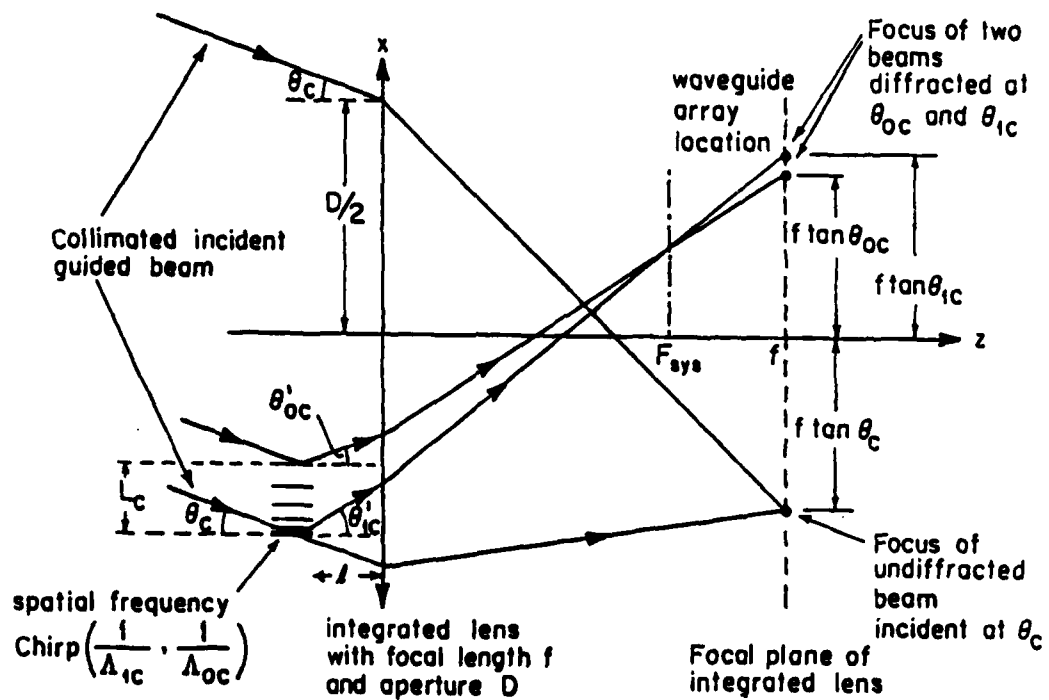
Figure 2.1: Geometrical optics of the guided beam incident upon a linear FM index modulation and an integrated lens combination (see text).

geometry, the incident guided beam is diffracted by the index modulation at angles that are in the range θ_{0c} - θ_{1c}. Since the incident beam cannot be at the Bragg angle across the entire aperture of the index modulation, the appropriate expression for the diffraction angles θ_{0c} and θ_{1c} (which we abbreviate as $\theta_{0,1c}$) is

$$\tan \theta_{0,1c} = \frac{\sin \theta_c - 2 \sin \theta_{0,1B}}{\cos \theta_c}, \tag{2.1}$$

in which the angle $\theta_{0,1B}$ is the Bragg angle at spatial frequnecy $\frac{1}{\Lambda_{0,1c}}$ and is given by

$$\Lambda_{0,1c} \sin \theta_{0,1B} = \frac{\pi}{\beta}. \tag{2.2}$$

In the above equation the parameter β is the longitudinal propagation constant of the guided mode.

The diffracted beams exiting the index modulation would cross at a distance f_c away, which is known as the focal length of the linear FM index modulation and can be geometrically determined to be given by

$$f_c = \frac{L_c}{\tan \theta_{1c} - \tan \theta_{0c}}. \tag{2.3}$$

The diffraction limited spot size of the focused beam S_c due to the chirped index modulation is given by

$$S_c = \frac{2\pi}{\beta} \frac{1}{\tan \theta_{1c} - \tan \theta_{0c}}. \tag{2.4}$$

In Eqs. 2.3 and 2.4, for small angles, the denominator can be approximated as

$$(\tan \theta_{1c} - \tan \theta_{0c}) = \frac{2\pi}{\beta} \left(\frac{1}{\Lambda_{1c}} - \frac{1}{\Lambda_{0c}} \right). \tag{2.5}$$

Therefore, the focal spot size (which is proportional to the resolution of the processor) is equal to the inverse of the spatial bandwidth of the processor.

Let us consider a typical example in which we have a linear FM modulation that is 3.5 mm long and is bound by spatial frequencies 114.7-129 lines/mm. Therefore, in this example, the spatial bandwidth is 14.3 lines/mm and the linear

FM chirp rate is 4.1 lines/mm². We will show later in Ch. 6 that such parameters are characteristic of SAW propagation in LiNbO₃. In order to determine the incidence and the diffraction angles we assumed a longitudinal propagation constant of 22.2 μm⁻¹, which will be shown later in Sect. 3.1 to be the longitudinal propagation constant that we used for titanium indiffused waveguides.

We selected the angle θ_c (see Fig. 2.1) in this example to be equal to 0.99^o in order to satisfy the Bragg condition at the center frequency of the example (*i.e.* 121.8 lines/mm). Therefore, from Eqs. 2.1 and 2.2, θ_{0c} and θ_{1c} are equal to 0.93^o and 1.04^o, respectively. We used these angles and the record length (L_c) of 3.5 mm in Eq. 2.3 and determined a 0.87 m focal length due to this linear FM chirp. In addition, Eq. 2.4 yielded a focal spot size 70 μm wide.

In order to reduce the focal length of the linear FM chirp signal used in an IO processor from the meter range to the centimeter range, integrated lenses can be employed, which also reduce the effective focal spot size of the system. In the geometry of Fig. 2.1, at a distance l_c away from the chirped index modulation, there is such a lens with a focal length of f and an aperture size of D. Using the geometrical optics method, it was determined that in the configuration of Fig. 2.1 the overal focal length of the index modulation-integrated lens combination ($F_{sys.}$, as measured from the integrated lens) is given by

$$F_{sys.} = \frac{f_c f - l_c f}{f_c + f - l_c}. \tag{2.6}$$

In an advanced IO processor, the waveguide array that is used to dissect the partially processed information should be situated at the plane $F_{sys.}$, in order for the system to focus into individual waveguides. In order to ensure efficient focusing into individual waveguides and also to prevent crosstalk, the diffraction limited spot size of the beam focused by the system of the index modulation-integrated lens combination ($S_{sys.}$) should be smaller than the width of the individual waveguides of the array. The spot size of the beam focused by the

30

system is given by

$$S_{sys.} = \frac{2\pi}{\beta}\frac{F_{sys.}}{L_c}. \tag{2.7}$$

For example, let us consider a situation in which a 2.7 cm wide integrated lens with a focal length of 10.8 cm is placed at a distance 5 mm away from the linear FM index modulation of the example given earlier in this section. This is an $f/4$ lens, and it will be shown later that such a lens can be fabricated without much difficulty. Using Eq. 2.6 for the geometry of this example, we determined that the focal length of the system is 9.5 cm (distance between the lens and the waveguide array). Such izes are manageable for implementation in LiNbO$_3$. We used the focal length of the system in Eq. 2.7 and calculated the focal spot size of the system to be approximately 8 μm wide. Therefore, the width of individual waveguides of the array should be larger than approximately 8 μm.

In order to determine the number of spots that the geometry of Fig. 2.1 can resolve (or the number of individual waveguides needed for the waveguide array), we have to first determine the range of focus in the back focal plane of the system when the index modulation record is within the aperture of the integrated lens. We geometrically determined that this range (which we call $\Delta x_{sys.}$) is given by

$$\Delta x_{sys.} = \frac{(D - L_c)F_{sys.}}{f_c}. \tag{2.8}$$

The number of resolvable spots ($N_{res.}$) is given by

$$N_{res.} = \frac{(D - L_c)\beta}{2\pi}\left(\tan\theta_{1c} - \tan\theta_{0c}\right). \tag{2.9}$$

This result was obtained by dividing $\Delta x_{sys.}$ by the diffraction limited spot size of the system $S_{sys.}$ (given by Eq. 2.7).

We then substituted for the parenthesis involving angles from Eq. 2.5 into Eq. 2.9, with the result that the number of resolvable spots was determined to

31

be the well known space bandwidth product, given by

$$N_{res.} \simeq (D - L_c) \times \left(\frac{1}{\Lambda_{1c}} - \frac{1}{\Lambda_{0c}} \right). \tag{2.10}$$

Therefore, for the case of a 3.5 mm long frequency chirp with a spatial bandwidth of 14.3 lines/mm and employing a 2.7 cm wide integrated lens, the number of resolvable spots was determined to be approximately 333. This is the number of individual waveguides within the array needed for such an example.

Associated with the beams diffracted by the index modulation, there are undiffracted beams that impinge upon the integrated lens and focus at a point $f \tan \theta_c$ below the axis along the focal plane of the integrated lens (see Fig. 2.1). In order to prevent such undiffracted modes from impinging upon the waveguide array, it was determined geometrically that the following inequality should be satisfied

$$(\tan \theta_{1c} + \tan \theta_c)(f_c - l_c) > D. \tag{2.11}$$

For the example considered in this section, the left hand side of Eq. 2.11 was determined to be 3 cm while the right hand side is 2.7 cm. Therefore, the undiffracted modes would not impinge upon the waveguide array in this example.

In some advanced IO processing applications such as IOSAR, there might be a need for a constant frequency index modulation used as a reference signal. The geometry for diffraction of the guided beam from such a constant frequency index modulation is shown in Fig. 2.2, in which the collimated guided incident beam diffracts at an angle θ_c and focuses at a point $f \tan \theta_c$ above the axis in the focal plane of the integrated lens. The width of the region after the lens that is illuminated by the diffracted reference beam depends on how far from the integrated lens the region is located. This width is given by

$$W_z = D \left(1 - \frac{z}{f} \right). \tag{2.12}$$
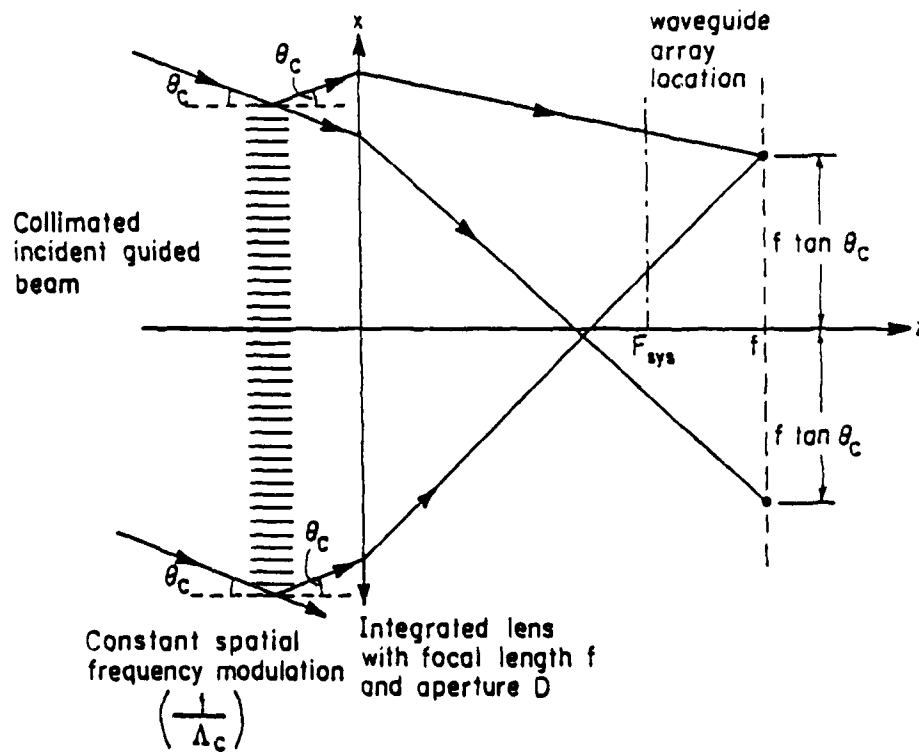
Figure 2.2: Geometrical optics of the guided beam incident upon a constant frequency index modulation and an integrated lens combination (see text).

33

At the focal plane of the system ($z = F_{sys.}$) the width of the reference beam is given by

$$W_F = \frac{Df}{f_c + f - l_c}.$$ (2.13)

The width of the reference beam at this location is wider than the waveguide array given by Eq. 2.8. Therefore, the array is completely illuminated by the reference wave. However, such illumination may cause phase curvature at the plane of the waveguides, which needs to be corrected in some applications.

2.2 Substrate

In designing integrated optical devices. choosing the right substrate is one of the first and also one of the most critical tasks. Here we will summarize the considerations that govern the selection of a suitable substrate material for our purposes. Since our effort is directed towards a proof of concept study, we will rely on a commercially available material rather than alternative materials that are more exotic. The capability to fabricate index gradients in substrates is essential since they are crucial to developing both optical waveguides and integrated lenses. In addition, propagation losses in such waveguides should be low enough to allow reasonable power levels in the resulting processors.

Earlier we showed that a number of integrated optical processors rely on SAW devices to input the signals. Efficient processing of the input signals is dependent on how well the SAW device performs on the substrate. Therefore, in these applications a substrate with high acoustooptic coefficients that provide high diffraction efficiencies is desired.

In Eq. 2.10, we derived that one factor determining the number of resolvable spots is the aperture size of the integrated lens minus the record length. In the configurations employing SAW transducers. the aperture of the surface acoustic wave that can be processed is equal to that of the integrated lens. Therefore, for

a fixed pulse duration, the number of resolvable spots is inversely proportional to the surface acoustic wave velocity. Hence, a low SAW velocity is desired in order to achieve a larger number of resolvable spots.

Considering the above requirements, $LiNbO_3$ (3m symmetry, $n_e = 2.2005$, and $n_o = 2.291$) is a uniaxial crystal particularly suited for these processing applications [1]. Waveguide fabrication techniques in $LiNbO_3$ through *titanium indiffusion* are well established [2,3,4,5,6,7]. Both the extraordinary and the ordinary refractive indices of $LiNbO_3$ substrate are increased by the titanium indiffusion technique. The extraordinary and ordinary refractive indices increase by as much as 0.05, and 0.005, respectively. The acoustooptic properties of this crystal have also been found by other investigators to be adequate [11,31].

A major drawback to the use of $LiNbO_3$ in IOSAR processors is its high surface acoustic wave velocity ($v_\alpha = 3488m/s$) [32]. In a configuration that relies on SAW transducers in $LiNbO_3$ to input the signal, such high surface acoustic velocities increase the record size L_c and reduce the spatial bandwidth in Eq. 2.10 (since spatial bandwidth is inversely proportional to the velocity); therefore, the number of resolvable spots are reduced.

At this level of examining the proof of concept of advanced IO signal processing components, the SAW velocity problem was determined to be not critical. In addition, the possibility of using electrooptic modulators as a means of inputing the signal can alleviate the problem of high surface acoustic wave velocity in $LiNbO_3$. Therefore, $LiNbO_3$ was maintained as the primary substrate for this research in spite of its high acoustic velocity.

In this research, the primary crystallographic orientation for $LiNbO_3$ substrate was Y-cut. In this orientation of $LiNbO_3$ good quality waveguides can be fabricated consistently. The waveguides were normally fabricated *parallel to the* X crystallographic axis with the c-axis (optic axis) orthogonal to the length of the waveguide. Since the refractive index gradients due to titanium indiffusion

35

and the TIPE process are maximized along the direction of the extraordinary axis, this particular choice of crystal cut provides good mode confinement when the input is TE polarized.

In the above choice of orientation, we can also employ the most suitable configuration for the SAW device in $LiNbO_3$. The preferred configuration used by other investigators that yields the highest diffraction efficiency of the guided mode is realized when the surface acoustic wave propagates along the optic axis of $LiNbO_3$ in a Y-cut crystal.

In more advanced IO processors, other materials such as the III-V compound semiconductors can potentially be used. For example, GaAs/AlGaAs ridge waveguides reported by Kapon and Bhat show great promise for such applications [33]. In addition, an abundant substrate material such as Si has also been used as the substrate for IO processors. Optical waveguides on Si have been formed by depositing As_2S_3 thin films (and SiO_2 buffer layers) [18]. The potential use of the above substrate materials in advanced IO signal processors needs to be investigated.

2.3   Laser Diode

Laser diodes are compact sources that are normally employed in integrated optics. At the present level of technology, laser diodes are often bonded in butt-coupled format to the polished edge of substrates providing efficient coupling of light from the diode into the optical waveguide. Potentially, laser diodes could be integrated into the substrates if III-V compound semiconductor substrates are used.

The divergence angle of the laser diode beam in a plane either parallel or perpendicular to the junction of the laser diode must be small enough to allow efficient butt-coupling of light into the waveguide [34]. This is because the

acceptance angle of an optical waveguide in the vertical direction is normally very small also.

Several unique losses are associated with IO processors that can place stringent requirements on the light sources. To name a few, waveguide propagation losses due to absorption, surface scattering losses, and coupling losses are amongst the most common. Of course, SAW diffraction losses and the through-put loss of integrated lenses can compound the previously mentioned losses. In order to retain enough photons for the excitation of photodetectors (such as the CCD array in the IOSAR application) and the employment of their full dynamic range, the laser diodes should have powers high enough to compensate for the device losses.

In specific IO applications that rely on surface acoustic waves for processing, the laser diode pulse duration must be very small. This is needed to ensure that during the time the laser diode is on, the SAW wave is almost stationary in order to prevent smearing of information from one waveguide to the next in the array. For example, if the focal spot size of the SAW wave in $LiNbO_3$ is 70 μm, then the laser diode pulse duration should be less than 20 nsec. In order to be able to pulse the laser for such a short duration, its modulation frequency should be greater than 50 MHz.

When a laser diode (LD) is pulsed, the time after the onset of laser oscillation in which the LD changes from its initial multimode operation to a single lasing mode is known as the coherence time [35]. For some of the advanced IO applications which process part of the information interferometrically, the phase information is critical. Hence, the coherence time of the laser diode must be a negligible portion of the pulse width to obtain coherence. In addition, the coherence length of the laser diode should be larger than the physical dimensions of the processor [34].

For example, let us consider a Hitachi model HLP1600 laser diode with the

37

following specifications: 30 mW output power at 0.85 μm wavelength; $\theta_{\parallel} = 10^{\circ}$, and $\theta_{\perp} = 24^{\circ}$ divergence angles; and 1 MHz-2 GHz modulation frequency. The coherence length of such laser diodes is about 15 m [36]. The coherence time of a typical Hitachi laser diode (model HLP1600) was determined by Haney (Ref. [35]) to be about 1 ns. Most performance characteristics of laser diodes satisfy the above requirements. In applications for which the laser diode beam divergence angle in the perpendicular direction is larger than the acceptance angle of the waveguide (i.e. 5 - 10° for Ti:LiNbO$_3$), graded-index (GRIN) lenses can be used to effectively focus the laser light into the waveguide.

It should be noted that all of the analysis and design specifications presented in this dissertation were conducted for the He-Ne wavelength of 0.633 μm used in our experimental characterization. Consequently, for the case of processors using semiconductor laser diodes (e.g. 0.85 μm) appropriate modifications to all of the parameters must be conducted in order to account for the wavelength difference [37].

2.4 Addition of the Reference Wave

As was mentioned in the previous chapter, in some of the advanced IO processors there is a need for a reference wave. For example, in IOSAR processing applications the addition of a reference wave to the SAR return signal was needed in order to utilize the doppler phase information needed for azimuth determination.

One method by which the reference signal can be introduced and mixed with the radar signal is electronically. In this technique, the radar return signal is mixed with a signal at the center frequency of the SAW transducer (f_1). The heterodyned signal is then electronically added to the reference signal with center frequency f_2 and then applied to the SAW transducer [28]. An inherent problem

with this method is that it reduces the available dynamic range by a factor of two.

It is also possible to add the reference signal to the radar return signal by using a secondary SAW transducer that is driven by the reference signal. This transducer is situated in series with the transducer driven by the radar return signal.

2.5   Input Transducers

In the architecture shown in Fig. 1.5, a surface acoustic wave (SAW) device is the transducer by which the radar return signals are input into the IOSAR processor. This method of inputing the radar signals is not unique. An alternative approach for spatially modulating the light guided in the processor is to use an electrooptic modulator array such as the linear array total internal reflection (TIR) electrooptic spatial light modulator (SLM) [38]. In such a configuration, the linear array of interdigital electrodes of the TIR spatial light modulator would be fabricated on the slab waveguide orthogonal to the path of beam propagation. The electrodes of the modulator are appropriately addressed electrically by the radar return signals in order to spatially modulate the guided light confined to the slab waveguide. Employing this type of a modulator to input the signal into an advanced IO processor circumvents the need for a travelling surface acoustic wave device. Therefore, this technique is particularly attractive when substrates with high surface acoustic wave velocities are used (such as $LiNbO_3$).

For example, currently TIR modulators with electrodes that are 5 μm wide and separated by 5 μm can be fabricated on $LiNbO_3$. In other words, 100 electrodes can be fabricated in 1 mm. Such a configuration of electrodes can generate a spatial bandwidth of approximately 50 lines/mm. Using this bandwidth with

a lens aperture size of 2.7 cm and a record length of 3.5 mm in Eq. 2.10, we determined that such a configuration can support 1175 resolvable spots.

In this research, however, SAW devices were primarily considered as a means of transducing the radar signals, in order to benefit from the previously established properties of acoustic transducers as used in similar applications [18,11,39].

In advanced IO signal processing applications such as SAR processing, it is important to have processors with larger bandwidths than those of the input signals in order not to lose information. In addition, high surface acoustic wave diffraction efficiencies are desired, in order to reduce the power requirements of the laser diode. The diffraction efficiency of a surface acoustic wave depends on the substrate acoustooptic properties and the wavelength of the guided mode being diffracted.

The performance of SAW devices on LiNbO$_3$ substrates used in optical processing and computing has been established by other investigators [11]. Surface acoustic wave devices used in such applications were operated at 500 MHz center frequencies with bandwidths of 90 MHz [11]. The possibility of 70% diffraction efficiencies at low rf drive power (about 400 mW) was reported by Tsai, *et al.* [11]. Such performance by SAW devices is quite adequate for certain IO processor applications.

2.6 Integrated Optical Lenses

In Sect. 2.1 we showed the need for integrated optical lenses in order to adjust some of the dimensions in advanced IO processors. In addition, such lenses have numerous other applications such as the collimation of the diverging guided modes coupled from the laser diode.

In Sect. 2.1, we also showed that the number of spots that IO processors can resolve depends on the aperture size of the lens employed. Therefore, it is

desirable to fabricate large aperture integrated lenses in such processors. However, for a specific F-number lens, a large aperture means a large focal length. Therefore, it is also desirable to fabricate lenses with low F-numbers in order to reduce the size of the resultant processors.

In this research effort, we limited our studies to 2.5 mm wide integrated lenses because of their ease of fabrication. One of the lenses that we fabricated had a focal length of about 1.2 cm for such an aperture size (F/4.8 lens). Such principles of operation and fabrication can be extended to larger size integrated lenses. One can foresee fabricating integrated lenses with aperture sizes of about 3-4 cm and focal lengths of about 12-16 cm with currently available technology.

Since phase information is critical in many IO processing applications, phase front distortion should be minimized. Phase front distortion can be induced by either irregularities in the surface of the integrated lens or inhomogeneities in its refractive index. Another cause of such distortions is spherical aberration, which can be minimized when lenses with aspherical boundaries are employed.

Integrated lenses that exhibit high throughput efficiencies are desired in any IO application since they reduce scattering noise and reduce the input power requirements at the same time. In addition, lens configurations that occupy minimum chip real estate are always favored in such applications.

Currently, the most promising technique of fabricating integrated lenses in $LiNbO_3$ is through modification of the refractive index by the titanium indiffused proton exchanged (TIPE) method [10]. Large aperture integrated lenses (4 mm) with short focal lengths (1.5 cm) have been developed by other investigators [10]. In this dissertation we will present the results of other index modification techniques employed in $LiNbO_3$, and also discuss several improvements in the TIPE process for fabricating integrated lenses that evolved from our experiments.

41

2.7 Channel/Rib Waveguide Arrays

Densely packed channel/rib waveguide arrays that exhibit low crosstalk are essential to the development of a number of advanced IO signal processing devices. Such a waveguide array dissects the partially processed information and expands it along the direction of propagation. Any time waveguides are closely packed, crosstalk due mainly to mode overlap becomes an issue. This is especially critical in the IOSAR processor configuration, because such crosstalk could cause errors in determining the range and azimuth information. This consideration favors the use of rib waveguide arrays in place of $Ti:LiNbO_3$ channel waveguide arrays. Rib waveguides in an array are separated by air, which provides better guided mode confinement than $Ti:LiNbO_3$ channel waveguides in the same configuration since they are separated by regions of the $LiNbO_3$ substrate. This comparison will be discussed in more detail later.

Outcoupling from the waveguide arrays discussed above excites the CCD elements that are located on the top surface of the waveguides. In order to efficiently use available CCD arrays and reduce registration error in CCD elements, the size of the individual waveguides should be smaller than the CCD pixel size (typically 10 μm). In addition, the pitch of the waveguide array must match the pitch of the CCD array exactly to eliminate the possibility of a runout problem when mating the CCD array to the waveguide array. Currently available CCD arrays sizes are as high as 1000 x 1000 in a 1 cm^2 area, which yields a 10 μm pitch. Hence, for this specific example the pitch of the waveguide array must also be exactly 10 μm.

The separation between the waveguides in the array is determined by their fabrication limitations as well as the minimization of crosstalk, and is about 2 μm. Hence, the width of the rib waveguides is about 8 μm for an overall 10 μm pitch. This is also equal to the minimum waveguide width determined for the

example given in Sect. 2.1.

In this research effort we aimed at developing highly uniform rib waveguide arrays (1000 elements with 8 μm widths and 2 μm separations), in order to match currently available CCD arrays. High surface uniformities are needed to minimize surface scattering which can contribute to both crosstalk and overall processor throughput loss.

Fabrication of larger arrays is also conceivable using the currently available technology. For example, rib waveguide arrays of 5000 elements 2 μm wide with 2 μm separations can also be fabricated without much added difficulty.

2.8 Outcoupling from the Waveguide Arrays

As was pointed out earlier, a unique feature of advanced IO signal processors is that the information confined to the plane of the processor is outcoupled in order to access the third dimension for further processing capabilities. Different techniques of outcoupling from individual Ti:LiNbO$_3$ waveguides have been demonstrated by other investigators [21,40]. Their work in this area has been aimed at high efficiency outcoupling from small areas.

Our requirements of outcoupling from arrays, however, are quite different. For our purposes, uniform outcoupling is conducted over a large area of the waveguide array, and thus the outcoupling efficiency per unit length should be low enough in order to distribute the outcoupled light over a waveguide array perhaps 1 cm long and to excite all of the CCD elements. Hence, the outcoupling efficiencies per unit length required for advanced IO processors are significantly lower than the efficiencies currently used in integrated optics. If the guided mode intensity in the waveguide was uniform throughout a 1 cm long waveguide, the required outcoupling efficiency would have been 10%/mm. However, the guided mode intensity decays along the waveguide due to both propagation loss and

outcoupling. Therefore, the required outcoupling efficiencies are in the range 10-100%/mm in order to compensate for the decaying intensity.

The guided mode in a rib waveguide that has a surface grating decays with distance due to both propagation losses and outcoupling. Therefore, it may be desired in some advanced IO processor applications to have the capability of modulating the outcoupling efficiencies of individual pixels depending on their location in order to compensate for the decaying guided mode power.

We will present in Ch. 3 the results of a study comparing evanescent field with surface grating outcoupling techniques subject to the above requirements [40,21,41,42,43]. It will be shown that the surface grating technique is more favorable for our purposes.

2.9 Mask/CCD Interface

In this section, considerations pertaining to the mask function needed for certain advanced IO processor applications are analyzed. The use of such masks, which are sandwiched between the waveguide array and the CCD array in such processors, has several implications on the performance of these arrays. Overlaying the thin film of the mask on top of the surface outcouplers will affect their performance. This effect is probably larger if evanescent field outcouplers rather than surface gratings are used. The mask material and mask/CCD interface technique should also be selected such that the mask will not damage the CCD pixels when they are in contact with one another. The above problems could possibly be circumvented if microspacers are used to introduce air gaps between the above elements. The development of suitable mask functions was considered not to be critical at this stage of the research in IOSAR processors; hence they are not considered any further herein.

Two dimensional CCD arrays are also important elements of advanced IO

processors such as IOSAR [19,20,44]. Such arrays are hybridized on top of the waveguide arrays in order to detect the information that is being selectively outcoupled from these waveguides [45]. In certain applications, a CCD array operating in the shift-and-add mode can perform a correlation of the outcoupled light with the mask function by means of temporal integration in order to perform processing in an additional dimension.

The interaction of the CCD array with the light scattered by surface nonuniformities directly affects the signal-to-noise ratio and the dynamic range of IO processors. The sidewalls of the rib waveguides under the CCD arrays should then be highly uniform, in order to minimize the unwanted scattering.

A critical issue in the design of an advanced IO processor is that of potential registration errors in the mating of the CCD detector with the waveguide array. Such errors can be caused by the excitation of CCD pixels from outcoupling elements that are not directly below them. These errors can be minimized by making the outcoupling element sizes smaller than the CCD pixel sizes (in the range of 10-30 μm). Another possible cause of registration error is the runout error. This error is caused when the separations between grating outcoupling pixels both along the rib waveguides and across the array do not match the CCD array exactly. The solution to this problem is nontrivial and needs to be investigated.

The dynamic range of advanced IO processors is controlled by the losses introduced by the integrated components, and also by the dynamic range of the CCD elements. The dynamic range of CCD elements is typically about 100:1 (as high as 1000:1 for some cases) since their saturation and detection threshold energy densities are of order 1.5×10^{-7} J/cm^2, and 0.015×10^{-7} J/cm^2, respectively.

Although in this research effort we have only used the CCD arrays as light detectors, further investigation needs to be conducted in order to establish their

time integration properties in the IOSAR processor configuration.

2.10   Summary

In this chapter we presented the results of our preliminary studies of advanced IO signal processors and their components. We determined that in a geometry of advanced IO processors utilizing a 3.5 mm long spatially modulated refractive index with a bandwidth of 14.3 lines/mm, and also a 2.7 cm wide integrated lens on $LiNbO_3$, the number of resolvable spots would be 333.

For our studies, we selected $LiNbO_3$ as the common substrate because fabrication of waveguides can be relatively easily accomplished through the titanium indiffusion technique. In addition, we can benefit from high diffraction efficiencies and large bandwidths when employing surface acoustic wave transducers on $LiNbO_3$. An example of such a device in $LiNbO_3$ exhibited 70% diffraction efficiency at 500 MHz center frequency and bandwidth of 90 MHz. This was indeed shown to be adequate for some SAR applications.

It was determined that a drawback to using $LiNbO_3$ in advanced IO processors was its high surface acoustic wave velocity, which limits the number of resolvable spots. As a means of eliminating the surface acoustic wave transducers, it was suggested that a modification of the TIR-SLM, which is an electrooptic method of inputing the information, should be investigated. Use of electrooptic techniques will circumvent the problems associated with the propagating surface acoustic wave in $LiNbO_3$. It was also determined that if an electrooptic modulator with 100 lines/mm is employed, along with a 2.7 cm wide lens and a record length of 3.5 mm, then the number of resolvable spots would be 1175.

We considered laser diodes as the light source in advanced IO signal processors. As an example, we considered a Hitachi model HLP1600 laser diode which can produce 30 mW of power. This power levels adequate for most advanced IO

signal processing applications. Such a laser can also be modulated in the range 1 MHz-2 GHz, which is adequate for laser pulse durations of about 20 nsec that are needed in order to freeze the surface acoustic wave index distribution during each pulse.

Large aperture integrated lenses with short focal lengths were determined to be essential for advanced IO signal processors. Such lenses are needed to collimate the guided mode and to shorten the focal lengths due to linear FM modulated index distributions. We determined that in order to increase the number of resolvable spots in advanced IO processors, low F-number integrated lenses should be developed. In this research effort, we limited our lenses to an aperture size of 2.5 mm in order to simplify the fabrication process. However, the developement of larger aperture lenses will follow the same principle. We will examine different techniques of fabricating such lenses in LiNbO$_3$ that are also compatible with the development of other IO components on the same substrate.

It was determined that the development of large area densely packed rib waveguide arrays are needed for advanced IO processors. In order to provide matching between the currently available CCD arrays and to provide high mode isolation we selected large area rib waveguide arrays with 1000 elements that are 8 μm wide with 2 μm separations.

Uniform outcoupling from the above arrays was determined to be critical in advanced IO signal processing applications in order to provide access to the third dimension of the processor. Although we require efficient outcoupling from the entire length of the waveguide, the outcoupling efficiency per unit length is low compared with other applications. This is to allow enough light intensity in a long waveguide to excite CCD elements that are further down the waveguide. For example, we determined that a first order approximation of the outcoupling efficiency along a 10 mm long waveguide would be as low as 10%/mm. It was also determined that in some applications it is desired to have

47

the capability of modulating the outcoupling efficiencies of individual pixels in order to compensate for the decaying guided mode power in the waveguide. We also determined that the use of the mask functions can cause perturbations in the performance of the outcoupling elements.

Chapter 3

Advanced IO Components: Theoretical Overview

An understanding of guided modes in optical waveguides and their respective parameters is essential for the design and analysis of waveguide arrays, outcoupling elements, and integrated lenses in the context of integrated optical processors. Two types of discrete optical waveguides are considered here. The first type is the Ti:LiNbO$_3$ channel waveguide which is commonly used in other integrated optical applications. A possible alternative to the channel waveguide geometry is the less commonly used rib waveguide geometry which provides superior guided mode confinement. Therefore, rib waveguides are potentially better candidates for applications that require densely packed waveguide arrays. An analysis of guided modes in both types of the above waveguides will be presented here.

As a means of outcoupling from the above waveguides or waveguide arrays, we will consider both evanescent field and surface grating outcoupling. These two techniques will be studied further to examine their merits and drawbacks.

Since the development of large aperture integrated lenses with short focal lengths was an integral part of this research, we will also consider the index modification techniques that are needed to fabricate such lenses in LiNbO$_3$. The effective refractive indices of both the guided modes in such index modified regions and the guided modes in Ti:LiNbO$_3$ will be used in the analysis of the integrated lenses. The gradient in the effective refractive index in combination

49

with the geometry of the integrated lens determines its focal length. The analysis of Sect. 3.3 provides a prediction for how integrated lenses fabricated through different techniques should perform.

Since the above integrated lenses are normally used to focus into individual waveguides, we will examine the coupling efficiencies of such focusing through the use of the mode overlap integral technique.

Finally, in this chapter the overall throughput efficiency of advanced IO signal processors will be estimated.

3.1 Field Distributions in Discrete Optical Waveguides

Two different typical geometries of integrated optical waveguides are channel waveguides (shown in Fig. 3.1) and rib waveguides (shown in Fig. 3.2) [46,47]. In these geometries the optical wave is guided in the strip with refractive index n_1, which is approximately 2.25 for Ti:LiNbO$_3$ waveguides. The substrate refractive index is given by n_2, which is approximately 2.2 if the substrate is LiNbO$_3$. The value of n_0 is normally 1 unless other elements such as CCD arrays or dielectric films are situated right above the waveguide. Comparing Figs. 3.1 and 3.2, it is evident that for a rib configuration the strip of waveguide is raised above the substrate, while for the channel configuration the strip of waveguide is imbedded in the substrate.

In order to ensure that the optical wave can total internally reflect at the upper and lower boundaries of the waveguide strip, the refractive index of the waveguide must be larger than the surrounding refractive indices. In most applications, the appropriate refractive indices satisfy $n_1 > n_2 > n_0$ [46]. In the case of Ti:LiNbO$_3$ waveguides on a LiNbO$_3$ substrate, the above inequality is in fact satisfied.

Later we will discuss the fact that the concentration of titanium is Gaus-

sian with depth in a Ti:LiNbO$_3$ waveguide. The refractive index increase in the Ti:LiNbO$_3$ substrate which is needed for waveguides is proportional to the titanium concentration. Therefore, the waveguide boundary in the vertical dimension (depth of indiffusion) is also Gaussian for both the rib and channel waveguide geometries [2]. Others have investigated the numerical solutions to mode distributions in such graded index waveguides [48,43,49]. However, we will assume that Ti:LiNbO$_3$ waveguide boundaries can be approximated by sharp transitions in order to simplify the analysis. The transition region is assumed to be at a depth for which the gradient of the titanium concentration is largest.

In the case of a Ti:LiNbO$_3$ channel waveguide, which is fabricated through the indiffusion of a strip of titanium film, similar exponentially decaying waveguide boundaries (associated with the exponentially decaying titanium concentrations) exist in the lateral dimension. Such soft boundaries in Ti:LiNbO$_3$ channel waveguides in combination with the resultant small refractive index gradients could cause the modes to be weakly confined to the waveguide, which can in turn lead to leakage of the guided mode [50].

In our discussion we will primarily consider the E_x polarized guided modes in which the electric fields are predominantly parallel to the x direction of the coordinate system. These modes experience the highest refractive index gradient in titanium indiffused (Ti:LiNbO$_3$) waveguides (Y-cut and X-propagating) compared to other polarizations. Hence, guided modes with this type of polarization are better confined to the waveguide region.

The propagation phase factors of the guided modes are of the form $exp[i(\omega t - \beta z)]$. The transverse field distribution in the core of the waveguide (regions I in both Fig. 3.1 and Fig. 3.2) is sinusoidal. The transverse field distributions in regions II and III are evanescent fields and decay exponentially away from the waveguide boundaries. The overlap of evanescent field distributions of two adjacent waveguides is the principal cause of interchannel crosstalk.

51
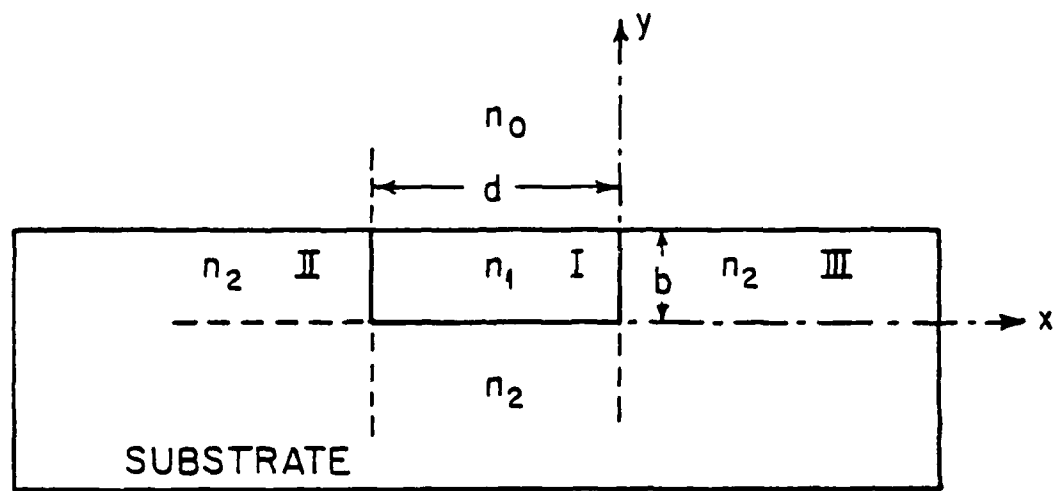
Figure 3.1: A typical channel waveguide geometry is shown schematically. The appropriate parameters used in the theoretical analysis described in the text are also shown.
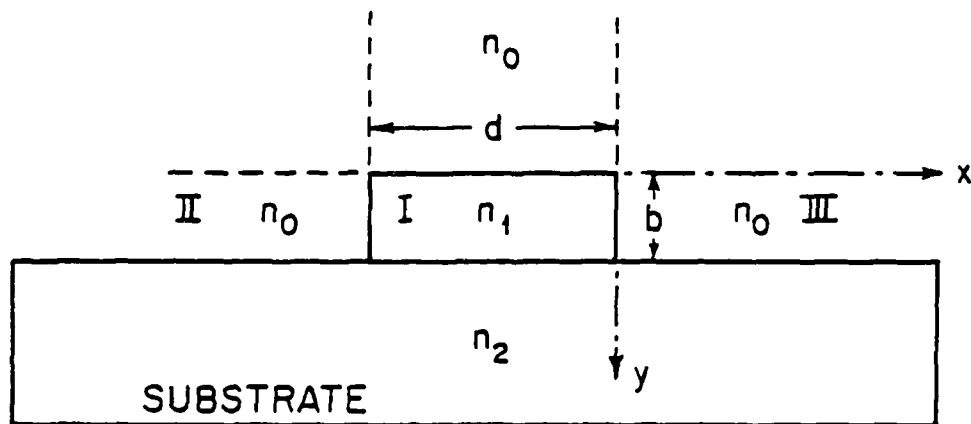
Figure 3.2: A typical rib waveguide geometry is shown schematically. The appropriate parameters used in the theoretical analysis described in the text are also shown.

Marcuse (Ref. [46]) has developed solutions for the guided mode distributions in dielectric optical waveguides with abrupt boundaries for different polarizations. In what follows below we will modify his results in order to provide E_x polarized transverse field distributions for the different regions of a rib waveguide. The modified versions of the appropriate eigenvalue equations (which are needed to extract the parameters of the field distributions) will also be given. In order to modify the following equations for channel waveguides, we merely need to replace n_0 with n_2 and γ_0 with γ_2. In addition, the y axis in channel geometry is opposite to that of the rib.

The transverse electric field distributions in the rib waveguide geometry of Fig. 3.2 are [46]:

$$Region\ I\ :\ E_x\ =\frac{iE_0}{k_x\beta}\left(n_1{}^2k^2-k_x{}^2\right)\sin k_x(x+\delta_x)\cos k_y(y+\delta_y) \qquad (3.1)$$

$$Region\ II\ :\ E_x\ =iE_0\left[\frac{\gamma_0{}^2+n_0{}^2k^2}{\gamma_0\beta}\right]\cos k_x(\delta_x-d)\cos k_y(y+\delta_y)\,exp\left[\gamma_0(x+d)\right]$$
$$(3.2)$$

$$Region\ III\ :\ E_x\ =-iE_0\left[\frac{\gamma_0{}^2+n_0{}^2k^2}{\gamma_0\beta}\right]\cos k_x\delta_x\cos k_y(y+\delta_y)\,exp\left[-\gamma_0 x\right] \qquad (3.3)$$

The parameter E_0 in all of the above equations is an arbitrary field amplitude. In Eqs. 3.2 and 3.3, the evanescent field decay constant (γ_0) in a region with refractive index n_0 is given by

$$\gamma_0\ =\ \sqrt{\left(n_1{}^2-n_0{}^2\right)k^2-k_x{}^2} \qquad (3.4)$$

In addition, k_x and k_y are the standing wave numbers in the x and y directions, respectively. The parameters k and β are the free space wave number and longitudinal propagation constant of the guided mode, respectively. In Eqs. 3.1-3.3, the parameters δ_x and δ_y are needed to assure the continuity of the fields at the waveguide boundaries. All other parameters are as defined in Fig. 3.2.

The critical parameters defined above are given by the following eigenvalue

equations [46]:

$$k = \frac{2\pi}{\lambda} \tag{3.5}$$

$$\tan k_x d = \frac{2n_1{}^2 n_0{}^2 k_x \gamma_0}{\left(n_0{}^4 k_x{}^2 - n_1{}^4 \gamma_0{}^2\right)} \tag{3.6}$$

$$\tan k_x \delta_x = -\left(\frac{n_0{}^2}{n_1{}^2}\right)\left(\frac{k_x}{\gamma_0}\right) \tag{3.7}$$

$$\tan k_y b = \frac{k_y (\gamma_2 + \gamma_0)}{k_y{}^2 - \gamma_2 \gamma_0} \tag{3.8}$$

$$\tan k_y \delta_y = -\frac{\gamma_0}{k_y}. \tag{3.9}$$

The above equations have been solved numerically for the examples that will be presented later to determine the standing wave numbers and phase factors.

The standing wave numbers are used in Eq. 3.4 for γ_0 and the following equations to determine the field decay constants and the longitudinal propagation constant. The determining equations for the remaining evanescent field decay constant γ_2 (in a region with refractive index n_2) and the longitudinal propagation constant β are:

$$\gamma_2 = \left[\left(n_1{}^2 - n_2{}^2\right)k^2 - k_y{}^2\right]^{1/2} \tag{3.10}$$

$$\beta = \left[n_1{}^2 k^2 - \left(k_x{}^2 + k_y{}^2\right)\right]^{1/2}. \tag{3.11}$$

A useful parameter of the guided mode in a waveguide is the effective refractive index (N) which can be determined from the relation

$$N = \frac{\beta}{k}. \tag{3.12}$$

As the guided mode propagates through the waveguide, a change in the refractive index will cause a change in the effective refractive index experienced by the mode. This change provides a means of calculating the focal lengths for integrated lenses with different geometries. Such analysis will be presented later in Sect. 3.3.

It was mentioned earlier that closely packed waveguide arrays might be required in some of the advanced integrated optical signal processors such as the IOSAR processor. In a geometry that has a number of closely spaced waveguides, the guided modes can couple from one waveguide to another. One reason for such coupling can be due to scattering of the guided modes into neighboring waveguides by means of surface inhomogeneities in the sidewalls of the waveguides. Another reason might be due to the weakly guided modes in channel waveguides with low refractive index discontinuities such as $Ti:LiNbO_3$ waveguides, as discussed earlier. In a geometry that employs closely packed and long $Ti:LiNbO_3$ waveguide arrays, weakly guided modes can potentially couple out of one waveguide and couple into the neighboring waveguide.

For the case of closely packed waveguides that have sharp boundaries and are strongly guiding, there could still be significant crosstalk due to mode overlap. The coupling occurs because the evanescent field in one waveguide extends outside its boundaries into the neighboring waveguide, causing the excitation of the guided mode in the second waveguide. If the coupling coefficient due to the mode overlap in such a situation is κ, the power in the first waveguide decays as $\exp(-\kappa z)$ while the power in the coupled waveguide grows as $\exp(\kappa z)$ along the waveguide.

The coupling coefficient between two discrete waveguides with abrupt boundaries has been determined by other investigators using mode coupling theory [51,52,53,54]. We will herein adopt the coupling coefficient (κ) determined by Kuznetsov (Ref. [51]) for our geometry in which two rib waveguides are separated by a distance W (or a gap between the waveguides of $W - d$). In order to modify this equation for the case of channel waveguides, again we substitute n_2 for n_0 and γ_2 for γ_0. The coupling coefficient determined for the rib waveguide

geometry is

$$\kappa = \frac{2(n_1/n_0)^2 k_x^2 \gamma_0 \, exp\left(-(W-d)\,\gamma_0\right)}{3d\left[k_x^2 + (n_1/n_0)^4 \gamma_0^2\right]}$$
$$\times \left[1 + \frac{2}{\gamma_0 d}(n_1/n_0)^2 \frac{k_x^2 + \gamma_0^2}{k_x^2 + (n_1/n_0)^4 \gamma_0^2}\right]. \tag{3.13}$$

The parameters in this equation are similar to those defined for the field distributions given earlier and also as shown in Fig. 3.2. A major determining parameter in the above equation is the evanescent field decay constant γ_0 (or γ_2 for the channel waveguide case).

For the case of rib waveguides, if we assume homogeneous surface quality the above coupling coefficient is a good approximation for the crosstalk, because the boundaries separating the rib waveguides are abrupt. In the case of Ti:LiNbO$_3$ channel waveguides, however, the waveguide boundaries are not abrupt, causing the actual coupling coefficient to be higher than the one determined from Eq. 3.13. This is because in the derivation of this equation, mode coupling due to weakly guided modes is ignored.

Next, we will use the analysis of the transverse field distributions and also of the coupling coefficient between two discrete waveguides presented in this section to study two examples of rib waveguides and Ti:LiNbO$_3$ channel waveguides. We will calculate the field distribution parameters including the field decay parameters. We will also determine the coupling coefficients between two neighboring waveguides for both waveguide types.

For example, let us consider rib waveguides suitable for use in the advanced IO processors discussed previously. It will be shown later that the $1/e$ depth of the Ti:LiNbO$_3$ waveguides is approximately 1 μm, which is considered to be the rib waveguide height (b). Other parameters for our example are: width (d) $\simeq 8$ μm, n_1 (Ti:LiNbO$_3$) = 2.25, n_2 (LiNbO$_3$) = 2.20, and n_0 (free space) = 1. These parameters were used in Eqs. 3.6, 3.7, 3.8, and 3.9, which were solved numerically in order to determine the mode parameters. The parameters for the

lowest order rib waveguide mode are: $k_x \simeq 0.4 \ \mu m^{-1}$, $k_y \simeq 2 \ \mu m^{-1}$, and $\gamma_0 \simeq 20$ μm^{-1}. The parameters δ_x and δ_y were determined to be approximately 0 and -0.7 μm, respectively. Using the above parameters in Eq. 3.11, the longitudinal propagation constant (β) was determined to be 22.2 μm^{-1}. For the He-Ne wavelength of 0.63 μm the value of the free space propagation constant k is about 9.9 μm^{-1}.

We next used the determined values for β and k in Eq. 3.12 to calculate the effective refractive index experienced by the lowest order guided mode (N) in this example of rib waveguide geometry to be approximately 2.23. This value will be used later in determining the outcoupling efficiencies of surface gratings on rib waveguide arrays.

For a typical Ti:LiNbO$_3$ channel waveguide with similar dimensions to that of the rib waveguide, the relevant parameters are (see Fig. 3.1): width (d) $\simeq 8 \ \mu m$, height (b) $\simeq 1 \ \mu m$, n_1 (Ti:LiNbO$_3$) = 2.25, n_2 (LiNbO$_3$)= 2.20, and n_0 (free space) =1. These parameters were used in Eqs. 3.6, 3.7, 3.8, and 3.9 as modified for the case of channel waveguides, which were solved numerically in order to determine the channel waveguide mode parameters. The parameters for the lowest order channel waveguide mode are: $k_x \simeq 0.37 \ \mu m^{-1}$, $k_y \simeq 2 \ \mu m^{-1}$, and $\gamma_2 \simeq 5 \ \mu m^{-1}$. The parameters δ_x and δ_y were determined to be approximately 0 and -0.6 μm, respectively. Using the above parameters in Eq. 3.11 the longitudinal propagation constant (β) was determined to be approximately 22.2 μm^{-1}. Similarly, the effective refractive index experienced by the lowest order mode in this example of a Ti:LiNbO$_3$ channel waveguide (N) was determined to be approximately 2.23.

Comparing the longitudinal propagation constant β of the Ti:LiNbO$_3$ channel waveguides with that of the rib waveguides in the above examples, it is determined that they are approximately equal. The equality of the longitudinal propagation constants results in the equality of the effective refractive indices

of the guided modes in the Ti:LiNbO$_3$ channel waveguide with those of the rib waveguide of comparable geometric parameters. We will try to explain why the propagation constants (and the effective refractive indices) are the same for the above two geometries next.

Comparing the parameters k_x and k_y determined for both channel and rib waveguide examples, we see that the former values are slightly different, while the latter values are exactly equal. In addition, the determined k_y values are much larger than k_x values. Therefore, from Eq. 3.11 it is obvious that k_y is the determining factor for β, which makes it equal for both channel and rib waveguide examples.

The reason why the values of k_y are similar for both channel and rib waveguide examples is that the major factors governing its value are the waveguide dimension in the y direction and the waveguide core refractive index. These two factors are the same for both channel and rib waveguides in the examples presented.

An extension of the reasoning just presented shows that both k_y and β of the modes in a 1 μm thick Ti:LiNbO$_3$ slab waveguide are equal to those of a Ti:LiNbO$_3$ channel waveguide. Numerical solutions of the characteristic Eq. 3.8 for such a slab waveguide yielded 3 distinct solutions for k_y, which means that the waveguide can support 3 modes that are polarized parallel to the x direction (TE modes).

It was shown earlier that rib waveguides differ from channel waveguides in the horizontal (x) dimension. In this dimension a rib waveguide is bounded by a much lower refractive index material (which is air for our example) than LiNbO$_3$, which surrounds a Ti:LiNbO$_3$ channel waveguide. Therefore, the guided modes in rib waveguides are better confined laterally than the modes guided in Ti:LiNbO$_3$ channel waveguides. The results of the examples presented earlier show that the evanescent field decay constant of the lowest order rib waveguide mode (γ_0)

is about 4 times larger than that of the lowest order channel waveguide mode (γ_2). This means that the guided modes in a rib waveguide decay much faster with distance in the transverse dimension than do guided modes in a Ti:LiNbO$_3$ channel waveguide of comparable geometric parameters.

Let us now consider two situations in which we have densely packed Ti:LiNbO$_3$ channel waveguide arrays in one, and rib waveguide arrays of comparable geometric parameters in the other. In both of the above situations we will use the waveguide geometries and propagation parameters presented earlier in Eq. 3.13, in order to determine the coupling coefficient due to the mode overlap of the neighboring waveguides. The gap between neighboring waveguides that we used in this analysis is 2 μm. This gap combined with the waveguide width of 8 μm provides a 10 μm pitch for the waveguide arrays, which is a suitable separation if we need to mate the waveguide arrays with CCD detector arrays in which the smallest pitch that is currently available is about 10 μm.

For the above examples, the coupling coefficients were determined using Eq. 3.13 to be approximately 8×10^{-19} cm^{-1} and 2×10^{-4} cm^{-1}, respectively. Therefore, for waveguides that are 1 cm long the coupling at the end of waveguides due to neighboring rib waveguides is approximately zero, and that due to neighboring Ti:LiNbO$_3$ channel waveguides is approximately 1%. In reality however, the actual power transfer from one Ti:LiNbO$_3$ channel waveguide to the neighboring waveguide is larger than the value shown above. Specifically, it was mentioned earlier that Eq. 3.13 is not adequately representative for the case of Ti:LiNbO$_3$ channel waveguide arrays, due to weakly confined guided modes in such waveguides which can cause significant additional crosstalk. On the other hand, the results obtained above are in fact representative of the power transfer in the rib waveguide array situation, given that the surfaces of the rib waveguides are highly uniform (to prevent scattering).

The above results suggest the potential of using rib waveguides in the densely

packed array configurations needed in advanced IO processors. We will show in Ch. 5 the results of fabricating large arrays of rib waveguides on Ti:LiNbO$_3$ substrates in which we examine their potential more closely. For this reason we consider only rib waveguide geometries in the following analysis.

3.2 Integrated Outcouplers

It was mentioned earlier that as one of the critical components required for advanced IO signal processors, we need to develop integrated outcouplers on rib waveguide arrays in order to make the third dimension of the processors accessible for processing functions. In the IOSAR processor, for example, the range focused light confined to the rib waveguides is outcoupled and incident on a two-dimensional CCD array through a mask function. Time integration correlation of the outcoupled light and the mask function is subsequently accomplished by the CCD array operating in the shift-and-add mode, in order to provide the required azimuth compression function. It was mentioned earlier that higher numbers of integration steps will yield better azimuth resolution. Cu:rently available CCD arrays have a maximum of 1000 pixels, in which the pixel size is about 10 μm; this translates into a CCD array that is 1 cm long. Therefore, in order to obtain the maximum performance from currently available CCD arrays, we need to match the CCD elements with the outcoupling elements over a 1 cm long distance.

In outcoupling light from rib waveguides over such distances, we need to extract the guided light as uniformly and as efficiently as possible. For example, if the integrated outcoupler on the surface of the rib waveguide array in an IOSAR processor provides an outcoupling efficiency per unit length of 10%/mm, by the end of the 1 cm rib waveguides all of the light confined to the waveguides is efficiently outcoupled. We define the outcoupling efficiency in units of

61

percent per millimeter as the ratio of the total power extracted by a 1 mm long outcoupler to the guided power incident upon the outcoupler. The outcoupled light, however, is not necessarily uniform over the entire length of the waveguides. This is because the intensity of the guided mode in a waveguide decays due to propagation loss. In addition, the introduction of surface outcouplers which partially outcouple light from the waveguide also causes a decay in the guided mode intensity. It is therefore desirable to compensate for such a decay by somehow modifying the outcoupling pixels so that the outcoupling efficiency increases along the rib waveguide. Any residual nonuniformity in the outcoupled intensity can possibly be corrected by modification of the mask function.

In this section, two major techniques of accomplishing the outcoupling of guided modes from optical waveguides will be discussed and compared subject to the above requirements. The first technique of interest is that of introducing a high refractive index detector at close proximity to the surface of the waveguide with a buffer thin film between the two elements, which has been used by other investigators to outcouple light from individual waveguides [40]. Surface gratings fabricated on top of a waveguide are another way of outcoupling the confined modes from the waveguide [55,21,9,41,56,57,58,59].

Surface outcoupling elements such as those analyzed and fabricated in this research are unique in three respects. The first major issue is the outcoupling efficiency per unit length requirements. Outcouplers that were typically used by other investigators have been designed for maximum or near maximum outcoupling efficiencies. For example, the outcoupling efficiencies reported by Huang and Lee for 500 μm long blazed gratings with different blaze angles, formed on channel waveguides fabricated on LiNbO$_3$ substrates, were 20-60% [21]. This translates into an outcoupling efficiency per unit length of 44.6-90%/mm. It was shown earlier that we may require a much broader range of outcoupling efficiencies per unit length in our research. For example, outcoupling efficiencies

62

in the range 10-100%/mm are more appropriate for advanced IO processors such as the IOSAR processor.

The second reason why the development of uniform outcouplers in this research is unique is that they have been fabricated on the nonuniform surface of fabricated large area rib waveguide arrays. The third point of departure from previous work is the potential for modification of the outcoupling efficiency according to the location of each outcoupling element along a particular waveguide.

In this section, the above two techniques (*i.e.* evanescent field and surface grating outcoupling) will be analyzed and compared according to these three criteria in order to determine their potential for use in integrated optical signal processors.

3.2.1 Evanescent Field Outcouplers

In the analysis of the optical waveguides, it was mentioned that associated with the guided modes there are also evanescent fields outside of the boundaries. Such fields decay exponentially away from the boundaries. In the technique of evanescent field outcouplers, if we introduce a high refractive index material such as a Si detector ($n = 3.8$) at close proximity to the waveguide, the evanescent fields will leak into the detector causing outcoupling [40].

We determined earlier that the evanescent decay constant in air for a Ti:LiNbO$_3$ waveguide (γ_0) is approximately 20 μm^{-1}; hence at a distance of 0.05 μm away from the boundary the field decays to $1/e$. This distance also approximates the distance between the detector and the waveguide. In order to allow more tolerance for the assembly of the detector to the waveguide, a thin film with a higher refractive index than air such as SiO$_2$ is used as a buffer layer between the two elements [40]. In such a geometry, the outcoupling efficiency from the waveguide to the detector can be controlled by the refractive index of the buffer layer and its thickness. The geometry of the evanescent outcoupling technique

is shown in Fig. 3.3, in which t_f and n_f are the thickness and refractive index of the buffer thin film. In addition, in this figure n_3 is the refractive index of the detector.

In order to maintain the guiding condition in the overlayed Ti:LiNbO$_3$ waveguide, the buffer layer should have a refractive index lower than that of the LiNbO$_3$ substrate ($n_e = 2.2$). This is indeed true for most buffer thin films that are used for this purpose. The reason for this choice of refractive indices is to maintain the total internal reflection (TIR) condition of the guided mode in the region with the overlayer, as will now be explained in more detail.

Let us consider the simplistic view of optical ray propagation in waveguides, which are composed of a high refractive index dielectric material in a lower refractive index surrounding. As was mentioned earlier, the negative gradient of the refractive index from the waveguide to the surrounding is needed so that the optical ray may total internally reflect at the waveguide boundaries. In order for the light ray to do so, the angle at which the ray is incident upon the waveguide boundaries should be larger than the critical angle θ_c. If the refractive index of the surrounding outside of the specific boundary is n_s and the refractive index of the waveguide is n_w, the critical angle is determined from

$$\sin(\theta_c) = \frac{n_s}{n_w} \tag{3.14}$$

In addition, the TIR angle for the guided mode must be equal for both upper and lower waveguide boundaries, since these boundaries are parallel. The above assertions reveal that the critical angle governing the TIR condition at the upper and lower boundaries is set by the lowest of the refractive index gradients across these boundaries. For a Ti:LiNbO$_3$ waveguide the lowest refractive index gradient is from Ti:LiNbO$_3$ ($n_w = 2.25$) to LiNbO$_3$ ($n_s = 2.2$).

In order to determine the evanescent field outcoupling efficiency, we must consider the electric field transmittance from the waveguide to the detector
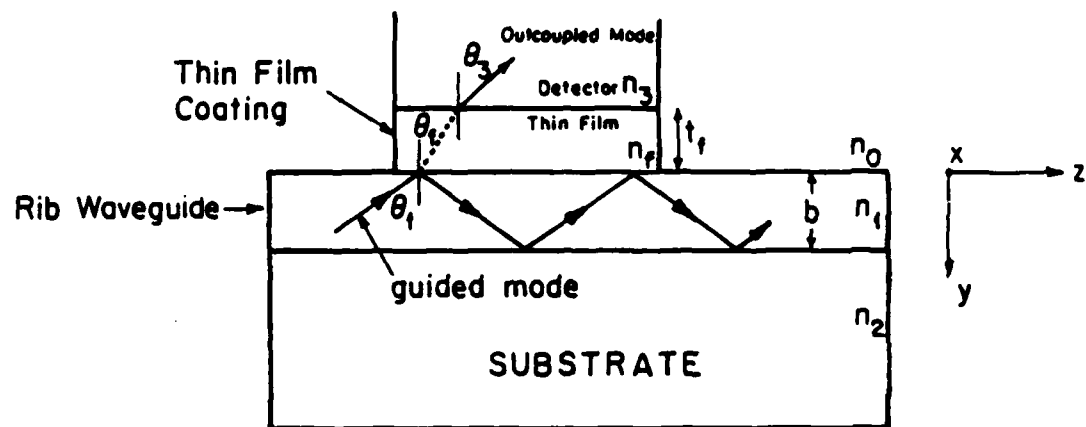
Figure 3.3: This schematic diagram depicts evanescent field coupling with a buffer thin film between the waveguide and the high refractive index detector. The appropriate parameters and refractive indices are shown.

every time the guided mode reflects from the region with overlayer. The partial outcoupling of the guided mode due to field transmittance causes the guided mode intensity to decay along the length of the thin film. If the electric field transmittance of the thin film on the waveguide is given by T_f, then every time the ray is reflected from the thin film the intensity outcoupling factor is equal to $|T_f|^2$. The number of times that the guided ray is reflected from an overlayed region that has length L_f multiplied by the intensity outcoupling factor determines the outcoupled intensity. From Fig. 3.3, we can determine that the separation between two reflection points is given by $2\,b\tan\theta_1$.

If we assume that the guided mode under the thin film region exponentially decays due to outcoupling with the leakage corresponding to an average decay constant α_f, the outcoupling efficiency of such a geometry will be given by

$$\frac{I_{out}}{I_{in}} = 1 - e^{-\alpha_f L_f} \tag{3.15}$$

The guided mode intensity decay factor α_f is the ratio of the power leaked out of the waveguide per unit length divided by the power carried in the waveguide [40]. Ranganath and Wang showed that the decay factor α_f is given by [40]

$$\alpha_f = \frac{|T_f|^2}{2b\tan\theta_1}. \tag{3.16}$$

The field transmittance at various dielectric interfaces for oblique incidence with different polarizations has been analyzed extensively by Klein, in which he has also considered multiple reflections within the dielectric film [60]. We can easily modify his results for the geometry of Fig. 3.3. For the E_x polarized guided modes, we determine that the field transmittance T_f is given by

$$T_f = \frac{\tau_w \tau_f exp(-i\Upsilon/2)}{1 + \rho_w \rho_f exp(-i\Upsilon)}. \tag{3.17}$$

The parameters τ_w and τ_f are the transmission coefficients of the waveguide to the buffer thin film, and of the buffer thin film to the detector, respectively.

66

The parameters ρ_w and ρ_f are the reflection coefficients at the above interfaces. The parameter Υ is the phase factor of the transmitted field with respect to the incident field in the waveguide. For the geometry of Fig. 3.3, the above parameters can be determined from the following relations:

$$\tau_w = \frac{2\tan\theta_f}{\tan\theta_1 + \tan\theta_f} \tag{3.18}$$

$$\tau_f = \frac{2\tan\theta_3}{\tan\theta_f + \tan\theta_3} \tag{3.19}$$

$$\rho_w = \frac{\tan\theta_f - \tan\theta_1}{\tan\theta_1 + \tan\theta_f} \tag{3.20}$$

$$\rho_f = \frac{\tan\theta_3 - \tan\theta_f}{\tan\theta_f + \tan\theta_3} \tag{3.21}$$

and

$$\Upsilon = \frac{4\pi n_f t_f \cos\theta_f}{\lambda}. \tag{3.22}$$

The angle θ_1 is the angle at which the guided mode is incident at the waveguide-thin film interface, and for a guided wave this angle can be determined from [46]

$$\sin\theta_1 = \frac{\beta}{n_1 k}. \tag{3.23}$$

At the waveguide-thin film interface, part of the guided mode is refracted into the thin film at angle θ_f. The refracted beam in the thin film is subsequently refracted out of the structure at angle θ_3 (see Fig. 3.3). The above angles all satisfy Snell's law:

$$n_1 \sin\theta_1 = n_f \sin\theta_f = n_3 \sin\theta_3. \tag{3.24}$$

Normally, the angle θ_f is imaginary due to the TIR condition. However, the above analysis still applies for such cases by using a complex number representation of the angles.

As an example of such an outcoupling technique, let us consider a situation in which a Si detector ($n_3 = 3.8$) is situated above a rib waveguide (considered

in Sect. 3.1) with a buffer thin film of SiO_2 ($n_f = 1.46$) sandwiched between them. We will attempt to determine the film thickness required to provide an outcoupling efficiency of 10%/mm.

The propagation parameter of the lowest order mode in the rib waveguide ($\beta \simeq 22.2 \ \mu m^{-1}$) along with the free space propagation constant of approximately $9.92 \ \mu m^{-1}$ for a He-Ne beam was used in Eq. 3.23 to determine the angle θ_1 to be $81°$. The remaining angles were determined from the Snell's law relationship presented in Eq. 3.24. The field transmittance of the SiO_2 thin film of thickness t_f sandwiched between the waveguide and the detector was determined using the appropriate parameters in Eq. 3.17. The resulting T_f was used in Eq. 3.16, in order to determine the guided mode intensity decay factor as a function of t_f. This factor was finally used in Eq. 3.15, in which the outcoupling efficiency was set equal to 10% and the film length L_f was set equal to 1 mm. Solving the resulting Eq. 3.15 for t_f we determine the thin film thickness needed for 10%/mm outcoupling efficiency to be approximately equal to $1000\text{\AA}$.

In order to examine the case of high efficiency evanescent outcoupling, we also calculated a required film thickness of 360 $\text{\AA}$ for 90%/mm. Therefore, the approximate range of SiO_2 film thicknesses needed for advanced IO signal processing applications is about 360-1000 $\text{\AA}$. Such thicknesses of SiO_2 can be deposited by both electron beam evaporation or sputtering techniques.

The effects of using three different film materials (air, SiO_2, and Si_3N_4 ($n_f = 1.95$)) for the buffer layer between the detector and the waveguide has been analyzed by Ranganath and Wang [40]. In their analysis they calculated the length of the buffer film required to extract 95% of the light from a single mode Ti:LiNbO$_3$ channel waveguide (i.e., the interaction length) as a function of the buffer film thickness, and their results are shown in Fig. 3.4.

The results plotted in Fig. 3.4 show that for the same interaction length, lower refractive index films require smaller thicknesses to extract 95% of the

68
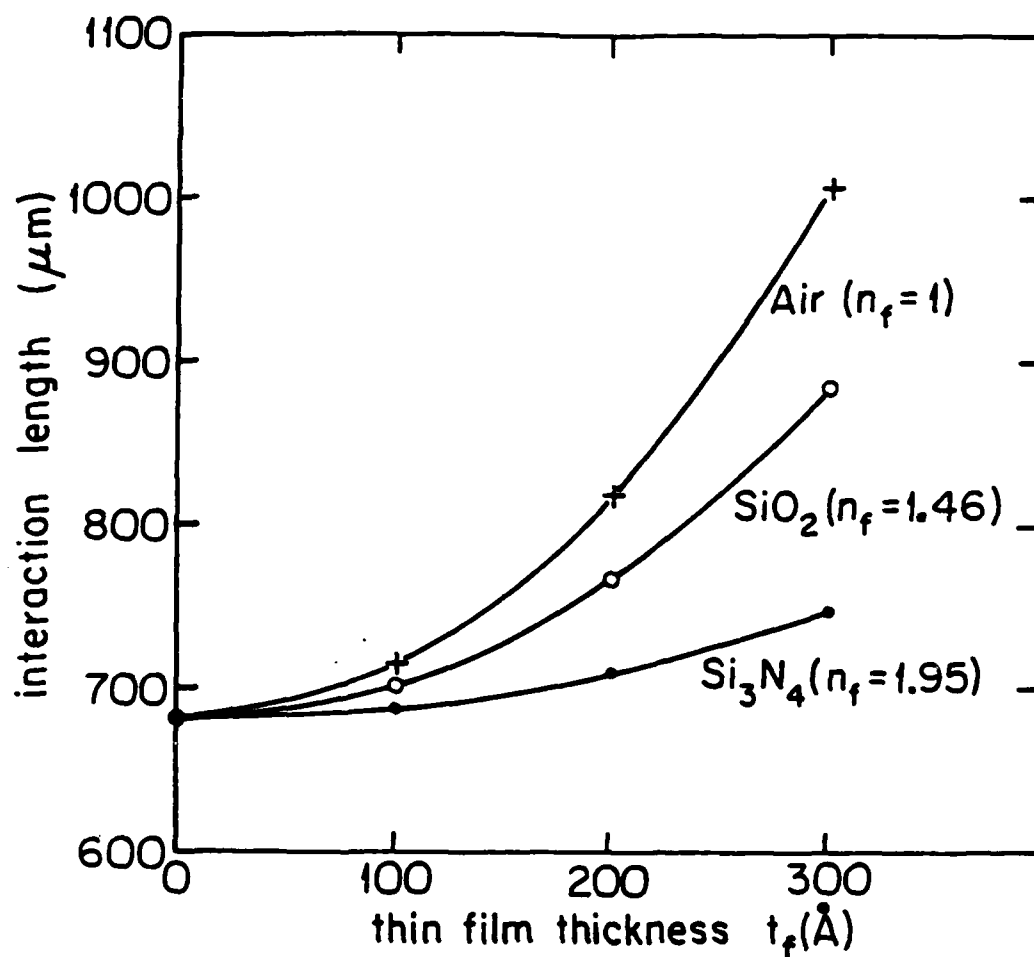
Figure 3.4: Length of the evanescent field coupling region (interaction length) required to extract 95% of the guided light from a single mode Ti:LiNbO$_3$ channel waveguide plotted for different thicknesses and refractive indices of the buffer region (after Ranganath and Wang [40]).

light. Therefore, the use of buffer films with higher refractive indices provides a less stringent proximity requirement between the detector and the waveguide, which can make the assembly of such elements easier.

An implication of the buffer film thicknesses determined for our example and also those given by Ranaganath and Wang, is that they are much smaller than the typical thicknesses of the masks, which are a few microns thick. Therefore, assembly of a mask (as is needed for advanced IO signal processors) between the detector and the waveguide can become impractical. A method by which such masks can be incorporated in the evanescent field coupling scheme is to area modulate the buffer layers in order to control the transmissivity from the waveguide to the detector.

3.2.2   Uniform Surface Grating Outcoupling

Gratings fabricated on the surfaces of waveguides are another means by which the guided light can be outcoupled [55,21,9]. A schematic diagram of rectangular surface gratings on a rib waveguide showing the appropriate geometrical parameters is shown in Fig. 3.5. The parameter d_1/Λ is the aspect ratio of the grating and Λ is the grating period. The parameters t_g and b are the grating and rib waveguide heights, respectively.

The guided modes incident into the region of the gratings are scattered into space harmonic fields that vary as $exp[i(\omega t - k_{zm}z)]$ [55,41,56,57,58,59]. The propagation parameters of the scattered fields are

$$k_{zm} = \beta_m + i\alpha_m = \beta_0 + \frac{2m\pi}{\Lambda} + i\alpha_m, \quad m = 0, \pm1, \pm2, \pm3, \dots \quad (3.25)$$

In Eq. 3.25, the parameter m is the order of the grating spatial harmonic giving rise to the scattered field.

In Eq. 3.25, the wave number β_0 is closely approximated by the longitudinal propagation constant (β) of the rib waveguide modes in regions without grating

70
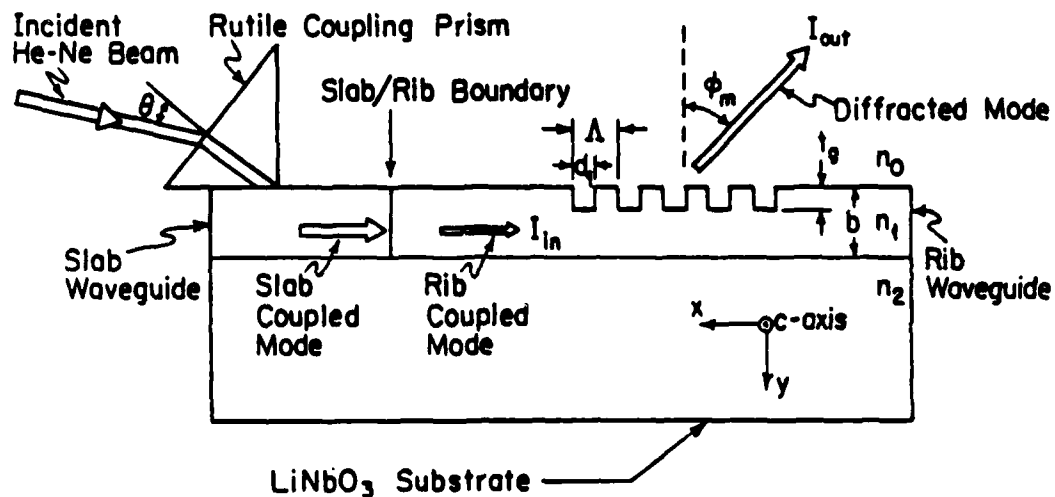
Figure 3.5: The fabrication of uniform surface gratings on rib waveguides is shown schematically. The light is incoupled into the slab waveguide via a rutile prism, and the guided mode is subsequently partially coupled into rib waveguides [61]. The modes that are excited in the rib waveguides are partially scattered out of the waveguides by the rectangular surface gratings. The parameters determining the performance of the gratings are shown in this figure. The appropriate crystallographic axes of $LiNbO_3$ as used in the analysis are also shown.

71

modulation [55]. This approximation is valid when the grating refractive index is the same as that of the waveguide. In addition, the grating height should be much smaller than the rib waveguide height. The parameter α_m in Eq. 3.25 is the decay constant of the guided modes propagating in the grating region. This decay of the guided modes is due to the transfer of energy from the guided modes into the modes that are outcoupled by the grating into the air and into the substrate.

The outcoupling efficiency into the mth mode is given by the following equation

$$\frac{I_{out}}{I_{in}} = 1 - e^{-2\alpha_m L_g} \tag{3.26}$$

in which L_g is the grating length, I_{in} is the incident intensity of the guided mode and I_{out} is the outcoupled mode intensity. The total outcoupling efficiency of all the modes can be determined from the same relation by performing a summation of all the leakage factors.

Due to the periodicity of the scattering elements of the gratings, the outcoupled modes form constructive interference at specific angles [55]. The radiation angles of these leaky waves are given by

$$\Phi_m = sin^{-1}\left(\frac{\beta_m}{k}\right), \quad m = 0, \pm 1, \pm 2, \dots \tag{3.27}$$

In order to obtain real outcoupling angles, the following inequality must be satisfied [55]

$$\left|\frac{\beta_m}{k}\right| < 1. \tag{3.28}$$

As before, in the above equations k is the free space propagation constant. It is evident from this inequality and Eq. 3.25 that only a few spatial harmonics satisfy the outcoupling criteria.

Tamir and Peng (Ref. [55]) have analyzed several different geometries of surface gratings extensively. Specifically, they have determined the guided mode decay factor α_m, which can be interpreted as the leakage factor for the mth mode

72

scattered by the grating. We modified the expression for the leakage factor α_m provided by Tamir and Peng in order to apply directly to the geometry of Fig. 3.5. We also limited our analysis to the case in which the aspect ratio (d_1/Λ) is equal to 0.5. This choice of aspect ratio provides the maximum outcoupling efficiency for a fixed grating height and grating period [55]. The outcoupling efficiencies for aspect ratios that are greater or less than 0.5 decrease from this maximum, and will ultimately be zero for gratings with aspect ratios that are 0 or 1, as expected.

For the case of an aspect ratio equal to 0.5, the leakage factor α_m for the mth mode scattered by the grating, when the incident beam is E_x polarized, can be determined from

$$\alpha_m \lambda \simeq \frac{2\left(n_1{}^2 - N^2\right)\left(n_1{}^2 - n_0{}^2\right)^2}{m^2 N \left(n_1{}^2 - n_0{}^2\right)} \times \frac{D}{t_{eff}} \left(\frac{t_g}{\lambda}\right)^2. \tag{3.29}$$

In the above equation, t_{eff} is the effective thickness of the rib waveguides as determined by proper consideration of the Goos-Haenchen shift [61]. This thickness, however, can be approximated by the waveguide thickness (b). The parameter N is the effective refractive index of the guided modes ($N \simeq \beta/k$), which was shown earlier to be about 2.23. The parameter D in Eq. 3.29 is given by

$$D \simeq \lambda \left[n_g{}^2 - \left(N + \frac{m\lambda}{\Lambda} \right)^2 \right]^{-1/2} \tag{3.30}$$

in which n_g is the volume average of the refractive index in the grating region $(n_g{}^2 = n_0{}^2 + [n_1{}^2 - n_0{}^2] \frac{d_1}{\Lambda}$; for our geometry, $d_1/\Lambda \simeq 0.5)$.

It is evident from the above analysis as well as intuitively that the grating outcoupling efficiency can be increased by increasing the grating height. However, there is a limit beyond which an increase in the grating height will not result in an increase of the outcoupling efficiency, because the evanescent fields scattered by the grating will decay substantially at this distance. This limiting grating height is known as the saturation height. Grating heights (t_g) that are

73

larger than the saturation height satisfy the following inequality [55]

$$\gamma_0\, t_g \;=\; 2\pi\left(N^2 - n_g^2\right)^{1/2}\left(\frac{t_g}{\lambda}\right) \geq 1. \tag{3.31}$$

When the grating height is larger than the saturation height the leakage factor for the mth mode, which therefore does not depend on the grating height, is

$$\alpha_{m,sat}\lambda \;\simeq\; -\frac{1}{m^2}\frac{\left(n_1^2 - N^2\right)\left(n_1^2 - n_0^2\right)^2}{2\pi^2 N\left(n_1^2 - n_0^2\right)\left(2N + m\lambda/\Lambda\right)} \times \frac{D}{t_{eff}}\frac{\Lambda}{m\lambda}. \tag{3.32}$$

According to Eqs. 3.29, 3.32, and 3.30 the waveguide parameters that determine the leakage factors of the guided modes outcoupled by surface gratings are the effective refractive indices of the guided modes, the waveguide thickness, and the appropriate refractive indices of the waveguides in the vertical dimension. The effective refractive indices of the guided modes and the refractive index profiles of the waveguides across the boundaries in the vertical dimension were determined in Sect. 3.1 to be the same for rib waveguides and Ti:LiNbO$_3$ waveguides (both channel and slab). Therefore, the leakage factor of a surface grating on a rib waveguide is approximately equal to the leakage factor of an equivalent grating profile on a slab waveguide, given that the refractive index profiles across the boundaries in the vertical dimensions are equal. Equality of the leakage factors implies that if such gratings (on a rib waveguide and on a slab waveguide) have equal lengths according to Eq. 3.26, the outcoupling efficiencies should also be equal.

As a matter of practicality, we should examine appropriate grating periods and grating heights as case studies that can be used for advanced IO signal processor applications. The analysis presented in this section will then be used in order to predict the performance of the grating geometries chosen for the case studies.

A major practical issue in developing surface gratings on rib waveguide arrays is the capability to fabricate such gratings. The photolithographic techniques

needed to pattern such gratings, and the subsequent ion milling of the samples to imprint the grating patterns on the rib waveguide arrays is currently limited to grating periods of about 1-2 μm. However, further work needs to be conducted in order to fabricate gratings with submicron periods. In some applications such as the IOSAR processor, we require the incorporation of CCD pixels on grating outcoupling pixels. Selecting larger grating periods will pose another limitation, which is its compatibility with the CCD element size. In other words, along the length of every CCD pixel (about 10 μm), we should have at the very least a few grating periods.

Another practical consideration in the fabrication of surface gratings on rib waveguides is the ability to control the grating height relatively accurately. In our fabrication of surface gratings on rib waveguides, the gratings heights that are larger than approximately 0.05 μm were relatively easy to control.

As practical examples of surface grating outcoupling, we will consider two grating periods of 2 μm and 4 μm formed on the surface of rib waveguides characterized by material and geometric parameters that were considered earlier. The choice of a 4 μm grating period only allows for 2.5 grating cycles along a 10 μm CCD pixel, which we assume to be a minimum number of cycles. The grating lengths and heights are approximately 1 mm and 0.05 μm, respectively. The reason for this choice of grating length is that due to the multitude of gratings on the same test patterning mask that we used in the fabrication of the gratings, we were limited to lengths of 1 mm. Therefore, the theoretical calculations for 1 mm grating lengths will correspond to the experimental analysis of gratings that are 1 mm long presented in a later chapter. For the above grating geometries we will now determine the number of modes outcoupled from the rib waveguide and their outcoupling efficiency. For all of the outcoupled modes, we will also calculate the saturation outcoupling efficiencies which, for the example of the rib waveguides presented earlier, occur for grating heights that are larger than

0.07 μm.

The rib waveguide propagation constant that was determined in Sect. 3.1 ($\beta = 22.2 \ \mu$m^{-1}) and the grating periods were used in the expression for β_m given in Eq. 3.25. The expression for β_m is then used in Eq. 3.27, subject to the inequality of Eq. 3.28, in order to determine the number of outcoupled modes for each outcoupling grating. It was calculated that gratings on rib waveguides with 2 and 4 μm periods generate 7 and 13 outcoupled modes, respectively. The appropriate parameters of the rib waveguide and the gratings were used in Eq. 3.29 in order to determine the leakage factors for the outcoupled modes. These leakage factors were used in Eq. 3.26 in order to determine the outcoupling efficiencies for gratings that are L_g long. In determining the saturation outcoupling efficiencies, we followed the same steps as above except for using Eq. 3.32 instead of Eq. 3.29. The calculated outcoupling efficiencies for all the modes outcoupled by 1 mm long gratings with 2 and 4 μm periods on the rib waveguide are presented in Figs. 3.6 and 3.7. The appropriate saturation outcoupling efficiencies, which occur for gratings that have heights larger than 0.07 μm, are also shown in Figs. 3.6 and 3.7. In these figures, we have also shown the outcoupling angles associated with the outcoupled mode numbers. The angles are measured from the vertical, and positive angles refer to the outcoupled beams that are codirectional to the direction of the guided mode propagation; the negative angles refer to the outcoupled beams that are contradirectional to the direction of the guided mode propagation.

The outcoupling efficiencies plotted in Figs. 3.6 and 3.7 increase with increasing angle. It is also evident from Figs. 3.6 and 3.7 that by increasing the grating height from 0.05 μm to 0.07 μm (saturation height), we can approximately double the outcoupling efficiency of each mode.

Let us compare the outcoupling efficiencies of the grating with a 2 μm period (Fig. 3.6) with that of the grating with a 4 μm period (Fig. 3.7). The comparison

2 Micron Grating (1mm long) Outcoupling Efficiencies
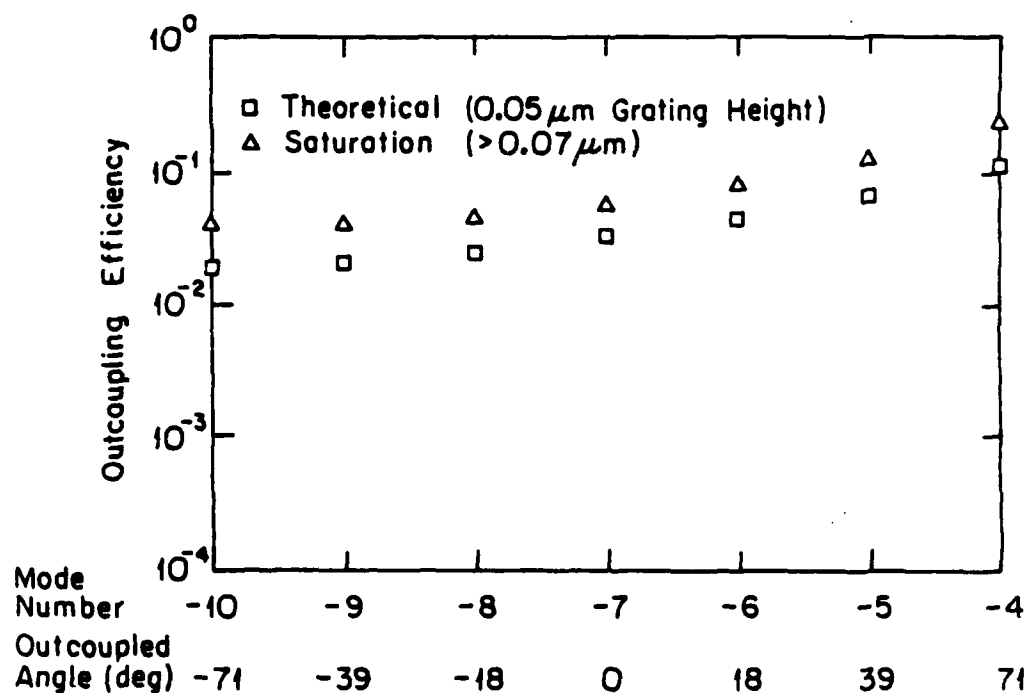
Figure 3.6: Calculated outcoupling efficiencies as a function of outcoupled mode numbers (and outcoupling angles) plotted for 2 μm grating periods that are 1 mm long. The calculations are for 0.05 μm grating heights (below saturation); also shown are theoretical calculations for gratings with heights greater than the saturation heights.

4 Micron Grating (1mm long) Outcoupling Efficiencies
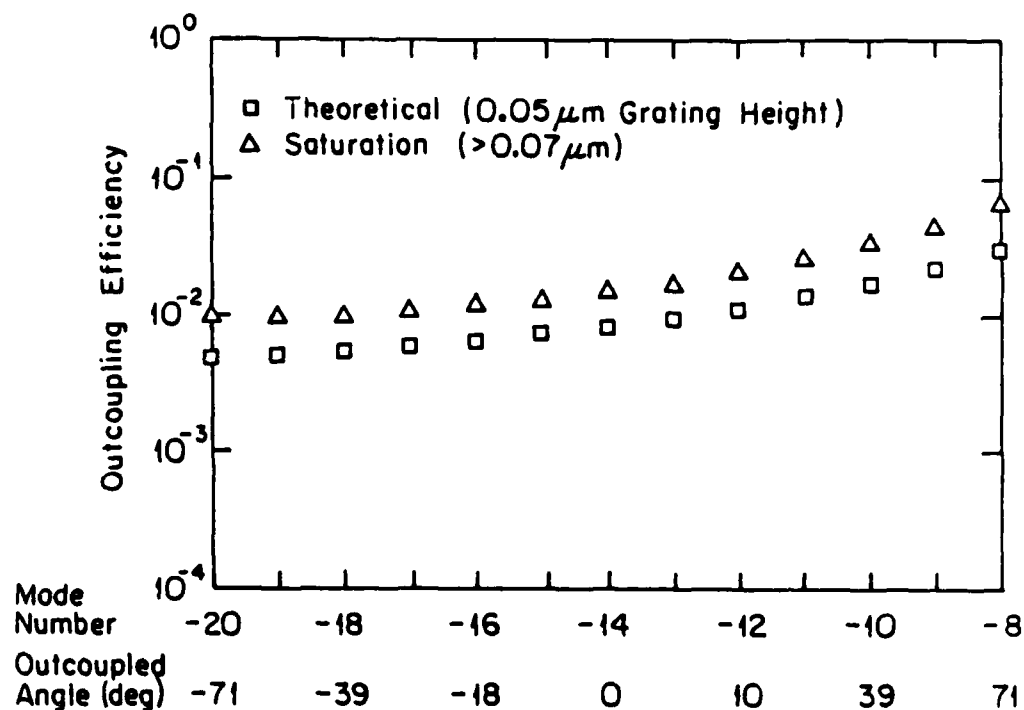
Figure 3.7: Calculated outcoupling efficiencies as a function of outcoupled mode numbers (and outcoupling angles) plotted for 4 μm grating periods that are 1 mm long. The calculations are for 0.05 μm grating heights (below saturation); also shown are theoretical calculations for gratings with heights greater than the saturation heights.

reveals that the grating with a 2 μm period in our example has outcoupling efficiencies for some modes that are approximately 4 times larger than those of the comparable modes outcoupled by the 4 μm grating.

For applications in advanced IO signal processors, however, we need to compare the total outcoupling efficiencies of the two grating examples, since ideally the detectors that are mounted on top of the gratings absorb all of the outcoupled modes collectively.

For a 1 mm grating with a 2 μm period, the total outcoupling efficiency due to all of the modes was calculated to be about 33%. The total saturation outcoupling efficiency was calculated to be about 64% for this grating period. Similar calculations for a grating with a 4 μm period yield a total outcoupling efficiency of about 15%, and a saturation outcoupling efficiency of about 29%. Comparing the total outcoupling efficiencies of the 2 μm and 4 μm gratings, we see that the former grating provides a total outcoupling efficiency that is about 2 times larger than that of the latter. Comparing the total saturation outcoupling efficiencies yields a similar result.

In other applications, grating heights are traditionally used as a means of modulating the outcoupling efficiency for fixed gratings, especially for high efficiency gratings. This is also evident from the examples given above in which we can almost double the outcoupling efficiency by increasing the grating height from 0.05 μm to 0.07 μm. Such a small variation in grating height, however, would not allow much tolerance for the fabrication of desired modulated gratings and would likely imply significant fabrication difficulties.

We propose instead to use the grating period as a more practical means of controlling the outcoupling efficiency. The above examples clearly show that by reducing the grating period from 4 μm to 2 μm, the outcoupling efficiency can be increased by a factor of 2. Such a dynamic range might not be adequate for most advanced IO processor applications. However, the possible use of gratings

with submicron periods can significantly enhance the available dynamic range. Therefore, further research in fabricating gratings with submicron periods needs to be conducted.

3.2.3 Comparison of Evanescent Field and Surface Grating Outcouplers

In this section, the two techniques of evanescent field and grating outcoupling from waveguides which were discussed previously are compared in order to assess their merits and drawbacks for advanced IO signal processing applications.

It was determined earlier that for these applications we need to uniformly and efficiently outcouple light over large distances (about 1 cm). These requirements can be satisfied by employing outcoupling elements that have low outcoupling efficiencies per unit length. At the same time, it is desirable to design the elements such that the outcoupling efficiency integrated over the entire length of the waveguide provides 100% total outcoupling efficiency. It may also be desired to modulate the outcoupling efficiencies of individual elements according to their location.

For thin film outcouplers this can be accomplished by modulating either the thicknesses or the refractive indices of the outcoupling elements. From a fabrication standpoint, controlling the refractive index as a function of outcoupler location on large area IO processor chips will likely prove to be somewhat impractical. Controlling the outcoupling efficiency of thin films by varying the thickness over a large area, on the other hand, is a more practical method. For example, in order to compensate for the decaying guided mode intensity along a rib waveguide, we can gradually reduce the deposited film thickness in order to increase the outcoupling efficiency per unit length.

Since thin films outcouplers rely on evanescent fields to outcouple the energy of the guided modes, they are required to be in close proximity to the photode-

80

tector elements. We determined that for 10-90%/mm outcoupling efficiency, we require SiO_2 film thicknesses in the range 360-1000 $\overset{\circ}{A}$. This close proximity requirement for the outcoupling elements and CCD photodetectors would be a drawback in cases requiring a mask to be sandwiched between the waveguide arrays and the CCD arrays.

Now let us consider the surface grating outcouplers. In such an outcoupling geometry, the outcoupling efficiency can be controlled by the heights or periods of such gratings. The fabrication of surface gratings with modulated heights in the range 0.05-0.07 μm (determined by our fabrication tolerance) on large area waveguide arrays such as those envisioned for advanced IO processors is impractical. Modulating the grating period, however, can potentially be used as a much more practical method of controlling the outcoupling efficiency of each pixel. To provide higher dynamic range for this technique, development of gratings with submicron periods on rib waveguide arrays is needed. The practicality of modulating the grating period stems from the fact that the mask that is used in generating the surface grating patterns can have grating lines with continuously varying separation.

Grating outcouplers provide outcoupled modes that are highly collimated away from the gratings. However, due to the multitude of diffracted orders, the largest outcoupled angle determines the proximity requirement of the photodetector to the grating. This is due to the fact that the large angle modes can excite neighboring photodetectors if the separation between these two elements is large enough.

In a number of advanced IO signal processing applications the power reflectivity of the guided modes due to any surface outcoupling elements needs to be minimized. For example, in the IOSAR processor application such reflectivities could give rise to azimuth smearing. The power reflectivity due to an evanescent field outcoupler on a rib waveguide array occurs more or less at at interface

81

between the region of the rib waveguide without a thin film layer, and the corresponding region with the layer. The grating outcoupler, on the other hand, can produce a distributed power reflectivity along the rib waveguide, influencing the outcoupled power distribution.

The power reflectivity of a surface grating can be minimized by selecting grating periods that are significantly larger than the Bragg period determined from $\Lambda_B = 2\pi/\beta$. The Bragg period determined for the rib waveguide of our example, for which β was determined to be about 22.2 μm^{-1}, is 0.1 μm. Therefore, for grating periods in the range 2-4 μm the power reflectivities are negligible. On the other hand, if gratings with submicron periods are employed such power reflectivities will become more significant.

Due to the potential advantages of surface grating outcouplers over thin film outcouplers, we have investigated grating outcouplers further during the course of this research.

3.3   Focal Properties of Integrated Lenses

Step-index or graded-index integrated lenses can provide focusing or defocusing of the guided optical beams in the plane parallel to the surface of the waveguide [24,23,62,63]. Over the years, different techniques have been implemented to fabricate integrated lenses on a variety of substrates such as LiNbO$_3$ [64,65,10,9]. One type of integrated lens developed on LiNbO$_3$ substrates is the geodesic lens. The structure of this type of lens is formed when a spherical depression is fabricated on the LiNbO$_3$ substrate. The substrate is then overcoated with a titanium thin film followed by a high temperature indiffusion, in order to fabricate the required Ti:LiNbO$_3$ waveguide. In this manner the guided modes incident at the depression will encounter different optical path lengths depending on their point of incidence, causing focusing to occur. Vahey *et al.* reported on

82

the fabrication of 0.6 cm wide geodesic lenses on $LiNbO_3$ that have focal lengths of about 1 cm (F/1.5 performance) [64]. Despite their satisfactory performance, geodesic lenses are extremely difficult to fabricate because the spherical depression in the substrate needed for such a lens must be diamond turned in order to produce an optically polished surface with minimal induced scattered light. Such a process is not easy to control or automate for mass production.

Another type of integrated lens is the so-called Luneburg lens, which is formed by depositing circular high refractive index thin films on the waveguide. The introduction of the high refractive index circular thin film on the waveguide causes the guided modes to be focused by altering the effective refractive index in the overcoated region of the waveguide. Luneburg lenses thus normally operate on the evanescent fields of the guided mode, while the geodesic lens operates directly on the field in the waveguide.

An exciting new method of fabricating integrated lenses in $LiNbO_3$ that has recently been developed is the titanium indiffused proton exchanged (TIPE) technique [66,67,68,69,70,71]. In this technique the $Ti:LiNbO_3$ substrate is first coated with a Si_3N_4 thin film in order to form a mask. Lens shaped openings are then etched in the mask to allow for the waveguide underneath to be proton exchanged in molten benzoic acid ($C_6H_5CO_2H$). In this process, the region of $Ti:LiNbO_3$ substrate that is exposed through the mask opening loses lithium ions in exchange for an equal number of protons. This exchange causes an increase in the extraordinary refractive index of approximately 0.1 compared to the unexchanged $Ti:LiNbO_3$ region [10,67]. Large aperture TIPE integrated lenses (4 mm) with short focal lengths (1.5 cm) have been reported by Zang and Tsai [10]. The TIPE technique has also been used to develop graded thickness Fresnel lenses for use in IO spectrum analyzers as shown in Fig. 1.1.

An important part of this research program was to explore additional possibilities by which the refractive index gradients required for large aperture in-

tegrated lenses may be formed in Ti:LiNbO$_3$. Three methods of modifying the refractive index in selected regions of Ti:LiNbO$_3$ waveguides were considered during the course of the research. In the first and second techniques, the Ti:LiNbO$_3$ material within the desired lens region is removed and replaced with thin films having either higher or lower refractive indices. Therefore, we will call these integrated lenses "thin film coated recessed lenses". By properly choosing the lens profile for either of the two possibilities of higher or lower index thin film coated recessed lenses, we can produce positive lensing. These two techniques to our knowledge have not been performed previously in LiNbO$_3$.

The third method of modifying the refractive index of LiNbO$_3$ is through a variation of the previously developed titanium indiffused proton exchanged (TIPE) technique [10,67,72]. The modification of the TIPE technique was prompted by several requirements for the components used in advanced IO processors. In such processors, it is desirable to further increase the degree of mode confinement available in Ti:LiNbO$_3$ slab waveguides. Integrated components should have the smallest possible footprint on the substrate in order to maximize the degree of miniaturization available. It is also required that the integrated lenses in such processors be fabricated by a process that is inherently compatible with the processes used to fabricate all of the other necessary components. The novel process described below was developed to meet these design requirements.

In our modified technique, we mask a Ti:LiNbO$_3$ substrate with a lens shaped thin film of SiO$_2$, followed by the proton exchange process. In this modified technique the refractive index of the Ti:LiNbO$_3$ slab waveguide is further increased by the proton exchange process while masking the integrated lens regions from this process. Hence, the refractive index of the lens region is maintained at a lower value (that of the Ti:LiNbO$_3$ waveguide) while the refractive index of the surrounding waveguide is raised to that characteristic of the TIPE process. The

84

result is a TI integrated lens in a TIPE slab waveguide. The geometry of this integrated lens is shown in Fig. 3.9, in which both the longitudinal cross section and view from above are depicted. In this geometry, the combination of the concave curvatures of the TI lens with the lower refractive index (as compared to the TIPE slab waveguide) provides positive lensing.

The use of an SiO_2 thin film mask eliminates the need for Si_3N_4 films (which typically require plasma CVD deposition). The thin film of SiO_2, which only covers the lens region, may be left on the substrate without a significant effect on the performance of the integrated lens. The thin film of Si_3N_4 on the other hand, covers all of the substrate except for the lens region, and hence has to be removed. The removal of a Si_3N_4 thin film is relatively more difficult to accomplish than a SiO_2 thin film.

The modifications described above significantly simplify the fabrication of integrated lenses that are formed through the use of the TIPE process. The method of fabricating a TI lens in a TIPE slab waveguide also provides better mode confinement in the slab waveguide. The other advantage is that for the same focal length and aperture size, the TI lens in a TIPE slab waveguide occupies a significantly smaller surface area than a TIPE lens in a TI slab waveguide. This can be verified by comparing the footprint of the convex pattern (used for a TIPE lens in a TI waveguide) with that of the concave pattern (used for a TI lens in a TI waveguide) in Fig. 3.8.

In all of the integrated lens geometries, if the effective refractive index of the slab waveguide is larger than the effective refractive index of the integrated lens, a concave lens profile (similar to the one shown in Fig. 3.9) will perform positive lensing (positive f). In this configuration, lenses with convex boundaries would act as negative lenses. Similarly, if the effective refractive index of the lens region is larger than that of the slab waveguide, then a convex lens profile will perform positive lensing. Negative lensing in this configuration will be performed by

Radii of circles = 1.25 mm

1.25 mm   1.25 mm

2.5 mm
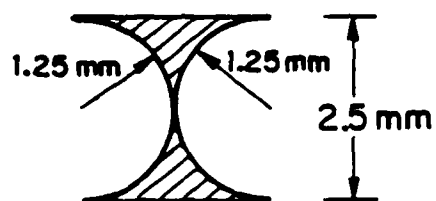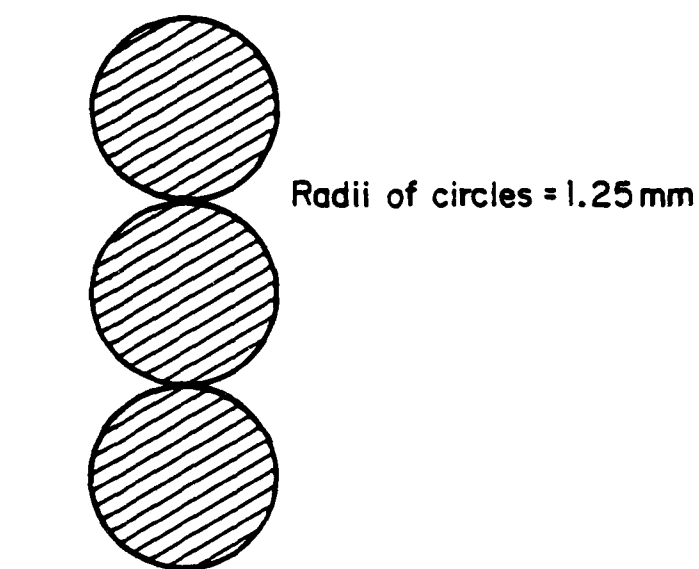
Transparent regions denoted by:

Figure 3.8: Schematic diagram of the contact mask used for patterning integrated lens geometries.

concave lenses.

Let us analyze the performance of the types of integrated lenses that we proposed to make in order to predict their focal properties. In order to simplify the analysis and experimental implementation, we will only consider integrated lenses with spherical boundaries. Spherical aberration is a problem associated with all lenses that have spherical boundaries [60]. This problem, however, can be minimized by using aspherical surfaces for the lens boundaries [65]. It is noteworthy that the simplicity of photolithographic mask definition makes the extension to far more sophisticated lens profiles straightforward.

The focal length (f) of an integrated lens is determined from the following simplified relation for thin lenses [60,65]

$$\frac{1}{f} = \frac{N_1 - N}{N} \left(\frac{1}{R_1} - \frac{1}{R_2} \right).\qquad(3.33)$$

In the above equation R_1 and R_2 are the radii of curvature of the two lens interfaces (see Fig. 3.9). The sign convention for these radii is positive and negative for convex and concave curvatures (as seen from the left), respectively. The two parameters N_1 and N are the effective refractive indices of the guided modes in the lens region and in the slab waveguide re: on, respectively. The effective refractive indices are determined from Eq. 3.12 by using the appropriate propagation constants (β) for each region.

For an E_x polarized guided beam of diameter (width) D focused by such an integrated lens, the diffraction limited spot size in the focal plane is given by $\lambda f/n_e D$. The parameter n_e is the refractive index which is excited by the E_x polarization, which in the case of Y-cut Ti:LiNbO$_3$ is the extraordinary refractive index.

The focal lengths of the integrated lenses fabricated by means of the three techniques described earlier can now be calculated using the above analysis. By the first (thin film coated recessed lens) technique, the refractive index of
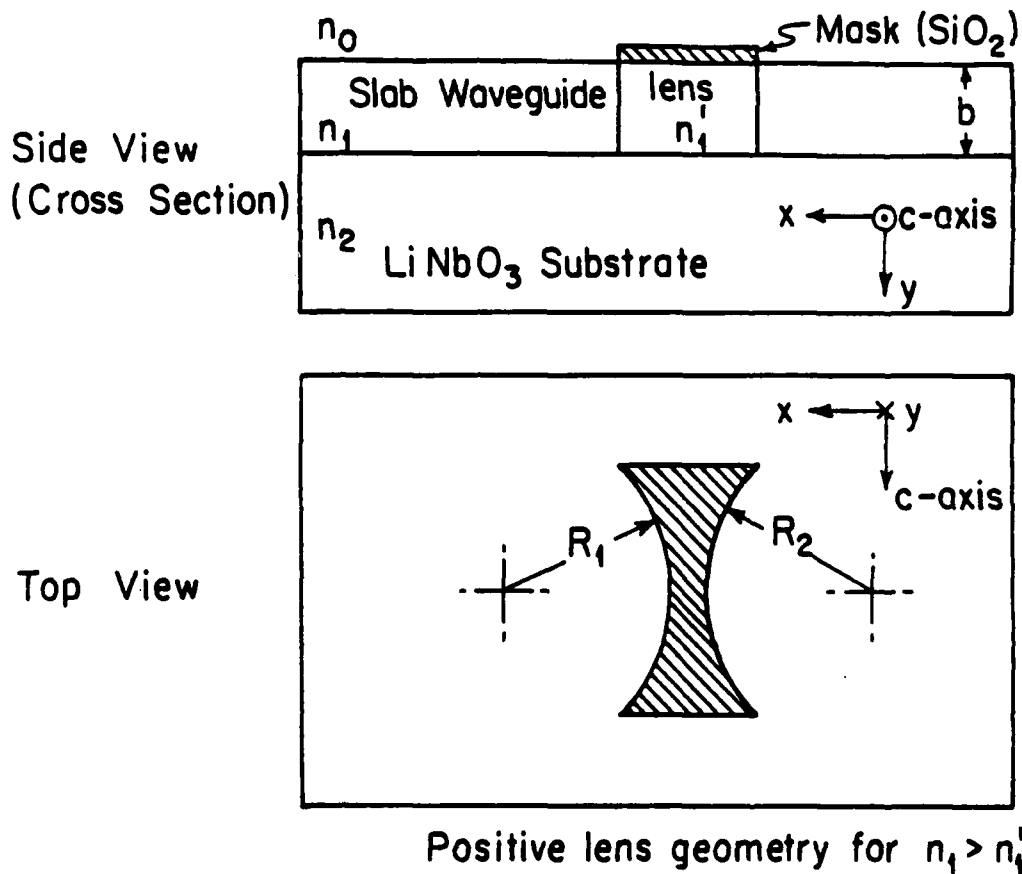
Figure 3.9: The upper and lower drawings are the cross section and top view of the integrated lens geometry discussed in the text, respectively. The appropriate dimensions and refractive indices are marked in the drawings. Note the crystallographic axes of LiNbO$_3$ as used in the advanced IO processor applications. The SiO$_2$ mask that is shown here is only required in the fabrication of titanium indiffused (TI) lenses in TIPE waveguides as discussed in the text.

the lens region in the Ti:LiNbO$_3$ ($n_e = 2.25$) waveguide is increased. This can be accomplished by replacing the waveguide material in the appropriate region with a thin film that has a higher refractive index (e.g. TiO$_2$, $n = 2.4$). For a 1 μm thick TiO$_2$ waveguide on a Ti:LiNbO$_3$ substrate (N about 2.23), calculation yields an effective refractive index of about 2.38. Using these two effective refractive indices in Eq. 3.33, we determine that a convex lens with radii of order 1.25 mm should have a focal length of about 9 mm (an F/4 lens).

Alternatively by the second (thin film coated recessed lens) technique, the material in a selected region of the waveguide is completely replaced with a lower refractive index thin film (e.g. SiO$_2$, $n = 1.46$). The use of a thin film with a refractive index lower than that of LiNbO$_3$ requires the use of a buffer material (such as MgF, $n = 1.38$) separating the thin film from the substrate. The refractive index of the buffer material should be lower than that of the thin film used in the lens region, in order to insure that the TIR condition is satisfied at the lower interface of the lens region. In this manner, in the lens region we will effectively have a SiO$_2$/MgF waveguide combination which replaces the Ti:LiNbO$_3$/LiNbO$_3$ waveguide combination.

The effective refractive index of the mode confined to a 1 μm thick SiO$_2$ film (deposited on a MgF buffer layer) was determined using the analysis of Sect. 3.1 to be 1.44. For a concave lens (with radii of order 1.25 mm) fabricated with this technique in a Ti:LiNbO$_3$ waveguide (N of order 2.22), in a manner similar to the TiO$_2$ coated lens, we calculated a focal length of about 2 mm (F/0.8). Integrated lenses with such low F-numbers can be very attractive for use in advanced IO processing applications, due to the fact that despite their large apertures they exhibit short focal lengths and diffraction limited spot sizes.

On the other hand, the large refractive index gradients that are characteristic of low F-number integrated lenses may cause back-reflection of the guided modes. In order to minimize the back-reflection problem, research should be conducted

in developing integrated anti-reflection (AR) coatings.

For the modified TIPE integrated lens, the effective refractive index of the guided mode in a TIPE waveguide (1 μm thick) was theoretically determined to be 2.3. The effective refractive index of the guided mode in the TI integrated lens was already shown to be 2.23. Calculations similar to those presented for the thin film coated recessed lenses, reveal that for a concave lens with radii of 1.25 mm the focal length is about 1.2 cm (F/4.8). Since, in our experiments we used a 1 mm wide He-Ne beam ($\lambda = 0.633$ μm), we determined the diffraction limited spot size for such a beam incident on a TI lens to be approximately 5 μm. If the aperture size of a TI lens in a TIPE waveguide is about 1 cm, the focal spot size for a beam filling the entire aperture would be approximately 1 μm. Such spot sizes are smaller than the rib waveguide widths (typically 8 μm), as required in order to provide efficient and discrete coupling into individual waveguide elements. The coupling of slab waveguide modes into individual waveguide modes via integrated lenses will be considered next.

3.4 Focused Gaussian Beam Coupling into Rib Waveguides

In advanced IO signal processors, the light that is guided in the slab waveguide is diffracted from the modulations in refractive index induced by the SAW device and focused by the integrated lens L_2 into individual waveguides of the array (see Fig. 1.5). Hence, it is imperative to analyze the coupling efficiencies of the slab waveguide modes focused by the integrated lens into the individual rib waveguide modes. In order to simplify the analysis of the mode coupling efficiency, it is assumed that there is no angular misalignment between the direction of propagation of the focused beam and the rib waveguides [73,74]. In real situations, however, slight angular misalignments could exist which can reduce the

mode coupling efficiency.

Let the transverse field profile of the focused beam at the back focal plane of the integrated lens, which is a Gaussian distribution, be denoted by E_G. Let the transverse field distribution in the rib waveguide be denoted by E_x as specified by Eqs. 3.1, 3.2, and 3.3. The mode coupling efficiency (η_c) determines how much of the mode distribution E_G overlaps with that of E_x. High overlap is required for successful coupling (high efficiencies). The mode coupling efficiency is determined from the following mode overlap integral [61]

$$\eta_c = \frac{\left| \int_{-\infty}^{\infty} E_G(x) \, E_x(x) \, d_x \right|^2}{\int_{-\infty}^{\infty} E_G{}^2(x) \, d_x \, \int_{-\infty}^{\infty} E_x{}^2(x) \, d_x}. \tag{3.34}$$

In the above equation, the x dimension is transverse to the direction of propagation and parallel to the surface of the slab waveguides (see Fig. 3.2). This is the direction in which there are discontinuities in the two modes involved in the overlap integral. There are no such discontinuities in the mode distributions in the vertical waveguide dimensions (y dimension in Fig. 3.2). Hence, the rib waveguide mode distributions appropriate for the mode overlap integral can be determined when terms involving y are eliminated from Eqs. 3.1, 3.2, and 3.3.

The electric field distribution at the waist of the integrated lens is a Gaussian distribution given by [75]

$$E_G(x) = \sqrt{\frac{2}{\pi}} \frac{exp\left[-\frac{k}{2Z_R'}\left(x + \frac{d}{2}\right)^2\right]}{W'(0)}. \tag{3.35}$$

In this equation Z_R' is the Rayleigh length of the focused Gaussian beam and $W'(0)$ is its waist size. Due to the choice of the origin in the coordinate system of Fig. 3.2, the dimensional parameter x is offset by one half the width of a single rib waveguide ($\frac{d}{2}$) in order to insure that the maximum of the Gaussian beam occurs at the center of the rib waveguide.

The waist size (for a beam focused by the TIPE lens) in our experiments was already determined to be about 5 μm. The relation between the Rayleigh

lengths before and after a focusing lens (with focal length f) is given by [75]

$$Z_R{}' = \frac{f^2}{Z_R}. \tag{3.36}$$

Since the Rayleigh length of the He-Ne beam that we used is about 2.2 m, this translates into a length of order 75 μm after the TIPE lens. The above waist size and the Rayleigh length were used in Eq. 3.35 to determine the Gaussian beam distribution.

The appropriate rib waveguide transverse mode distributions (along the x direction) were determined using the parameters given in Sect. 3.1. These distributions and the focused Gaussian beam distributions were then used in Eq. 3.34 in order to determine the coupling efficiencies. The integrals in Eq. 3.34 were solved numerically to yield a coupling efficiency of about 92% (which corresponds to a loss of about 1 dB).

If a 2.7 cm wide TI lens in a TIPE slab waveguide is used in the above coupling efficiency analysis, the focal spot size will be about 1 μm. This implies that the coupling by such a lens into the rib waveguides will be better than 92%.

These results indicate that by focusing the guided beams into the rib waveguides using integrated lenses, high coupling efficiencies can be achieved. In advanced IO processors characterized by large area waveguide arrays, however, these efficiencies could be somewhat lower due to angular misalignment of the focused Gaussian beams and the various individual rib waveguides. In reality the focal spot sizes of the integrated lenses may be somewhat larger than the calculated values due to fabrication inaccuracies, which may further reduce the coupling efficiency between the focused guided beams and the rib waveguides.

3.5 System Throughput Efficiency

Up to now the performance efficiencies of the individual components needed for advanced IO processors have been considered; in this section, however, the

overall throughput efficiencies of typical advanced IO processor systems will be estimated. This estimation is based on the theoretical analysis presented herein and as such is subject to the same set of assumptions and approximations. The experimental verification of some of the contributing efficiency factors will be given later.

One of the major sources of losses arise from reflections of the guided modes at the dielectric interfaces. The reflection coefficient ($R_{boundary}$), the transmission coefficient ($T_{boundary}$), and the loss (dB) for a guided wave incident on a dielectric with effective refractive index N_t from a medium with effective refractive index N_i is given approximately by [61]

$$R_{boundary} \; = \; \left| \frac{N_t - N_i}{N_t + N_i} \right|^2 \qquad (3.37)$$

$$T_{boundary} \; = \; 1 - R_{boundary} \qquad (3.38)$$

$$Loss \; (dB) \; = \; -10 \log T_{boundary} \; . \qquad (3.39)$$

These equations can be used to determine to a first order of approximation the losses at all of the dielectric interfaces in such processor configurations. Specifically, these interfaces are the laser-slab waveguide interface ($N_i = 1$ and $N_t = 2.22$), and the slab waveguide-integrated lens interfaces ($N_i = 2.23$ and $N_t = 2.3$). In the slab waveguide-rib waveguide transition "interface", we have assumed that there is no mode mismatch. This is indeed a good assumption, since for both waveguides the longitudinal propagation constant is 22.2 μm^{-1}.

The loss at the laser diode-waveguide interface is approximately 1 dB. In this approximation, it is assumed that the laser mode size has been made to match that of the slab waveguide by the use of a GRIN lens. In addition, it is assumed that the laser beam is normally incident at the waveguide edge, which is in turn perfectly polished. It is also assumed that the source is not bonded to the edge of the waveguide. Such bonding with an optical cement (refractive index of about 2) will further lower the coupling loss [76].

In order to estimate the losses at the slab waveguide-integrated lens interfaces, the simplifying assumption was made that the guided modes are normally incident at the lens boundaries. Losses due to two integrated lenses were estimated to be about 0.4 dB (each lens has two interfaces; at each interface, there will be a 0.1 dB reflection loss).

In the advanced IO processor configuration discussed herein, if we use one 2.7 cm wide integrated lens with focal length of 10.8 after the transducer and another one with a focal length of about 1 cm after the laser diode, the length of the waveguide (slab waveguide added to the array waveguides) is approximately 13 cm long. The propagation losses for the $Ti:LiNbO_3$ waveguides have been determined by others to be approximately 1 dB/cm [2]. The total propagation losses for the waveguides hence are estimated at 13 dB. It will be shown later that for some of the advanced IO signal processors it is desired to use TIPE slab waveguides for higher mode confinement. Propagation losses in TIPE slab waveguides could be slightly higher than those of the TI slab waveguides. Other investigators are working on the reduction of the propagation losses associated with TIPE waveguides [71].

The unwanted scattering losses due to the surface gratings and the integrated lens interfaces are not well characterized at this point in the research. These losses are roughly estimated at 1 dB. Other losses that were determined earlier include surface acoustic wave (SAW) device diffraction losses of order 3 dB, and mode coupling losses of the focused beams into rib waveguides of order 1 dB. Hence, the total loss of the system should be about 20 dB. In Ch. 6 we will use a system loss of approximately 20 dB in order to determine the laser diode power requirements for the IOSAR processor example.

Chapter 4

Advanced IO Processors: Fabrication of Critical Components

In this chapter the fabrication of critical components for advanced integrated optical signal processors on $LiNbO_3$ substrates will be discussed. These elements are: $Ti:LiNbO_3$ waveguides (slab and channel), large area rib waveguide arrays, surface outcoupling gratings (holographically patterned and contact mask patterned) on rib waveguide arrays, and large aperture integrated lenses (thin film coated recessed lenses and TIPE lenses).

In the fabrication of low loss $Ti:LiNbO_3$ waveguides (both slab and channel), we basically employ the fabrication technique of titanium indiffusion developed by others [2,5,6,77,4]. The fabrication of individual rib waveguides on $LiNbO_3$ has also been reported by Belanger and Yip [78]. They have fabricated rib waveguides that are 8 μm wide and 3 μm high through the reactive ion beam etching technique. To our knowledge, however, the fabrication of large area rib waveguide arrays has not been reported. Hence, we will herein present the fabrication steps required to form such arrays on $LiNbO_3$ substrates.

In addition, the fabrication of surface outcoupling gratings on rib waveguide arrays is not well established either. Therefore, we will also present the appropriate fabrication procedures to form such gratings on rib waveguide arrays. Grating patterns will be formed both holographically and using a contact mask, in a photoresist coating on top of the substrate followed by ion beam milling to form surface gratings. The performance of the above two techniques will be

compared.

It was mentioned earlier that new techniques of developing large aperture integrated lenses (0.2 cm) with short focal lengths (1-3 cm) will also be investigated here. Two new techniques were examined to fabricate such integrated lenses. In these techniques the Ti:LiNbO$_3$ material within the desired lens region is removed and replaced with thin films having either higher or lower refractive indices. By properly choosing the lens profile in either of the two geometries, we can produce positive lensing.

Through the preliminary experimental evaluation that is presented later, it was observed that the above lenses did not perform satisfactorily. This prompted us to examine the technique of fabricating TI integrated lenses in TIPE slab waveguides as was discussed in Sect. 3.3. Therefore, the fabrication of these lenses will also be presented.

We will present the fabrication issues for integrating the critical components such as integrated lenses, rib waveguide arrays and the surface outcoupling gratings in Ch. 5.

4.1 Fabrication of Low Loss Ti:LiNbO$_3$ Waveguides

As was mentioned in Sect. 2.2, the substrate that was chosen for the initial fabrication of proof-of-principle advanced IO signal processor components is LiNbO$_3$, which is a uniaxial crystal [1]. Through the considerations that were also presented in Sect. 2.2, it was determined that the preferred crystallographic orientation for use in the fabrication process is Y-cut. Optical-waveguide-quality wafers of Y-cut LiNbO$_3$, with the top surfaces optically polished to $\lambda/10$, were obtained commercially from Crystal Technology, Palo Alto, CA.

The wafers were then wire-sawed to appropriate dimensions with lengths (directions of propagation) that were parallel to the crystallographic X-axis and

widths parallel to the optic axis (c-axis) (see Fig. 3.5). The reasons leading to this choice of orientations were also presented in Sect. 2.2. It should be pointed out that the crystallographic axes as shown on the substrate in Fig. 3.5 are not the same as the coordinate system used in the analysis of Ch. 3 (see Figs. 3.2 and 3.1).

Slab waveguide fabrication in $LiNbO_3$ was accomplished through the technique of titanium indiffusion [2,5,6,4]. In this technique, thin films of titanium (100 - 500 $\mathring{A}$) are vacuum deposited on process cleaned $LiNbO_3$ substrates [79]. The titanium film is then indiffused into the substrate at high temperatures (900-1050° C) to form $Ti:LiNbO_3$ waveguides.

In order to prepare the substrates for waveguide fabrication, they were first cleaned in 18 $M\Omega$-cm deionized (DI) water and Micro cleaning solution (purchased from Cole Parmer, Chicago, Ill.). The substrates were then immersed in 1,1,1 trichloroethane (40 °C) for 10 min. followed by immersion in DI water, acetone, and methanol in order to remove any cleaning solution or grease residue. In order to remove any metallic ions from the surface of the substrates that could cause scattering elements after the indiffusion, they were immersed in a hydrochloric acid-hydrogen peroxide-DI water (1:1:5) solution that was heated to 75 °C for 20 min. Following the above procedures the substrates were rinsed with DI water, dryed with nitrogen gas and baked at 150 °C for 30 min.

In order to fabricate the waveguides needed for our purposes, titanium films with thicknesses of 400$\mathring{A}$ were deposited on cleaned Y-cut $LiNbO_3$ substrates. This choice of titanium thickness provides multimode waveguides (3 TE) that are approximately 1 μm deep, which were needed for some of our experiments. In order to fabricate single mode waveguides which are eventually needed for advanced IO processors, the thickness of the titanium thin film should be reduced to approximately 100$\mathring{A}$.

The Ti deposition was accomplished in a Balzers BAK 640 electron beam

evaporation system at pressures of order 10^{-8} Torr. The targets used were 99.99% pure titanium pellets. The rate of deposition was as low as a few angstroms per second to allow high film uniformity and good adhesion to the substrate.

The indiffusion of titanium was conducted in a quartz chamber of a programmable furnace. The temperature of the furnace was increased from room temperature to the indiffusion temperature of 1000° C in 2 hrs. The indiffusion was conducted for 3 hrs then the furnace was turned off to allow normal cool down to room temperature.

According to Burns, *et al.* a steady flow of ultra high purity argon or oxygen should be maintained through the indiffusion chamber in order prevent lithium outdiffusion, which leads to degradation of the fabricated waveguides [2]. In our fabrication process, however, the use of argon produced waveguides with low surface qualities due to reasons that are not well understood. Maintaining a constant flow of wet oxygen (1.5 liters/min) which is heated to 35 °C, on the other hand, helped in fabricating waveguides with good surface quality.

Below the surface of a Ti:LiNbO$_3$ waveguide, the titanium concentration profile is a complementary error function [2,80]. This function is the solution of the diffusion equation in the constant source (undepleted surface concentration) approximation. This complementary error function, however, can be approximated by the simpler Gaussian profile in the bulk for long diffusion times in which the diffusion depths are much larger than the film thicknesses [2]. The concentration profiles in such cases are given by

$$C(y,t) = \left(2/\sqrt{\pi}\right)(\alpha_a t_{Ti}/D)\exp\left[-(y/D)^2\right]. \qquad (4.1)$$

In this equation t_{Ti} is the titanium film thickness ($\sim 400\mathring{A}$), y is the depth below the surface, and α_a is the atomic density of the titanium film (of order 5.65×10^{22} atoms/cm^3). The diffusion depth (D) is related to the diffusion coefficient D_c

(which is equal to 9.4×10^{-13} cm^2/sec at $1000°$ C) and to the diffusion time (t) by [2]

$$D = 2\sqrt{D_c t}. \qquad (4.2)$$

In the analysis of Chs. 3 and 5, we have assumed that there is an abrupt boundary at the depth of 1 μm below the waveguide. This is the depth at which the largest gradient in the titanium concentration (or the refractive index) occured for the waveguides that we fabricated. Comparison of the experimentally determined longitudinal propagation constant of the fabricated slab waveguide with the calculated values presented in Ch. 5 will show that the above assumption is indeed a good one for our purposes. In cases for which a more accurate analysis considering the graded index profile of the Ti:LiNbO$_3$ waveguides is needed, numerical methods similar to those reported by others should be used [43,48].

The fabrication of Ti:LiNbO$_3$ channel waveguides was accomplished through the indiffusion of strips of titanium (widths $\sim 6 - 15$ μm) following the steps described earlier. In order to generate strips of titanium on LiNbO$_3$ substrates, photolithographic techniques and a lift-off process designed for Ti (which is standard for certain types of integrated circuit fabrication) was used [81].

In our technique the substrate was spin coated with Shipley S1400-27 positive photoresist at 5000 RPM for 30 seconds. The use of positive photoresist allows the formation of high resolution patterns. According to the specifications for S1400-27 the thickness of the photoresist film that is formed is about 1.14 μm. The pre-exposure and post-exposure treatment of the photoresist layer was conducted according to the steps prescribed in the Shipley data sheet.

Contact masks with appropriate channel patterns which are needed for exposure purposes were ordered from ASET electromask, Woodland Hills, CA. The photoresist coated substrate was exposed in a Karl Suss MJB 3 mask aligner using a mask with an appropriate pattern. The exposure time was generally in

the 10-20 second range.

The exposed photoresist was then developed in a 1:1 mixture of deionized water and Shipley Concentrated Developer for a few seconds, until the patterns were visible on the photoresist coating. The patterns are generated when the exposed regions of photoresist are removed in the developer, while the unexposed regions are left intact.

A titanium thin film was then deposited on the substrate, over the patterned photoresist (as discussed for the slab waveguide case). The substrate was then immersed in either acetone or Shipley Microposit Remover 140. This process dissolves the photoresist, which also lifts off the titanium film that is deposited on top of the photoresist coating. This leaves a pattern of titanium in the regions of the substrate that were not covered with photoresist (due to exposure and development). In this way, strips of titanium can be formed on the surface of the $LiNbO_3$ substrate. The indiffusion of the titanium strips to form channel waveguides is then achieved with times, temperatures, and wet oxygen flow rates similar to those used for the case of slab $Ti:LiNbO_3$ waveguides [4].

A channel waveguide fabricated by means of the indiffusion of a 5 μm wide titanium strip (1 cm long along the crystallographic X-axis) on a Y-cut crystal is shown in Fig. 4.1. This image was produced using the Nomarski technique in a Leitz model SM-LUX-HL polarization microscope.

A critical issue that affects the indiffusion of strips of titanium in $LiNbO_3$ is lateral diffusion in the direction of the crystallographic Z-axis [5]. This causes the $Ti:LiNbO_3$ channel waveguides to be wider than the corresponding titanium strips prior to indiffusion, causing smearing of the waveguide boundaries (see Fig. 4.1). The width of an indiffused channel waveguide can be approximately 1-3 μm wider than a 10 μm titanium strip used for its fabrication [5].

It was mentioned earlier that for the efficient butt-coupling of a laser diode to a $Ti:LiNbO_3$ slab waveguide, the edge of the waveguide should be optically
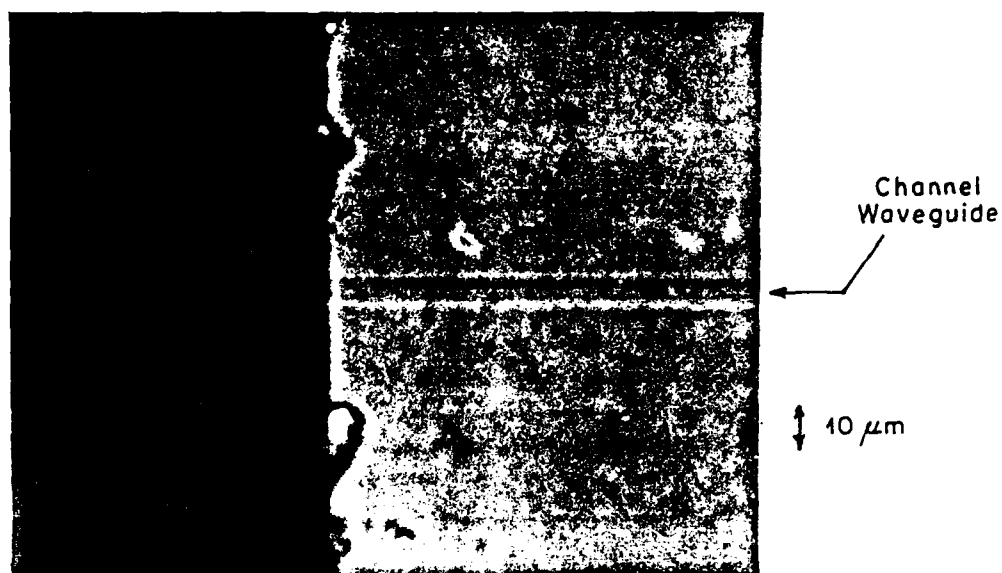
Figure 4.1: Optical micrograph (500X) of a nominally 5 μm wide Ti:LiNbO$_3$ channel waveguide taken with a phase contrast microscope (Nomarski mode). The actual channel width is of order 6 μm. This increase in width was caused by lateral diffusion of the deposited titanium strip (5 μm wide). Note the polished edge of the sample where the channel waveguide is terminated.

101

polished. High edge surface quality is also needed for fiber butt-coupling of laser light into Ti:LiNbO$_3$ channel waveguides.

In order to edge polish LiNbO$_3$ substrates with Ti:LiNbO$_3$ waveguides, we used the technique developed by Furch, *et al.* [82]. In their technique, a specially designed jig was used to securely hold the substrate so that only its edge is exposed for polishing. We used a similar jig for our purpose. The sample that was secured in the jig was then rough lapped successively with polishing compounds that have 30, 15, and 10 μm grit sizes. Finer polishing was accomplished on an R. H. Strausbaugh, Inc. 6DA-1 mechanical polisher using silica compound solution (0.1 μm particle size) for lengths of time up to 2 hrs. The final result of the polished edge of one of the samples that has a Ti:LiNbO$_3$ channel waveguide is shown in Fig. 4.1. Despite the roughnesses in some parts of the edge, the edge quality is highly uniform at the channel waveguide termination, which is precisely what is needed for fiber butt-coupling. The results of fiber-butt coupling into this Ti:LiNbO$_3$ channel waveguide will be presented in the next chapter.

4.2 Fabrication of Rib Waveguide Arrays

It was mentioned earlier that the fabrication of high quality rib waveguide arrays with high packing densities was a major point of this research. Specifically, for advanced IO signal processors such as the IOSAR processor, waveguide arrays in which the individual ribs are about 8 μm wide and separated by 2 μm gaps (10 μm pitch) might be needed. For this purpose rib waveguide arrays with 660 elements (in 6.6 mm) were fabricated on Ti:LiNbO$_3$ slab waveguides [83]. The number of elements in the rib waveguide arrays was chosen for experimental flexibility as will be discussed later. The total number of elements in such arrays can easily be extended to 1000 or more elements in 1 cm (with the same dimensions as above), which might ultimately be required in advanced

IO processing applications. The fabrication steps applicable to rib waveguide arrays are discussed in detail next, and are shown schematically in Fig. 4.2.

The substrate used for the purpose of fabricating each rib waveguide array was a Ti:LiNbO$_3$ slab waveguide processed as discussed earlier in Sect. 4.1. Rib waveguide arrays were fabricated by employing the selective ion beam milling technique in order to generate the troughs and associated ridges necessary to form rib structures.

In order to mask the desired rib waveguides we used appropriately patterned Shipley S1400-33 photoresist coating (2.2 μm thick) on the substrate. The use of thick photoresist is one of the essential steps in fabricating a rib waveguide array with high surface quality because such layers can provide sufficient protection against the ion beam milling process. We determined that the use of photoresist layers that are thicker than 2.2 μm (such as S1400-37) would not produce acceptable arrays, since the 2 μm openings needed in some of the array patterns could not be properly exposed.

The mask that we used for patterning the rib waveguides was obtained from ASET Electromask Co., Woodland Hills, CA. In order to make maximum use of this mask, it was designed to have both a densely packed rib waveguide array pattern and a low density rib waveguide array pattern. The densely packed rib waveguide pattern consisted of 2 cm long ribs with 8 μm wide openings and 2 μm separations. Due to the limited space available on the mask, we were limited to 660 elements (or 660 rib waveguides after the completion of the fabrication steps). The low density waveguide array pattern on the mask consisted of openings in the range of 5-20 μm with comparable separations. By appropriately situating the substrate to be exposed under this multipurpose mask in the mask aligner, we were able to generate several types of rib waveguide arrays with different geometries.

Exposures through the mask were such that the long axes of the rib wave-
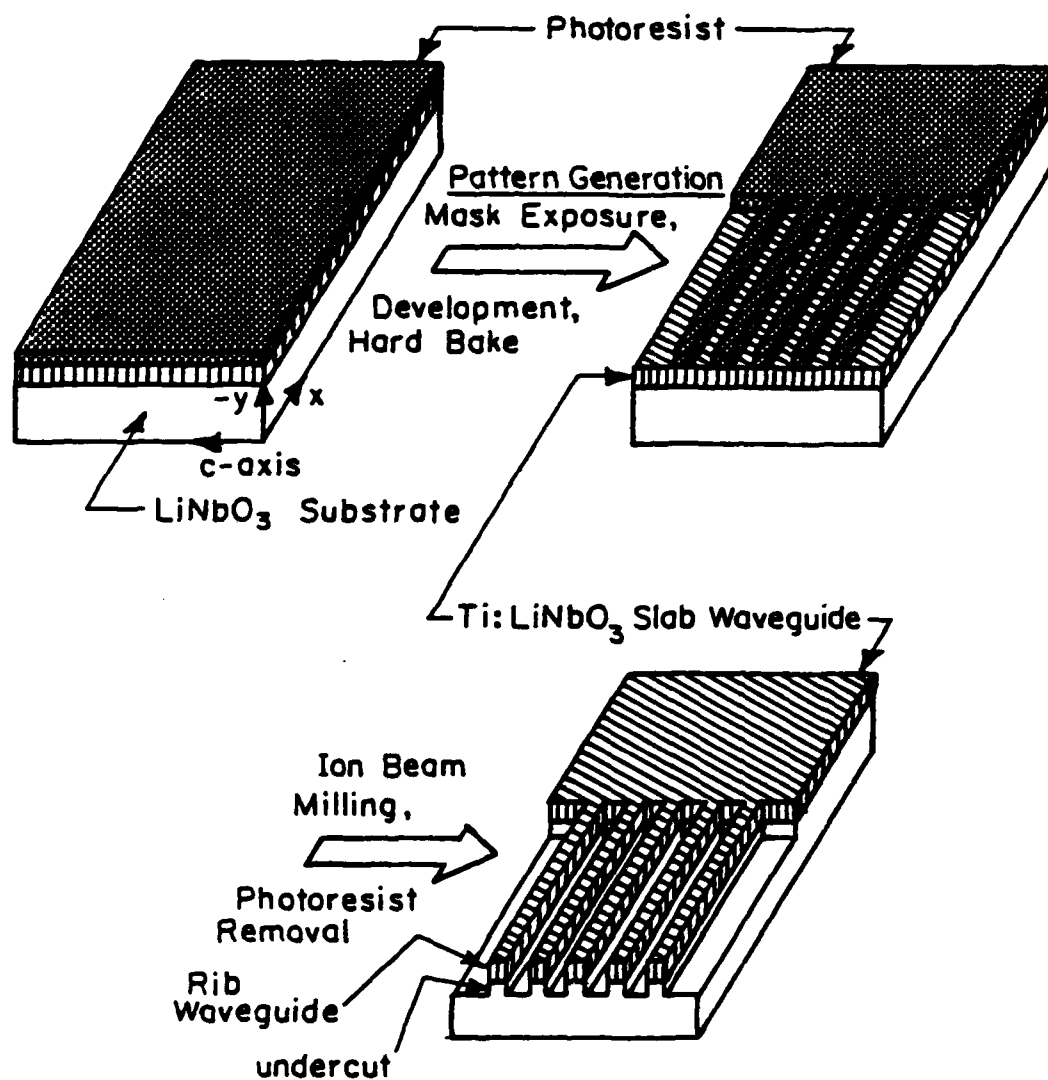
Figure 4.2: The steps required in the fabrication of rib waveguide arrays on Ti:LiNbO$_3$ substrates are depicted here. Details of the steps are given in the text.

guide patterns were oriented parallel to the crystallographic X-axes of the substrates.

It was suggested by others that the photoresist coating on the substrate needs to be hardened at high temperatures in order to withstand the ion beam milling process [78,21]. We experimented with different temperatures and durations of such a hard bake. It was determined that when the photoresist layer is baked at 140° C for 2 hrs, it hardens sufficiently to withstand ion beam milling for the combination of times and energies appropriate for rib waveguide fabrication in Ti:LiNbO$_3$. Therefore, this is the procedure by which we hard baked the photolithographically-defined photoresist patterns on the Ti:LiNbO$_3$ substrates following pattern development.

In order to imprint the photoresist patterns onto the substrate and form the rib waveguide structure (see Fig. 3.2), the baked sample was subsequently ion milled using argon ions [84,79]. A Commonwealth (3 centimeter in diameter) ion gun was used in a vacuum chamber for ion beam milling. The pressure in the chamber was first reduced to 4×10^{-6} Torr; then ultra high purity (99.999% pure) argon gas was bled into the chamber in order to increase its pressure to about 2×10^{-4} Torr. The gas was purchased from MG Industries, Valley Forge, PA.

The beam current and voltage were adjusted in the ion gun to approximately 7 mA and 150 V, respectively. At these settings, the ion gun current density was rougly estimated to be about 0.1 mA/cm^2. We examined the mill rate of Ti:LiNbO$_3$ in the above system by milling different samples (with photoresist rib patterns) for different durations using the ion beam settings just described. By correlating the heights of the fabricated rib waveguides with the ion beam milling durations, we determined that this milling rate is approximately 0.4 μm/hr.

Ion beam milling of the substrates with photoresist-defined rib patterns pro-

duces troughs in regions without a photoresist coating; the regions that have a photoresist coating are not ion milled, and thus produce rib waveguides (as shown in Fig. 4.2). In advanced IO signal processors, other components such as integrated lenses and SAW transducers need to be integrated along with rib waveguide arrays. Hence, mesas (as shown in Fig. 4.2) are needed on the substrates in order to accommodate such components.

It was mentioned earlier that differnent substrates with hard baked photoresist patterns were ion milled for different durations. It was determined that ion milling could only be conducted up to a maximum of 2 hrs and 30 minutes, after which the photoresist started to discolor and could no longer withstand the ion beam milling process.

Continuous ion beam milling of the substrates conducted for 2 hrs and 30 minutes formed rib waveguides that are about 1 μm high. Arrays of 660 rib waveguides (8 μm wide, 1 μm high, 1 cm long, with 2 μm separations) were fabricated on Ti:LiNbO$_3$ substrates using the above technique. An optical micrograph of a portion of such an array (taken in a Nomarski phase contrast mode) is shown in Fig. 4.3, which shows high surface uniformity on all surfaces. The number of waveguides in such arrays can easily be extended to 1000 elements in order to occupy a full 1 cm^2 area.

Up to this point, we have assumed the lower boundary of the Ti:LiNbO$_3$ waveguides to be at about 1 μm below the surface. In the particular situation of the rib waveguide arrays discussed above, some residual Ti:LiNbO$_3$ waveguide material will still exist in the trough regions (due to the Gaussian refractive index distribution in the waveguide) which can in some cases allow for partial guiding. Such guiding in the trough regions can be a cause of crosstalk. Fortunately, due to the same Gaussian distribution of the refractive index with depth, lower guided modes are mostly confined close to the top surface. Therefore, crosstalk due to guiding in the troughs for such modes can be minimal. A more accurate

106
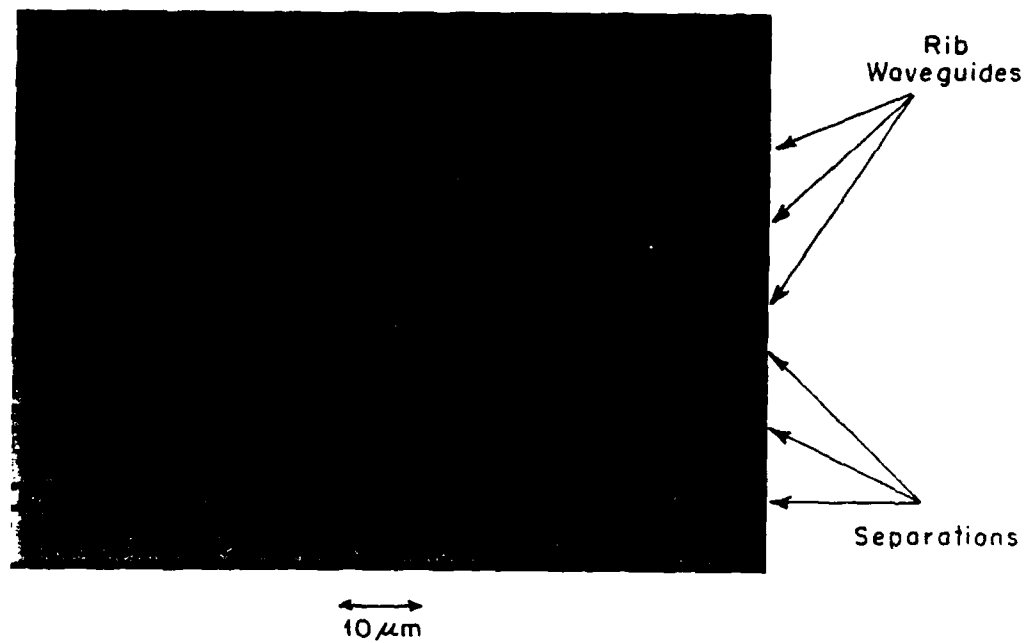
Figure 4.3: Optical micrograph (1.000X) of a portion of an array of 660 rib waveguides (8 μm wide, 1 μm high, 1 cm long, with 2 μm separations).

analysis of such crosstalk needs to be conducted.

In applications that require significantly higher rib waveguide isolation, how-ever, the troughs need to be deeper than 1 μm in order to effectively undercut the waveguide defining boundary as shown in Fig. 4.2. In fabricating rib wave-guide arrays for these situations, we cannot use photoresist as the protective mask of ion beam milling because of its degradation during a prolonged milling process. In those situations, alternative mask materials for the ion beam milling process which has a much lower mill rate than that of Ti:LiNbO$_3$ should be investigated.

In parallel with the fabrication of the large area densely packed rib wave-guide arrays, we also fabricated sparsely spaced rib waveguide arrays on different substrates, for fiber coupling and other experiments which require such geome-tries. For example, a scanning electron microscope (SEM) micrograph of a rib waveguide that is 5 μm wide and about 0.5 μm high (milled for 1 hr) is shown in Fig. 4.4. It is evident that the surfaces of the fabricated waveguide are highly uniform; such uniformity is needed in order to achieve low scattering losses in such a waveguide structure. The results of coupling experiments conducted with rib waveguides (in both individual and array geometries) will be presented in Ch. 5.

In producing the SEM micrographs that are presented herein, we used a Cambridge model S$\div$10 scanning electron microscope (SEM), with an accelerat-ing voltage of 20 KV and a filament current about 20 μA.

4.3 Fabrication of Uniform Surface Gratings on Rib Waveguide Arrays

In the analysis of Sect. 3.2, we presented a comparison of thin film and surface grating outcouplers from rib waveguide arrays for use in advanced IO
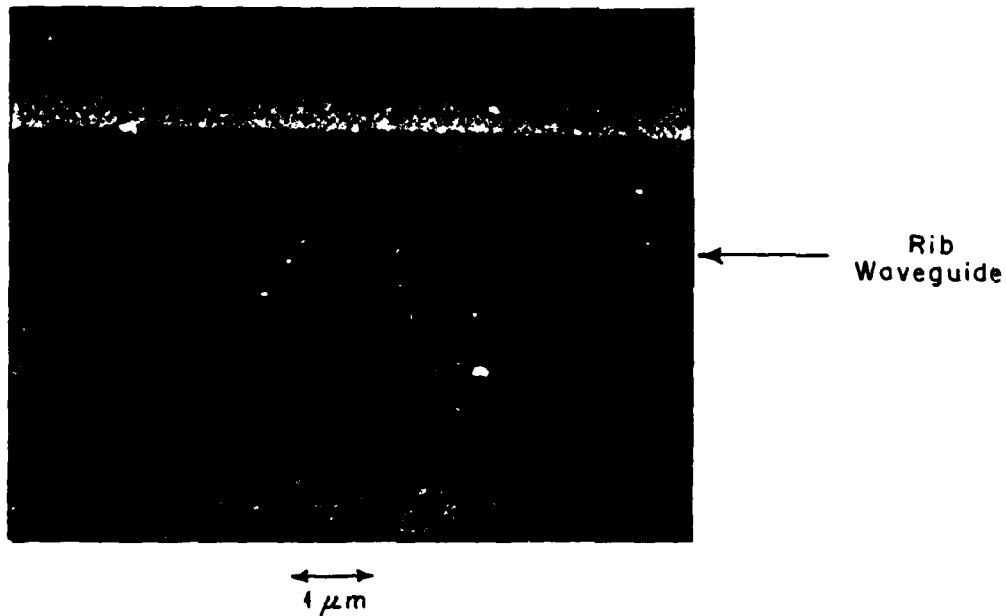
Figure 4.4: Scanning electron microscope image (10,000X) of a 5 μm wide and 0.5 μm high rib waveguide. High uniformity of the top surface and sidewalls is evident in this photograph.

signal processors. We decided to explore the possibilities of surface gratings on rib waveguides further, because of the several potential advantages they exhibit over thin film outcouplers, as discussed in Sect. 3.2.

We also mentioned that others have produced highly efficient surface gratings to outcouple light from individual Ti:LiNbO$_3$ channel waveguides in short distances [21]. For our application, however, we faced new challenges. Our requirement was to outcouple light from a long waveguide uniformly and efficiently, which translates in some cases into much lower outcoupling efficiencies per unit length (roughly 10%/mm). One of the implications of this requirement is that the grating heights are smaller than those used by others. The other implication is that longer grating periods are used in order to reduce the outcoupling efficiency. Another major difficulty that we faced was that we needed to fabricate uniform surface gratings on the nonuniform surface characteristic of a rib waveguide array, subject to the performance criteria given above.

In the analysis of Sect. 3.2, we also limited the grating periods to range from 1 to 4 μm. The lower bound in this range is dictated by the minimum photolithographic resolution that we can achieve in a photoresist layer that at the same time is a well-defined, resistant mask for subsequent ion beam milling of the surface gratings. The upper bound was set by the minimum number of grating cycles that we need to have under a 10 μm long CCD pixel.

In this section, we will present the techniques by which we attempted to fabricate surface gratings on rib waveguide arrays through the selective ion beam milling process. We will explore the two different techniques of holographic exposure and exposure through a contact mask in order to form grating patterns in photoresist layers. In order to imprint the gratings onto the surface of a rib waveguide array, first we generated a similar grating pattern in the photoresist coating of the rib waveguide array, such that the gratings are oriented orthogonal to the long axis of the array. This was followed by ion beam milling to imprint

110

the gratings on the top surface of the array. Afterwards the photoresist coating is removed, so that the resulting surface gratings on top of the rib waveguides will have a similar geometry to that of Fig. 3.5.

We will now discuss the methods by which such surface gratings can be formed in more detail. First, we will consider the holographically patterned surface gratings. This is followed by a discussion of the contact mask patterned surface gratings.

4.3.1 Holographically Patterned Surface Gratings

In the holographic patterning technique, two beams derived from a He-Cd laser are interfered within a photoresist coating on the substrate to form a photoresist grating [85,86,87]. A simple and versatile method of holographically fabricating such surface gratings in a photoresist layer can be accomplished in a setup as shown schematically in Fig. 4.5 [86].

In this setup, the portion of the incident He-Cd beam ($\lambda = 0.44\,\mu$m) reflected from the mirror interferes with the direct beam to form a grating within the photoresist coating deposited on the substrate. The angle between the plane of the mirror and substrate is $90°$, and they are mounted so that they can be translated transverse to the incident beam path. This is needed in order to control the area of the substrate that is being exposed by the beams. The exposure time is controlled by a programmable shutter.

In order to control the grating period, the angle ϕ_h can be varied by rotating the mount about the axis (common to the plane of the mirror and the plane of the substrate as shown in Fig. 4.5). The grating period (Λ) can be determined from the condition

$$\Lambda = \frac{\lambda}{2 \sin \phi_h}. \tag{4.3}$$

In cases for which chirped (frequency modulated) gratings are needed, a cylin-

111
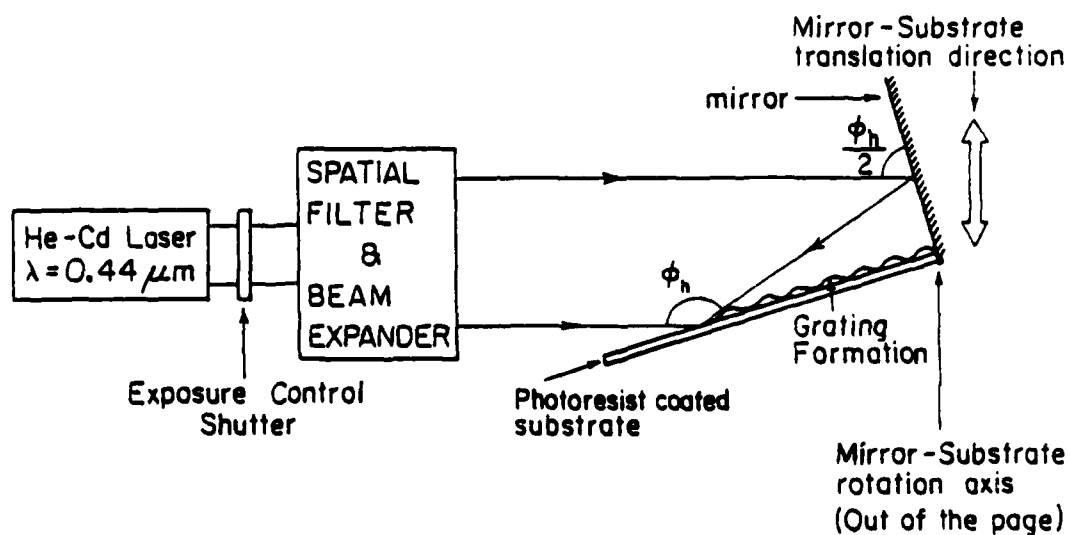
Figure 4.5: This schematic diagram depicts the required elements and their orientations for the holographic generation of gratings in photoresist. The beam of a He-Cd laser (0.44 μm) which has been spatially filtered and expanded is used as a source of coherent illumination. For the purpose of exposure control, a programmable shutter is used. Details of operation are as given in the text.

112

drical lens can be used in order to curve the phase front of one of the writing beams, consequently varying the grating period along the direction of propagation [87,86].

In order to examine the holographic grating quality and the range of grating periods that can be fabricated, several $LiNbO_3$ substrates were spin coated with Shipley S1400-17 (positive photoresist) at 5000 RPM for 30 seconds to produce coatings that are about 0.4 μm thick (according to Shipley specifications). The choice of positive photoresist was made in order to allow higher resolution grating features.

The appropriate exposure time and photoresist development time for each grating period was determined by multiple trials. Using the above technique, we fabricated gratings with fundamental periods in the range 0.6-1.6 μm.

We also examined the suitability of S1400-27, which has double the thickness of S1400-17 for a similar spin rate, for holographically generated gratings. This thicker photoresist did not prove to be suitable for this purpose, since we could not generate features with resolution close to 1 μm in it.

In order to examine the surface uniformity of the holographically patterned gratings, we examined a few of the substrates with different grating periods in the same SEM, the use of which was discussed before. For example, a SEM micrograph of a grating with a 1.3 μm period is shown in Fig. 4.6. There were observable nonuniformities (0.2 μm features) on the surface of grating that is shown in Fig. 4.6; these nonuniformities were characteristic of all of the gratings examined. Other investigators have also observed such surface nonuniformities on holographically generated gratings [88].

These nonuniformites may be due to inhomogeneities in photoresist composition, which varies the exposure requirements of the photoresist locally. An optical interference pattern that causes a grating by nature exhibits an analog spatial intensity modulation. Therefore, exposure intensities incident on the
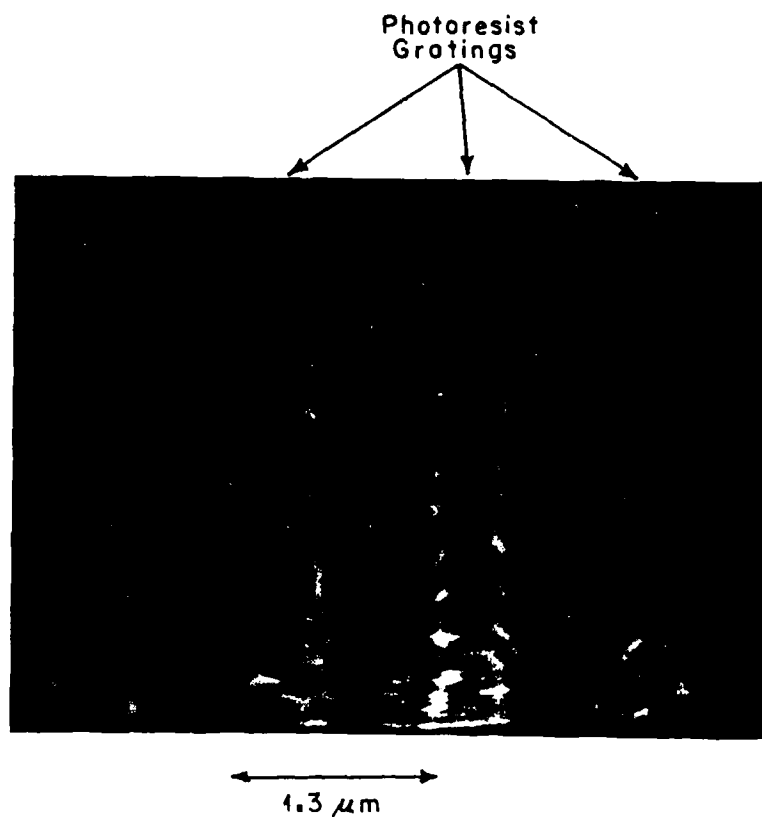
Figure 4.6: Scanning electron microscope (SEM) micrograph (20.000X) of a grating ($\Lambda \sim 1.3$ μm) holographically formed in Shipley S1400-17 photoresist. Note the grating nonuniformities.

114

photoresist also vary locally, producing local anomalies in response to minor compositional variances. Such nonuniformities would not be observed in the more traditional utilization of such photoresist layers in integrated circuit manufacture, since in this case the exposure is binary, and can be below and above threshold in unexposed and exposed regions, respectively, regardless of minor local sensitivity variations.

We also examined the surface quality of gratings that were holographically patterned and ion milled on the surface of a single 5 μm wide rib waveguide. This experiment was conducted in order to determine what fraction of the photoresist nonuniformities would be transfered onto the milled grating on a rib waveguide.

For this purpose we holographically patterned a surface grating with a 1.3 μm fundamental period on a sample with a rib waveguide geometry (5 μm wide and 0.5 μm high), using a similar procedure as that previously described for the fabrication of such gratings on slab waveguide in LiNbO$_3$. Prior to the ion beam milling process, we hard baked the above sample at 140 °C for 2 hrs. Ion beam milling of such holographically-defined grating patterns was conducted with parameters similar to those employed in the milling of the rib waveguide arrays, except for reductions in the ion beam current to 6 mA. The beam current densities were thus slightly lower than 0.1 mA/cm^2, producing lower ion milling rates than the current density used in fabricating the rib waveguides. Due to the use of thin S1400-17 photoresist layers, we were limited to short durations of ion beam milling up to 45 min. It was rougly estimated that during the fabrication of surface gratings, ion milling for durations of 20-30 min. will generate grating heights of 400-500 Å, which is the range of grating heights that we normally fabricated.

An ion beam milled grating with a 1.3 μm period fabricated on a single 5 μm wide rib waveguide is shown in Fig. 4.7. As was expected, the nonuniformities apparent in the photoresist grating were imprinted onto the surface of the ion

115

milled grating. Such nonuniformities may cause unwanted scattering in advanced IO processors that could prove unacceptable for some applications. We have not conducted a quantitative measurement of the unwanted scattering by the holographically patterned ion milled gratings. This measurement needs to be conducted in order to determine their potential advantages and drawbacks more definitively.

On the basis of the surface nonuniformities observed for the holographically formed gratings, we decided to investigate the possibilities of contact mask patterned surface gratings. Gratings patterned on photoresist via the contact mask approach had the potential for better surface uniformity. This is because there is no gradual variation of the intensity that is exposing the photoresist through the contact mask. Indeed, the intensity that exposes the photoresist (after the mask) is either zero (behind the opaque part of the mask), or very high (under the opening). Such a binary variation of intensity can potentially provide highly uniform features in the photoresist after developing, even in the presence of minor compositional and/or photosensitivity variations.

4.3.2 Contact Mask Patterned Surface Gratings

We mentioned earlier that the gratings that are needed for advanced IO signal processors cover an area of approximately 1 cm^2, and have periods in the range 1-4 μm. We also mentioned that a rectangular grating that has an aspect ratio equal to 0.5 has the maximum outcoupling efficiency compared to a grating which has the same grating period and grating height, but which has a different aspect ratio. Hence, for patterning gratings using a contact mask we needed a mask with features that were in the range 0.5 - 2 μm. Masks with such a high resolution are normally produced through a computer controlled electron beam lithographic process (at a generally high cost).

We ordered such a mask from Advance Reproduction Corp., N. Andover,
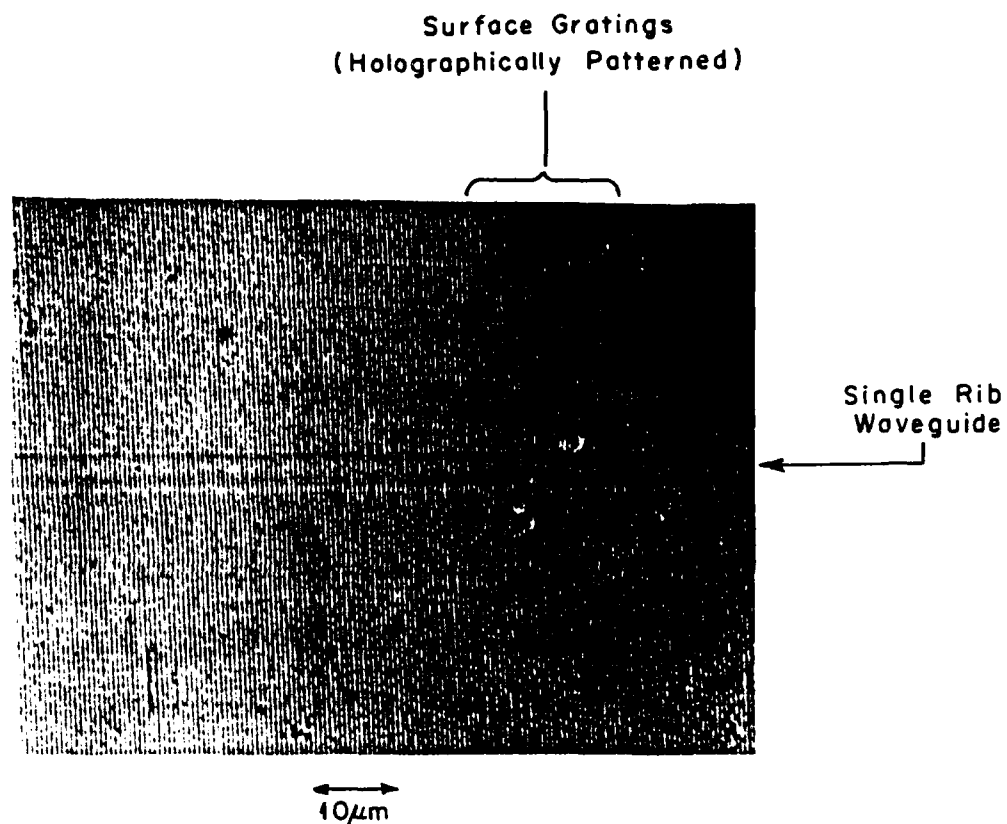
Figure 4.7: An optical micrograph (1,000X) of a surface outcoupling grating (1.3 μm period, with a 500 Å height) ion milled onto the surface of a single rib waveguide. The surface grating was originally patterned holographically in photoresist prior to ion beam milling. Nonuniformities of the grating are visible in this photograph.

MA. The grating patterns on this mask included three sets of gratings with periods of 1, 2, and 4 μm. In order to accomodate all of the above gratings on the same mask, however, we were limited to gratings that were only 1 mm long. Although this length is smaller than the desired 1 cm, at this level of the research it is quite adequate for evaluating the grating performance. This is the reason why we used 1 mm long gratings in the surface grating examples that we solved earlier in Sect. 3.2. This facilitates correlating the outcome of the theoretical examples with that of the experimental evaluation of the surface gratings that will be presented later (see Ch. 5).

As was mentioned earlier, the primary aspect that distinguishes our effort from those of others is that we desired to fabricate highly uniform surface gratings on the inherently nonuniform surface of rib waveguide arrays. The nonuniformity of the rib waveguide arrays posed a problem in uniformly coating photoresist over the entire array. Such uniformity of the photoresist layer on the top surface of the rib waveguides is especially important in order to generate uniform surface gratings.

Despite the above problems, we attempted the most straightforward approach by spin coating the substrates (on which rib waveguide arrays had been previously fabricated) with photoresist and then exposing them through the contact mask. After developing the exposed photoresist, we in fact observed highly uniform grating patterns on the top surfaces of the rib waveguide arrays. These results will be considered in more detail next.

The photoresist chosen for the purpose of contact mask patterning the surface gratings was S1400-17, as was used for the holographically patterned gratings discussed previously. Substrates with 1 cm long rib waveguide arrays (660 elements, that are individually 8 μm wide, 1 μm high, and are separated by 2 μm gaps) were spin coated with 0.4 μm thick photoresist. The pre-exposure steps recommended in the specifications for Shipley S1400-17 photoresist were again

followed.

The substrates were individually aligned with the mask in the mask aligner, such that the gratings were orthogonal to the long axes of rib waveguides, followed by exposure. The exposure time and developing time required to generate high quality gratings normally varied from one sample to another. However, both times were in the range of a few seconds. The resulting gratings with 2 and 4 μm periods formed in the photoresist layers deposited on the rib waveguide arrays were highly uniform. Further studies need to be conducted in order to develop gratings with submicron periods on the surface of rib waveguide arrays.

The successful photoresist grating generation (2 and 4 μm periods) on the surface of the rib waveguide arrays using a contact mask prompted the further investigation of ion milled surface gratings on such arrays. Ion milling of the photolithographically defined (and hard baked) samples was conducted following the same procedures as given earlier for the holographically patterned gratings, producing grating heights of approximately 500 $\mathring{A}$. This height was estimated in a manner similar to the estimation of the heights of the holographically patterned gratings. We fabricated a grating with a 2 μm period on one sample, and a grating with a 4 μm period on another sample. Although all of the grating patterns with different periods (resulting from the multiplexing of such patterns on the contact mask) were formed in the photoresist deposited on all of the samples, we covered the unwanted gratings on each sample with cover glass slides during the ion beam milling process. After the ion beam milling step, the protective photoresist coating was removed by Shipley Microposit Remover 140.

An example of a 2 μm grating fabricated on an array of 660 rib waveguides (discussed in Sect. 4.2) is shown in the optical micrograph (1000X) of Fig. 4.8. Excellent uniformity of the surface grating formed on the rib waveguide array can be seen in this micrograph. The degree of uniformity of the surface outcoupling gratings fabricated on rib waveguide arrays is further revealed in the

119

SEM photograph shown in Fig. 4.9. One rib waveguide is shown in the middle of the photograph, and parts of the neighboring waveguides are shown at the top and at the bottom (all oriented from left to right). The uniform surface grating fabricated on the top surfaces of these waveguides is delineated by the vertically oriented narrow bright lines (which mark the ridges of the gratings).

The aspect ratios of the fabricated gratings (as seen in Fig. 4.9) were determined to be approximately 0.2. This reduction in the aspect ratio from the value of 0.5 characteristic of the original pattern is understood to be due to the reduction in the width of individual masking photoresist strips that occurs when they are hard baked. The results of several outcoupling experiments, and the evaluation of the outcoupling efficiencies of different modes that are presented in Ch. 5 will indeed reveal that the actual outcoupling efficiencies are lower than expected partially due to such reductions in the aspect ratios of the different gratings.

It is evident from Fig. 4.9 that gratings were also formed in the separation regions between the rib waveguides (*i.e.* in the cladding regions). The widths of the grating ridges in the cladding regions, however, increased from the upper boundaries of the claddings towards the lower boundaries. This can be due to the accumulation of photoresist next to one sidewall of each trough when the process of spin coating is started.

It was mentioned earlier that modulation of the outcoupling efficiency of the grating pixels depending on their location may be desirable for certain IO signal processing applications such as IOSAR processor configurations. The most practical method of performing such a space-variant modulation was determined in Sect. 3.2 to be variation of the grating period along the rib waveguides. This can be easily accomplished by using a contact mask that has gratings with appropriate periods depending on their locations already patterned on it. This advantage of contact mask patterning of surface gratings in addition to the experimentally
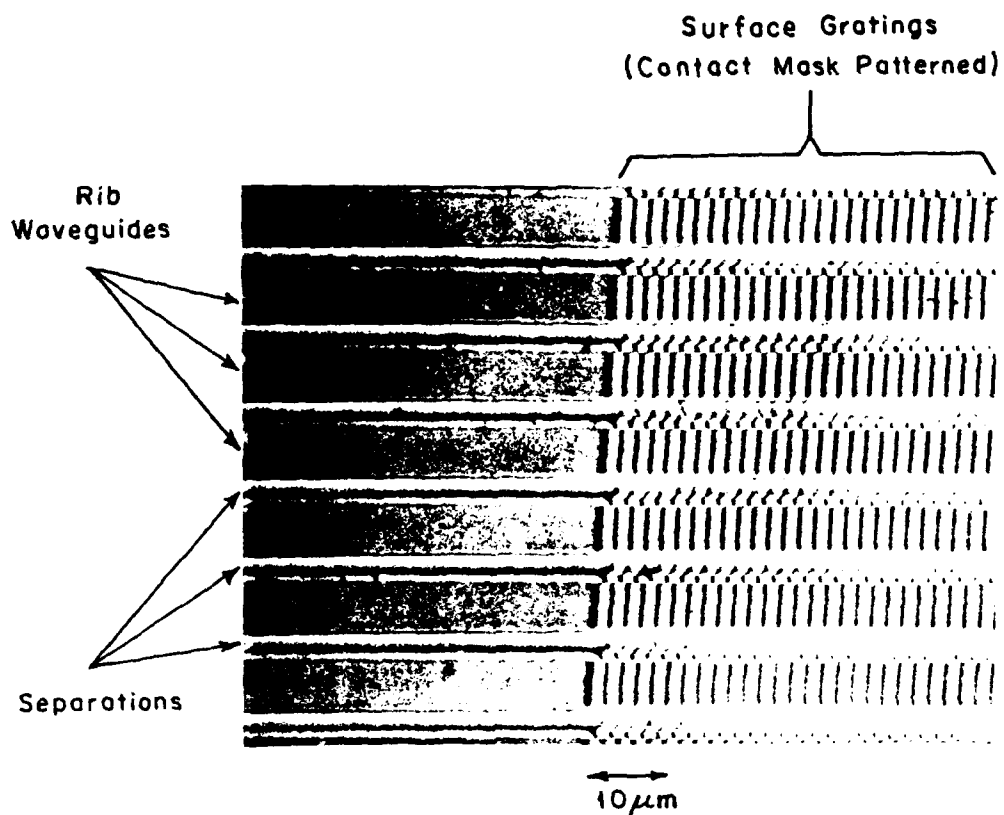
Figure 4.8: Optical micrograph (1,000X) of 2 μm gratings with 500 Å heights fabricated on an array of rib waveguides (8 μm wide, 1 μm high, with 2 μm separations). The waveguides are oriented left to right, while the gratings are oriented from top to bottom.
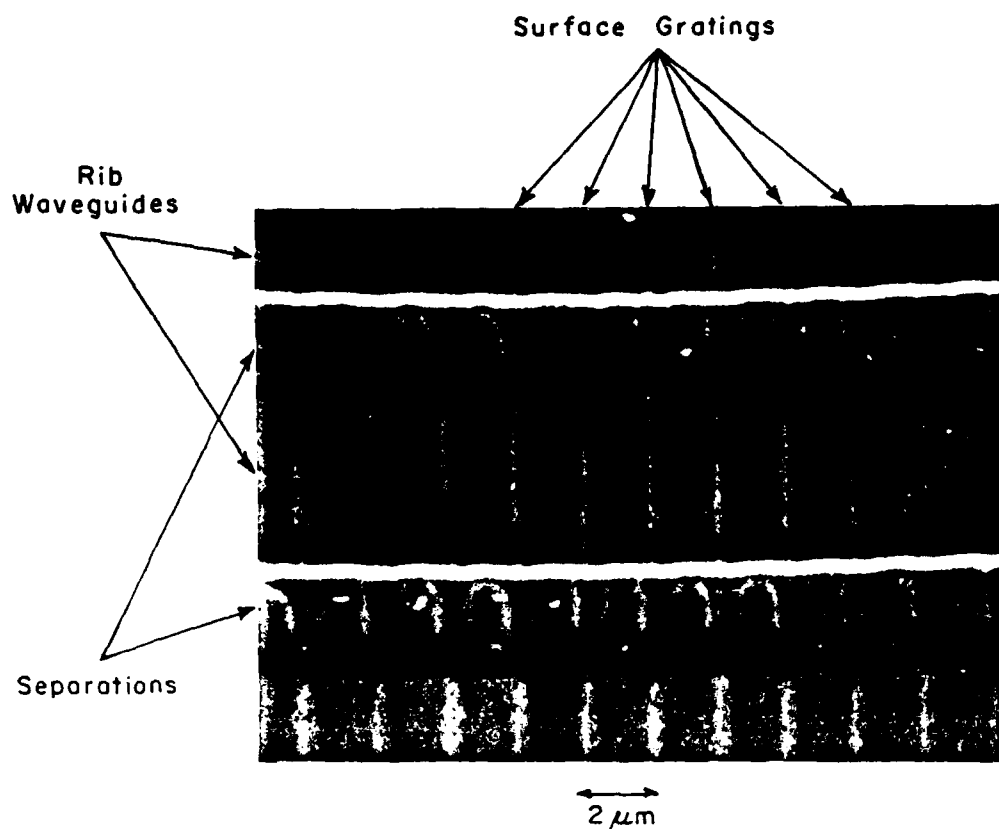
Figure 4.9: Scanning electron microscope (5.000X) micrograph of 2 μm gratings with 500 Å heights fabricated on an array of rib waveguides (8 μm wide. 1 μm high. with 2 μm separations). The waveguides are oriented left to right. while the gratings are oriented from top to bottom. Note the uniformity of the gratings and rib waveguide surfaces.

verified surface uniformity of such gratings (which minimizes unwanted scattering) make this technique superior to the use of holographically patterned gratings for advanced integrated optical signal processing applications.

4.4 Fabrication of Integrated Lenses

In Sect. 3.3, we mentioned that a major thrust of this research was to explore new possibilities in the fabrication of large aperture, low F-number integrated lenses on $LiNbO_3$. One of the techniques that was outlined in Sect. 3.3 was the method of fabricating thin film coated recessed lenses by using either a high refractive index or a low refractive index thin film in the recess of the lens region. We will present the fabrication process utilized for such lenses, in which we employed TiO_2 thin films for the high refractive index material and SiO_2 thin films for the low refractive index material.

Ideally, for thin film coated recessed lenses we would prefer to replace the waveguide material completely with the thin film. A cross sectional view of such a lens in a waveguide is shown schematically for the TiO_2 coated recessed lens case in Fig. 4.10 (a). In this situation, there would be some loss of the guided modes due to reflections from the interfaces. As shown in Fig. 4.10 (b) it is also possible to have a geometry in which the recess is not as high as the waveguide in which it is being fabricated. Another possible geometry is shown in Fig. 4.10 (c), in which the recess is <u>higher</u> than the waveguide. In both of these cases, the protrusions of the thin film can cause additional scattering of the guided mode.

For the case of the SiO_2 coated recessed lens, possibilities similar to those of TiO_2 coated lens (shown in Fig. 4.10) can exist. It was mentioned in Sect. 3.3, however, that a buffer layer of low refractive index material is required to separate the low refractive index thin film from the high refractive index $LiNbO_3$ in order to ensure the TIR condition. For this purpose we have selected a MgF
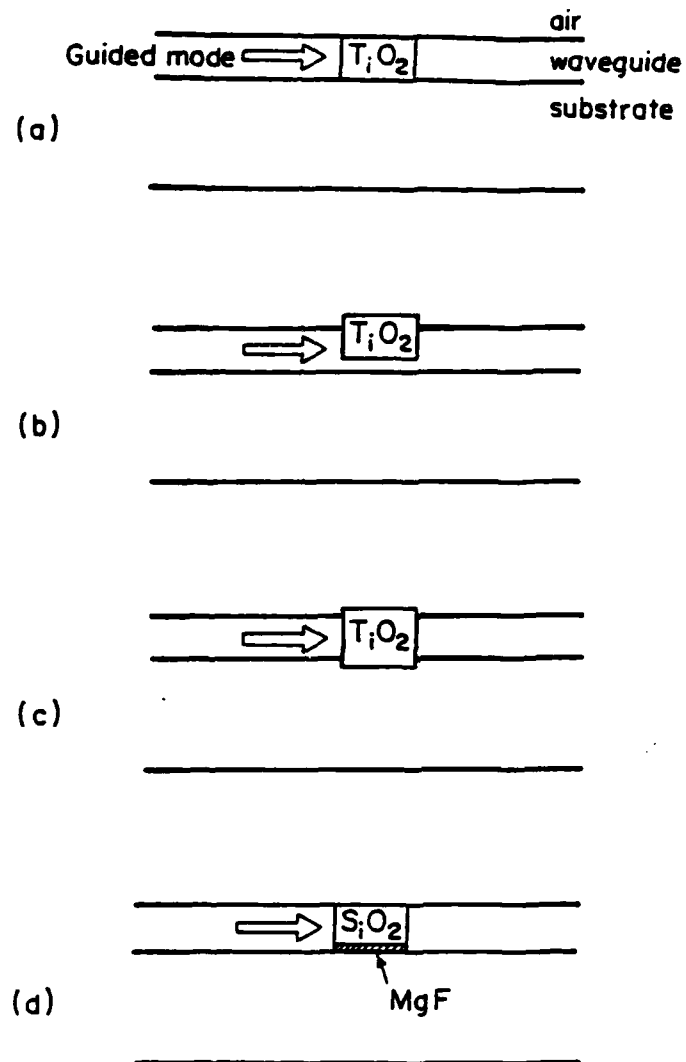
Figure 4.10: Cross sectional view of possible geometries for thin film coated recessed lenses (see text).

thin film, which has a refractive index of 1.38 (see Fig. 4.10 (d)).

Through the experimental evaluation that is presented later, the above lenses did not perform satisfactorily due to reasons that we do not understand fully. This prompted us to examine the technique of fabricating TI integrated lenses in TIPE slab waveguides as was discussed in Sect. 3.3. Therefore, the fabrication of these lenses will also be presented.

4.4.1 Thin Film Coated Recessed Lenses

Substrates that we have selected for the purpose of fabricating thin film coated recessed lenses were similar to the substrates for which we previously presented the fabrication process in Sect. 4.1.

Fabrication of thin film coated recessed lenses on Ti:LiNbO$_3$ can be categorized into two steps: selective ion beam milling, and thin film deposition. For the selective ion beam milling process we used Shipley S1400-33 photoresist (2.2 μm thick) that was properly exposed and developed through a mask which contained numerous lens patterns (see Fig. 3.8). Exposure times needed to generate the lens patterns were generally in the range 10-15 seconds. After developing the photoresist, the resultant patterns were lens shaped openings (both convex and concave).

An important part of the fabrication of thin film coated recessed lenses is that the same photoresist coating used in the ion beam milling process must also be used in the subsequent lift-off process required in order to define the thin film overlayer deposited into the recessed region. Therefore, the photoresist layers on the substrates were not removed after ion beam milling prior to thin film deposition.

In order to selectively remove the Ti:LiNbO$_3$ waveguide material from the lens regions, the substrates were ion beam milled. Again, hard-baked photoresist coatings (140° C for 2 hrs) were used as the protective mask during the ion beam

125

milling process. These samples were ion beam milled for durations of up to 2 hrs and 30 min (depths of about 1 μm), using the same parameters as discussed in Sec. 4.2. The ion beam milling process created recesses in the Ti:LiNbO$_3$ substrates that were shaped like convex or concave lenses.

The substrates were then coated with the appropriate thin films in order to form the integrated lenses. After the lift-off process, excess thin film material will be removed from the region surrounding the lens leaving the thin film overlayer in the recessed lens region only.

Samples that were prepared according to the steps discussed above were used for the deposition of both high (TiO$_2$ film) or low (SiO$_2$ thin film and MgF buffer layer) refractive index materials, as described in more detail below.

One thin film material that was chosen to <u>increase</u> the refractive indices of the recessed lens patterns was titanium dioxide (TiO$_2$). The refractive indices of thin films of TiO$_2$ are approximately 1.9-2.54 depending on the particular method of electron beam deposition employed. [89,90].

We deposited TiO$_2$ thin films using titanium dioxide crystals in the Balzers BAK 640 electron beam deposition system. During electron beam evaporation, TiO$_2$ films are decomposed due to excessive heat generation into

$$TiO_2 + heat \longrightarrow TiO_x + O_{2-x} \qquad (4.4)$$
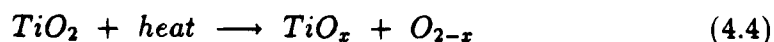
The resultant TiO$_x$ films are highly absorptive and have refractive indices that are not well determined. We attempted to partially reverse the process of decomposition of TiO$_2$ by increasing the pressure within the deposition chamber to 5×10^{-5} Torr (from a base pressure of 10^{-8} Torr) by back-bleeding ultra high purity oxygen (99.999% purity oxygen obtained from MG Industries) during the deposition run.

Different samples with recessed lens patterns were electron beam coated (at a rate of a few angstroms per second) with TiO$_2$ thin films ranging in thickness

from 0.5 μm to 0.7 μm. Due to limitations in the crucible capacity of the electron beam evaporator used, we could not deposit thicknesses larger than 0.7 μm in one run to match the waveguide thicknesses of about 1 μm in some of our samples. In those cases, the surfaces of the lenses were slightly below the surface of the Ti:LiNbO$_3$ substrates.

The thin film coatings from the unwanted regions were removed using the lift-off process in Microposit Remover 140 that was slightly heated to assist the removal of hard baked photoresist. A 20X optical micrograph of two resultant convex lenses (radii of 1.25 mm with a 2.5 mm aperture) are shown in Fig. 4.11. Minor defects at the boundaries of these lenses are visible. Such defects should n-t prove significant in the coupling experiments that are presented later to examine the focal properties of these lenses.

In order to fabricate lenses with lower refractive indices than those of the Ti:LiNbO$_3$ waveguide, substrates with recessed lens patterns as discussed earlier in this section were again used. The thin film selected with a lower refractive index than that of Ti:LiNbO$_3$ waveguides was SiO$_2$ ($n \sim 1.46$). During the electron beam evaporation of SiO$_2$, decomposition similar to that observed in the case of TiO$_2$ takes place [90]. In order to minimize such decomposition, therefore, back-bleeding of oxygen into the deposition chamber was conducted during the deposition. In such lenses, prior to the deposition of SiO$_2$ (about 0.8 μm thick) thin buffer layers of MgF (about 0.07 μm thick) were deposited on the substrates. The thin films deposited on the regions outside of the lenses were again removed using the lift-off technique. The quality of the lenses fabricated using this procedure was similar to that observed for the lenses fabricated with TiO$_2$ coatings (see Fig. 4.11).

Results of examining thin film coated recessed lenses (which will be presented later) revealed that at this level of research we were not successful in obtaining focusing by such lenses. Hence, we will explore the fabrication of TI lenses in

127

TIPE waveguides in the next section.

4.4.2 TI Lenses in TIPE Waveguides

It was mentioned in Sect. 3.3 that other investigators have used the proton exchange technique of modifying the refractive index of Ti:LiNbO$_3$ waveguides to fabricate integrated lenses [10,67]. They used either plasma enhanced chemical vapor deposited (CVD) films of Si$_3$N$_4$, or thin metal films (i.e. Ti or Cr) as the mask for the proton exchange process on Ti:LiNbO$_3$. Lens shaped openings were then photolithographically formed in the Si$_3$N$_4$ or metallic thin films. Hence, only the regions of the Ti:LiNbO$_3$ waveguides under the openings were transformed by the proton exchange process into TIPE material. Subsequently, the thin film masks were required to be removed, leaving Ti:LiNbO$_3$ waveguides with integrated TIPE lenses.

We determined in Sect. 3.3 that for advanced IO signal processing applications it is often desirable to increase the degree of mode confinement of the Ti:LiNbO$_3$ slab waveguides. The integrated lenses in such processors should also be easy to fabricate, and their surface areas should be as small as possible. In addition, the lens fabrication process must be compatible with that used to integrate other required components such as the rib waveguide array. The above requirements prompted us to attempt a modification of the standard TIPE technique that resulted in the fabrication of novel integrated lenses with several attractive features.

In this modified technique, the refractive index of the Ti:LiNbO$_3$ slab waveguide was further increased by the proton exchange process while masking the integrated lens regions from this process [70,66,71,67]. Hence, the refractive index of the lens region was maintained at the lower value characteristic of an unmodified Ti:LiNbO$_3$ waveguide. The combination of concave curvatures of these TI lenses (see Fig. 3.9) and their lower refractive indices (as compared to

128
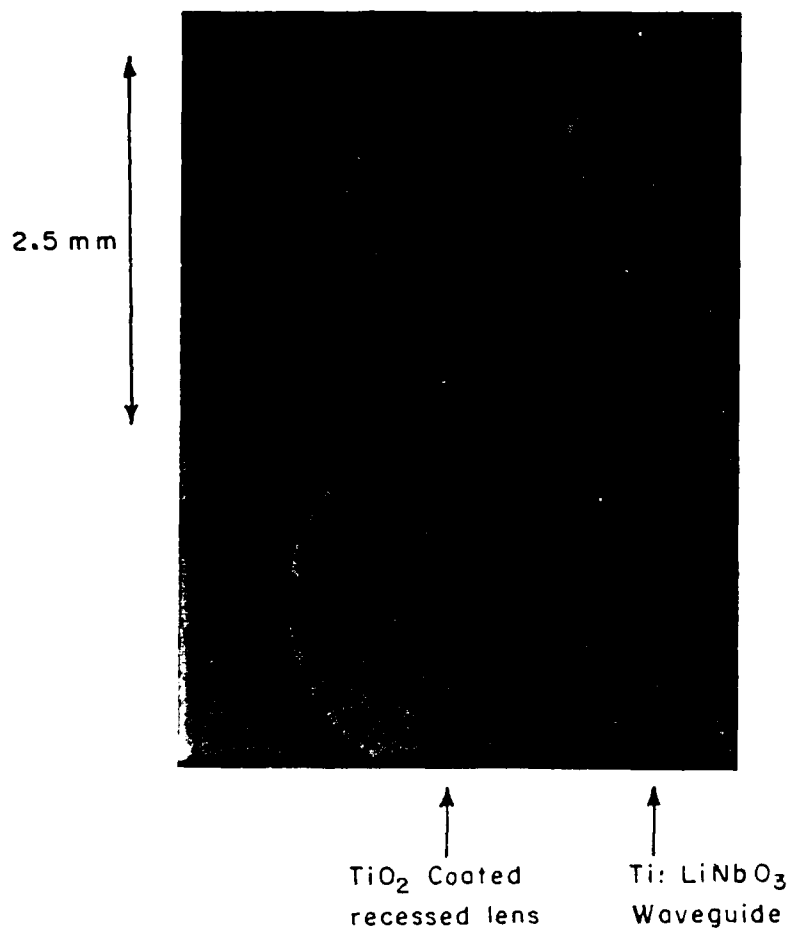
Figure 4.11: Optical micrograph (20X) of a 0.7 μm thick TiO_2-coated recessed convex two lens array fabricated on a Ti:LiNbO$_3$ substrate. The depth of the recessed region is about 1 μm. The picture was taken with a phase contrast microscope.

the TIPE slab waveguides) provided positive lensing characteristics.

In the fabrication of these lenses, thin films of SiO_2 were used as masks for the proton exchange technique (see Sect. 3.3). The masks only cover the lenses, and due to their relatively small refractive index they can be left on the substrate without significant perturbation to the performance of the lenses. The SiO_2 thin films can be removed if the samples are submerged in hydroflouric (HF) acid for a few seconds, if such removal is required.

In the fabrication of TIPE integrated lenses in TI slab waveguides used by others, Si_3N_4 ($n = 1.95$) masks were used that cover the entire substrate except for the lens pattern openings. Hence, this film should be removed after the proton exchange process. Deposition and removal of Si_3N_4 thin films are relatively more difficult process than those for SiO_2 thin films.

Besides the relative ease of fabrication, this method of fabricating TI lenses in TiPE slab waveguides also provides better mode confinement in the slab waveguide regions. Another advantage is that for the same focal lengths and aperture sizes, the TI lenses in TIPE slab waveguides occupy much smaller surface areas than the TIPE lenses in TI slab waveguides. A disadvantage of fabricating TIPE slab waveguides, which is characteristic of our technique, is that they normally exhibit higher propagation losses than TI waveguides (by as much as a few dB/cm depending on the method of proton exchange). This loss can lower the dynamic range of processors that employ TIPE waveguides [70,66,67,68,69,31]. Currently, promising work is being conducted by other investigators that could significantly reduce propagation losses in TIPE waveguides in the future [71].

The specific details of TI lens fabrication in TIPE waveguides are presented here. The substrates used here were similar in their fabrication parameters to the ones used to fabricate the thin film coated recessed lenses. In order to form SiO_2 thin film lens patterns on these substrates, we employed similar photoresist coating and exposure parameters as was discussed for the SiO_2 thin film coated

recessed lens. Thin films of SiO_2 (approximate thickness 400 Å) were deposited on the prepared samples. Following the lift-off process, the thin films were patterned on the slab waveguides as shown in Fig. 3.9.

In order to start the proton exchange (PE) process, the above samples were immersed in molten benzoic acid (C_6H_5COOH, freezing point $122°$ C) when the acid temperature was at $140°$ C, and the temperature was subsequently increased to $225°$ C. Different samples were proton exchanged for 3 and 6 hrs in order to examine the change in the refactive indices and the change in propagation losses as a function of proton exchange time. At the end of the proton exchange process the acid was cooled to $140°$ C and the substrates were then removed from the acid baths. The gradual increase and decrease of the acid temperature is required in order to prevent thermal shock induced cracks in the $LiNbO_3$ substrates.

An example of the resulting concave TI integrated lens (1.25 mm radii of curvature, and 2.5 mm aperture size) in a TIPE slab waveguide is shown in Fig. 4.12. Lenses of this type were used in a number of experiments that will be presented in Ch. 5 to determine their focal properties, and such lenses produced quite satisfactory results.

TIPE Waveguide

TI lens (SiO₂ Coated)

0.4 mm
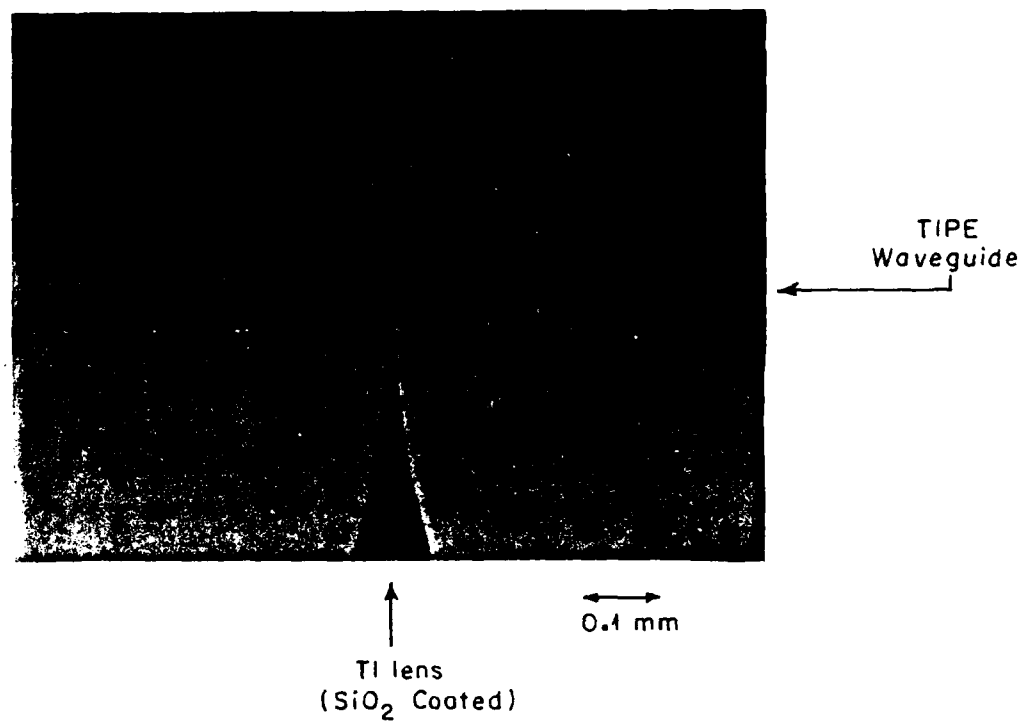
Figure 4.12: Optical micrograph (100X) of a concave TI integrated lens fabricated in a TIPE waveguide as discussed in the text. The SiO₂ mask for the proton exchange process remains on the lens surface.

Chapter 5

Experimental Characterization of the Fabricated Components

In this chapter, we further analyze and characterize the critical components required for advanced IO signal processors, for which we presented the fabrication procedures and issues in Ch. 4. Furthermore, we will compare these characterization experiments to the results of the analysis presented in Ch. 3, in order to develop a better understanding of the performance limitations, advantages and potential problems of these components. An outline of the principle characterization experiments and results is provided in what follows.

As part of the characterization program, we determined the number of TE and TM modes that can be supported in a fabricated Ti:LiNbO$_3$ slab waveguide by prism coupling of different polarization He-Ne beams at different angles, and the results are presented in Sect. 5.1. The number of modes that can propagate in a slab waveguide is an important characteristic of modes confined in the vertical direction to channel and rib waveguides due to the reasons described in Sect. 3.1. In addition, we excited the guided modes of a Ti:LiNbO$_3$ channel waveguide by a fiber-butt coupling technique, in order to investigate if the guided modes would stay confined to the channel over distances in the cm range. These results are presented in Sect. 5.2.

We have also prism coupled a TE polarized He-Ne beam into a fabricated rib waveguide array, in order that multiple measurements of the power at the end of the array could be conducted for different array lengths. These mea-

surements can be used to determine the propagation loss of the rib waveguide array. An increase of the propagation loss over the Ti:LiNbO$_3$ slab waveguide case was observed, which was primarily due to increased scattering loss at the sidewalls. Such scattering can induce background noise in CCD arrays, and hence reduce the dynamic range of IO processors. The results of propagation loss measurements of rib waveguide arrays are presented in Sect. 5.3.

An analysis of surface gratings with low surface modulation depths, as are needed to outcouple light from waveguides in order to access the third dimension of the processor, was an important thrust of this research. In addition, it is of considerable importance to determine the issues that attend to the fabrication of such gratings on the surface of rib waveguide arrays.

We needed to determine the outcoupling efficiency of the guided modes of rib waveguide arrays due to such surface gratings. However, experimental complications due to the inherent nonuniformity of the surface of a rib waveguide array (in addition to their relatively high scattering), prompted us to first investigate the performance of low modulation surface gratings on a slab waveguide. Therefore, 1 mm long surface gratings with 2 and 4 μm periods and heights of 0.1 μm were fabricated on a Ti:LiNbO$_3$ slab waveguide. The lowest order guided mode of the slab waveguide was excited using a prism, and the outcoupled modes due to the surface gratings were observed. We measured the resultant power levels in each mode outcoupled by the two gratings. An estimate of the guided mode power incident upon each grating was determined by measuring the power at the end of the slab waveguide for a beam that was not incident upon the gratings. The ratio of the guided mode power to that of each outcoupled mode provided an estimate of the outcoupling efficiency for that mode. The determined outcoupling efficiencies were lower than the calculated values presented in Sect. 3.2. We will present an analysis in Sect. 5.4 to explain such discrepencies.

We then measured the outcoupling efficiencies due to surface gratings on rib

waveguide arrays using techniques similar to the one described for gratings on slab waveguides. It will be shown in Sect. 5.5 that these experimentally determined outcoupling efficiencies were lower than those determined for comparable modes outcoupled from the slab waveguide case.

In Sect. 5.6, results of experiments in which we prism coupled a collimated beam into several slab waveguides, each having a different type of fabricated integrated lens, will be presented. The fabricated thin film coated recessed lenses did not produce any focusing despite the predictions of theory as presented in Sect. 3.3. We will present an analysis of why such lenses did not perform as expected in Sect. 5.6.

Fabricated TI integrated lenses in TIPE slab waveguides, on the other hand, produced focusing at focal lengths close to those predicted by the theory presented in Sect. 3.3. We measured the throughput efficiency of one of the TI lenses in a TIPE slab waveguide. The results of experiments with such lenses will be presented in Sect. 5.6.

In order to determine the focal spot size of TI lenses, we fabricated rib waveguide arrays at the lens focal planes on a large TIPE substrate. Collimated beams were then excited in the TIPE substrate and were subsequently focused into individual waveguides within a large area rib array. By determining the number of waveguides excited in this manner we were able to estimate the focal spot sizes of such lenses. In addition, it was determined that fabrication of rib waveguide arrays at the focal planes of such integrated lenses can be conducted with relative ease. The outcome of these experiments are presented in Sect. 5.7.

The guided modes of the rib waveguides that were focused into by the integrated lens were then outcoupled using surface gratings fabricated on the rib waveguide arrays, in order to access the third dimension of the chip and therefore to simulate the similar process proposed for advanced IO signal processors. These experimental results are also presented in Sect. 5.7.

5.1 Titanium Indiffused (Ti:LiNbO$_3$) Slab Waveguides

In this section, we will present the results of experiments in which mode coupling into a Ti:LiNbO$_3$ slab waveguide was conducted by a prism. These experiments were needed in order to determine the number of different modes that the slab waveguide can support [61,91]. The fabrication parameters of the Ti:LiNbO$_3$ slab waveguide that were used for this purpose were the same as those of the waveguide discussed in Sect. 4.1. Since similar Ti:LiNbO$_3$ slab waveguides were used as substrates for all of the experiments presented here, the number of guided modes in such waveguides was also characteristic of the channel and rib waveguides in the vertical direction because of the assertions in Sect. 3.1.

For the purposes of these experiments and all of the other prism coupling experiments that are presented later, we employed a rutile prism ($n_e = 2.871$ and $n_o = 2.583$) oriented with its optic axis perpendicular to the triangular sides of the prism, in a setup similar to the one shown in Fig. 3.5. The method by which a beam is coupled into the waveguide by a prism is effectively the reciprocal of the evanescent coupling geometry shown in Fig. 3.3. In the evanescent coupling geometry, higher refractive index of the detector (compared to the waveguide) provides higher coupling efficiency.

Therefore, in the reciprocal situation, a higher refractive index of the prism will provide a higher coupling efficiency. Hence, we selected this particular optic axis orientation of the coupling prism in order to enhance the coupling efficiency for E$_x$ polarized input beams (which then experience the extraordinary refractive index of the rutile prism).

For the prism coupling situation, the beam is made incident at the bottom of the prism at an angle which is always larger than the critical angle; therefore, evanescent fields are induced in the air gap between the prism and the waveguide.

136

For the cases in which the air gap is thin enough, and the phase propagation velocity of the evanescent field along the surface of the waveguide matches the phase velocity of specific guided mode, the incident light will then couple into that mode of the waveguide efficiently [61]. In our setup the air gap between the prism and the waveguide is optimized by using a clamp to hold the prism onto the waveguide.

A TE polarized He-Ne beam was coupled into the slab waveguide. By varying the incidence angle of the beam onto the prism we were able to excite 3 distinct TE modes. This number of TE modes is exactly equal to the number of modes that we predicted in Sect. 3.1. In the analysis of Sect. 3.1, we assumed an abrupt Ti:LiNbO$_3$ waveguide boundary that was 1 μm thick. Therefore, such assumptions proved adequate for the determination of the number of modes.

In another experiment, we investigated the propagation loss of the fabricated Ti:LiNbO$_3$ slab waveguides. We prism coupled into a slab waveguide (prepared in the same manner as the one used for the mode determination) and measured the guided mode power at the end of the waveguide for different waveguide lengths. This method of determining the propagation loss of waveguides will be discussed in more detail later. We determined a propagation loss of approximately 1-2 dB/cm, which was in agreement with the losses reported by Jerominek, *et al.* [3] for typical Ti:LiNbO$_3$ waveguides.

5.2 Titanium Indiffused (Ti:LiNbO$_3$) Channel Waveguides on an Edge Polished Substrate

In the experiment that is presented here, we used an optical fiber to excite the guided modes of a 5 μm wide (1 cm long) channel waveguide on an edge polished substrate that was fabricated as presented earlier in Sect. 4.1. This experiment was conducted in order to examine the possibility of soft guiding in Ti:LiNbO$_3$

137

channel waveguides, which can cause leakage of guided light from the waveguide over long propagation distances. In addition, we desired to investigate how suitable the edge polished surface was for fiber butt-coupling into the channel waveguide, in an attempt to simulate the laser diode-slab waveguide coupling configuration (needed for IO processors).

The channel waveguide used in our experiments is shown in Fig. 4.1. In our setup for butt-coupling experiments, we coupled a circularly polarized He-Ne beam into a Newport F-SV single mode fiber (4 μm core diameter) using a 20X microscope objective. The fiber was secured at its output end to a stage with two dimensional translation and tilt capability, in order to align the fiber with the channel for optimum coupling.

The resultant guided mode of the channel waveguide as seen looking down on the substrate is shown in Fig. 5.1. The fiber used for butt-coupling is seen as the faint line oriented from left to right against the left edge of the substrate. The bright streak within the substrate is about 1 cm long, and is an indication of the light confined to the channel waveguide. The edge of the substrate at the output end of the channel waveguide (edge on the right side) was not polished, which thus exhibited significant scattering in the form of blooming at this end. The scattered light visible at the left end of the substrate maybe due to chipped edges of the substrate.

The degree of confinement of the guided modes to the Ti:LiNbO$_3$ channel waveguide was not determined quantitatively. However, close inspection of the guided light shown in Fig. 5.1 suggested that in the photograph the beam width increased from approximately 0.1 mm to approximately 1 mm from a point close to the input end of the channel towards the output end. Since the magnification associated with the photograph was 2.5 times, the actual beam width increased from approximately 0.04 mm to 0.4 mm. This is characteristic of soft guiding in Ti:LiNbO$_3$ channel waveguides (see Sect. 3.1), which exists both in the vertical

Fiber

Channel Guide Mode

$LiNbO_3$ **Substrate**
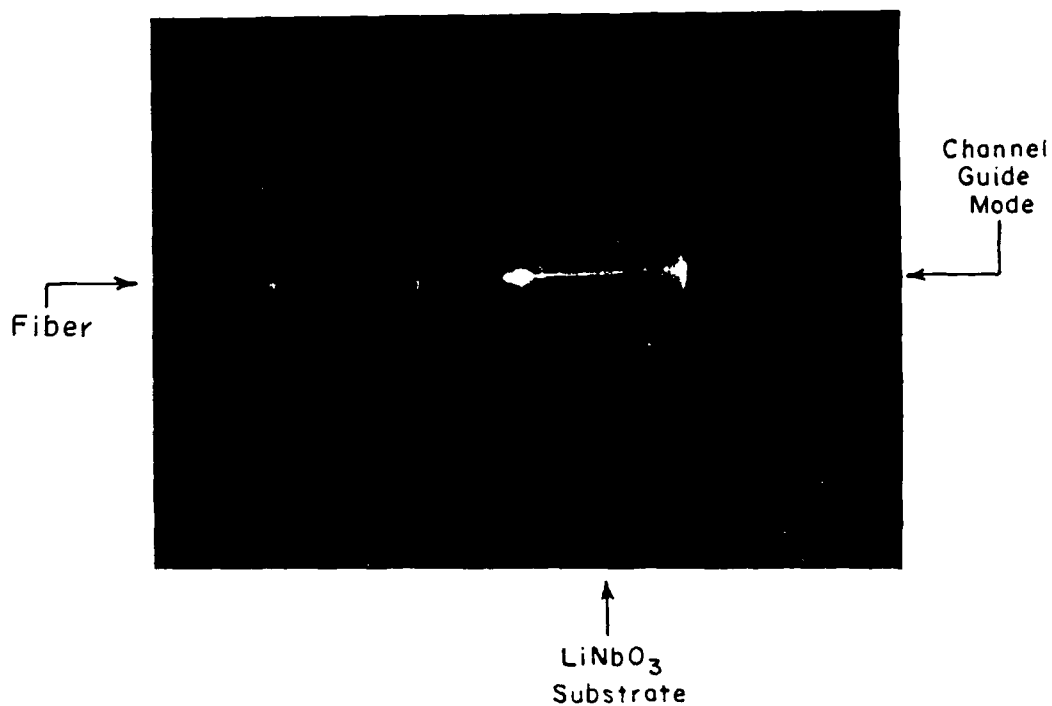
Figure 5.1: This photograph is a top view of the guided modes in a Ti:LiNb-O_3 channel waveguide. which is butt-coupled to an optical fiber. The beam is soft-guided since the beam width increases in the direction of propagation. The coupling fiber in contact with the left polished edge of the substrate is faintly visible. The right edge of the substrate is not polished. causing visible scattering at this end.

and the lateral dimensions. This was one of several reasons that prompted us to use the TIPE waveguides in order to better the degree of mode confinement.

In the above fiber butt-coupling experiments, the quality of the edge polished surface seemed to be satisfactory. The angular and linear alignment of the fiber to the channel for efficient coupling were estimated to be sensitive to $0.5°$ and 0.5 μm, respectively.

5.3   Rib Waveguide Arrays

In Sect. 3.1, we showed that rib waveguides are potentially better candidates than channel waveguides for use in large area arrays due to their crosstalk and mode confinement performance.

In this section we will present the experimental results that were obtained for characterizing rib waveguide arrays and determining their impact on the performance of advanced IO processors. Specifically, we determined the propagation loss of a typical fabricated rib waveguide array. For this purpose, we used a LiNbO$_3$ substrate with a 1 cm long rib waveguide array (with 660 elements separated by 2 μm gaps; each element is 8 μm wide and 1 μm high), the fabrication of which was presented in Sect. 4.2.

In order to determine the propagation loss of the above rib array we determined how the guided mode power decayed as a function of distance along the array. The power in the rib waveguide array decayed from $p(z_1)$ to $p(z_2)$ when propagating from a distance z_1 to a distance z_2 further down the array. Hence, we were able to determine the propagation loss in the rib waveguide array (α_{rib} in dB/length) from

$$\alpha_{rib} = \frac{10 \log \left(\frac{P(z_1)}{P(z_2)} \right)}{z_2 - z_1}. \tag{5.1}$$

Guided modes of the rib waveguide array (E$_x$ polarized) were excited using a rutile prism in contact with the array top surface in a manner similar to that

used for coupling into slab waveguides as described in Sect. 5.1. The coupled beam width was about 2 mm, which excited approximately 200 rib waveguides.

Since it was experimentally difficult to measure the power within a single rib waveguide at different locations, we instead cut the array at different lengths, and each time positioned a flat detector against the waveguide end and measured the power at the end of the array.

Each time we needed to cut the array (by means of a diamond impregnated wire saw), we had to remove the substrate from the prism coupling setup. Therefore, there was a possibility of a change in prism coupling efficiency from trial to trial(due to a change in the air gap thickness) that lead to an inherent estimated error of 10% in power decay measurements performed by this technique. In addition, since we did not optically polish the output ends, they induced scatter that could vary from trial to trial.

In our experiment, the distance z was measured from the edge of the prism to the output end of the rib array. The output power measurements for three different distances are plotted in Fig. 5.2. Using this information in Eq. 5.1, we determined that the rib waveguide array exhibited a propagation loss of about 6 dB/cm. This loss was about 4 dB/cm larger than that of the fabricated Ti:LiNbO$_3$ slab waveguide. This increase in the propagation loss can be partially attributed to scattering by nonuniformities in the ion milled sidewalls. In addition, the rib waveguides might not have been sufficiently undercut, which could induce significant scatter of the guided light at the sharp edges of the troughs.

The increase in scattering that was observed for a rib waveguide array has certain implications for its use in advanced IO signal processors, since the incorporated CCD array on the rib waveguide array will pick up the scatter noise, thus reducing the signal-to-noise ratio. Therefore, further work needs to be conducted in order to reduce such scattering in rib waveguide arrays. A possible

Rib Waveguide Propagation Loss

8 μm wide; 2 μm gaps
Loss = 6 dB/cm @
λ = 6328 Å

OUTPUT POWER (mW)

RIB WAVEGUIDE LENGTH (cm)
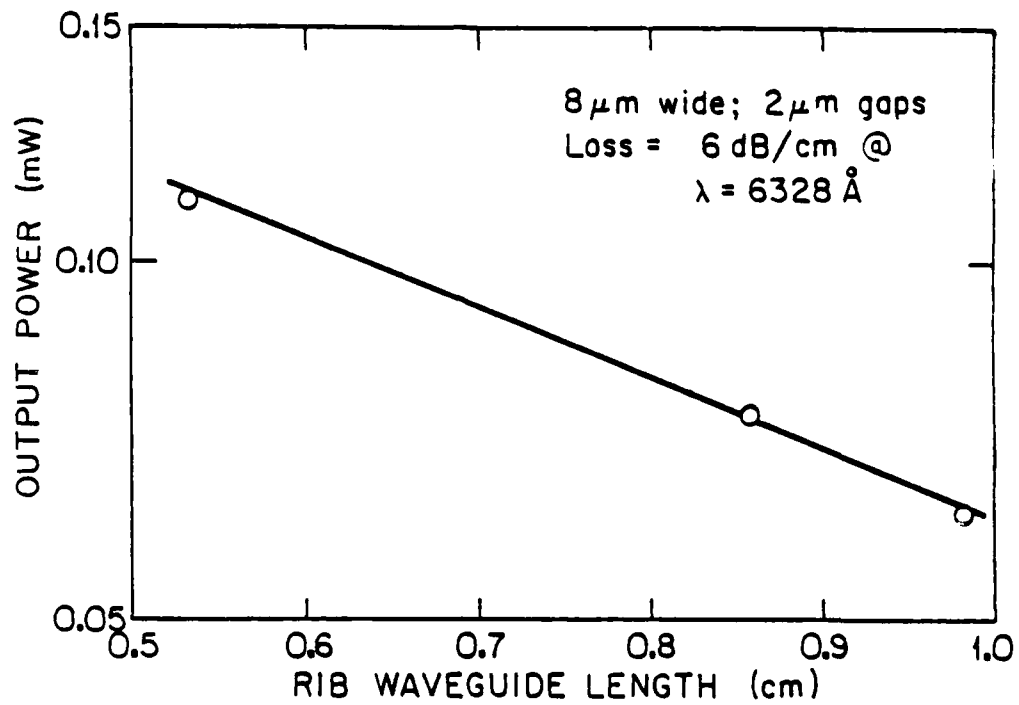
Figure 5.2: Output power as a function of rib waveguide length for an 8 μm wide rib waveguide within a rib waveguide array of 200 ribs with 2 μm gaps. Note that the ordinate scale is logarithmic, such that the slope yields the propagation loss of an individual rib waveguide.

avenue that needs to be investigated is the possibility of using reactive ion beam etching (RIBE) with C_2F_6 (Freon 116) gas for the fabrication of rib waveguide arrays with better sidewall quality and higher undercuts [92].

5.4 Grating Outcoupling From a Ti:LiNbO₃ Slab Waveguide

In the theoretical consideration of surface gratings with low surface modulation on rib waveguide arrays presented in Sect. 3.2, we predicted the efficiencies of the modes outcoupled from rib waveguides by surface gratings characterized by parameters representative of the fabricated gratings. We then needed to determine how the actual outcoupling efficiencies for these modes compared to the predictions.

Surface gratings on rib waveguide arrays constitute relatively complex structures, which made the experimental verification of outcoupling efficiencies due to rectangular surface gratings rather difficult. Such difficulty was due to scattering by the fabricated rib waveguide arrays. In addition, variations of the fabricated grating profiles from the original design added more complexity to their understanding. Therefore, we examined large area surface gratings with low surface modulation on a Ti:LiNbO₃ slab waveguide in order to circumvent the problems mentioned above. The results of this examination may also prove useful for other applications, since to our knowledge the fabrication, characterization, and analysis of large area surface gratings with low modulation on a Ti:LiNbO₃ slab waveguide has not been reported previously.

We fabricated 1 mm long gratings with both 2 and 4 μm periods on a standard Ti:LiNbO₃ slab waveguide (see Sect. 4.1). In fabricating these surface gratings, we followed procedures similar to those used for fabricating gratings with 2 and 4 μm periods on rib waveguide arrays as discussed in Sect. 4.3. The

143

resultant surface gratings are shown in the scanning electron microscope micrographs of Fig. 5.3 (2 μm grating period), and Fig. 5.4 (4 μm grating period). It is evident from these micrographs that the gratings fabricated on the slab waveguide were also characterized by a reduction of the aspect ratio similar to that observed for the gratings on rib waveguide arrays (as discussed in Sect. 4.3). The aspect ratios of the fabricated gratings on the slab waveguide were determined to be about 0.2 for the 2 μm grating case and about 0.3 for the 4 μm grating case. The effect of this reduced aspect ratio on the outcoupling efficiency will be presented shortly.

Although the ion beam milling times and settings used for fabricating surface gratings on the slab waveguide were equal to the times and settings used for gratings on the rib arrays, the grating heights for both 2 and 4 μm periods were estimated from Figs. 5.3 and 5.4 to be about 0.1 μm as opposed to the height of 0.05 μm (characteristic of the gratings on rib arrays) that was intended. This might be due to variations in the location of the substrate with respect to the Gaussian profile of the ion beam used for milling. In Sect. 3.2, we calculated the saturation grating height to be about 0.07 μm. Therefore, the gratings on the slab waveguide should be in the saturation regime.

We employed the above surface gratings to outcouple light that was prism coupled into the Ti:LiNbO$_3$ slab waveguide. The gratings were situated on the slab waveguide such that by translating the incident beam in the transverse dimension, we were able to excite either of the gratings individually, or neither of them. This provision was needed in order to estimate the guided mode power that was incident onto the gratings. In Fig. 5.5, the light that is outcoupled by the 2 μm grating is shown. In Fig. 5.6, on the other hand, the light that is outcoupled by the 4 μm grating is shown. In both figures, the guided mode in the slab propagated from the top to the bottom of the substrate.

Associated with every mode outcoupled into the air by the surface grating

144
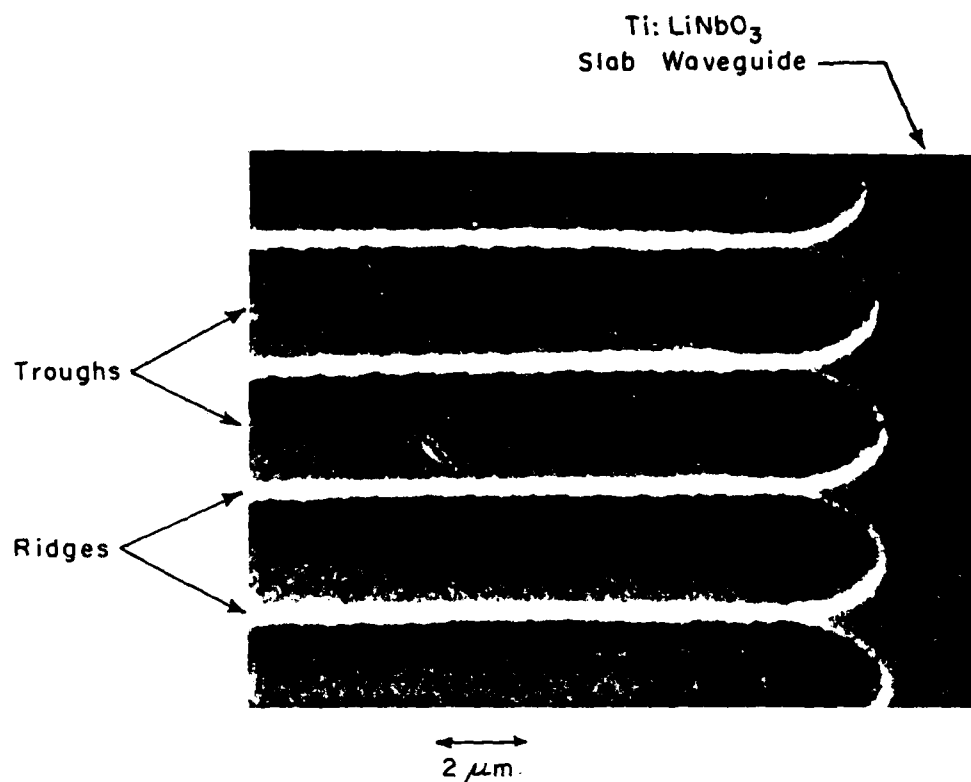
Figure 5.3: A scanning electron microscope micrograph of an outcoupling grating (with a 2 μm period and a height of 0.1 μm) fabricated on a Ti:LiNbO$_3$ slab waveguide is shown here. The uniform region to the right is the surface of the Ti:LiNbO$_3$ slab waveguide. Note that the aspect ratio of the grating is about 0.2 (less than 0.5) which reduces the outcoupling efficiency.

145
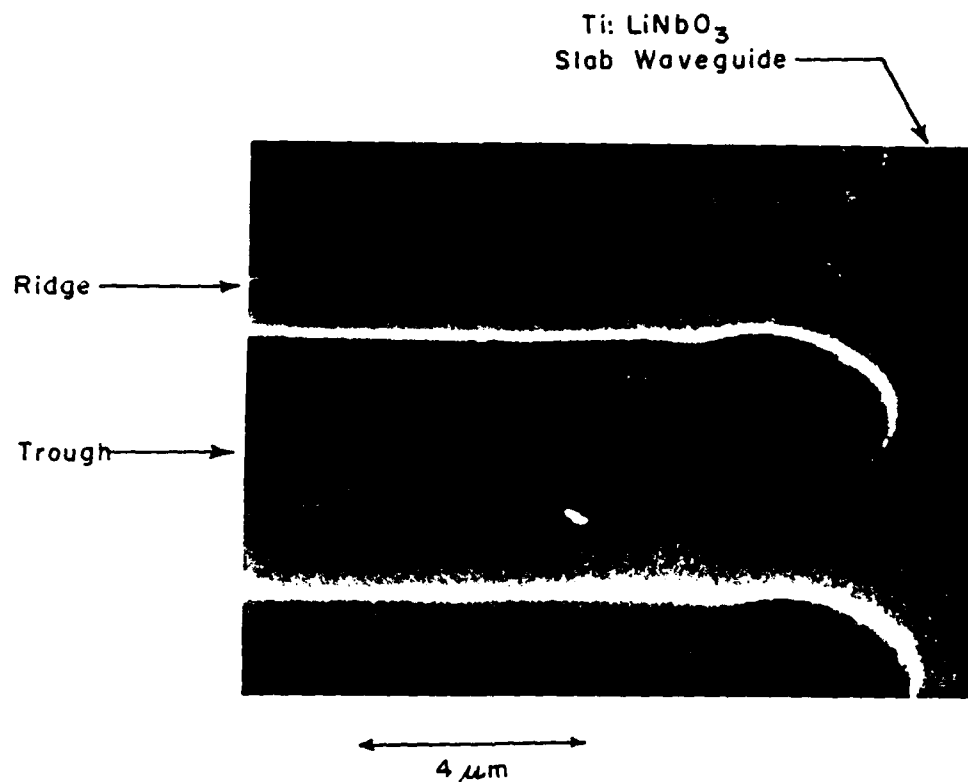
Figure 5.4: A scanning electron microscope micrograph of an outcoupling grating (with a 4 μm period and a height of 0.1 μm) fabricated on a Ti:LiNbO$_3$ slab waveguide is shown here. The uniform region to the right is the surface of the Ti:LiNbO$_3$ slab waveguide. Note that the aspect ratio of the grating is about 0.4 (less than 0.5) which reduces the outcoupling efficiency.
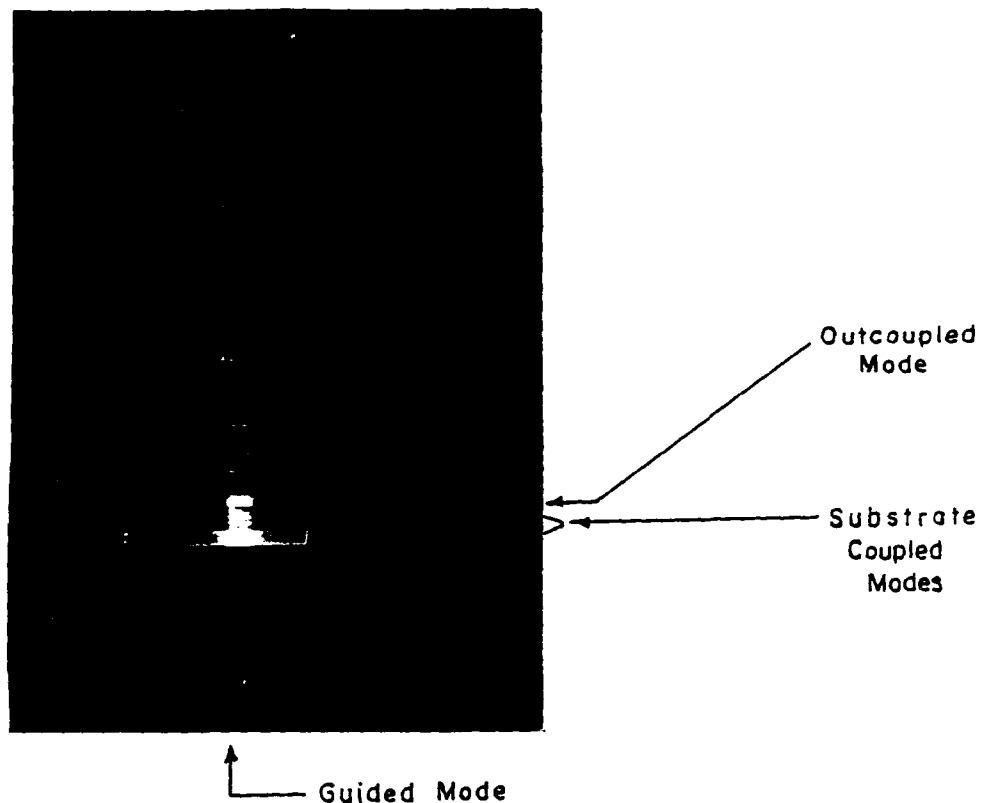
Figure 5.5: Prism incoupling and grating outcoupling from a Ti:LiNbO$_3$ slab waveguide. The grating (1 mm long, with a 2 μm period) is oriented from left to right. Many of the modes scattered into the substrate by the grating are also shown (see text).

147
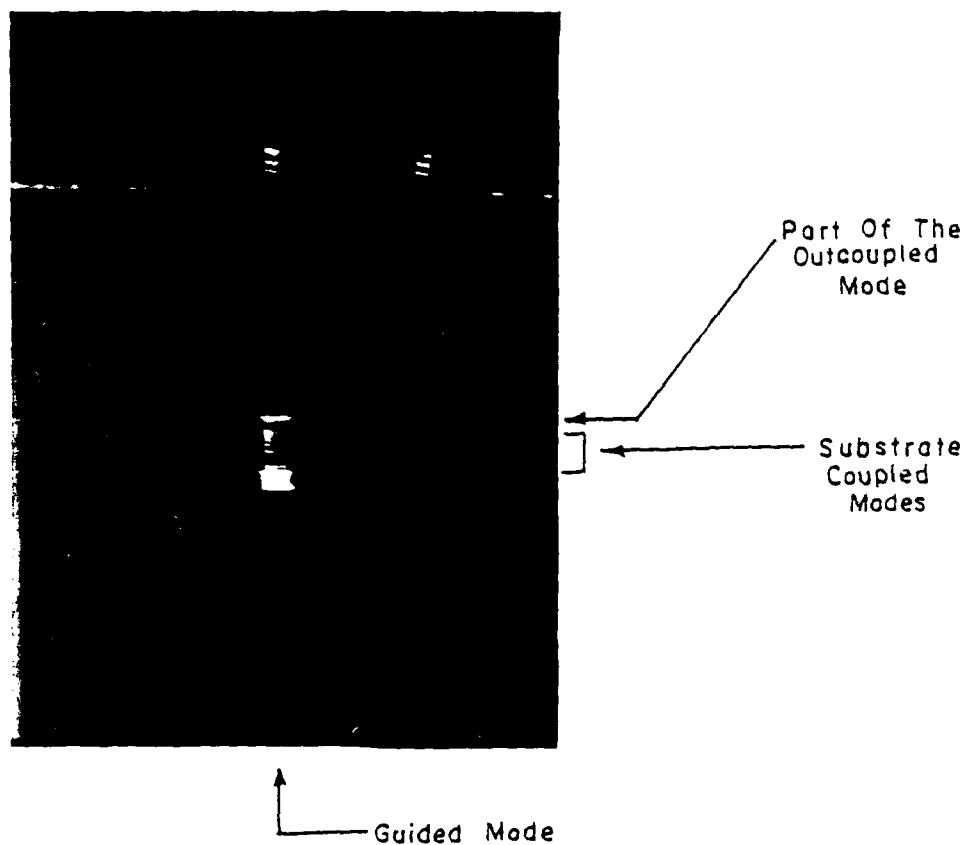
Figure 5.6: Prism incoupling and grating outcoupling from a Ti:LiNbO$_3$ slab waveguide. The grating (1 mm long with a 4 μm period) is oriented from left to right. Many of the modes scattered into the substrate by the grating are also shown (see text).

on the substrate are modes that are coupled down into the substrate from the waveguide, which we call substrate modes [55]. In our situation, the substrate modes were scattered from the unpolished surface at the bottom of the substrate, forming the series of bright lines which are visible in Figs. 5.5 and 5.6. Between the outcoupled modes and the end of the substrate in these two figures, there were 4 and 7 visible substrate modes for the 2 μm and 4 μm gratings, respectively. In applications that such substrate modes are undesirable, blazed gratings can be used which de-emphasize the power in such modes in favor of outcoupled modes [21].

The determined number of outcoupled modes for both gratings agreed with the predicted numbers shown in Figs. 3.6 and 3.7. In addition, the outcoupling angles were in close agreement with the predicted angles of Figs. 3.6 and 3.7. These results indicated that the value of longitudinal propagation constant of the slab waveguide used in Sect. 3.2 was a reasonable approximation to that of the actual waveguide.

We measured the outcoupled powers in each mode as a first step in determining the outcoupling efficiencies. In order to reduce the effect of scattered light on the measurement of the outcoupled powers, we covered both the top surface of the substrate and its end. The only exposed area was the grating region, in order to allow the outcoupled light to exit. In addition, we measured the outcoupled power levels at a large enough distance to reduce the effects of undesirable scattering. As was expected (from Figs. 3.6 and 3.7), the outcoupled power levels steadily decreased from the codirectional modes towards the contradirectional modes. This made the weaker power levels of the contradirectional modes more susceptible to measurement error.

We then translated the guided beam into the region with no grating, and measured the power at the output end of the Ti:LiNbO$_3$ waveguide, in order to estimate the power of the guided mode incident upon the gratings (as was

149

needed for the determination of the outcoupling efficiencies). Since the gratings were situated close to the output end of the Ti:LiNbO$_3$ slab waveguide, the measured power at the output end was a good approximation of the input power level incident upon the gratings. We also estimated the power reflection at the output interface in order to adjust the measured output power accordingly.

By dividing the power in each outcoupled mode by the input power incident upon the gratings, we determined the outcoupling efficiencies for the 2 and 4 μm period cases. The resulting outcoupling efficiencies are plotted for each mode of the two gratings in Fig. 5.7 (for the 2 μm case) and Fig. 5.8 (for the 4 μm case). The experimental points that are missing in these two figures correspond to the outcoupling efficiencies of modes that were difficult to measure reliably. Also plotted in these figures are the theoretically predicted outcoupling efficiencies for each case (for heights larger than 0.07 μm) and the predicted outcoupling efficiencies for grating heights of 0.05 μm.

The outcoupling efficiencies due to the 2 μm grating (as shown in Fig. 5.7) were generally lower than the expected outcoupling efficiencies (saturation out-coupling efficiencies). The ratio of the experimental to the expected outcoupling efficiencies ranged from 0.7 (for mode $m = -4$) to 0.03 (for mode $m = -9$). The outcoupling efficiencies due to the 4 μm grating (as shown in Fig. 5.8) were also generally lower than the expected outcoupling efficiencies denoted by the saturation outcoupling efficiencies. The ratio of the experimental to the expected outcoupling efficiencies in this case ranged from 0.15 (for mode $m = -8$) to 0.01 (for mode $m = -14$).

We attributed part of these reductions in the outcoupling efficiencies compared to the expected values to the observed reductions of the fabricated aspect ratios (in the range 0.2-0.3) from the intended value of 0.5. According to Tamir and Peng, the dependence of the grating outcoupled mode leakage factors (α

2 Micron Grating (1mm long) Outcoupling Efficiencies
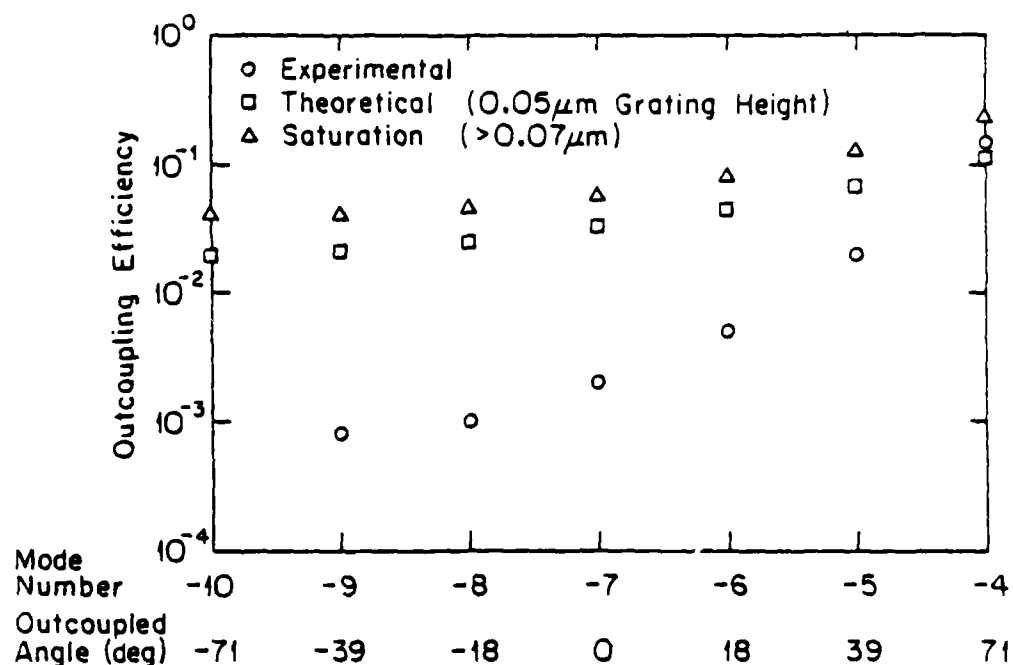
Figure 5.7: Outcoupling efficiency as a function of outcoupled mode number (and outcoupling angle) plotted for a 2 μm grating period that is 1 mm long and 0.1 μm high (above saturation height). The plotted values include those theoretically calculated for saturation and also the experimentally determined outcoupling efficiencies (see text). Also shown are the theoretical calculations for a grating that has a height of 0.05 μm.

4 Micron Grating (1mm long) Outcoupling Efficiencies
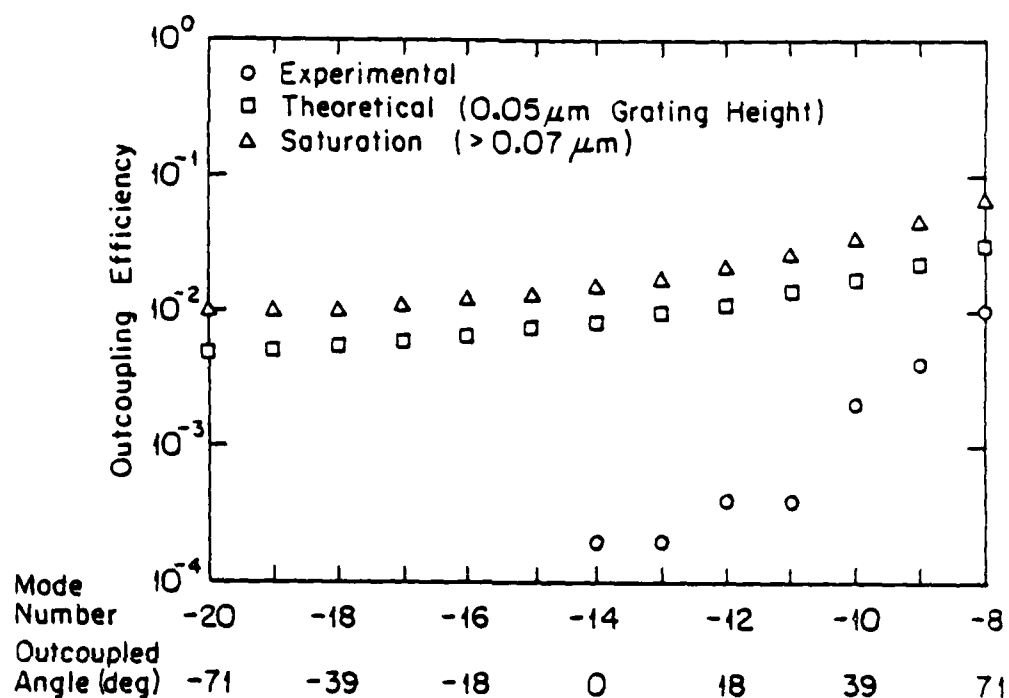
Figure 5.8: Outcoupling efficiency as a function of outcoupled mode number (and outcoupling angle) plotted for a 4 μm grating period that is 1 mm long and 0.1 μm high (above saturation height). The plotted values include those theoretically calculated for saturation and also the experimentally determined outcoupling efficiencies (see text). Also shown are the theoretical calculations for a grating that has a height of 0.05 μm.

and α_{sat}, defined in Sect. 3.2) on the aspect ratio (d_1/Λ) is given by [55]

$$\alpha \propto \sin^2(\pi d_1/\Lambda). \tag{5.2}$$

From this equation we determined that the leakage factors for a 0.2 aspect ratio grating were 0.3 times those for a 0.5 aspect ratio. Similarly, the leakage factors for a 0.3 aspect ratio grating are about 0.65 times those for a 0.5 aspect ratio.

We used the saturation leakage factors for both gratings that were appropriately corrected for the aspect ratios (as shown above) in Eq. 3.26 in order to determine the corrected expected outcoupling efficiencies for 1 mm long gratings. We then determined the ratio between the measured outcoupling efficiencies and those of the corrected expected outcoupling efficiencies. For the case of the 2 μm grating, the above ratio ranges from 1.5 ($m = -4$ mode) to 0.12 ($m = -9$ mode). Similarly, for the case of 4 μm grating the above ratio ranges from 0.5 ($m = -8$ mode) to 0.04 ($m = -14$ mode).

The above results reveal that for the lower order outcoupled modes, the measured outcoupling efficiencies were in better agreement with the theoretical predictions (corrected for aspect ratio) than those for the higher order modes. The higher order outcoupled modes in a rectangular grating are induced by higher spatial frequencies due to the sharp corners of such gratings [55]. Therefore, we believe that the fabricated gratings were slightly rounded around the edges for both gratings, causing reduced power levels in the higher order outcoupled modes. This claim, however, needs to be investigated further and if found true, a better theoretical model of the fabricated gratings needs to be developed. In any case, it may turn out to be advantageous for processor integration to de-emphasize the higher order contradirectional modes, in order to enhance the outcoupling of the codirectional modes for coupling through the mask and into the CCD array.

153

5.5 Grating Outcoupling From Rib Waveguide Arrays

In this section, we will present the results of experiments in which 2 μm and 4 μm gratings were used to outcouple the guided light from rib waveguide arrays on two samples. In addition, the measured outcoupling efficiencies will be presented and compared to those determined for the Ti:LiNbO$_3$ slab waveguide case presented previously.

Both samples that were used in these experiments had 1 cm long rib waveguide arrays (with 660 individual waveguides 8 μm wide, 1 μm high, and separated by 2 μm gaps). On the first sample, which we will refer to as sample 1, a 1 mm long grating with a 4 μm period and a 0.05 μm grating height was fabricated on the array. The second sample, which we will refer to as sample 2, was essentially the same as sample 1 except for the grating period, which in this case was 2 μm (for the fabrication details pertaining to these samples, see Sect. 4.3).

In each case, a TE polarized He-Ne beam (2 mm wide) was prism coupled, hence, exciting about 200 rib waveguides of the 660 element arrays. The guided modes of the rib waveguide array of sample 1 were outcoupled by the 4 μm grating into modes at discrete angles. The number of the outcoupled modes and their respective angles agreed (within the measurement error) with the predicted numbers and angles shown in Fig. 3.7. The measured outcoupling efficiencies will be discussed later.

One of the outcoupled modes in the above experiment ($m = -8$ at 71°) is shown in a direct photograph in Fig. 5.9. In this photograph, the guided modes of the rib waveguide propagate from top to bottom. The rectangular beam which appears highly uniform in this photograph is the mode outcoupled from the waveguide array by the 4 μm grating. Other bright spots in the photograph that appear on the substrate were due to scatter of the refracted light from the

154

coupling prism, and are characteristic of prism coupling experiments.

In another experiment, the 2 μm gratings of sample 2 were employed to outcouple light from 200 rib waveguides (in a manner similar to that of sample 1). We will present the measured outcoupling efficiencies for this experiment later. The number of outcoupled modes and their respective angles for this case were also in agreement with the predicted values of Fig. 3.6. The maximum outcoupled angle for sample 2 was the same as that of sample 1, which was the result of one grating having a period twice that of the other.

One of the resultant modes outcoupled by the 2 μm grating ($m = -4$ at 71°) from 200 rib waveguides was imaged by a Fairchild CCD camera model 3000, and is shown in Fig. 5.10. In this figure, the guided modes in the rib waveguide array propagate from top to bottom. The outcoupled mode appeared as the bright rectangular region, which was the result of a highly angle sensitive outcoupled beam impinging upon the CCD camera. The bright spot above the outcoupled beam was due to the scatter of the refracted beam from the incoupling prism. The bright band across the top of the photograph was due to the reflection from the clamp holding the prism to the sample.

The above result showed that the outcoupled beam intensities were large enough to excite a CCD array. In advanced IO signal processor applications, such a two dimensional CCD array needs to be ultimately assembled upon the rib waveguide array.

We will now present the results of measured outcoupling efficiencies for the two experiments that employed sample 1 and sample 2 as was discussed earlier. The power levels in the outcoupled modes for both sample 1 and sample 2 were below levels measured for similar outcoupled modes in the slab waveguide case presented in Sect. 5.4. One possible reason for such lower power levels was that the grating heights for samples 1 and 2 were about 0.05 μm, as opposed to a grating height of 0.1 μm for the slab case. In addition, we expected larger

155
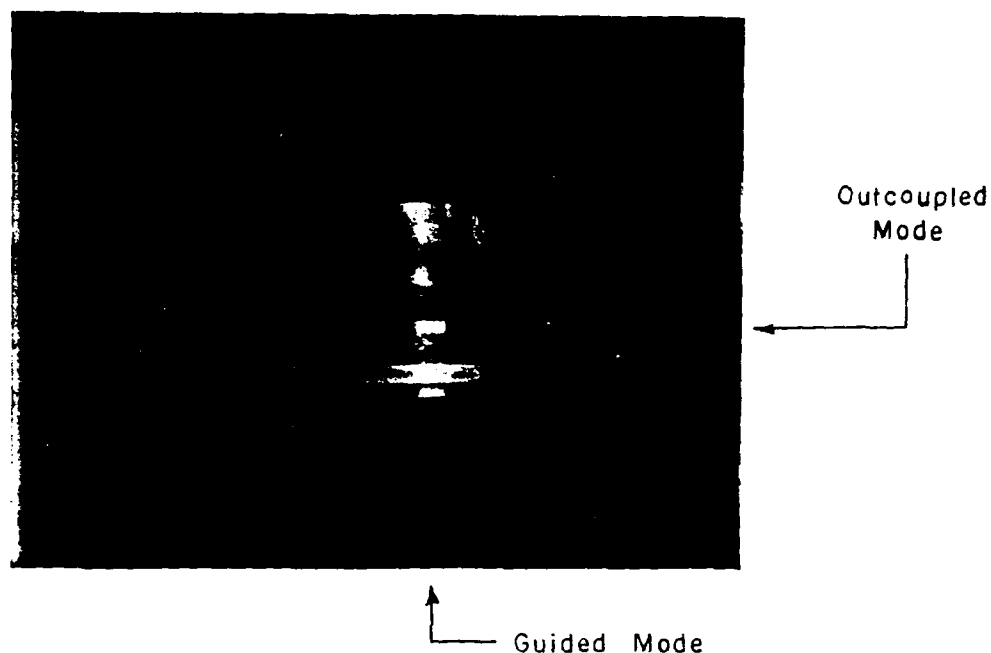
Figure 5.9: Photograph of the outcoupled mode from an array of 200 rib waveguides. A 1 mm long grating with a 4 μm period and a height of approximately 0.05 μm was used to outcouple several such modes from the rib waveguides. The rib waveguides are oriented on the substrate from top to bottom in the photograph. The grating is oriented from left to right. Note the uniformity of the outcoupled mode.
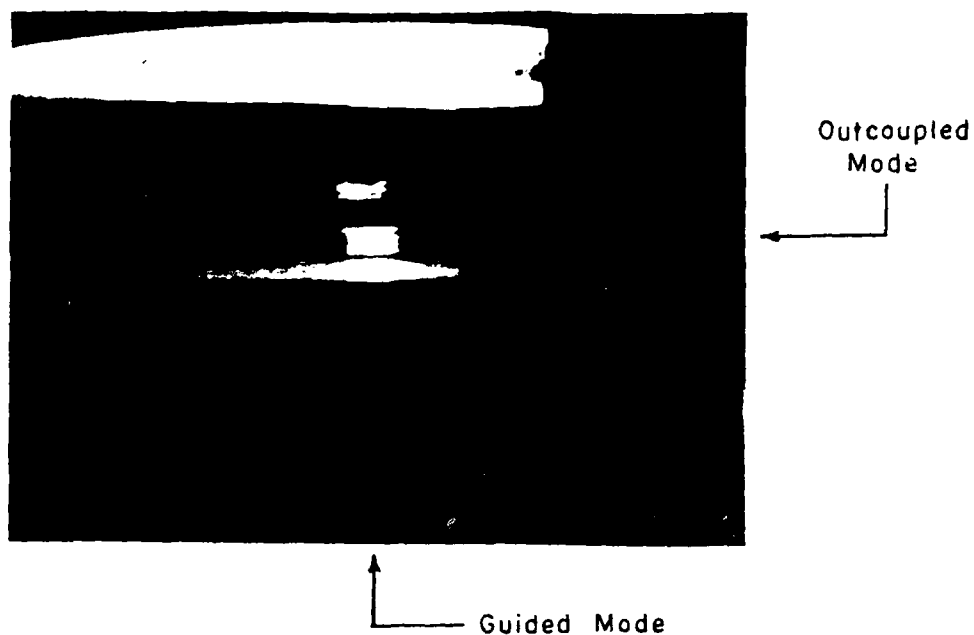
Figure 5.10: A CCD camera image of one of the modes outcoupled from an array of 200 rib waveguides by a grating with a 2 μm period (see text). The rib waveguides are oriented on the substrate from top to bottom in the photograph. The grating is oriented from left to right. Note the uniformity of the outcoupled mode.

propagation losses in the rib waveguide arrays (compared to a Ti:LiNbO$_3$ slab waveguide), which in turn causes a reduction in the available power incident upon the gratings in samples 1 and 2. The reduced power levels incident upon the gratings resulted in lower absolute outcoupled power levels.

Hence, we were only able to accurately measure the power of the outcoupled mode with the highest power for each sample. In order to estimate the incident guided mode powers for the two samples, we measured the power of the guided modes at the output ends of the rib arrays. We then accounted for the part of the guided power that was outcoupled, in addition to the part of the power reflected at the output interface.

For sample 1, the outcoupled mode ($m = -8$ at 71°) was estimated to be about 0.05 μW, and the incident power for this sample was estimated at 0.03 mW. Therefore, the outcoupling efficiency into this mode due to a 1 mm long 4 μm grating on the rib waveguide array of sample 1 was estimated at 0.2%/mm.

In Sect. 5.4, we measured the outcoupling efficiency into mode $m = -8$ due to the 4 μm grating on the slab waveguide to be about 0.01. Comparing this efficiency with that of the grating on the rib array shown above, we determined that the outcoupling efficiency due to the grating on the slab waveguide was 5 times larger than that of the rib waveguide array case.

For sample 2, the outcoupled mode ($m = -4$ at 71 °) was measured (in a manner similar to that for sample 1) to be about 0.14 μW, and the incident power was also determined to be approximately 0.03 mW. Hence, the outcoupling efficiency into this mode by the 2 μm grating on the rib waveguide array was determined to be about 0.5%/mm.

We also compared the above outcoupling efficiency to that of the mode $m = -4$ outcoupled by the 2 μm grating from the slab waveguide (which was determined to be 0.15). The comparison revealed that the outcoupling efficiency due to the slab waveguide in this case was approximately 30 times larger than

158

that of the rib waveguide case. The accuracy of the outcoupling efficiency of this mode for the slab waveguide case was in doubt, hence a second measurement was conducted yielding an outcoupling efficiency of 0.05. Therefore, the ratio of the outcoupling efficiency of the slab waveguide case to that of the rib waveguide was reduced to 10.

The height of the gratings on the rib waveguides were about 0.05 μm, as opposed to 0.1 μm for gratings on the slab. Therefore, part of the reduction in outcoupling efficiencies in the rib waveguide case can be explained by such a reduction in height. Another more important factor, however, was possibly due to changes in the shape of the gratings fabricated on the rib arrays, which were not rectangular as expected. Therefore, a better process model should be developed that accounts for the change in the shape of the fabricated grating on a rib array from the prescribed rectangular form.

In advanced IO signal processing applications, the need for grating outcoupling efficiencies that are larger than 10%/mm implies that the shape of the gratings on rib waveguide arrays should be optimized for performance by variations in height, aspect ratio and blaze. In addition, in order to improve on the outcoupling efficiency, surface gratings with submicron periods should be developed on rib waveguide arrays. The development of gratings with submicron periods will lend itself well to the idea of using the grating period as a technique of modulating the outcoupling efficiencies. This is because such gratings would greatly improve on the dynamic range of modulation, which is limited by geometry to a factor of 2 for our fabricated gratings.

Although the outcoupled beams visually appeared to be uniform, quantitative measurements of how their intensities decay along the array have not yet been determined. Such measurements are needed in order to determine the uniformity of the outcoupled modes, since such uniformities are critical for advanced IO signal processor applications.

5.6 Integrated Lenses

In this section, we will present the results of experiments conducted to determine the focal properties of the integrated lenses that were fabricated during the course of this research. In these experiments, we prism coupled two parallel TE polarized beams (1 mm separation) into the slab waveguides containing the integrated lenses. The two parallel beams were formed by putting an aperture (with two openings 0.2 mm wide) in the path of the incident collimated beam immediately before the prism.

The location behind the lens at which the two guided beams crossed revealed the focal point of such lenses. We examined the focal power of both fabricated thin film coated recessed lenses and TI lenses on TIPE waveguides (the fabrication procedures for these lenses were presented in Sect. 4.4). These results were then compared to the focal properties predicted by the theory presented in Sect. 3.3, as described in detail below.

5.6.1 Thin Film Coated Recessed Lenses

In this section, we will present the results of experiments conducted in order to determine the focal properties of thin film coated recessed lenses.

First, we coupled the two beams into the Ti:LiNbO$_3$ substrate having the TiO$_2$ coated recessed lenses with convex patterns as shown in Fig. 3.8. The recess in this lens was about 1 μm deep, and the deposited film thickness was about 0.7 μm. The two guided beams that were parallel before the lens remained parallel until the output end of the substrate, which was about 1.5 cm away from the lenses.

Theoretically, however, the two parallel guided beams should have refracted at the lens interfaces and intersected about 9 mm away from the lens (see Sect. 3.3). The fact that this type thin film coated recessed lens did not perform

as expected was likely due to the lack of a significant index gradient across the lens boundaries. The reduction in the refractive index of the thin film from the desired value was possibly due to the method of deposition.

We examined the laser power reflectivity of the top surface of the thin film of TiO_2 in order to estimate its refractive index from Eq. 3.37. This power reflection coefficient was determined to be about 0.15, which when used in Eq. 3.37 yielded a refractive index of about 2.24 for the TiO_2 thin film. The fact that this refractive index was close to that of $Ti:LiNbO_3$ (2.25) can partly explain the lack of refractive index gradient across the lens boundary. For depositing TiO_2 thin films for such lenses, we could perhaps employ the technique of ion assisted electron beam evaporation reported by Martin, *et al.*, by which they were able to achieve refractive indices as high as 2.5 [89]; other possible techniques include ion beam deposition and RF sputtering.

In another experiment, we coupled the two parallel beams into a $Ti:LiNbO_3$ substrate with a concave SiO_2 (with MgF buffer layer) coated recessed lens (the dimensions of this lens are also shown in Fig. 3.8.) The parallel guided beams again remained parallel after the lens, despite our theoretical predictions of a 2 mm focal length (see Sect. 3.3). The above result also suggested that the index gradients across the lens boundaries were not sufficient. This was a plausible possibility, since during the electron beam evaporation of SiO_2 it might have fractionated and decomposed, leaving a film of stoichiometry nearer that of SiO, which has a refractive index of 2.2. This value also is too close to that of $Ti:LiNbO_3$ to produce strong focusing.

However, SiO_2 coated recessed lenses show tremendous potential for the development of low F-number integrated lenses. Such lenses have numerous applications in advanced IO signal processing applications that require large apertures. Alternatively, integrated lenses fabricated through modifications of the proton exchange technique in $Ti:LiNbO_3$ were examined, and the results are

presented next.

5.6.2 TI lenses in TIPE Waveguides

In this section, we will present the results of experiments conducted to determine the focal properties of concave TI integrated lenses (1.25 mm radii of curvature) fabricated on TIPE slab waveguides (see Sect. 4.4.2). For this purpose, two different substrates, proton exchanged for 3 and 6 hrs, were used.

Similar to the previous lens experiments, two parallel TE polarized He-Ne beams (with a 1 mm separation) were prism coupled into the TIPE slab waveguides, and were then incident onto the TI integrated lenses in order to determine where they intersected.

We first coupled the two beams into the lowest order guided mode of the TIPE slab waveguide proton exchanged for 3 hrs; the two guided beams intersected at a distance approximately 1.2 cm away from the integrated lens, as shown in Fig. 5.11. This experimentally determined focal length was in close agreement with the calculated focal length of approximately 1.3 cm, as predicted in Sect. 3.3 for such a geometry. We then prism coupled the two parallel beams into the TIPE slab waveguide that was proton exchanged for 6 hrs, and the TI lens on this sample also focused at a distance of approximately 1.2 cm from the lens.

The slab waveguide proton exchanged for 6 hrs, however, showed high propagation losses which were large enough to render the intensity of the guided mode undetectable after 2 cm of propagation. For the case of slab waveguides proton exchanged for 3 hrs, on the other hand, the guided light did not decay significantly even after 3 cm of propagation. The propagation loss comparison, and the fact that longer proton exchange times did not produce significantly larger refractive index gradients, prompted us to limit the proton exchange times to 3 hrs for substrates that were subsequently used for the integration of elements.

162

Figure 5.11: Photograph of the focal property of a TI lens integrated in a TIPE slab waveguide (proton exchanged for 3 hrs). Two parallel beams (1 mm separation) of TE polarized He-Ne light were prism coupled into the TIPE slab waveguide from the left (exciting the lowest order mode). The TI lens is located on the slab abeam the zero marker of the scale on top. The two parallel beams were refracted after the concave integrated lens, and subsequently crossed at a point 1.2 cm from the lens.

In order to measure the throughput efficiency of a TI integrated lens in a TIPE waveguide (proton exchanged for 3 hrs), the output power of the guided mode after the integrated lens was measured. The prism-substrate setup was then translated transverse to the beam propagation direction so that the guided mode would not be incident onto the integrated lens. The output power of the guided mode was again measured in this configuration. The reduction of power from the second measurement to the first measurement yielded a throughput efficiency of about 75% (loss $\sim$ 1.3 dB). This measured throughput efficiency is 0.8 dB lower than the estimate presented in Sect. 3.5, which can be due to additional scattering from nonuniformities at the lens-slab interface. The measured throughput efficiency, however, was higher than the previously reported value of 71% for TIPE lenses fabricated in TI slab waveguides [10].

An important property observed for these lenses was that when coupling into the next higher mode of the TIPE slab waveguide, the focal length of the same TI lens was increased to 2.5 cm. This is shown in Fig. 5.12, in which the substrate and the TI lens are the same as the one shown in Fig. 5.11; however, in the case of Fig. 5.12 the next higher mode of the slab waveguide was excited.

In order to investigate the reason for the increase in the focal length, we calculated the effective refractive index of the second guided mode of the TIPE slab waveguide, and it was about 2.28. Calculation of the effective refractive index of the second order guided mode in the TI lens revealed that it was approximately the same as that of the lowest order mode in these waveguides (about 2.22). Using the second order mode effective refractive indices of the TIPE and the TI waveguides in the analysis of Sect. 3.3, it was determined that in this case the focal length of the concave lens with radii of 1.25 mm was approximately 2.5 cm, which was in close agreement with the experimental result.

In some advanced IO signal processing applications such as SAR image formation, it might be required to fabricate integrated lenses that have singular
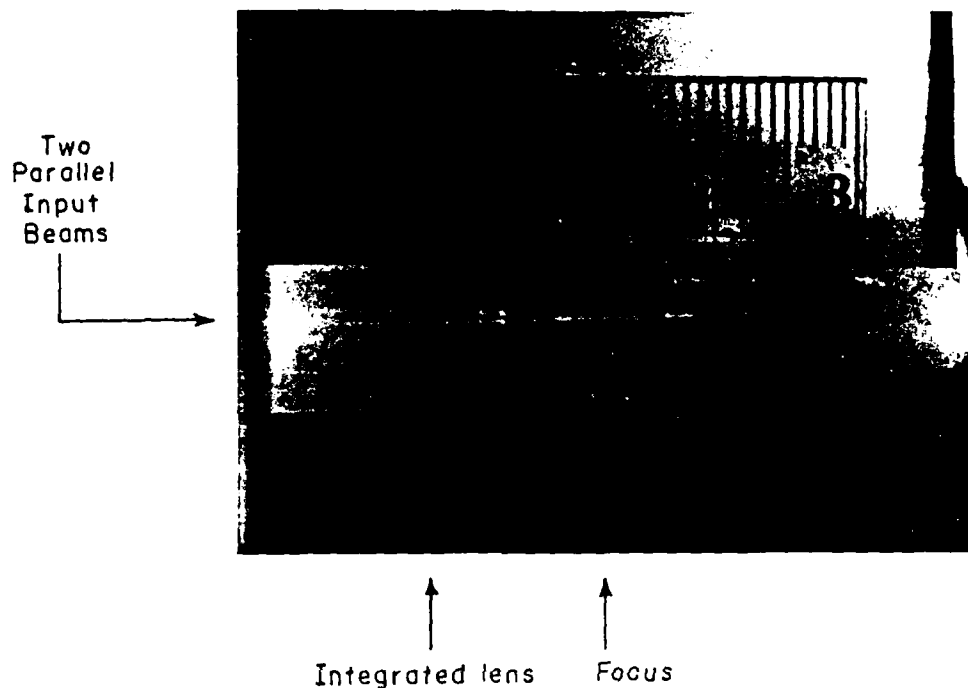
164
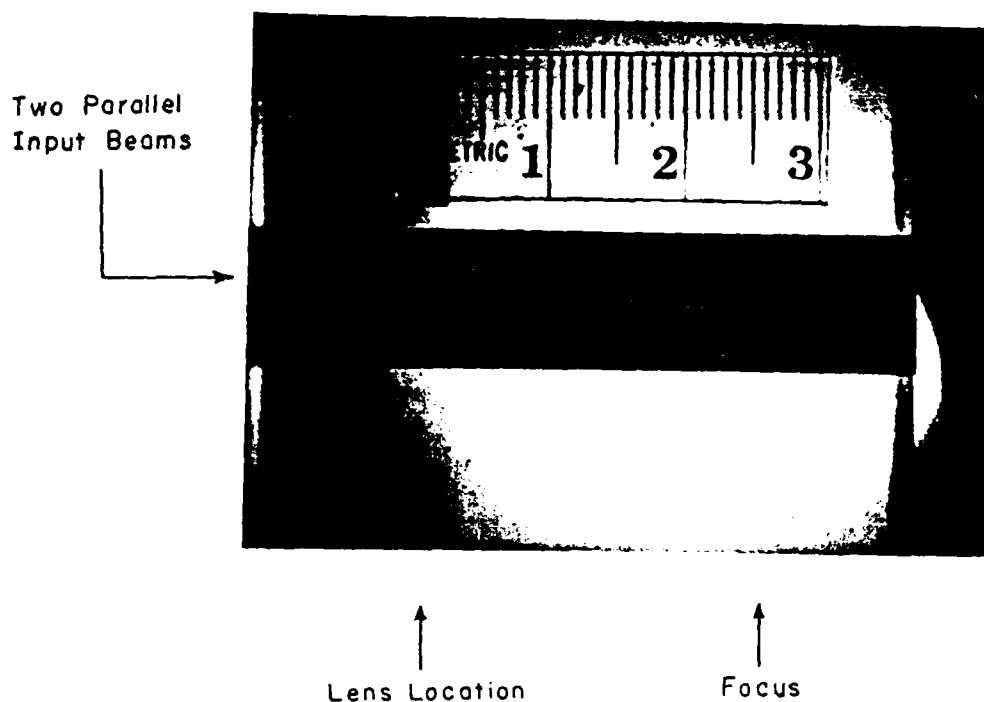
Figure 5.12: Photograph of the focal property of a TI lens integrated in a TIPE slab waveguide (proton exchanged for 3 hrs). Two parallel beams (1 mm separation) of TE polarized He-Ne light were prism coupled into the TIPE slab waveguide from the left (exciting the second order mode). The TI lens is located on the slab abeam the zero marker of the scale on top. The two parallel beams were refracted after the concave integrated lens, and subsequently crossed at a point 2.5 cm from the lens.

focal lengths. This is needed because when buttcoupling laser diodes to a TIPE substrate as used in such processors, possibly more than one guided mode will be excited, which will cause multi-focusing of the incident beam. In these situations, it is desirable to fabricate single mode TIPE slab waveguides, which can be accomplished by fabricating single mode $Ti:LiNbO_3$ waveguides followed by reduced proton exchange times. Ultimately, hybrid integrated configurations of the laser-substrate coupling geometry can be envisioned that selectively excite only a single substrate mode through the use, for example, of gradient-index (GRIN) lenses.

5.6.3   Comparison of Fabricated Lenses

The results of experiments conducted in order to determine the focal properties of the fabricated integrated lenses revealed that both types of thin film coated recessed lenses, one with a high index thin film (TiO_2) and the other with a low index thin film (SiO_2), did not produce any easily detectable focusing. It was determined that the refractive index of the TiO_2 thin film used in the fabrication of the lens was close to that of the $Ti:LiNbO_3$ substrate; hence, the index gradient was not large enough to produce observable focusing.

For the thin film coated recessed lens requiring an SiO_2 thin film, it was suggested that the actual deposited thin film was close to the stoichiometry of SiO, which again exhibited a refractive index close to that of $Ti:LiNbO_3$. However, due to the potential of fabricating low F-number large aperture integrated lenses and its implications for advanced IO signal processing applications, both TiO_2 and SiO_2 coated thin film lenses should be investigated further.

Results of experiments conducted to determine the focal properties of the fabricated TI lenses in TIPE waveguides revealed that the lenses did in fact focus the guided modes at the predicted focal lengths. It was determined that a concave (1.25 mm radii) TI lens focused the lowest order guided mode of the

TIPE slab waveguide at a distance of 1.2 cm. The same lens focused the next higher guided mode at 2.5 cm away from the lens. The reason for the increase in the focal length was due to a decrease in the effective refractive index gradient when the higher order mode of the TIPE slab waveguide was excited.

We also determined that a proton exchange time of 3 hrs provided better propagation loss performance than the 6 hrs proton exchange time without any loss in the available refractive index gradient. This made the TIPE slab waveguides proton exchanged for 3 hrs more attractive for use in the subsequent integration of elements, the results of which will be presented in the next section. Such integration provided valuable information about the focal spot size properties of the above lenses, in addition to the integration issues.

This novel configuration of TI lenses in TIPE waveguides provided a relatively easy method of fabricating integrated lenses which at the same time provided good mode confinement of the information guided in the waveguides. The use of concave lenses in this configuration also provided positive lensing, while exhibiting surface areas that were smaller than those expected for convex lenses (TIPE lenses in TI waveguides) having similar focal lengths.

In IOSAR processor and related applications, care must be taken to fabricate single mode TIPE slab waveguides in order to provide single focal lengths when TI lenses are fabricated. This can be accomplished through the fabrication of single mode titanium indiffused waveguides followed by reduced proton exchange times.

The lenses that were fabricated here suffered from aberrations because of the simple spherical design of the boundaries of the lenses. This design was chosen to simplify the production of the mask which was required to pattern such lenses. Such aberrations can be easily minimized by using masks with lens patterns that have aspherical boundaries.

5.7 Lens, Rib Array, and Grating Outcoupler Integration on the Same Substrate

In this research effort, it was essential to develop an understanding of the issues that accrue to the integration of fabricated components on the same substrate. In addition, we needed to determine if the focal spot sizes of the fabricated integrated lenses were adequate for focusing a relatively wide guided beam into individual waveguides of a large area array. Therefore, we decided to integrate TI integrated lenses and large area rib waveguide arrays with surface gratings on the same TIPE substrate.

In order to fabricate the TIPE slab waveguide, we selected two 4 cm long Ti:LiNbO$_3$ slab waveguides (which were fabricated as presented in Sect. 4.1). In the fabrication of a pair of TI integrated lenses (with the same dimensions as discussed in the previous section) on the above slab waveguides, we followed the procedure presented in Sect. 4.4.2.

We needed to locate the focal plane of the fabricated lens on the substrate as accurately as possible in order to integrate the rib waveguide array precisely at this plane. Earlier, we determined that the same TI lens exhibited two focal lengths depending on the mode that was coupled into the TIPE waveguide. Therefore, we located these focal planes by prism coupling into the appropriate mode of the above TIPE substrates.

On one substrate, we fabricated the rib waveguide array at the shorter focal length (1.2 cm), and on the other one they were fabricated at the longer focal length (2.5 cm). The rib waveguides consisted of 660 elements (with individual waveguides 8 μm wide and 1 μm high with 2 μm separations), and they were fabricated following the procedure given in Sect. 4.2.

In order to complete the integration of elements, we fabricated a 1 mm long outcoupling grating (4 μm period and 0.05 μm grating height) on the surface

of the rib waveguide array that was situated at the 1.2 cm focal plane. In the fabrication of such a surface grating, we followed the procedures explained in Sect. 4.3.2. A photograph of the resultant guided wave optical chip with the above elements is shown in Fig. 5.13. The pair of TI integrated lenses are visible close to the left edge of the TIPE substrate. In this photograph, the rib waveguide array is oriented from left to right, and the surface gratings are oriented from top to bottom close to the right edge of the substrate.

In order to use the integrated lens to focus into individual rib waveguides of the array, we prism coupled a 1 mm wide TE polarized beam into each of the fabricated chips. The schematic diagram of this experiment for the integrated chip with surface gratings on the rib waveguide array is shown in Fig. 5.14. By examining the cut end of the rib waveguide array we were able to determine the number of rib waveguides excited by the integrated lens in each case. The modes of the rib waveguides were imaged using an appropriately aligned CCD camera (with a 50X microscope objective head), which provided a magnification of about 200X making the detection of individual rib waveguides (8 μm wide with 2 μm separations) possible.

We used the integrated chip in which the array was at the 1.2 cm focal plane in the setup of Fig. 5.14, and excited the lowest order mode of the slab waveguide. The CCD camera image of the cleaved end of the rib array is shown in Fig. 5.15 which clearly shows 5 distinct rib waveguide modes (with 10 μm center to center separations).

The calculations of Sect. 3.3 showed that the focal spot size of the above integrated lens for an incident beam of 1 mm in diameter was approximately 3 μm. With this beam incident onto the above rib waveguide array, it should therefore have been possible to excite exactly one rib waveguide. The result of Fig. 5.15, however, clearly shows that 5 such rib waveguides were excited.
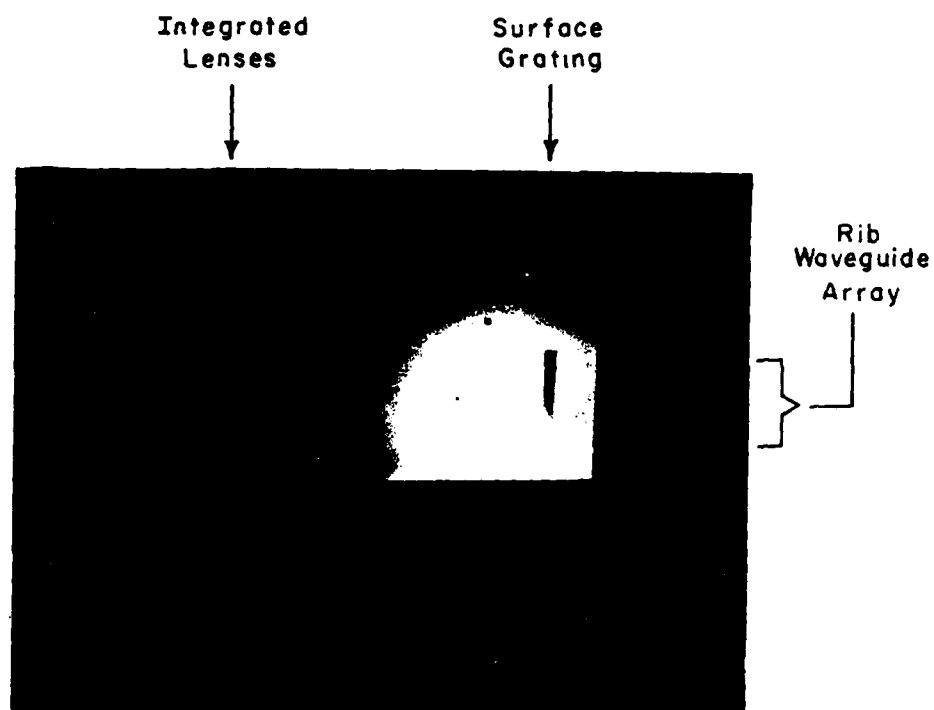
Figure 5.13: Photograph of a guided wave optical chip with integrated lenses. rib waveguide array, and surface outcoupling grating.

170
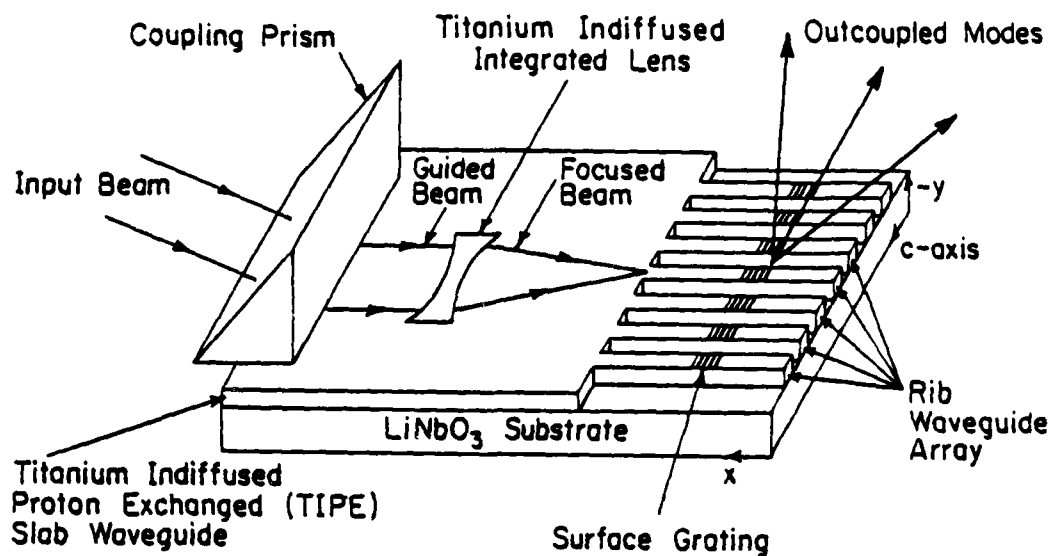
Figure 5.14: Schematic diagram of the guided wave optical chip with the following integrated IOSAR processor elements: TI lens in TIPE slab waveguide, rib waveguide array, and surface outcoupling grating. The input beam is coupled into the TIPE slab waveguide via a prism, and the guided beam is focused by the TI integrated lens into individual rib waveguides which can be observed at its cleaved end. The light guided in the rib waveguides is subsequently outcoupled by the surface grating. Note the appropriate crystallographic axes of the substrate.

Figure 5.15: CCD camera image (with 50X microscope objective head) of the cleaved end of a rib waveguide array. Shown are 5 rib waveguide modes. In this case, the rib waveguides are located at the 1.2 cm focal plane (first order guided mode) of the TI integrated lens.

The excitation of more rib waveguides than expected might have been due to the fabrication of the rib waveguide array at a plane that was not exactly on the focal plane. Considering the divergence angle of this focused beam which is about 5°, a displacement of approximately 600 μm from the focal plane could account for the excitation of 5 rib waveguides.

The individual rib waveguide modes focused into by the integrated lens were then outcoupled into the third dimension of the chip by the 4 μm surface gratings (1 mm long) on the rib arrays (see Fig. 5.14). Discrete outcoupled modes were visually observed at the expected outcoupled angles. A photograph of one of the modes outcoupled from 5 rib waveguides via the surface grating is shown in Fig. 5.16. In this photograph, the guided light propagated from left to right. The bright spot to the left of the photograph was due to scattering induced by the prism coupling. Moving to the right of the photograph, the first bright light region observed is the grating outcoupled mode, which was highly directional. Other bright bands observed in the photograph were due to scattering of the substrate modes outcoupled by the grating.

In another experiment, the TI lens on the second chip was used to focus the guided light into the rib waveguides located at the 2.5 cm focal plane. The end view CCD image of the guided mode of a single rib waveguide, as well as the weak mode of a neighboring rib waveguide excited by the integrated lens, is shown in Fig. 5.17. It is evident from Fig. 5.17 that the spot size of this fabricated TI integrated lens was in fact about 10 μm for a 1 mm wide incident beam, which agrees well with the calculated value of 7 μm.

An implication of the results of coupling into individual waveguides by the integrated lens was that such waveguides should be located at the focal plane of the integrated lens within 60 μm to prevent misfocusing into multiple rib waveguides. In addition, guided modes of such rib waveguide arrays can in fact be coupled into the plane perpendicular to the plane of the processor by surface
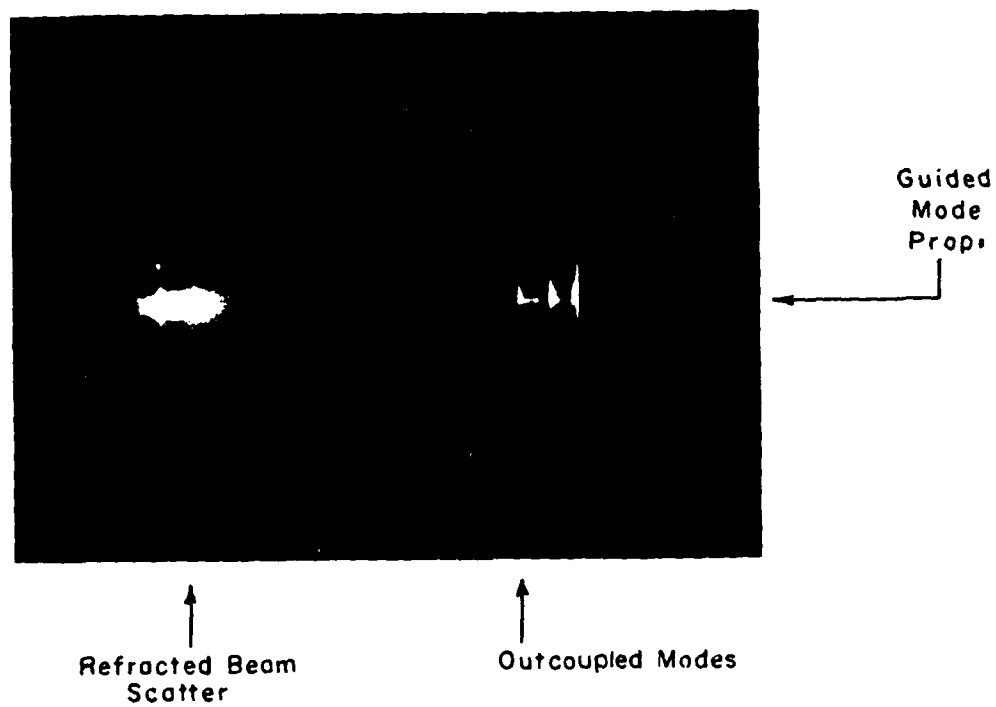
Figure 5.16: Photograph of one of the resultant outcoupled modes from 5 rib waveguides scattered by a 4 μm surface grating. These rib waveguides were excited with light focused by the integrated TI lens in the TIPE slab waveguide.
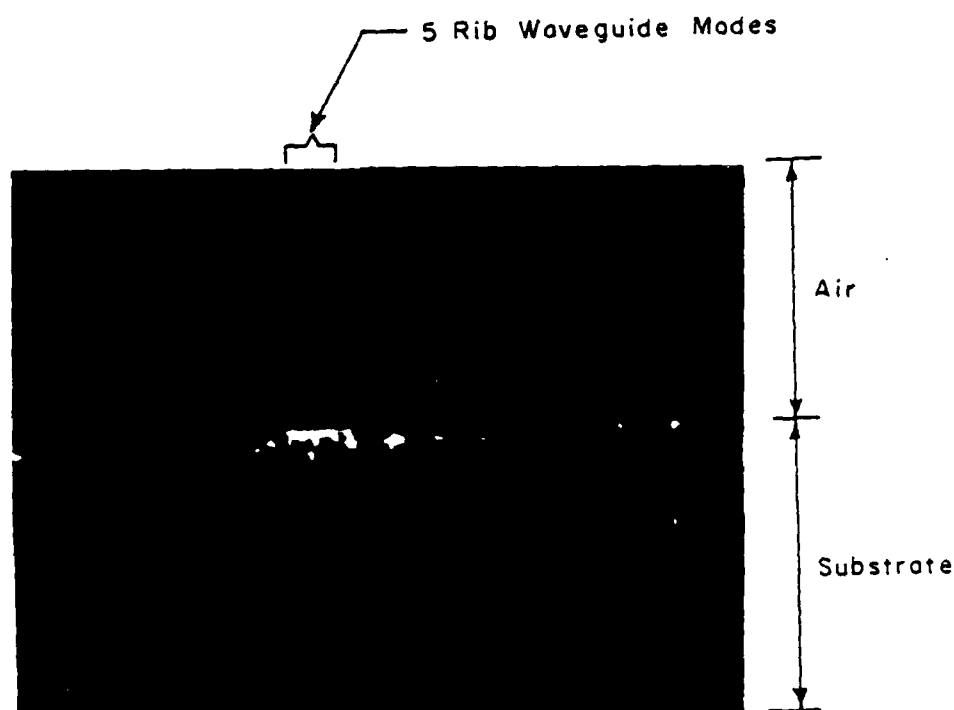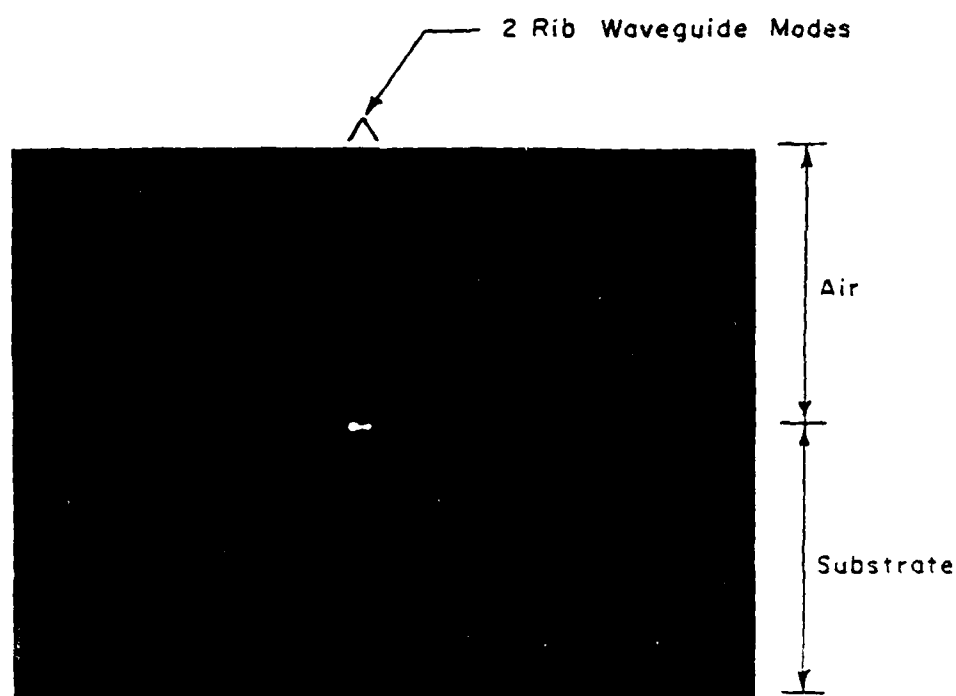
Figure 5.17: CCD camera image (with 50X microscope objective head) of the cut end of a rib waveguide array. Shown are the rib waveguide modes of a single rib: a second rib waveguide is partially excited. The rib waveguides are located at the 2.5 cm focal plane (second order guided mode) of the TI integrated lens.

gratings.

At this point in the research, we have shown that the fabricated advanced IO signal processor components performed predictably. However, further work is needed to significantly improve the performance of some of the components. For example, the propagation loss of the rib waveguide arrays should be reduced further, in order to reduce scatter and thus to increase the signal to noise performance of the IO processors. Uniform surface gratings on rib waveguide arrays should be examined using a more accurate model in order to account for the reduction in the actual outcoupling efficiencies. In addition, thin film coated recessed lenses should be investigated further as potential alternatives to TI lenses in TIPE waveguides in developing large aperture low F-number integrated lenses. Further research directions are discussed in Ch.7.

Chapter 6

IOSAR Processors

Up to this point in the dissertation, we have been concerned with the issues involved in developing components needed for advanced IO signal processors. As an immediate application we also briefly considered the IOSAR processor example (see Fig. 1.5), which can benefit from such components. In this chapter, however, we will investigate the example of the IOSAR processor more closely. We will evaluate the critical issues involved in developing such a processor using both the components that were presented here, and also other technologies that are currently available. In this investigation we will use typical radar parameters, and we will attempt to examine how variations in these parameters affect the processor configuration and design rules. Finally, a more sophisticated architecture for the IOSAR processor will be presented that can potentially overcome some of the problems associated with the preliminary architecture of Fig. 1.5.

Implementations of IOSAR processors are assumed to be fabricated on Y-cut $LiNbO_3$ substrates, since a decided advantage accrues to the use of currently available technology. In addition to $LiNbO_3$, we will also present examples for TeO_2 as an alternative material.

The use of $LiNbO_3$ allows us to integrate lenses, rib waveguide arrays, and surface grating outcouplers on the same substrate using the techniques presented herein. In addition, we need to borrow technological achievements from a wide variety of IO applications in order to fabricate input devices such as the SAW device IDT and to butt-couple the laser diode against the substrate. Finally,

in order to make the IOSAR processor complete, further research should be conducted in the hybridization of the CCD array and the mask function on the rib waveguide array.

Let us consider in the discussion that follows the example of an upchirp linear FM radar signal that has a 50 MHz bandwidth transmitted at a starting frequency (f_0) of 10 GHz. Radar pulses were assumed to have durations (τ) of 1 μsec and a transmitted pulse repetition frequency of 1 kHz (a period of 1 msec). The size of the range swath of the airborne system is assumed to be 1 km and it is flying at 170 m/sec. The time that is required for the radar signal to make one round trip across the range swath was determined to be 6.6 μsec.

The chirp rate of the above linear FM signal was determined to be 5 x 10^{13} Hz/sec. In order to determine the radar range resolution, we multiplied the chirp rate just determined by the factor π and used it as the factor B in Eq. 1.12, which yielded a range resolution of 3 m. Therefore, the number of resolvable points of the radar system was determined to be 333 by dividing the range swath by the range resolution.

In order to input the radar signal to the IOSAR processor, we need to heterodyne it to the center frequency of the SAW device (typically 400 MHz). Therefore, the range of frequencies driving the SAW IDT are from 400-450 MHz, which when divided by the surface acoustic wave velocity in LiNbO$_3$, yielded spatial frequencies of 114.7-129 lines/mm (as utilized in the example of Ch. 2). Multiplying the radar pulse duration by the SAW velocity in LiNbO$_3$ we also obtained an index modulation length of 3.5 mm.

During the time that the radar pulse is applied to the SAW IDT, surface acoustic waves emanate from the IDT and propagate across the processor. Thus, we must allow enough aperture for the radar signal to cover the required range swath and resolution. Hence, the total time that the processor should be capable of handling is 1 μsec plus 6.6 μsec, or 7.6 μsec. Therefore, the product

178

of this time with the SAW velocity in LiNbO$_3$ (v_α of 3488 m/sec) yields the maximum required processor (and integrated lens aperture) width needed for full processing of the radar signal. This width for our example is about 2.7 cm. Such widths are within the capabilities of integrated lens fabrication currently available.

The size of the integrated lens determined above, in addition to the spatial frequencies and the modulation length determined earlier in this chapter are equal to the values used in the example given in Sect. 2.1. Therefore, the analysis of that section directly applies to the example given here, which means that this processor is capable of resolving approximately 333 points. In other words, the full range and swath of such a radar signal processor can theoretically be processed by the IOSAR processor.

In applications such as spaceborne radars that require large swath sizes (larger than a few kilometers) and large pulse durations (larger than a few microseconds), direct processing of the signals input by SAW transducers are impractical. However, using pulse compression and bandwidth expansion techniques common to signal processing, the return signals from such radars can be preprocessed and then used in the IOSAR processors.

Since the high surface acoustic wave velocity of LiNbO$_3$ is not suitable for some applications of SAR processing, let us consider TeO$_2$ ($v_\alpha = 620$ m/s) as a potential substrate for applications requiring large time delays. This consideration is despite the fact that the methods of fabricating waveguides and integrated lenses in TeO$_2$ are not well established.

This material suffers from a relatively high acoustooptic propagation loss of 90 dB/cm GHz^2 (compared to that of LiNbO$_3$ which is about 2.6 dB/cm GHz^2) [93]. Therefore, in order to keep such losses low we will consider an acoustooptic frequency of 100 MHz which translates into a propagation loss of 1.8 dB/cm. In addition, the aperture size of the integrated lens is assumed to be 1 cm, which

179

yields a nonuniformity across the input aperture of 1.8 dB.

We used the radar parameters of the example given at the beginning of this chapter (a 50 MHz bandwidth and a pulse duration of 1 μsec) to determine a spatial bandwidth and record length in TeO_2 of 80.6 lines/mm and 0.6 mm, respectively. The focal length of the frequency chirp in this material (which has a refractive index of 2.2) when driven by this radar signal was approximated from Eq. 2.3 to be about 2.6 cm. The number of resolvable spots was determined from the above parameters and a 1 cm wide lens in Eq. 2.10 to be 758. Although this number looks attractive, using the appropriate parameters (and a temporal frequency of 100 MHz) in Eq. 2.11 we determined that there is a complete overlap between the undiffracted mode and the region of the waveguide array. This problem may be rectified by using a downchirp FM signal which allows the removal of undiffracted orders before the waveguide array.

Another interesting method of inputing radar signals into IOSAR processors that needs to be investigated further is the electrooptic modulator array discussed earlier. In Sect. 2.5, we determined that for a specific geometry the processor capability can be increased to 1175 resolvable points. Therefore, for the radar parameters used in the example given at the beginning of this chapter, in an electrooptic modulator array configuration, the processor can accommodate swath sizes of approximately 1175 x 3 m, or about 3.5 km.

Up to this point in this chapter, we have concentrated on the front end of the IOSAR processors, $i.e.$, the portion of the processor that performs the range compression. Next, in this chapter, the results of considerations pertaining the other end of the processor that performs the azimuth compression will be presented.

The mask used in IOSAR processors contains the doppler phase history of the azimuth function as shown in Fig. 1.9. In addition, such masks can be modified appropriately in order to account for possible phase anomalies in the

180

reference signal and the range signal that could exist at the input end of the waveguide array.

The range focused signal that is outcoupled from the waveguide array and multiplied by the above mask function is then time integrated by the CCD array. Since the saturation energy density of the CCD array is of order 1.5×10^{-7} J/cm^2, and the array area size is 1 cm^2, therefore, the total saturation energy of the array needed for a full dynamic range is 1.5×10^{-7} J. The number of integration steps is equal to the number of CCD elements along each waveguide (about 1000). Therefore, the total saturation energy per integration step is 1.5×10^{-10} J.

Let us now determine the peak power required for the laser diode for the example of the IOSAR processor. The pulsed laser diode should provide enough power to compensate for losses in the processor and also saturate the CCD array. In Sect. 3.5, we estimated a total throughput loss in the IOSAR processor of about 20 dB. This loss is due to propagation, surface acoustic wave diffraction, and interfaces in the processor. In calculating this loss we assumed that the total outcoupling efficiency due to the surface outcouplers is 100%.

In IOSAR processor applications, the laser diode is pulsed for short durations (for example 20 nsec) so that the surface acoustic wave is effectively frozen in time in order to prevent range smearing. Using such pulse durations, the peak saturation power needed for the CCD array was therefore determined to be 7.5 mW. Considering the total throughput loss of the IOSAR processor, the peak power requirement of the laser diode is approximately 750 mW. Since the laser diode in most advanced IO processors with SAW input transducers is pulsed, the required average laser diode power is lower than the peak power. For example, the derating factor due to pulse mode operation in our example is determined from the ratio of the laser diode pulse duration (20 ns) to the pulse repetition period (1 ms) which yields 2×10^{-5}. Hence, the average power requirement

for our example is about 0.015 mW, which is easily attainable from laser diodes that are currently available. Developing lo er F-number lenses will significantly reduce the propagation losses of the system which in turn will reduce the peak power requirements.

A critical issue in image formation on the CCD array of the IOSAR processor (that was refered to earlier in passing), is bias buildup on the CCD array (see Eq. 1.11), which can reduce both the image fidelity and the dynamic range. The bias terms consist of a reference dependent pedestal term which is ideally uniform over the entire CCD array, and other -ignal dependent terms present in the range bins (rib waveguides) [35]. Therefore, for efficient removal of the bias terms, the center frequency of the reference wave is chosen such that it is higher than the center frequency of the SAW device by the bandwidth of the radar signal [28].

A modified IOSAR processor archit .ure is proposed in Fig. 6.1 which can ideally correct for the bias buildup. In this modified version of the IOSAR processor the function of the laser diode, integrated lenses, and the surface acoustic wave device is similar to the original architecture of Fig. 1.5.

A major difference between the original architecture and the modified version is the use of a secondary rib waveguide array and a secondary CCD array (without the mask function) to determine the bias level. In addition, the refractive index of a strip of the substrate after the focusing lens is modified such that it acts as an integrated beam splitter. This beam splitter causes focusing of the range processed information into the primary and the secondary rib waveguide arrays.

The functions of the primary rib waveguide array, its associated mask, and the CCD array are the same as those of the unmodified IOSAR processor. The bias determination is accomplished by reflecting part of the range focused signal into the secondary rib waveguide array, followed by time integrating the out-

secondary rib waveguide
array for bias determination

integrated
beam splitter

rib waveguide
array

laser
diode

L_1

L_2

rib waveguide
for undiffracted
order removal

SAW
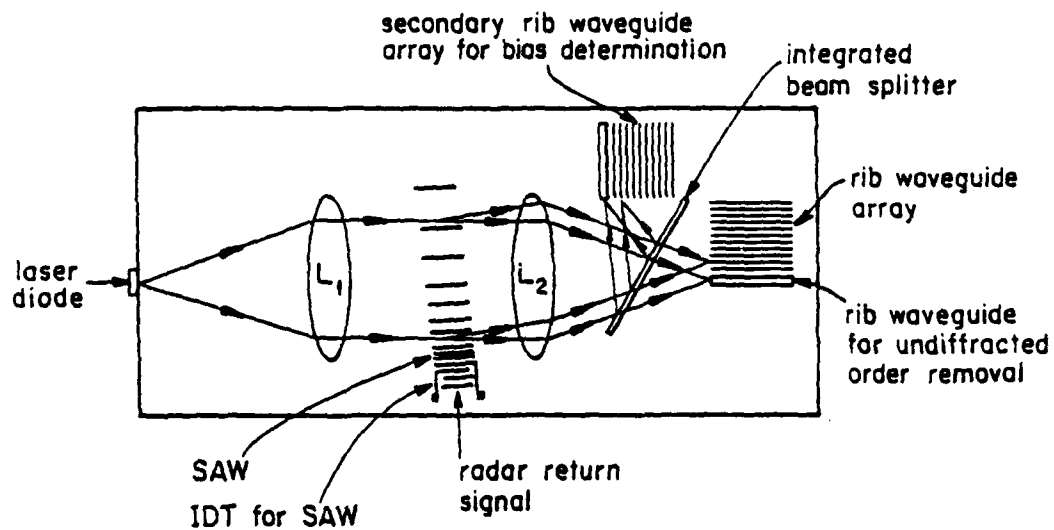
IDT for SAW

radar return
signal

Figure 6.1: Modified version of the IOSAR processor architecture which can correct for bias buildup. A secondary rib waveguide array with surface outcoupler is used to excite a secondary CCD array to determine the bias (see text). A wide rib waveguide is used to remove the undiffracted order. Other components are similar to the preliminary IOSAR architecture.

coupled light from the array that is incident on a secondary CCD array. The bias is then removed by the direct subtraction technique [35].

Differences in the illumination levels of the two CCD arrays can be corrected by varying the gain of the video signals from the CCD arrays. In the modified IOSAR processor architecture of Fig. 6.1, we also show a relatively wide rib waveguide that is used to efficiently capture the undiffracted order.

In some applications that require a relatively modest number of rib waveguides, the bias determination can be accomplished by using alternating rib waveguides in the original array for this purpose. In order to perform this task, the range focused beam in the IOSAR processor is focused into two neighboring rib waveguides, instead of one rib waveguide in the original architecture. Surface grating outcouplers on both of the neighboring waveguides outcouple light from both such waveguides. The mask containing the algorithm-defining function is mounted on the surface of one of the above rib waveguides. The CCD array, however, covers both waveguides. The signals generated from the rib waveguide without the mask determine the bias level, while the signals from the rib waveguide with the mask determine the azimuth information. These two signals are then subtracted electronically in order to remove the bias signal.

Possibilities of employing new algorithms in integrated form to process SAR signals should be investigated further. One such possibility is the joint collinear interferometric configuration analyzed by Daniel, which can improve the bias buildup problem, and in addition allows for wider range swaths to be accommodated [94].

Chapter 7

Conclusions

7.1 Summary

In this research effort we have studied the theoretical and technological feasibility of developing advanced integrated optical components needed for multidimensional signal processing applications. An example of such an application is the Integrated Optical Synthetic Aperture Radar (IOSAR) processor architecture, which could immediately benefit from these advanced components. Large arrays of densely packed waveguides that exhibit low crosstalk and low propagation losses were among the more important components considered. Such waveguide arrays can be used in multi-dimensional IO processing applications to dissect the partially processed information (*i.e.* range information for the IOSAR processor example) and expand it along the plane of the processor.

We investigated both Ti:LiNbO$_3$ channel waveguides and rib waveguides as possible candidates for use in waveguide arrays with the requirements presented earlier. Rib waveguides were determined to have better mode confinement and hence have potentially lower crosstalk in an array configuration. The above conclusion led us to fabricate highly uniform rib waveguide arrays (660 guides, 8 μm wide, 1 μm high, 2 μm separations, and 1 cm long) on Ti:LiNbO$_3$ substrates. The number of waveguides in the array with the same pitch can easily be extended to 1000 elements in order to match currently available CCD arrays. The fabrication of such rib waveguide arrays was accomplished through

185

the selective ion beam milling of $LiNbO_3$ substrates. Standard photoresist was photolithographically patterned and used as the mask for the ion beam milling process. The photoresist mask was hard baked (140 °C for 2 hrs) in order to harden it sufficiently to allow for suitably deep ion beam milling processes.

The above rib waveguide widths and separations were chosen so that the waveguide separation matches the typical CCD pixel separation of 10 μm. In order to examine the guiding properties of the rib waveguide arrays, we conducted coupling experiments that revealed propagation losses of better than 6 dB/cm for such arrays.

In order to expand the processing capability of IO processors, the information confined to the waveguide array needs to be selectively outcoupled in order to access the third dimension of the processor for further processing. Hence, uniform outcouplers on the surface of the waveguide arrays were essential in order to accomplish the above task. The required outcoupling efficiencies of the surface outcouplers are determined by the application at hand. For the IOSAR processor example, such efficiencies are required to be approximately 10-100 %/mm. This requirement stems from the fact that in the IOSAR processor application, 1 cm long CCD arrays (of 1000 x 1000 elements) are hybridized on top of the waveguide array for imaging purposes, and hence outcoupling efficiencies of this magnitude can be employed to ensure significant but uniform illumination along the entire length of the waveguide array.

We considered both thin film outcoupling and surface grating outcoupling techniques from the waveguide arrays, and the former technique was determined to be less practical than the latter technique. This was primarily due to the fact that grating outcouplers provide added flexibility: control of the outcoupling efficiency of each pixel, through control of the grating period or aspect ratio at constant grating height. This flexibility is particularly appropriate for the IOSAR processor example, since the outcoupling efficiency will require compen-

sation for any guided mode decay along the rib waveguides.

Highly uniform surface gratings were fabricated on the nonuniform surface of the rib waveguide arrays through the ion beam milling technique. The grating pattern was first generated within a photoresist coating on the rib waveguides. The grating patterns were generated both holographically and by contact mask exposure. The surface uniformities of patterns made by the latter technique were far superior to those of the former. Uniform surface gratings (patterned by a contact mask) with 2 μm and 4 μm periods (aspect ratios 0.2-0.3) that were 1 mm long and 0.05 μm high were fabricated on rib waveguide arrays. In addition, 0.1 μm high gratings with the same periods and lengths were fabricated on a Ti:LiNbO$_3$ slab waveguide.

The surface gratings on the Ti:LiNbO$_3$ slab waveguide were employed in order to examine the outcoupling properties of low modulation surface gratings. The number of outcoupled modes and their respective outcoupling angles at both fabricated grating periods were in close agreement with the theoretical predictions. Experimentally determined outcoupling efficiencies for the gratings on slab waveguides revealed that they are generally lower than the theoretical calculations. For the 2 μm grating, the outcoupling efficiencies were 1 - 0.12 times the expected values (for $m = -5$ to $m = -9$), and for the 4 μm grating they were 0.5 - 0.04 times the expected values (for $m = -8$ to $m = -14$). Hence, higher order modes produced much lower outcoupling efficiencies than expected. We believe this to be due to rounding of the grating corners, which in turn de-emphasizes the higher orders of gratings.

Results for fabricated grating outcouplers on rib waveguide arrays revealed that their outcoupling efficiencies were even lower than those of the appropriate modes on the slab waveguide case (by a factor of 5 - 10). Part of this reduction (up to a factor of 4) can be explained by the reduced grating heights used for the rib waveguide array cases.

Other critical components that can benefit both currently existing IO processors and advanced versions include large aperture integrated lenses with short focal lengths. Such lenses are especially needed in order to adjust the dimensions characteristic of advanced IO processors. The large apertures of such lenses are needed in order to allow processing of a large number of resolvable spots.

We investigated the development of large aperture (0.25 cm) integrated lenses with short focal lengths (1-3 cm) in LiNbO$_3$. First we examined the development of thin film coated recessed lenses. These included both TiO$_2$ coated recessed integrated lenses and SiO$_2$ coated recessed lenses (with a MgF buffer layer). In this technique, a lens shaped region of the Ti:LiNbO$_3$ waveguide is replaced with either a higher refractive index (TiO$_2$) or a lower refractive index (SiO$_2$) thin film.

Experiments did not produce conclusive evidence of focusing by either of the above architectures for integrated lenses. We speculate that the reason for this behavior is that the refractive indices of the thin films deposited in the recessed lens regions were either lower than expected (for TiO$_x$ thin films) or higher than expected (for SiO$_x$ with an index of about 2.2) which in either case could produce very large focal lengths. In the case of the multi-film coated recessed lens (SiO$_2$ and MgF thin films), the complexity of the structure used could also have a bearing on why such integrated lenses did not perform as expected.

The above results prompted us to investigate the titanium indiffused proton exchanged (TIPE), technique which has been developed by others as a means of index modification for Ti:LiNbO$_3$. We used a modification of the above technique to increase the refractive index of the slab waveguides while maintaining the desired lens region at the lower refractive index of Ti:LiNbO$_3$. In this technique, we protected the desired lens pattern (1.25 mm radii with a 2.5 mm wide aperture) with a thin film of SiO$_2$ while proton exchanging the substrate. The increase in the refractive index of TIPE slab waveguide compared to that of the

188

Ti:LiNbO$_3$ lens region combined with the concave lens pattern produces positive lensing.

Collimated guided modes of TIPE slab waveguides with similar integrated lenses on them were excited. The collimated modes were focused at two distinct focal lengths by the same integrated lens depending on the particular mode that was excited. The first order mode was focused at 1.2 cm (F-number $\sim$ 4.8), and the focal length of the second order mode increased to 2.5 cm (F-number $\sim$ 10). This increase in focal length is observed because the change in the effective refractive indices from the lowest guided mode to the next in our TIPE waveguide is larger than the change in similar effective refractive indices for the TI waveguide case. Therefore, the lowest order mode experiences a larger index gradient compared to the next higher mode.

The lenses that we fabricated through a modification of the TIPE technique have several advantages over the TIPE lenses fabricated by other investigators. Relative ease of fabrication is achieved by using an electron beam evaporated SiO$_2$ thin film as the proton exchange mask instead of the plasma chemical vapor deposited (CVD) Si$_3$N$_4$ thin film used by others (which is more difficult to deposit, pattern and finally remove). Other investigators have used this mask to cover the slab waveguide region while leaving an opening with the shape of the lens to allow for the proton exchange process. Following the proton exchange process, it is then necessary to remove the Si$_3$N$_4$ thin film. In our technique, however, the SiO$_2$ mask covering the TI integrated lens could be left on the substrate without significant perturbation to the performance of the lens.

Since the Ti:LiNbO$_3$ slab waveguide was proton exchanged, the refractive index of the slab waveguides was further increased, providing even better mode confinement. This configuration in which a higher refractive index surrounds a lower refractive index integrated lens allows the use of concave boundaries, which in turn reduces the surface area of such a lens when compared to the

surface area of a convex TIPE integrated lens having a similar focal length. The throughput efficiency of one of our integrated lenses was measured to be about 75%, which is higher than the 71% throughput efficiency measured for the TIPE lenses used by others.

We also integrated all of the components reported so far that performed satisfactorily on the same substrate in order to examine their coupling interaction. The components consisted of rib waveguide arrays with associated surface outcoupling gratings and TI integrated lenses (which required a TIPE substrate). The integrated lenses were used in coupling 1 mm wide beams into individual rib waveguides (8 μm wide) which showed that the diffraction limited beam sizes at the focal planes of such lenses were less than 10 μm as expected. The modes excited in individual rib waveguides by focused beams were subsequently outcoupled successfully from the guides by the associated surface gratings.

The above studies revealed that at this stage, the new components that have been developed here perform as expected, and that they can potentially be used for advanced integrated optical signal processors. For example, the development of the IOSAR processor can readily benefit from such components and their integration. However, in this example the use of LiNbO$_3$ (which has a high surface acoustic velocity) as the primary substrate combined with the SAW method of inputing the signal causes several limitations in the performance of the processor such as lowering the range resolution or reducing the range swath size.

7.2   Future Research Directions

In this research program we developed and characterized a number of critical components for advanced IO signal processors; however, the work is by no means complete. More work is needed in further characterizing the above elements, and

also investigating related issues that are important for the IOSAR processor example such as hybridization of the imaging CCD arrays on top of the rib waveguide arrays.

We have not as yet determined the crosstalk between the neighboring rib waveguides quantitatively, and this is a task which needs to be investigated. This can be accomplished by fiber coupling into individual rib waveguides, and determining the beam profiles of neighboring rib waveguides that are in close proximity. This study should also shed light on the coupling coefficients between the neighboring rib waveguides due to mode overlap and scattering. There is need for fabricating rib waveguide arrays with higher sidewalls. Such rib waveguides should be fabricated and also analyzed for scattering.

Outcoupling efficiencies due to surface gratings should be measured more accurately. In addition, the uniformity of outcoupling by surface gratings on rib waveguides needs to be studied further. Specifically, the outcoupled beam profiles along rib waveguides need to be studied in order to determine the decay rates of such beams. Also, outcoupled mode profiles of surface gratings with a decreasing spacing along the rib waveguides should be examined to determine whether such increases can compensate for the decay of the guided beams. The unwanted scattering from such gratings must also be analyzed quantitatively in order to develop a better understanding of the background noise generated in hybrid-coupled CCD arrays.

The diffraction limited spot sizes of larger aperture TI integrated lenses in TIPE waveguides need to be examined at their focal planes in order to determine accurately if they are capable of exciting individual rib waveguides. These lenses also must be corrected for spherical aberrations.

Two dimensional CCD arrays and mask functions can be mounted on the surface of rib waveguide arrays with associated surface outcoupling gratings, in order to determine the charge buildup due to background noise, and also

to perform the time integration correlations by using appropriately modulated input light and mask functions.

In some applications such as IOSAR processors, it is desirable to replace the use of surface acoustic wave devices for inputing the signal. We propose the investigation of electrooptic modulators as a means by which signals can be input to such processors, which eliminates the need for SAW devices. In addition to the other techniques of inputing signals, new algorithms and the possibility of their implementation in integrated form should be investigated. One such algorithm is that employed in the joint collinear interferometric configuration, which can improve the swath sizes that can be processed.

One can clearly envision the development of monolithically integrated advanced IO signal processors in III-V compounds such as GaAs in the near future. In such processors, outcoupling elements can ultimately be programmable, providing highly desirable dynamic system flexibility.

References

[1] R. S. Weis and T. K. Gaylord. Lithium Niobate: Summary of Physical Properties and Crystal Structure. *Appl. Phys. A*, (37):191–203, 1985.

[2] W. K. Burns, P. H. Klein, E. J. West, and L. E. Plew. Ti Diffusion in Ti:LiNbO$_3$ Planar and Channel Optical Waveguides. *J. Appl. Phys.*, 50(10):6175–6182, 1979.

[3] H. Jerominek, R. Trembloy, and Z. Opilski. Optical Waveguide Formed in Y-cut LiNbO$_3$ Crystals by Ti Indiffusion in Stationary Air Atmosphere. *Optica Applicata*, XIV(3):365–373, 1984.

[4] S. Sriram, T. Waiss, K. Rastani, S. W. McCahon, and A. R. Tanguay, Jr. Integrated Optical Devices in Lithium Niobate. *O-E LASE' 86, SPIE First Annual Symposium*, 1986.

[5] M. Minakata, S. Saito, and M. Shibata. Two Dimensional Distribution of Refractive-Index in Ti-Diffused Strip Waveguides. *J. Appl. Phys.*, 5(50):3063–3067, 1979.

[6] R. V. Schmidt and I. P. Kaminow. Metal-Diffused Optical Waveguides in LiNbO$_3$. *Appl. Phys. Lett.*, 25(8):458–460, 1974.

[7] A. C. G. Nutt and E. Sudo. Simple Control of Ti-Diffused LiNbO$_3$ Waveguide Profile and Propagation Characteristics. *Electron. Lett.*, 24(1):56–58, 1988.

[8] C. S. Tsai. Guided-Wave Acoustooptic Bragg Modulator for Wide Band Integrated-Optic Communication and Signal Processing. *IEEE Trans. Circuits Syst.*, CAS-26:1072–1098, 1974.

[9] T. Suhara and H. Nishihara. Integrated Optics Components and Devices Using Periodic Structures. *IEEE J. Quantum Electron.*, QE-22(6):845–867, 1986.

[10] D. Y. Zang and C. S. Tsai. Single-Mode Waveguide Microlenses and Microlens Arrays Fabrication in LiNbO$_3$ Using Titanium Indiffused Proton Exchange Technique. *Appl. Phys. Lett.*, 46(8):703-705, 1985.

[11] C. S. Tsai, D. Y. Zang, and P. Le. Acousto-optic Bragg Diffraction in a LiNbO$_3$ Channel-Planar Composite Waveguide with Application to Optical Computing. *Appl. Phys. Lett.*, 47(6):549-551, 1985.

[12] C. L. Chang and C. S. Tsai. Electro-optic Analog-to-Digital Converter Using Channel Waveguide Fabry-Perot Modulator Array. *Appl. Phys. Lett.*, 43(1):22-24, 1983.

[13] C. M. Verber. Integrated Optical Approaches to Signal and Data Processing. *Proc. National Aerospace and Electronics Conference (NAECON 84) Dayton, Ohio*, May, 1984.

[14] C. M. Verber, R. P. Kenan, and J. R. Busch. Correlator Based on an Integrated Optical Spatial Light Modulator. *Appl. Opt.*, 20:1626-1629, 1981.

[15] T. Thylen and L. Stensland. Electrooptic Approach to an Integrated Optics Spectrum Analyzer. *Appl. Opt.*, 20:1825-1832, 1981.

[16] I. W. Yao and C. S. Tsai. A Time-Integrating Correlator Using Guided-Wave Acoustooptic Interactions. *IEEE Symp. on Real-Time Signal Processing*, 87-90, 1978. IEEE Cat. 78CH1344-1SU.

[17] E. Voges and A. Neyer. Integrated-Optic Devices on LiNbO$_3$ for Optical Communication. *J. of Lightwave Tech.*, LT-5(9):1229-1238, 1987.

[18] T. Suhara, T. Shiono, H. Nishihara, and J. Koyama. An Integrated-Optic Fourier Processor Using an Acoustooptic Deflector and Fresnel Lenses in an As$_2$S$_3$ Waveguide. *J. of Lightwave Tech.*, LT-1(4):624-629, 1983.

[19] T. Bicknell, D. Psaltis, and A. R. Tanguay, Jr. Integrated Optical Synthetic Aperture Radar Processor. *1985 Annual Meeting of the Optical Society of America, Washington, D.C.*, 1985.

[20] T. Bicknell, D. Psaltis, and A. R. Tanguay, Jr. Integrated Optical Synthetic Aperture Radar Processor. *J. Opt. Soc. Am. A*, 2(13):8, 1985.

[21] S. Y. Huang and S. H. Lee. Blazed Grating Couplers on LiNbO$_3$ Optical Channel Waveguides and their Applications to Integrated Optical Circuits. *J. Lightwave Tech.*, LT-4(9):3155–3161, 1986.

[22] D. W. Vahey, R. P. Kenan, and W. K. Burns. Effects of Anisotropic and Curvature Losses on the Operation of Geodesic Lenses in Ti:LiNbO$_3$ Waveguides. *Appl. Opt.*, 19(2):270–275, 1980.

[23] T. Suhara, K. Kobayashi, H. Nishihara, and J. Koyama. Graded-Index Fresnel Lenses for Integrated Optics. *Appl. Opt.*, 21(11):1966–1971, 1982.

[24] D. B. Anderson, R. L. Davis, J. T. Boyd, and R. R. August. Comparison of Optical Waveguide Lens Technologies. *IEEE J. Quantum Electron.*, QE-13(4):275–282, 1977.

[25] J. J. Kovaly. *Synthetic Aperture Radar.* Artech House, Inc., 1976.

[26] C. D. Daniel. Concepts and Techniques for Real-Time Optical Synthetic Aperture Radar Data Processing. *IEE Proceedings,*, 133(1):7–25, 1986.

[27] D. Psaltis. Two Dimensional Optical Processing Using One Dimensional Input Transducers. *Proc. IEEE*, 72:962–974, 1984.

[28] D. Psaltis and K. Wagner. Real-Time Synthetic Aperture Radar (SAR) Processor. *Opt. Eng.*, 21:822–828, 1982.

[29] D. Psaltis, M. Haney, and K. Wagner. Real Time Synthetic Aperture Radar Processing. *Proc. NASA Conference on Optical Information Procesing for Aerospace Applications.II*, 1983. Langley, Virginia.

[30] I. Abramov, Y. Owechko, A. R. Tanguay, Jr., and T. J. Bicknell. Real Time Synthetic Aperture Image Formation Utilizing an Electrooptic Spatial Light Modulator. *Proc. NASA Spaceborne Imaging Radar Symposium, Jet Propulsion Laboratory Publication*, (83-11), 1983.

[31] V. Hinkov. Proton Exchanged Waveguides for Surface Acoustic Waves on LiNbO$_3$. *J. Appl. Phys.*, 62(9):3573–3578, 1987.

[32] L. P. Solie. Surface Acoustic Wave Velocities for Two Metal Layers on Lithium Niobate and Bismuth Germanium Oxide Substrates. *IEEE Tran. Sonics and Ultrasonics*, SU-20(4):379–382, 1973.

[33] E. Kapon and R. Bhat. Low-Loss Single-Mode GaAs/AlGaAs Optical Waveguides Grown by Organometallic Vapor Phase Epitaxy. *Appl. Opt.*, 50(23):1628–1630, 1985.

[34] W. L. Emkey. Optical Coupling Between Single-Mode Semiconductor Lasers and Strip Waveguides. *J. of Lightwave Tech.*, LT-1(2):436–443, 1983.

[35] M. W. Haney. *Acousto-Optical Time-and-Space Integration Processors for Real-Time Synthetic Aperture Radar Imaging.* Ph.D. Dissertation, California Institute of Technology, 1986.

[36] K. Creath. Interferometric Investigation of a Diode Laser Source. *Appl. Opt.*, 24(9):1291–1293, 1985.

[37] S. Fouchet, A. Carenco, C. Daguet, R. Guglielmi, and L. Riviere. Wavelength Dispersion of Ti Induced Refractive Index Change in LiNbO$_3$ as a Function of Diffusion Parameters. *J. of Lightwave Tech.*, LT-5(5):700–708, 1987.

[38] R. V. Johnson, D. L. Hecht, R. A. Sprague, L. N. Flores, D. A. Steinmetz, and W. D. Turner. Characteristics of the Linear Array Total Internal Reflection (TIR) Electrooptic Spatial Light Modulator for Optical Information Processing. *Opt. Eng.*, 22(6):665–674, 1983.

[39] C. H. Von Helmolt. Integrated Optic Strip Waveguide Phase Modulator Driven by a SAW. *J. of Lightwave Tech.*, LT-5(2):218–228, 1987.

[40] T. R. Ranganath and S. Wang. Light Detection in Dielectric Waveguides by a Photodiode Through Direct Evanescent Field Coupling. *Appl. Phys. Lett.*, 31(12):803–806, 1977.

[41] M. Yamada and K. Sakuda. Analysis of Almost-Periodic Distributed Feedback Slab Waveguides via a Fundamental Matrix Approach. *Appl. Opt.*, 26(16):3474–3478, 1987.

[42] K. C. Chang and T. Tamir. Simplified Approach to Surface-Wave Scattering by Blazed Dielectric Gratings. *Appl. Opt.*, 19(2):282–288, 1980.

[43] V. Ramaswamy and R. K. Lagu. Numerical Field Solution for an Arbitrary Asymmetrical Graded-Index Planar Waveguide. *J. of Lightwave Tech.*, LT-1(2):408–417, 1983.

[44] A. Roberts and B. Mathews. Charge-Coupled Device (CCD) Camera/Memory Optimization for Expendable Autonomous Vehicles. *Opt. Eng.*, 21(2):354–358, 1982.

[45] S. Y. Huang, S. Esener, and S. H. Lee. N-p-n Silicon Lateral Phototransistors for Hybrid Integrated Optical Circuits. *IEEE Trans. Electron Dev.*, ED-33(4):433–441, 1986.

[46] D. Marcuse. *Theory of Dielectric Optical Waveguides*. Academic Press, 1974.

[47] N. Dagli and C. G. Fonstad. Analysis of Rib Dielectric Waveguides. *IEEE J. Quantum Electron.*, QE-21(4):315–321, 1985.

[48] J. C. Baumert and J. A. Hoffnagle. Numerical Method for the Calculation of Mode Fields and Propagation Constants in Optical Waveguides. *J. of Lightwave Tech.*, LT-4(11):1626–1630, 1986.

[49] H. Diestel. A Method for Calculating the Guided Modes of Strip-Loaded Optical Waveguides with Arbitrary Index Profile. *IEEE J. Quantum Electron.*, QE-20(11):1288–1293, 1984.

[50] J. Ctyroky, M. Hofman, J. Janata, and J. Schrofel. 3-D Analysis of LiNbO$_3$: Ti Channel Waveguides and Directional Couplers. *IEEE J. Quantum Electron.*, QE-20(4):400–409, 1984.

[51] M. Kuznetsov. Expressions for the Coupling Coefficient of a Rectangular Waveguide Directional Coupler. *Opt. Lett.*, 8(9):499–501, 1983.

[52] H. A. Haus, W. P. Huang, S. Kawakami, and N. A. Whitaker. Coupled-Mode Theory of Optical Waveguides. *J. of Lightwave Tech.*, LT-5(1):16–23, 1987.

[53] S. Kawakami and H. A. Haus. Continuum Analog of Coupled Multiple Waveguides. *J. of Lightwave Tech.*, LT-4(2):160–16S, 1986.

[54] A. Hardy and W. Streifer. Coupled Mode Theory of Parallel Waveguides. *J. of Lightwave Tech.*, LT-3(5):1135–1146, 1985.

[55] T. Tamir and T. Peng. Analysis and Design of Grating Couplers. *Appl. Phys.*, 14:235–254, 1977.

197

[56] D. Marcuse. Directional Couplers Made of Nonidentical Asymmetric Slabs. Part II: Grating-Assisted Couplers. *J. of Lightwave Tech.*, LT-5(2):268–273, 1987.

[57] G. A. Golubenko, A. S. Svakhin, and V. A. Sychugov. Diffraction Charactersitics of Planar Corrugated Waveguides. *Optical and Quantum Electron.*, (18):123–128, 1986.

[58] M. T. Wlodarczyk and S. R. Seshardi. Analysis of Grating Couplers in Planar Waveguides for Waves at Oblique Incidence. *J. Opt. Soc. Am. A.*, 2(2):171–185, 1985.

[59] M. T. Wlodarczyk and S. R. Seshardi. Analysis of Grating Couplers for Planar Dielectric Waveguides. *J. Appl. Phys.*, 58(1):69–87, 1985.

[60] M. V. Klein. *Optics*. John Wiley & Sons, 1970.

[61] H. G. Unger. *Planar Optical Waveguides and Fibers*. Clarendon Press, Oxford, 1977.

[62] P. K. Tien, S. Riva-Sanseverino, R. J. Martin, and G. Smolinsky. Two-Layered Construction of Integrated Optical Circuits and Formation of Thin-Film Prisms, Lenses, and Reflectors. *Appl. Phys. Lett.*, 24(11):547–549, 1974.

[63] B. Chen, E. Macon, and R. J. Morrison. Diffraction-Limited Geodesic Lens for Integrated Optical Circuits. *Appl. Phys. Lett.*, 33(6):511–513, 1978.

[64] D. W. Vahey, R. P. Kenan, and W. K. Burns. Effects of Anisotropic and Curvature Losses on the Operation of Geodesic Lenses in Ti:LiNbO$_3$ Waveguides. *Appl. Opt.*, 19(2):270–275, 1980.

[65] Z. D. Yu. Waveguide Optical Planar Lenses in LiNbO$_3$ - Theory and Experiments. *Opt. Comm.*, 47(4):248–250, 1983.

[66] R. Chen and W. S. C. Chang. Anomalous Attenuation and Depolarization Scattering in Y-Cut LiNbO$_3$ Proton Exchanged Waveguides. *IEEE J. Quantum Electron.*, QE-22(6):880–882, 1986.

[67] M. Rottschalk, A. Rasch, and W. Karthe. Temperature Dependence of the Extraordinary Refractive Index in Proton Exchanged LiNbO$_3$ Waveguides. *J. of Opt. Comm.*, 6(1):10–13, 1985.

[68] M. De Micheli, J. Botineau, P. Sibillot, and D. B. Ostrowsky. Fabrication and Characterization of Titanium Indiffused Proton Exchanged (TIPE) Waveguides in Lithium Niobate. *Opt. Commun.*, 42(2):101–103, 1982.

[69] J. L. Jackel, C. E. Rice, and J. J. Veselka. Proton Exchange for High-Index Waveguides in LiNbO$_3$. *Appl. Phys. Lett.*, 41(1):607–608, 1982.

[70] V. Hinkov and E. Ise. Control of Birefringence in Ti:LiNbO$_3$ Optical Waveguides by Proton Exchange of Lithium Ions. *J. of Lightwave Tech.*, LT-4(4):444–448, 1986.

[71] P. G. Suchoski, T. K. Findakly, and F. J. Leonberger. Low-Loss High-Extinction Polarizers Fabricated in LiNbO$_3$ by Proton Exchange. *Opt. Lett.*, 13(2):172–174, 1988.

[72] J. Ctyroky. Light Propagation in Proton-Exchanged LiNbO$_3$ Waveguides. *J. of Opt. Comm.*, 5(1):16–19, 1984.

[73] D. Marcuse. Tilt, Offset, and End-Separation Loss of Lowest Order Slab Waveguide Mode. *J. of Lightwave Tech.*, LT-4(11):1647–1650, 1986.

[74] W. B. Joyce and B. C. DeLoach. Alignment of Gaussian Beams. *Appl. Opt.*, 23(23):4187–4196, 1984.

[75] A. Yariv and P. Yeh. *Optical Waves in Crystals*. John Wiley & Sons, Inc., 1984.

[76] L. A. Kompalova, Y. G. Korolev, I. D. Torbin, and A. A. Berezhnoi. Dielectric Properties of Optical Cements. *Sov. J. Opt. Technol.*, 51(8):441–442, 1984.

[77] M. J. Li, M. P. De Micheli, D. B. Ostrowsky, and M. Papuchon. High Index Low Loss LiNbO$_3$ Waveguides. *Opt. Commun.*, 62(1):17–20, 1987.

[78] M. Belanger and G. L. Yip. A Novel Ti:LiNbO$_3$ Ridge Waveguide Linear Mode Confinement Modulator Fabricated By Reactive Ion-Beam Etching. *J. of Lightwave Tech.*, L^T-5(9):1252–1257, 1987.

[79] J. M. Harper and R. J. Gambino. Combined Ion Beam Deposition and Etching for Thin Film Studies. *J. Vac. Sci. Technol.*, 16(6):1901–1905, 1979.

[80] L. McCaughan and E. E. Bergmann. Index Distribution of Optical Waveguides from Their Mode Profile. *J. of Lightwave Tech.*, LT-1(1):241-244, 1983.

[81] W. R. Brunsvold, D. M. Crockatt, G. J. Hefferon, and C. F. Lyons. Resist Technology for Submicrometer Optical Lithography. *Opt. Eng.*, 26(4):330-336, 1987.

[82] B. Furch, E. Bratengeyer, and H. Rauch. Fast High Quality Edge Polishing of $LiNbO_3$. *J. Opt. Commun.*, 4(2):47-50, 1983.

[83] K. Rastani and A. R. Tanguay, Jr. Grating Outcoupling From Large Area Rib Waveguide Arrays Fabricated on Titanium Indiffused Lithium Niobate Substrates. *Integrated and Guided-Wave Optics, 1988 Technical Digest Series, (Optical Society of America, Washington, D.C.)*, 5:281-284, 1988; to be published.

[84] B. R. Appleton, G. M. Beardsley, G. C. Farlow, and W. H. Christie. Ion Beam Processing of $LiNbO_3$. *J. Mater. Res.*, 1(1):104-113, 1986.

[85] J. E. Bjorkholm and L. Eichner. Monitoring the Growth of Nonuniform Gratings Written Holographically by Gaussian Laser Beams. *J. Appl. Phys.*, 57(7):2402-2405, 1985.

[86] X. Mai, R. Moshrefzadeh, U. J. Gibson, G. I. Stegeman, and C. T. Seaton. Simple Versatile Method for Fabricating Guided-Wave Gratings. *Appl. Opt.*, 24(19):3155-3166, 1985.

[87] A. Katzir, A. C. Livanos, J. B. Shellan, and A. Yariv. Chirped Gratings in Integrated Optics. *IEEE J. Quantum Electron.*, QE-13(4):296-304, 1977.

[88] D. G. Hall. *Private communication.* University of Rochester.

[89] P.J. Martin, H. A. Macleod, R. P. Netterfield, and W. G. Sainty. Ion-Beam-Assisted Deposition of Thin Films. *Appl. Opt.*, 22(1):178-185, 1983.

[90] J. R. McNeil, G. A. Al-Jumaily, K. C. Jungling, and A. C. Barron. Properties of TiO_2 and SiO_2 Thin Films Deposited Using Ion Assisted Deposition. *Appl. Opt.*, 24(4):486-489, 1985.

[91] J. M. Naden, G. T. Reed, and B. Weiss. Analysis of Prism-Waveguide

Coupling in Anisotropic Media. *J. of Lightwave Tech.*, LT-4(2):156–159, 1986.

[92] B. Zhang, S. Forouhar, S. Y. Huang, and W. S. Chang. C_2F_6 Reactive Ion-Beam Etching of $LiNbO_3$ and Nb_2O_5 and their Application to Optical Waveguides. *J. of Lightwave Tech.*, LT-2(4):528–530, 1984.

[93] M Gottlieb, C. L. M. Ireland, and J. M. Ley. *Electro-Optic and Acousto-Optic Scanning and Deflection*. Marcel Decker, Inc, 1983.

[94] C. D. Daniel. Concepts and Techniques for Real-Time Optical Synthetic Aperture Radar Data Processing. *IEE Proc.*, 133(1):7–25, 1986.